Dissertation zur Erlangung des Doktorgrades

der Fakultät für Chemie und Pharmazie

der Ludwig-Maximilians-Universität München

Designing Single-Molecule Assays towards Directed Emission with DNA Origami Nanoantennas

Kristina Anna Hübner

aus

Rotenburg (Wümme), Deutschland

2022

Erklärung

Diese Dissertation wurde im Sinne von § 7 der Promotionsordnung vom 28. November von Herrn Prof. Dr. Philip Tinnefeld betreut.

Eidesstattliche Versicherung

Diese Dissertation wurde eigenständig und ohne unerlaubte Hilfe erarbeitet.

München, den 13.12.2021

Kristina Hübner

Dissertation eingereicht am:	13.12.2021
1. Gutachter:	Prof. Dr. Philip Tinnefeld
2. Gutachter:	Prof. Dr. Guillermo Acuna
Mündliche Prüfung am:	03.02.2022

Veröffentlichungen

K. Hübner, M. Pilo-Pais, F. Selbach, T. Liedl, P. Tinnefeld, F. D. Stefani, G. P. Acuna, Directing Single-Molecule Emission with DNA Origami-Assembled Optical Antennas, *Nano Letters*, **2019**, *19* (9), 6629-6634.

K. Hübner, H. Joshi, A. Aksimentiev, F. D. Stefani, P. Tinnefeld, G. P. Acuna, Determining the In-Plane Orientation and Binding Mode of Single Fluorescent Dyes in DNA Origami Structures, *ACS Nano*, **2021**, *15* (3),5109-5117.

K. Hübner, M. Raab, J. Bohlen, P. Tinnefeld, Salt-Induced Conformational Switching of a Flat Rectangular DNA Origami Structure, *Nanoscale*, **2022**, *14*, 7898-7905.

Abstract

Nanoscale light-control requires the precise positioning of nanooptical elements such as single quantum emitters and different kinds of nanoparticles. In this context, DNA origami nanostructures have proven a versatile scaffold to control positions and stoichiometry in an efficient self-assembly process. Besides spatial control, the close environment of organic fluorescent dyes often used as quantum emitters plays an important role. Changes in the environment can impact the properties of exposed fluorophores and DNA origami structures. In this thesis, DNA origami nanostructures are used to assemble a gap nanoantenna with directed emission properties using gold nanoparticles. Different single-molecule assays are developed to detail environmental effects relevant for the assembly of nanoantennas and other complex assemblies based on DNA origami structures.

For optical antennas, single quantum emitters have to be placed at the best coupling position between the emitter and the nanophotonic structure, which is the plasmonic hotspot. Besides a precise placement, the orientation of the fluorophore's transition dipole moment is a critical parameter for optimal coupling. Studying the importance of transition dipole moment orientations in an optical antenna is the subject of the first part of this thesis. A freely rotating dye is compared to a dye coupled to an optical antenna. The data shows that it is not only the emission transition dipole moment that has a defined orientation but also the absorption transition dipole moment. In addition, an alignment of both transition dipole moments is disclosed, revealing that the antenna's main resonance mode dominates the absorption as well as the emission. Conclusively, this study suggests that controlling the transition dipole orientations of fluorophores can create highly efficient antennas with the ability to control light at the nanoscale, such as complex routers or directors. As the alignment of fluorophores is not straight forward the second part of this thesis deals with the development of an assay to report on the relative orientation of a single fluorophore in a DNA origami structure. By a unique combination of super-resolution microscopy and polarization-resolved excitation microscopy, the orientations of structurally different dyes in different DNA origami nano-environments are determined. Supplementary molecular dynamic simulations help to rationalize the measured orientations and to assign possible conformational states. It is shown that the immediate surrounding such as missing nucleotides but also the molecular structures of the fluorophores play an important role for preferred dye-DNA interactions. All studies presented in this thesis are carried out in aqueous buffers with additive salts to stabilize the DNA origami structures. However, the concentration and identity of added salts can be crucial for DNA origami stability and functionality. In this context, super-resolution imaging reveals the fortuitous finding that changes in the concentrations of bivalent salts yield structural changes in a DNA origami rectangle. An energy transfer assay employing a gold nanoparticle as acceptor even reveals dynamical changes and indicates rolling-up of the structure along the diagonal axis that cannot easily be detected by common microscopy techniques. Furthermore, it is proven that dynamic structures do not need to be built with complex motifs like hinges, joints or catenanes or even hybridization locks to be functional.

To gain as many insights on the single-entity level, one main focus of this work is placed on the development of single-molecule assays. Developed single-molecule fluorescent microscopy techniques include a combination of polarization-resolved wide-field imaging and defocused imaging to report on

the orientations of the absorption and emission transition dipole moments. With combined DNA-PAINT and polarization-resolved wide-filed measurements the orientations of DNA origami rectangles and related fluorophore orientations in the DNA origami structures can be revealed. Finally, by a combination of DNA-PAINT and scanning confocal fluorescence lifetime microscopy, high structural and temporal resolution in a dynamically switching DNA origami structure is gained. The developed assays have the potential to be useful for answering other scientific questions, in particular on the single-entity level.

Table of Contents

1. Introduction

Fluorescence microscopy has emerged to be a basic tool in science and is based on the findings by Stokes, who observed a red shift of the emission compared to the absorption spectrum[1], which opened up the field of single-molecule fluorescence microscopy (SMFM).[2–4] Here, isolated emitters are studied in contrast to conventional studies on the average of many. Thus, photophysical properties of individual entities can be investigated, and heterogeneities in samples can be addressed without being buried under broad distributions.

1.1 Optical Antennas to Control Light at the Nanoscale

One big field that has emerged to be studied with SMFM is the field of plamonics. In plasmonic assemblies, metal nanoparticles (NPs) are placed in predefined geometries. The NPs are much smaller than the wavelength of the illuminating light, which causes a collective oscillation of free electrons in the metal. This phenomenon is called localized surface plasmon resonances (LSPRs). These oscillations create an enhanced electric field in the NP's near field. Thus, an NP can act as a receiver for electromagnetic waves creating an enhanced near field close to the NP's surface (*Figure 1a*), or, if an emitter is placed in the near field of the NP, it can act as a transmitter transferring emitted light from the near field to the far field leading to a directionality of the signal (*Figure 1b*).[5] So its basic behavior is pretty similar to its counterparts in the radio and micro wave regime.

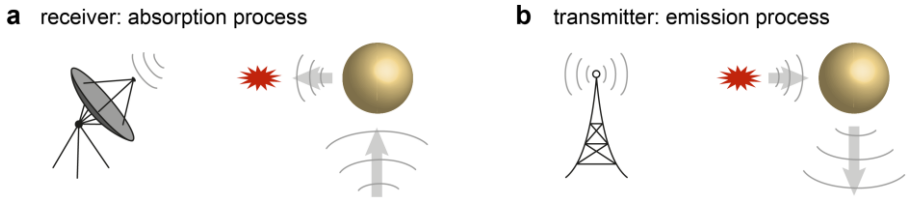

Figure 1: Antennas in the radio/micro wave regime and in the nanoscale. Antennas can act as receivers (a) or as transmitters (b) corresponding to absorption and emission processes in the nanoscale, respectively.

For the coupling of a fluorophore and an OA, the spectral overlap of both plays an important role. NPs behave differently depending on their size. This is not only visible in their color but also in their photophysical behavior. While big NPs lead to an enhancement of the fluorophores emission, smaller NPs cause a quenching effect.[6,7] Often, plasmonic NPs are arranged in dimer structures that are able to interact with light in the visible wavelength regime and that can be referred to as optical antennas (OAs).[8] OAs interacting with incoming light create an enhanced electric field between the two particles, which is called the hot spot region.[5,9] Methods to create OAs are for example e-beam lithography or ion beam milling. Shortcomings of these top-down processes are the limited throughput and the time-consuming procedure going along with a serial production of the structures. Other disadvantages are the limitation of materials that can be used for fabrication as well as the difficult precise and

stoichiometric positioning of single fluorescent molecules in the hot spot region of OAs[5]. Hence, many lithographically created OAs are measured in dye solutions with fluorescent molecules diffusing through the hot spot region to study the dye OA interactions. One prominent example is the bowtie antenna built from two triangular gold platelets (*Figure 2*a).[10] Disadvantages of this and comparable assemblies are the high background signal of free diffusing dyes in solution and the lack of positional control of the dyes with respect to the OA structure. The correct placement of a single fluorophore plays an important role in coupled dye-OA systems because of the influence on the fluorophore's photophysical properties, such as the excitation and emission rate. As a consequence, the fluorescence enhancement and quantum yield are also highly dependent on the fluorophore's relative orientation to the OA.[11]

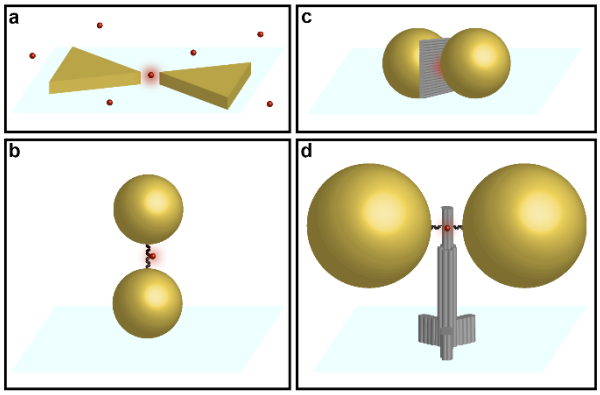

Figure 2: Dimer antenna structures. (a) Lithographically produced bowtie antenna surrounded by fluorophores in aqueous solution (adapted from [10]). (b) DNA hybridized gold nanoparticle dimer antenna with an attached fluorophore (adapted from [12]). (c) and (d) DNA origami structures as bread boards to build different kinds of dimer antennas with controlled gap size and a fluorophore in the hot spot region (adapted from [13] and [14]). All antenna structures can be immobilized on a glass surface for single-molecule studies.

To overcome the fabrication issues of lithography, other techniques are used to assemble dimer antennas. The polymeric DNA molecule has shown to be a good choice as DNA is not interacting with the visible wavelength region of light and provides the possibility to control the distance between two NPs. In the simplest assemblies, a double stranded DNA helix is used to bridge two NPs (*Figure 2*b).[15] In this way it is possible to control the distance between the NPs. In more complex assemblies, DNA origami structures are used as bread boards to position two NPs to build dimer OAs (*Figure 2*c and d).[11,13,14] DNA origami is a bottom-up technique[16,17], which relies on the high flexibility and the modulation capability of the DNA biomolecule. Furthermore, the specific base pairing between the four nucleobases (adenine with thymine, guanine with cytosine) and its robustness owing to stabilizing cross-overs between the single helices are basic benefits of this method. DNA origami structures can adopt nearly every shape in 2D but also in 3D in the nanometer range.[18] They have the advantage of controlling geometric and stoichiometric placement of NPs and emitters, based on a self-assembly process, which is easy to handle and shows a high reproducibility. Studies based on DNA origami structures as bread boards range from fundamental research to study the effect of the OA on the photophysics of a fluorescent dye[19–24] to diagnostic assays to detect target molecules by signal

amplification.[25–28] Besides fluorescence studies, numerous Raman[29–32], SERS[31] and dark field measurements[30,33] have also been performed.

Due to the advantage of attaching a fluorescent molecule by a linker to the DNA, single fluorophores can be easily placed in the hot spot region of OAs. This is advantageous because the molecule's excitation rate is proportional to $\langle \vec{E} \cdot \overrightarrow{\mu_G} \rangle^2$, with $\vec{E}$ being the electric field vector created in the hot spot region by the incidence field and the induced field from the OA, and $\overrightarrow{\mu_G}$ being the molecules absorption transition dipole moment.[34] Fluorophores linked to DNA have the ability to rotate freely around their linkers if surrounded by an aqueous solution. Yet also fixed orientations can be taken that are either undefined through interactions with the immediate surrounding or defined for a doubly linked[35] fluorophore. The orientation of the dye is therefore important as the radiative decay rates of fluorophores depend on the relative orientation between the emission dipole transition moment $\overrightarrow{\mu_E}$ and the OA. This can lead to a complete suppression of the fluorescence, if oriented perpendicular to the OA's axis, but also to a strong enhancement in a parallel orientation.[11,13,36–38] The effect of fluorescence intensity modulation in emission can be explained by the creation of image charges in the NPs from the transition dipole moment of the fluorophore. If the transition dipole moment of the fluorophore is aligned to the OA's dimer axis (radial), a coupling between the fluorophore and the OA will occur, enhancing the fluorescence intensity. But if the transition dipole moment is perpendicular (tangential) to the dimer axis, the dipoles of the fluorophore and NPs will cancel out each other leading to a fluorescence quenching. The effect on the emission of a coupled fluorophore can also be studied theoretically.[6,39] In addition, the effect of strong enhancement is highest if the polarization of excitation matches the OA's axis.[20]

The task at hand is to establish an assay that can map the polarizability in emission and absorption processes (chapter 4.1 and associated publication P1). Fluorescent dyes are checked for their ability to behave like an isotropic emitter in an aqueous medium. After the isotropic behavior is determined, it should be checked how the emission and absorption properties will change if coupled to an OA. To this end, OAs with a fluorophore placed in the hot spot region are self-assembled on a DNA origami structure. To measure the emission and absorption polarizability of these coupled systems, an assay is developed. On the one hand, defocused imaging pictures the emission pattern of the imaged system. The pattern sheds light on an isotropic or anisotropic emission behavior and at the same time reveals the orientation of the dipole emitter to a surface. On the other hand, with the help of polarization-resolved wide-field measurements it is possible to not only show an anisotropic behavior in the absorption but also indicate the orientation of the absorption dipole due to the knowledge of excitation polarization at any time.

1.2 Dye Orientations in Energy Transfer Assemblies

The two-fold importance of the orientations of fluorescent molecules in OA assemblies has already been discussed above. Calculations of the normalized quantum yield of an emitter placed in the hot spot region of an OA are depicted in *Figure 3a*. Here, the strong dependence of the quantum yield on the relative orientation of the fluorophore is illustrated in correlation with the excitation wavelength. The main

conclusion of the graph is the strong quenching in a perpendicular orientation, while the parallel orientation is enhanced. However, dye orientations do play a crucial role not only in OA assemblies but also in other energy transfer assemblies like FRET (Förster resonance energy transfer)[40,41], GET (graphene energy transfer)[42–44], MIET (metal induced energy transfer)[45,46], or in super-resolution localization precision[47–51]. Often, the relative orientation between two dipolar systems plays an important role, such as in FRET assemblies, where an energy transfer occurs between a spectrally overlapping donor-acceptor pair separated by a distance below 10 nm. The efficiency of the energy transfer strongly depends on the relative orientations between the two molecules and is described by the orientation factor κ^2. This factor maximizes to a value of 4 if the two dipoles of the fluorophores are aligned and has a minimum of 0 for a perpendicular orientation (*Figure 3*b).[3]

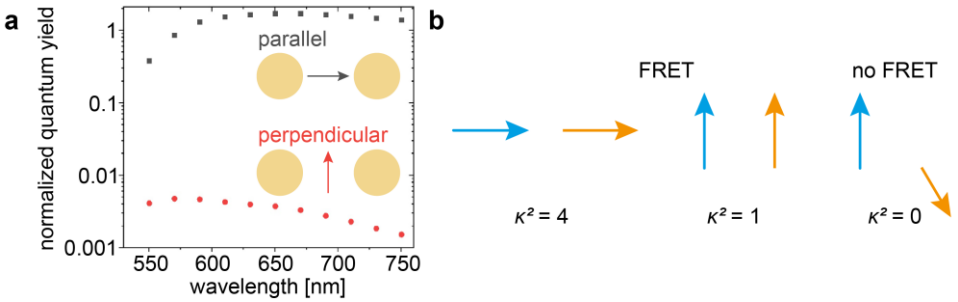

Figure 3: Dipole orientations in OA and FRET assemblies. Normalized quantum yield of Cy5 in an OA at parallel and perpendicular orientations in dependence of the excitation wavelength (a). Different dipole orientations in FRET (b) yield individual orientation factors (κ^2). In a head-to-tail aligned case, κ^2 is 4, parallel to each other it is 2, and in a perpendicular orientation it is 0. (a) Reprinted with permission from [13].

Usually, fluorescent dyes attached to DNA are assumed to rotate freely fixed in one position by a linker. However, not all dyes show the ability of free rotation but are able to interact with their immediate surrounding that can hold them in a fixed position. Although the orientation of for example metal nanorods[52] or triangles[53] can be controlled, there is nearly no control to orient fluorescent molecules in DNA. Principally, two different methods exist to attach dyes to DNA. First, they can be attached non-covalently through an interaction with the double stranded DNA (dsDNA) helix. The interaction thereby depends on the molecular identity of the dye, which can interact with the base pairs in the dsDNA (intercalators), bind to the major groove of the dsDNA helix or adhere to the DNA's backbone.[54] Gopinath et al showed that the intercalating dye TOTO-3 always binds with a preferred orientation of 70°± 10° to DNA.[55] Although an orientation control is given, a stoichiometric or geometric control is not present. Here, again, the big advantage of DNA origami structures comes into play. Due to the high specificity of DNA hybridization, fluorescent dyes linked to a short single stranded DNA sequence can bind covalently with a high geometrical and stoichiometric control. However, the orientation control is not given. Fluorescent molecules can be either attached to the 3'- or 5'-end or even internally by e.g. the use of an amino-C6 linker. Besides the lack of orientation control in DNA origami structures, no reliable methods exist that can help to retrieve the orientations of covalently attached fluorescent dyes in DNA origami structures. Earlier work shows for example, that Cy3 and Cy5 attached to DNA maintain preferential orientations due to blunt end sticking when attached by a C3-linker[56] but remain freely

rotating when attached by other linkers[57]. So the choice of linkers in DNA assemblies has a great importance. Other studies based on FRET can report on the relative orientations between the two fluorophore dipoles but not on the relative orientations in the DNA assembly. A study to extract the relative orientation of fluorophores in a short dsDNA helix was performed using single-molecule localization techniques.[58] Because of the short length of the helix, it can be assumed to be rectilinear, but the DNA was adsorbed to a positively charged surface, which could impact the fluorophores orientation. It is still challenging to control the orientation of fluorophores in DNA origami structures, although fluorophores exist that can be labeled at two ends[35]. Furthermore, an extraction of the relative orientation in DNA origami structures also remains challenging.

To answer the question of fixed dye orientations in DNA origami structures, a new assay is developed and examined (chapter 4.2 and associated publication P2). Dye orientations can be extracted with the help of polarization-resolved wide-field measurements yielding modulating traces for fixed dipole orientations with a 180° resolution. Besides the orientation of the dyes, the orientation of the DNA origami structure to which the dye is attached also needs to be known. To resolve this orientation a DNA-PAINT measurement is operated with a designed asymmetric pattern of DNA-PAINT binding sides on the DNA origami structure. The asymmetric pattern enables to resolve the orientation of the DNA origami structures with a 360° resolution on the glass surface. Furthermore, it can report on an upside-down binding of the structures. After both measurements have been performed, two angles can be assigned to each other yielding the relative orientation of the dyes in the DNA origami structures. As the sticking of dyes in DNA origami structures can vary with the dye's position, different classes of dyes in different nano-environments are studied. As the measurements alone only give rise to the orientation but cannot resolve the molecular structure, all atom molecular dynamics (MD) simulations are carried out. The experimental and theoretical results together can give a good picture on how and in which orientation fluorophores can stick to DNA.

1.3 DNA Origami Structures at the Influence of High Salt Concentration

Not only dyes can be locked in certain orientations, but dynamic structures can also show similar effects. For example, in four-way junctions, also called Holliday Junctions[59], an alternation between two isomerization states is observed. These states are stabilized by bridging magnesium ions between neighboring DNA helices and can have long-lived salt-nucleic acid interactions showing a kind of memory effect[60]. Elevated magnesium ion concentrations can slow down the switching kinetics of the junctions.[61] This shows that ions play an important role in bridging and stabilizing DNA helices as well as DNA origami structures.[62] Thus, DNA origami structures, especially the twist-corrected rectangular DNA origami structure (NRO) of the original RRO from Rothemund, shows a response on increased magnesium concentrations. A diagonal distance measured on the NRO with a DNA-PAINT experiment decreases, while the long axis appears to be slightly increased (*Figure 4*).[63]

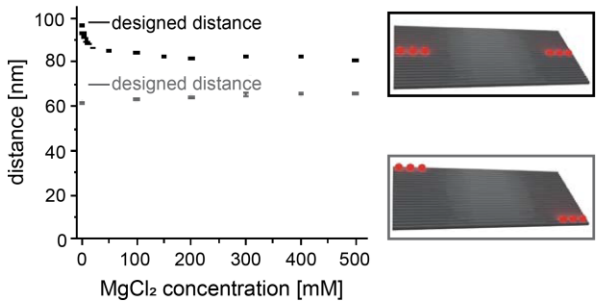

Figure 4: Distance changes in a rectangular DNA origami structure (NRO) due to the increase of $MgCl_2$ concentration. Distances on the DNA origami structures are measured along the long side and the diagonal showing a decrease and a nearly continuous distance, respectively. Reprinted with permission from [63].

In oxDNA simulations of an NRO structure, a bending of the rectangle along two possible diagonal axes is observed.[64] The effect of distance reduction due to increased salt concentrations and bending of the rectangular DNA origami structure gives rise to the question whether both findings can be combined. To observe possible static or dynamic changes in the DNA origami structures, tools are needed that yield more than average values. These tools include optical[65–67] and mechanical[68–70] single-molecule methods or molecular dynamic simulations[71]. Therefore, in this thesis an assay to monitor the structural changes in the DNA origami rectangle with high structural and temporal resolution is developed (chapter 4.3 and associated publication P3). An arrangement of DNA-PAINT binding sides on the rectangular DNA origami structure at the long sides permits to detect structural changes. Distance measurements between the two imaged parallel lines help to answer the question with regard to a possible gradual structural change in the DNA origami structure. However, the finding is that two different kind of structures are present in the super-resolved images, which possibly imply a rolling-up. This fortuitous effect is interesting to study as usually structural changes are only obtained by the implementation of special motifs like hinges[72], joints[65,67,73,74], or catenanes[75]. But to provide evidence of underlying dynamics, the method of DNA-PAINT is not practical as the acquisition times are in the minutes' time range. So a more sensitive assay has to be developed to gain structural and temporal resolution to answer the question of possible dynamics. To this end, an energy transfer assembly is introduced to the DNA origami structure. Usually, FRET assemblies are used to report on structural changes in dynamic systems, which show the disadvantage of acceptor bleaching and small working ranges, where the distance of 50% energy transfer is limited to about 6 nm. Here an energy transfer between a single fluorophore and a 10 nm gold nanoparticle is used, with the NP as an unbleachable acceptor and a distance of 50% energy transfer of 10.4 nm[19]. The introduced energy transfer relies on the ability of small NPs to quench the fluorescence intensity and lifetime. In the presented assay a quenching occurs when the fluorophore approaches the NP. This effect can be monitored by confocal lifetime imaging.

1.4 Implementation of Combined Single-Molecule Methods

The studies presented in this thesis range from imaging the polarizability in emission as well as absorption processes to the extraction of dye orientations in DNA origami structures through to the resolution of structural and dynamic processes in flexible DNA origami structures. To study these effects on the single-molecule level, new assays are required. These assays are a combination of defocused and polarization-resolved wide-field imaging to gain information about the emission and absorption dipole orientations. A combination of DNA-PAINT and polarization-resolved wide-field imaging allows to extract the relative orientations of fluorescent dyes in DNA origami structures. Lastly, to observe the structural changes in DNA origami structures with a high spatial and temporal resolution, DNA-PAINT measurements are combined with an energy transfer assembly in scanning confocal lifetime imaging. These assays can be used for a broader range of studies as discussed in chapter 5. Hence, one main focus of this thesis is to expand the toolbox of single-molecule imaging and assays.

2. Theoretical Background

This chapter provides an overview of the theoretical principles needed for the understanding of the processes studied in this work. The basics of the photophysics of organic dyes is explained, and strategies to prevent the dyes from photobleaching and blinking are discussed. Additionally, plasmonic NPs are introduced together with a short theoretical explanation of the basic principles of localized surface plasmon resonances. Then, the interaction between a plasmonic NP and an organic fluorophore is explained. In the last part, the technique of DNA origami folding is introduced.

2.1 Photophysics of Organic Dyes

Fluorescence is a spontaneous process that might take place after exciting a molecule with light. For an excitation process to happen, the energy of the exciting photon has to match the energy for an electron to overcome the energy barrier between the electronic ground and the excited state.[3] The energy of a photon can be described by Planck's law[76]:

$$E = \frac{h \cdot c}{\lambda} \tag{2.1}$$

Here, h is the Planck constant ($6.626 \cdot 10^{-34}$ J/Hz), c the speed of light ($2.998 \cdot 10^{8}$ m/s) and λ the excitation wavelength. The process of excitation through energy absorption is regulated by the Franck-Condon principle.[77,78] It states that excitation is a transition of an electron from the ground state into the excited state and only occurs if the vibrational wave functions between the different states show a high symmetry. An important assumption that has to be made to explain these processes is the Born-Oppenheimer approximation[79], which says that the heavier nuclei of the molecules can be assumed to be static compared to the lighter electrons.

Following the rules explained above, the transitions in excitation/absorption and emission processes can be summed up in a Jablonski diagram (*Figure 5a*).[80] Involved processes can be radiative (solid arrows) or non-radiative (dashed arrows). After excitation from the ground into the excited state S_1 (blue arrow) at a rate constant k_{exc}, the excited molecule can take different paths to decay to the ground state (S_0). Besides the excitation to the S_1 state, higher electronic states (S_2 – S_N) can also get populated, which, for reasons of simplicity, is not depicted here. A depletion from the excited state to the ground state can appear through heat dissipation (k_{nr}; dark gray dashed arrow) or through the radiation of a photon as fluorescence (red arrow) with a rate constant k_{fl}. This process shows a lower energy than the excitation, which is also indicated by the length of the arrows. The loss in energy results in a spectral red-shift of the emitted wavelength compared to the excitation wavelength (*Figure 5b*), which is also known as Stokes shift[1]. It is important to note that due to Kasha's rule[81], emission can only result from the vibrational ground state of the excited S_1 state. Thus, if the molecule is excited to higher vibrational states, it first has to undergo internal conversion (light gray dashed arrows) before a transition to the electronic ground state S_0 takes place, as stated by the Stokes shift. This shift enables the separation of emission from the excitation light by the simple use of spectral filters. The broadening of the absorption

and emission spectra in *Figure 5b* thereby results from transitions involving not only the vibrational ground states of S_0 and S_1. In the excitation spectrum, this broadening arises from the excitation to higher vibrational states of the S_1 state. In the emission spectrum, a depletion from the vibrational ground state of S_1 to higher vibrational states of the S_0 state is leading to the spectral broadening.[3] In addition to the directly decaying processes from the S_1 to the S_0 state, the molecule can undergo intersystem crossing (k_{isc}; orange dashed arrow) from the singlet S_1 to the triplet T_1 state. This process requires a spin flip of an electron, which is an unlikely and un-favored process taking place on a relatively long time scale compared to the other processes. Once the transition into the triplet state happens, phosphorescence (k_{phos}; green arrow) under light radiation or a non-radiative process (k_{nr}; dark gray dashed arrow) through heat dissipation to the ground state S_0 can occur.

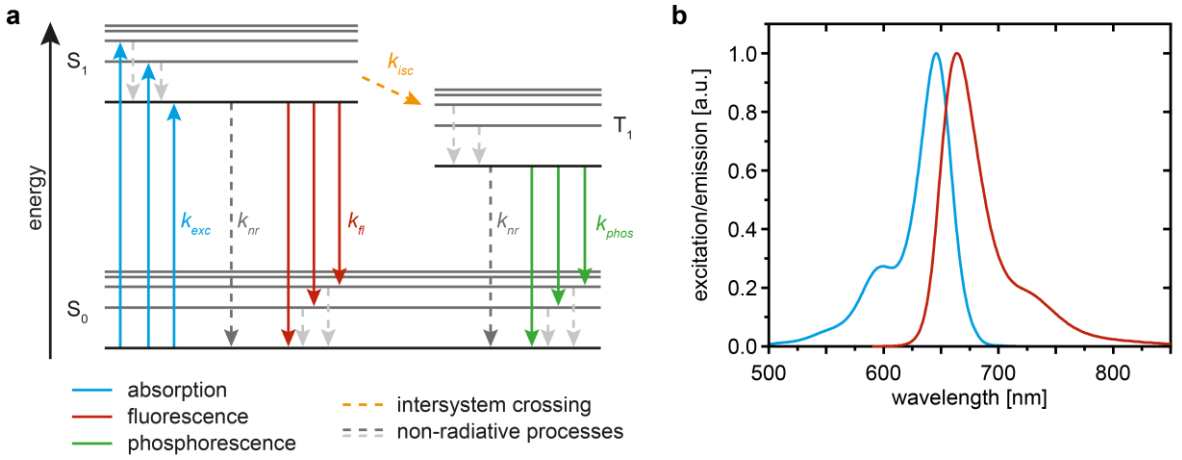

Figure 5: Jablonski diagram and excitation/emission spectra of ATTO 647N. (a) Jablonski diagram showing the processes during fluorescence. The singlet states S_0 and S_1 as well as a triplet state T_1 with rotational levels are involved in the transitions. These transitions, i.e. the excitation/absorption process (blue) with its rate constant k_{exc}, the emission/fluorescence process (red) with the rate constant k_{fl}, and the phosphorescence (green) with k_{phos}, are radiative processes. The internal conversion (light grey), the non-radiative decay (dark grey) with k_{nr}, and intersystem crossing (orange) with k_{isc} are non-radiative processes. (b) Exemplary absorption (blue) and emission (red) spectra of the ATTO 647N dye[82].

Each fluorophore is characterized by further photophysical parameters, which are emission and absorption spectra, the fluorescence quantum yield, and the fluorescence lifetime. The fluorescence quantum yield ϕ_{fl} (equation 2.2) is a measure of the fraction of emitted photons N_{em} compared to absorbed photons N_{abs}. It can be written as the ratio of the fluorescence rate constant (k_{fl}) to the sum of all rate constants of the processes depopulating the S_1 state (k_{fl}, k_{nr}, k_{isc}).

$$\phi_{fl} = \frac{N_{em}}{N_{abs}} = \frac{k_{fl}}{\sum k} \tag{2.2}$$

A value of ϕ = 1 means that all absorbed photons are emitted without any losses. The fluorescence quantum yield can take values between 0 and 1.

The average time that a molecule spends in the excited S_1 state is the fluorescence lifetime, which is defined by

$$\tau_{S_1} = \left(k_{fl} + k_{nr} + k_{ISC}\right)^{-1} \tag{2.3}$$

The fluorescence lifetime is in the range of 10^{-9} to 10^{-8} s, whereas phosphorescence takes place on longer time scales in the 10^{-3} to 10^{0} s.

2.1.1 Radiation Characteristics of Dipole Emitters

To fully describe the processes illustrated in chapter 2.1, the radiation characteristics of dipole emitters have to be considered, too. Therefore, the dipole character of organic dyes with a transition dipole moment and the radiation propagation of the electric field in the emission process has to be taken into account. Fluorophores can be treated as Hertzian dipoles, which are harmonically oscillating point dipoles with a transition dipole moment *μ*. The dipole moment will be oriented according to the molecular structure of the dye (*Figure 6a*) in the delocalized π-electron-system.[3,83]

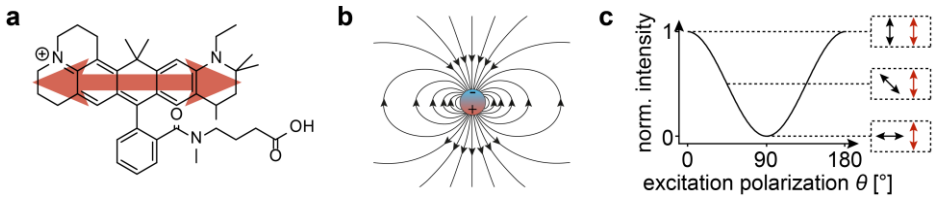

Figure 6: Dipole character of a fluorescent dye. (a) Molecular structure of ATTO 647N with an arrow illustrating the transition dipole moment μ. (b) Electric field vectors created around an electric dipole. (c) Schematic of the emission intensity of a fixed fluorophore (red arrow) by linear polarized light (black arrow) of different relative orientations to the emitter.

Emission of an organic dye always occurs perpendicular to the orientation of its dipole moment and is zero along the dipole axis (*Figure 6b, Figure 7a*). As the dipole is oscillating, the charges change periodically and the created field is broken and builds up again. For a dye situated close to an interface of two different media with different refractive indices (e.g. water–glass), the radiation is altered by an evanescence field coupling. The evanescent field couples to the medium of higher refractive index, which results for the case of a water–glass interface (with water above and glass below) in a radiation mainly into the glass (*Figure 7b, c*).[84] *Figure 7 b* and *c* show how the angular power radiation of a dipole is varied for different dye orientations (vertical and horizontal) at the water-glass interface.

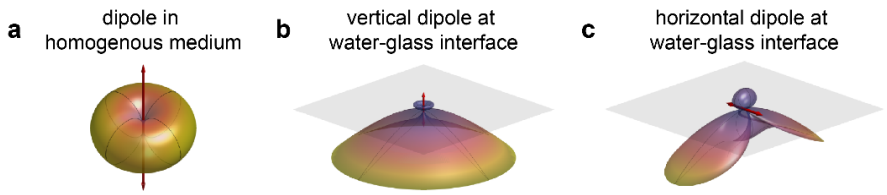

Figure 7: Emission of a dipole emitter. Agular power radiation in a homogenous medium (a) and close to a water-glass interface with a vertically (b) and horizontally (c) oriented dipole. (Adapted from [85])

In light microscopy, the direction of preferred emission into glass is related to the collection direction of emitted light. In single-molecule experiments, fluorescent dyes are often studied in aqueous solutions. Under these conditions the dye is able to rotate freely and has the character of an isotropic emitter, meaning it emits homogenously in all directions. A dye that is either fixed by a solid surrounding medium, dried on a surface or hold in one position by other means behaves like an anisotropic emitter. Here, the nature of organic dyes of preferentially absorbing light with an electric field vector parallel to its transition dipole orientation comes into play. Thus, the fluorescence intensity is maximized for the orientation of excitation polarization θ parallel to the orientation of the transition dipole moment φ and minimized in a perpendicular situation (*Figure 6c*). Knowing the angle of the linear polarized excitation light enables the extraction of the orientation of a fixed fluorescent dye in the lateral plane.

2.1.2 Photostabilization of Organic Dyes

Huge drawbacks of organic fluorophores are photobleaching and blinking processes. After excitation, the fluorophore can enter a triplet state instead of relaxing to the ground state via fluorescence radiation (*Figure 8a*). In the triplet state the fluorophore can interact with oxygen, which has a triplet character in its ground state. A result from this interaction is singlet oxygen, which is highly reactive and can irreversibly oxidize the chromophoric system.[86] To circumvent the process of photobleaching, oxygen scavenging chemicals are added to the measurement buffer. These agents are enzymatic systems like a combination of glucose oxidase, catalase, and glucose. The reaction of glucose with the oxygen in solution is catalyzed by glucose-oxidase giving glucolactone and hydrogen peroxide as reaction products (*Figure 8b*). Additional added catalase decomposes the hydrogen peroxide to oxygen and water.[87,88] This process induces a longer-lived triplet state that can no longer be depopulated by the interaction with oxygen, and therefore longer off-times occur.

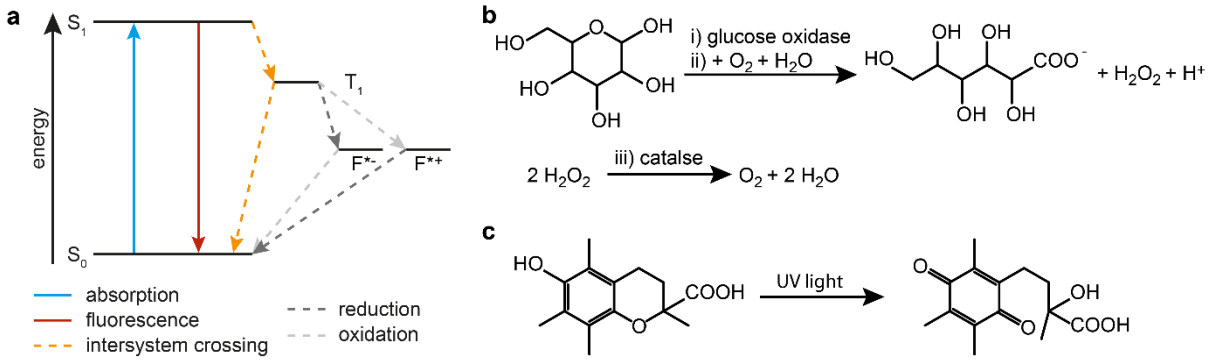

Figure 8: Modified Jablonski diagram for ROX system, oxygen scavenging reaction, and trolox conversion. (a) Jablonski diagram showing the excitation (blue) and emission (red) process with additional pathway (orange) to the triplet state T_1 from where reduction (dark gray) and oxidation (light gray) through transient radical states ($F^{\bullet-}$ and $F^{\bullet+}$) occur. (b) Reaction of glucose with glucose oxidase and catalase for oxygen scavenging. (c) Conversion of trolox to trolox quinone by UV irradiation.

The second limiting process in single-molecule studies is the blinking of fluorescent dyes that occurs due to a temporary occupation of dark states like the triplet state. To circumvent this limitation, a depopulation of the triplet state can be induced by reducing and oxidizing (ROX) chemicals (*Figure 8a*),

where two pathways are possible. One possibility is that the fluorophore first gets reduced entering a radical anion state before the oxidation to the ground state S_0 occurs, and the second possibility is that the process takes place via a radical cation intermediate state. As a ROX system, the vitamin E analogue trolox and its quinone can be used to depopulate the triplet state.[89,90] The quinone is synthesized by the irradiation of trolox with UV light (*Figure 8c*) until both forms are equally concentrated in solution.

By combining both systems, i.e. the oxygen scavenging and ROX agents, the fluorescent dyes can be protected from photobleaching as well as from blinking kinetics that makes them very photostable and useful in a broad range of SMFM applications.

2.2 Metal Nanoparticles

The use of the photophysical properties of metallic NPs dates back to the Roman times when the particles were used to dye ceramics or to create shiny glasses like sacral windows. Although the theory behind the origin of the color was not understood at that time, it was widely used. One of the most famous examples is the Lycargus cup, where gold and silver particles are dispersed in glass. This cup shows a red color when illuminated from the back and green when illuminated from the front.[91]

Later, the physics behind the color has been more and more understood and described by several theories. A model for the charge transport in metals through the interaction with an electromagnetic field was first developed by Drude in 1900.[92,93] This model was added by Arnold Sommerfeld in1933[94], who showed the absorption and scattering of light. Exact calculations of the absorption and scattering of spherical NPs were made by Gustav Mie in 1908.[95] The field of nanoantennas made from metallic NPs that act as receivers or emitters of electromagnetic light was introduced by Wessel in 1985. Furthermore, NPs can transverse light into a local field and affect emitters close by, something which is used in a broad variety of applications.

In this chapter, the theory behind the color and the interaction of metal NPs smaller than the wavelength of light with impinging electromagnetic waves is discussed. Moreover, the coupling of a plasmonic NP with another NP and a fluorescent dye is introduced afterwards.

2.2.1 Plasmonic Nanoparticles

Metals like gold or silver are known in daily life as jewelry but not for their property to interact with light. However, as their size decreases new properties arise, which can be of advantage in scientific assemblies. These so-called metallic nanoparticles can exhibit different optical properties depending on their material, size, and shape.[96,97] Mostly, rod-like structures or spherical NPs are the subject of studies, but also triangles[53,98], disks[99,100] or even nanostars[101,102] have been examined. *Figure 9* shows a series of gold and silver NPs of different sizes. The color of the NPs thereby is given through the spectral regions where absorption and scattering processes occur. Gold NPs absorb and scatter in the green wavelength region, so they appear red to our eyes, whereas for silver these processes take place in the blue region, making them yellow.

Figure 9: Spherical gold and silver nanoparticles of different sizes exhibit different colors in solution. Adapted from [103].

The absorption and scattering cross-sections are defined by the resonance behavior of the metal interacting with an electric field (e.g. light). An electromagnetic wave impinging on the metal's surface induces a light matter interaction of the propagating light wave with the electrons in the conduction band of the metal atoms. A result of this interaction is a displacement of the electron cloud from its equilibrium position. The separation of charges induces a restoring force through Coulomb attraction, and the electron gas starts to oscillate as depicted in *Figure 10a*.[6,104,105] The oscillation driven by the restoring forces only occurs at a specific size-dependent frequency. A condition which has to be fulfilled for this type of interaction is that the NPs need to be much smaller than the wavelength of light ($R/\lambda < 0.1$, with R being the radius of NP and λ the incidence wavelength).[106] In this case, the NP acts as an oscillator with an induced dipole moment, and its resonance behavior determines the optical properties of the NP.[8,106] The oscillating charges can also be described as plasmons. At a planar interface the plasmons are called surface plasmon polaritons, and they propagate freely along the interface. In the case of NPs, plasmons are confined to the NP's geometry and are termed localized surface plasmon resonances (LSPRs).[6] The penetration of the electromagnetic field into the NP is limited to a certain depth, called the skin depth, and is about 15 nm in the vis-NIR region for gold.[107,108] The strength of oscillation is impacted by the NP's size as well as by damping effects through radiative and non-radiative processes (*Figure 10b*). On the one hand, energy losses can occur through a radiative decay via the emission of a photon. On the other hand, non-radiative transitions can occur as interband or intraband transitions with an excitation from the *d*-band to the conduction band or within the conduction band, respectively.[109]

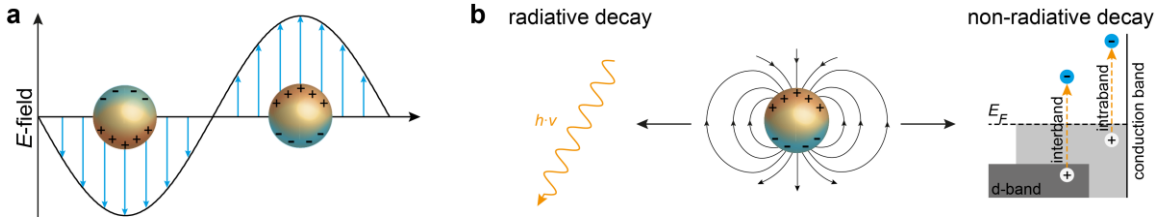

Figure 10: Oscillating NPs and decay processes in NPs after light irradiation. (a) In-phase oscillation of the electron gas in a metal nanoparticle with the electric field of a propagating electromagnetic wave. (b) Surface plasmons can decay radiatively by the emission of a photon or non-radiatively by building electron-hole pairs through interband and intraband transitions from the d-band to the conduction band or within the conduction band. (Adapted from [109])

The Mie theory provides a full analytical model to calculate the LSPRs of spherical nanoparticles.[95,110] For NPs much smaller than the wavelength of light, the Rayleigh approximation can be used.[111,112] This

approximation helps to explain the distortion of the electron cloud in response to an external electric field through the polarizability α, given by

$$\alpha(\lambda) = 4\pi\varepsilon_0 R^3 \frac{\varepsilon(\lambda)-\varepsilon_m(\lambda)}{\varepsilon(\lambda)+2\varepsilon_m(\lambda)} \tag{2.4}$$

Here, λ is the wavelength of light, *R* the NP's radius, ε_0 the vacuum permittivity, ε_m the dielectric constant of the surrounding medium, and $\varepsilon = \varepsilon' + i\varepsilon''$ the complex relative permittivity of the NP. The surface plasmon resonance is reached when α is maximized, which occurs when the denominator in equation 2.4 is minimized.[113] This condition is met when $\varepsilon(\lambda) = -2\,\varepsilon_m(\lambda)$, which is referred to as Fröhlich condition.[114] It is important to note that both the dielectric function of the NP, which is dependent on the wavelength, and the medium impact the resonance condition.

The Rayleigh theory, which is valid for small NPs (< 50 nm), helps to describe the elastic scattering of light.[115] This leads to the expressions for the scattering cross-section[116]

$$\sigma_{sca} = \frac{k^4|\alpha(\lambda)|^2}{6\pi\varepsilon_0^2} = \frac{8\pi k^4 R^6}{3}\left|\frac{\varepsilon(\lambda)-\varepsilon_m(\lambda)}{\varepsilon(\lambda)+2\varepsilon_m(\lambda)}\right|^2 \tag{2.5}$$

and the absorption cross-section[116]

$$\sigma_{abs} = \frac{k}{\varepsilon_0}\,\mathrm{Im}[\alpha(\lambda)] = 4\pi k R^3 \mathbf{Im}\left[\frac{\varepsilon(\lambda)-\varepsilon_m(\lambda)}{\varepsilon(\lambda)+2\varepsilon_m(\lambda)}\right] \tag{2.6}$$

Here, k is the wave vector, and $\mathbf{Im}[\alpha(\lambda)]$ is the imaginary part of the polarizability. Equations 2.5 and 2.6 show a clear R^3 dependence for the absorption, whereas the scattering shows an R^6 dependence. This explains why smaller NPs show less scattering than bigger NPs, and smaller NPs absorb much stronger.[6]

2.2.2 Coupling of Two Plasmonic Nanoparticles

Two nanoparticles can be assembled next to each other by means of lithography or the use of DNA origami structures (see section 2.3). Depending on the polarization of the incidence electric field, NPs can act as single plasmonic NPs or as a coupled dimer antenna. The interacting particles can be described in terms of hybridization of the plasmon modes following the methods to treat electronic orbitals in molecules (*Figure 11a*).[108,117] Two modes in the NP dimer are exhibited, which can be parallel or perpendicular to the dimer axis, with a bonding mode at the lowest energy showing a net dipole moment. In this context, the far field optical properties are only defined by the two modes showing a net dipole moment (marked with a star in *Figure 11a*). Other modes show a net dipole moment of zero as the dipoles of the particles cancel out each other. The relative splitting between the bonding and antibonding mode in the hybridization diagram is dependent on the gap size of the dimer antenna.[108,117] Compared to monomer NPs, coupled dimer antennas show a red shift of the LSPR.[96]

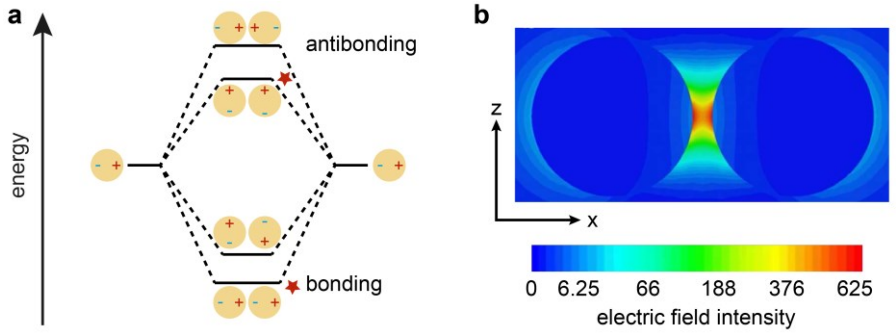

Figure 11: Plasmon mode hybridization and electric field enhancement. (a) Plasmon mode hybridization of two close-by gold NPs. + and – indicate the dipole oscillation direction. Depending on the oscillating mode of each NP, different combinations of bonding and antibonding modes occur. Only states marked with a star are optically active. (b) Electric field intensity of a 100 nm Au NP dimer with an interparticle distance of 12 nm at an excitation wavelength of 640 nm. The excitation propagates in z direction and is polarized along x. Reprinted with permission from [22].

NPs show not only an induced electric dipole moment within the particle but also an external dipolar field surrounding the NP, which is driven by the resonantly enhanced field inside the NP. The distribution of the enhanced electric field intensity surrounding the metal NP dimer is depicted in *Figure 11b*.[22] It should be noticed that a very confined electric field is created between two NPs[9], which is often referred to as hot spot region and has just the size of a few nanometers.[5]

2.2.3 Coupling of Plasmonic Nanoparticles with Organic Dyes

Noble metal NPs like gold and silver are commonly used, and LSPRs in the visible region of the electromagnetic spectrum are exhibited.[118] Thus, they can couple to a long range of organic dyes in this spectral region. OAs can act as receivers or *vice versa* as transmitters. As a receiver, the OA focuses the far field radiation to the emitter's near field. In case of transmitting properties, it couples to the electromagnetic field of an emitter and transfers the signal to the far field. An emitter placed in close proximity to an NP therefore experiences an influence on its photophysical properties (*Figure 12a*) with a complex influence on all rate constants.[6,119] The excitation rate constant k_{exc} of the dye is enhanced because it is proportional to $\left|\vec{\mu}_{ab}\vec{E}\right|^2$, where $\vec{\mu}_{ab}$ represents the absorption dipole moment of the fluorophore and $\vec{E}$ the electric field.[120,121] Consequently, the enhancement of the excitation rate constant is strongly dependent on its relative position to the NP dimer.[7,19] This can be seen in *Figure 11b*, which shows that the electric field is intensified close to the NPs' surface and creates a hot spot region in between the two NPs. Furthermore, the distance (*z*) to the NP's surface is important (*Figure 12b*).[7,122] With a decreasing distance to the NP, the excitation rate is enhanced. This leads to an enhancement in the fluorescence signal as the excitation rate is directly connected with the fluorescence intensity, which is defined by

$$I_{fl} = k_{exc}\frac{k_{fl}}{k_{fl}+k_{nr}} = k_{exc}\phi \qquad (2.7)$$

The second quantity involved in equation (2.7) is the quantum yield ϕ, which is defined in equation (2.2) and is directly correlated to the fluorescence intensity as illustrated in equation (2.7). The quantum yield expresses the efficiency of the emitting system and includes the radiative and non-radiative decay rates, which are both influenced by the NP. The presence of an NP opens up new pathways for the depopulation of the S_1 state. For short distances of the dye to the NP's surface, energy is directly transferred to the NP, enhancing the non-radiative decay rate constant k_{nr}.[6] During this process the energy dissipates through heat by Ohmic losses. At larger distances, the radiative decay rate k_r, which is influenced by the photonic mode density (PMD), plays a more important role.[6] The rate can be higher[123] or lower[124] depending on whether the fluorophore is placed in a region of high or low PMD.[6]

While the excitation rate of a quantum emitter near the NP's surface is enhanced when the distance decreases, the quantum yield is reduced because the non-radiative decay rates get higher.[7,122] *Figure 12b* shows a diagram with the excitation rate enhancement and the change in quantum yield for an emitter with $\phi = 1$. At a certain position, both curves cross each other. This is where at shorter distances fluorescence quenching becomes important. Similar to the excitation rate, the emission rate constant is also impacted by a change in the distance between the dye and the NP (*Figure 12c*). At distances below 10 nm quenching occurs, whereas a strong enhancement is visible between 10 and 20 nm.

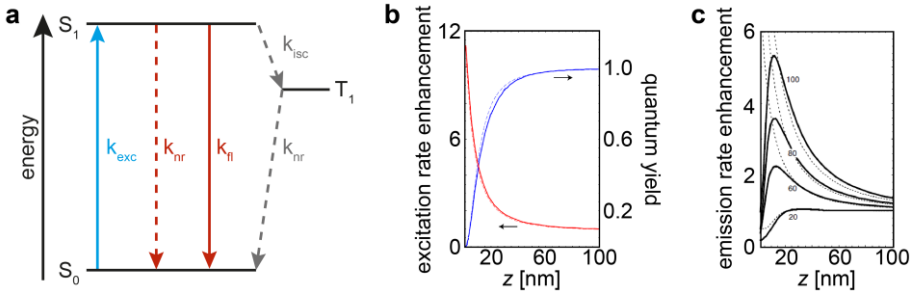

Figure 12: Jablonski diagram for NP-dye coupling and rate constant changes of a dye. (a) Jablonski diagram of an organic dye molecule situated close to a plasmonic NP showing the rates influenced by the NP. Fluorophore situated at a distance z to an 80 nm gold nanoparticle excited with a wavelength of 650 nm. (b) Excitation rate enhancement (red) and quantum yield (blue), (c) emission rate enhancement as function of the dye NP separation z. Solid lines represent exact results and dashed lines are approximations. (b) and (c) Reprinted with permissions from [122] and [34].

The enhancement of the rate constants is not only dependent on the relative distance between the emitter and the metallic NP, but also the size of the NP plays an important role (*Figure 12c*). With an increase in the NP's diameter the emission rate becomes higher.

In addition to the distance, the relative orientation of the emitters transition dipole moment to the NP also plays an important role in the dye-NP interaction. The coupling between a fluorophore located in the hot spot and a NP dimer assembly will be discussed below.[11] *Figure 13*a and *b* show sketches of a gold NP OA with a fluorophore, illustrated by its transition dipole moment (red arrow), in the gap region. The fluorophore's dipole creates image charges in the NPs (black arrows). The discussion only focuses on the two extreme cases of a radial (*Figure 13a*) and tangential (*Figure 13b*) orientation with respect to the dimer axis. In an aqueous surrounding a fluorophore usually is able to rotate freely and behaves

like an isotropic emitter. For a fluorophore inside an OA, the dye is still able to take all possible orientations, but the radiation characteristics change. In a radial orientation, the dye can couple to the resonant mode of the antenna. On the other extreme, which is the tangential mode, the emission will be suppressed. These two effects can be explained with the help of *Figure 13a* and *b*: in a parallel orientation the dipole is intensified by the image dipoles (*Figure 13a*), whereas in the perpendicular orientation it is canceled out (*Figure 13b*). This is further illustrated by the simulations shown in *Figure 13c*, where the relative change in the quantum yield of an ATTO 647N dye placed in the hot spot of a dimer or close to a monomer antenna is drawn as a function of the NP diameter.[11] The quantum yield is simulated for a parallel (radial) and perpendicular (tangential) orientation of the dye in the hot spot region in a dimer and monomer assembly. The splitting of the two cases again shows what was illustrated before by the image charges created by a quantum emitter in the NP's hot spot. The combination of these two effects enhances the emission, and the emitter's radiation coupled to the antenna becomes anisotropic.[125]

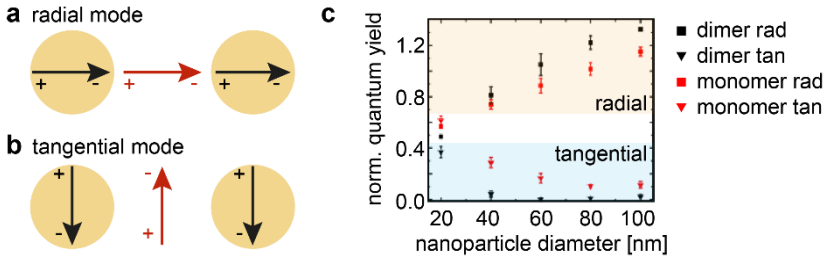

Figure 13: Dye-NP coupling illustrated by image charges and quantum yield changes. Image charges (black arrows) in a gold NP dimer induced by the dipole moment of a fluorescent dye (red arrow) with parallel/radial (a) and perpendicular/tangential (b) orientation to the dimer axis. (c) Simulated quantum yield of a single emitter in monomer and dimer NP structures as a function of the NP's diameter. Values are normalized to the quantum yield of 0.65 for ATTO 647N. (c) Reprinted with permission from [11].

Based on the influence of plasmonic nanoparticles, excitation as well as emission processes get altered. This in turn leads to an adaption of the aforementioned quantum yield, but also the fluorescence intensity and lifetime will be affected. A factor to describe the ratio of the modified k_r' and unmodified k_r radiative decay rate is known as the Purcell factor. In the following contributions, another characteristic that quantifies the influence of a metallic NP on a fluorophore is used, which is the fluorescence enhancement (FE) factor. This factor is described as the ratio between the modified I_{fl}' and unmodified I_{fl} fluorescence intensity.

2.3 DNA Origami Nanostructures

DNA is a biomolecule carrying genetic information of organisms and viruses. It exists as a right or left handed double helical structure (*Figure 14a*) corresponding to A- and B- or Z-DNA, respectively. The most common form is the B-DNA, decoded by Watson and Crick.[126,127] Each strand of the double helix has a 3'- and 5'-end that in a paired case run antiparallel to each other and consist of a sugar phosphate backbone connecting the nucleobases. These bases are the purines adenine (A) and guanine (G) as

well as the pyrimidines thymine (T) and cytosine (C). To form the double helical structure, two of the four bases build specific base pairs (*Figure 14b*) through hydrogen bond formation. Hence, adenine pairs up with thymine and guanine with cytosine.

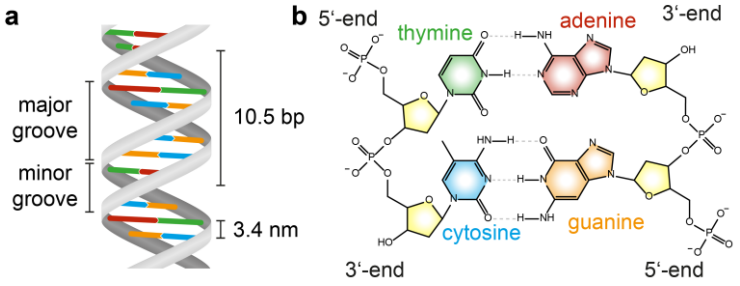

Figure 14: Molecular structure of DNA. (a) B-DNA double helical structure with a major and a minor groove. One whole turn is reached after 10.5 base pairs (bp), and the distance between two adjacent base pairs is 3.4 nm. (b) Structural composition of the DNA base pairs and DNA sugar phosphate backbone. Thymine (green) and adenine (red) as well as cytosine (blue) and guanine (orange) build base pairs via hydrogen bonds.

The specificity of DNA can be used to build predefined structures with the help of the DNA origami technique introduced by Paul Rothemund[16] and based on previous work of Nadrian Seeman[17]. With the help of the program caDNAno[128] two- or three-dimensional DNA origami structures can be designed.[18,129] The process of DNA origami folding is shown in *Figure 15a*. As a basis for the structures a circular single stranded DNA (scaffold), built from several thousand bases and extracted from a bacteriophage, is folded with the help of about 200 short single stranded DNA strands (staples) into a predefined shape. To fold the structures, a temperature gradient over time is applied to a buffered mixture of salts, scaffold, and staple strands. Here, the temperature gradient, which starts at 70 °C, forces the scaffold strand through the short staple strands into the designed shape. The time needed for this process is dependent on the final structure. Complex 3D structures usually take longer to fold than 2D structures (1.5 – 26 h).

An example of folded structures is given in *Figure 15b*, which shows an atomic force microscopy (AFM) image of folded and purified rectangular DNA origami structures (NRO[63]). The technique of DNA origami is not only helpful for the design of different shapes, but it is highly modular as well as it is possible to modify DNA with different functional groups, fluorescent dyes (red sphere and inset in *Figure 15c*) or biomolecules to position them on the structures with stoichiometric and nanometer accuracy. Also, DNA extensions can be introduced that are able to bind bigger particles (yellow sphere in *Figure 15c*), such as nanoparticles covered with a complementary sequence, or that can be used for DNA-PAINT experiments (see 3.2.3.1). For immobilization on a glass surfaces, the DNA origami structures have biomolecules (biotin) attached (*Figure 15c*). The glass surface is functionalized with BSA-biotin and neutrAvidin to bind the biotins from the DNA origami structures with high stability enabling single-molecule experiments. Thus, DNA origami structures are highly versatile and modular platforms.

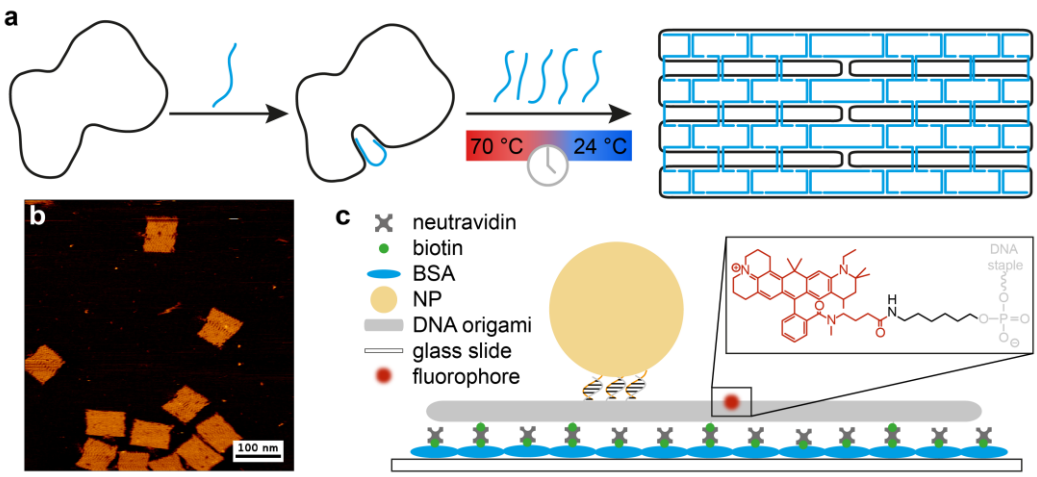

Figure 15: DNA origami folding and functionalization properties. (a) Folding process of a DNA origami structure. A circular single stranded scaffold strand (black) is folded by short single stranded staple strands (blue) with the help of a temperature gradient into the predefined shape (here: rectangular structure). (b) Atomic force microscopy (AFM) image of folded rectangular DNA origami structures. (c) Immobilization of DNA origami structures on a functionalized glass surface with BSA via biotin and neutrAvidin, attachment chemistry of a fluorophore to a DNA staple, and binding of gold NPs via DNA hybridization.

3. Microscopy Techniques

Many different measurement techniques are used in fluorescence spectroscopy to address photophysical, biological and other related problems. They can be divided into ensemble and single-molecule techniques, where the method of choice depends on the exploratory problem. The focus of this thesis is on single-molecule techniques. In the following chapters, measurement techniques are introduced that are used for the problems addressed in this thesis. They can be subdivided into temporal, orientation and sub-diffraction distance resolution measurement techniques. A differentiation between confocal[130] and wide-field microscopy[3] is made, and special implementations in each of these microscopy techniques are introduced. Modifications in these basic microscopy principles are versatile and span huge areas of applications. The focus of this thesis lies on time-resolved confocal measurements with fluorescence lifetime extraction (chapter 3.1) in different probe assemblies. Furthermore, the modifications required for polarization-resolved measurements (chapter 3.2.1), defocused imaging (chapter 3.2.2), and spatial resolution by DNA-PAINT measurements (chapter 3.2.3.1) are explained.

3.1 Confocal Microscopy

In confocal microscopy, a laser beam is focused to the sample surface, and the emission of the excited molecules is collected by the same objective that is also used in the excitation process. With the help of a dichroic beam splitter, the emission light is separated from excitation light and focused on an APD (avalanche photo diode). By the use of pulsed lasers and time correlated single photon counting (TCSPC) modules the fluorescence lifetime of a molecule can be measured.

The confocal setup used in this thesis, which is depicted in *Figure 16,* is based on an inverted Olympus-IX81 microscope. For excitation, a pulsed white light laser source (78 MHz, SuperK Extreme, NKT Photonics) is used. With a first AOTF (acousto-optical tunable filter, 2012608, Crystal Technology Inc.) the wavelength of the laser can be set e.g. to 532 nm and 639 nm, and with a second AOTF (AA.AOTF.nsTN, A-Opto-Electronic) an alternation of both laser lines can be achieved. By using a neutral density filter (nd filter, ndF, OF 0-2, Thorlabs), the laser power of the excitation laser can be tuned before it is coupled into a polarization-maintaining single mode fiber (PM-fiber, P1-488PM-FC-2, Thorlabs). The laser is further directed through a combination of a linear polarizer (LPVISE100-A, Thorlabs,), an EOM (electro-optical modulator, L 0202, Qioptiq), and a quarter-waveplate (AQWP05M-600, Thorlabs) in order to generate linear polarized light that can be rotated about its own axis with a specific frequency. Thus, all molecules with a fixed electric dipole moment can be excited with the matching polarization to gain the best excitation and highest fluorescence response. The laser beam is then focused in the sample plane through an immersion oil objective (UPlanSApo 100x, NA = 1.4, WD = 0.12 mm, Olympus). Scanning in x- and y-direction of the sample is performed with a piezo stage (P-517.3CL, E-501.00, Physik Instrumente GmbH & Co. KG). The emitted light is collected by the same objective used in excitation and separated from the excitation light by a dichroic beam splitter. After separation, the emitted light is focused in the plane of a pinhole (50 µm, Linos) to block scattered light

and out-of-focus emission from dyes and particles in solution. Afterwards, the light is directed to an APD (Avalanche Photo Diode, SPCM, AQR 14, Perkin Elmer) by a combination of two lenses. For spectral separation of emitted light of different wavelengths, a dichroic mirror is used to direct the light to two independent APDs. The light is filtered by emission filters (green: BrightLine HC 582/75, Semrock Inc.; red: RazorEdge 647, Semrock Inc.) before impinging on the APDs.

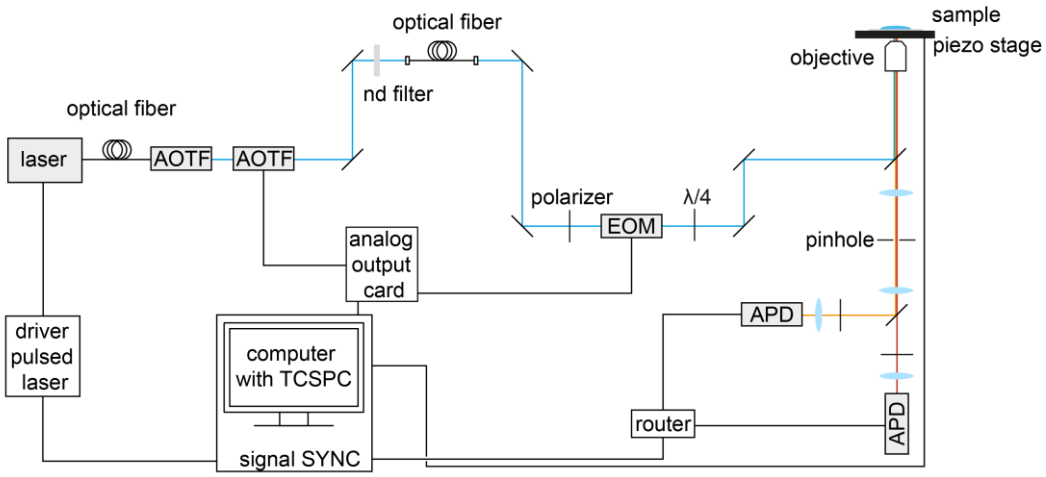

Figure 16: Scheme of the confocal setup used in this thesis. The excitation path is illustrated by a blue line, emission by a red/orange line. Electric connections are visualized by black lines.

To perform time correlated single photon counting, a TCSPC system (Hydra Harp 400, PicoQuant, Germany) is implemented (further details see the following chapter), and data processing is performed by a custom written LabVIEW software.

3.1.1 Time-Resolved Confocal Microscopy

The confocal microscope used in this thesis is connected with a TCSPC module to accurately detect the photon arrival times and extract the fluorescence lifetime. To this end, a pulsed white light laser source is used to excite the sample, with the starting point of the laser pulse being known. After the excitation of a molecule, a photon may be emitted and detected on an APD. This point in time is set into relation to the starting point of excitation (*Figure 17a*). The lag time between the excitation and emission pulses gives the decay time of a single emission event (*Figure 17b*). Through many repetitions (1-*N*) of this process, a histogram of the decay times is gained, which resembles the shape of the decay (*Figure 17c*). By fitting the slope of this decay with a mono-exponential function, the fluorescence lifetime of an emitter can be extracted. The limitation of this technique is based on the repetition rate of the laser (in the presented studies 78 MHz) and the lag times in the electronics. A measure to describe the limit of the shortest measureable fluorescence lifetime is the IRF (instrument response function). The IRF depends on the shape of the excitation pulse and is limited by the detector as well as the timing electronics.[3] Measured fluorescence lifetimes are usually de-convoluted from the IRF to extract the real fluorescence lifetimes.

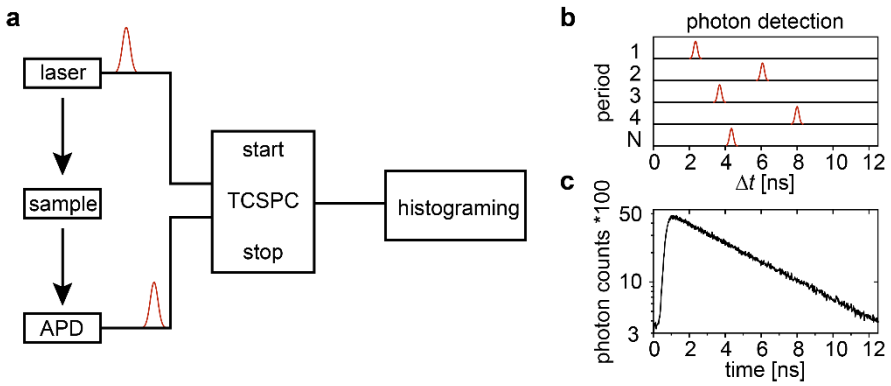

Figure 17: TCSPC in confocal microscopy. (a) Schematic of the TCSPC principle. A sample is excited with a laser that sends an electric signal to the TCSPC module to start. The emission is detected by an APD, which sends a stop signal to the TCSPC module. The time between both pulses is plotted in a histogram. The single events of emission occur at different delay times Δt to the excitation pulse (b). All of these 1–N events sum up in a histogram which resembles the waveform of the decay time (c). Here, a fluorescence decay of ATTO 647N is shown.

Besides the extraction of fluorescence lifetimes from intensity transients, fluorescence lifetime imaging microscopy (FLIM) can be performed. To gain FLIM images, the collected data from the scanned confocal images is used to calculate the fluorescence lifetime of each scanned pixel with the help of a home written LabView software.

3.2 Wide-Field Microscopy

In contrast to confocal imaging, in wide-field microscopy the laser is not focused in the sample plane, but in the back focal plane of an objective and then directed to the sample, illuminating a large area. Due to the larger imaging area, wide-field illumination enables the detection of many molecules at a time.

The used wide-field setup, a sketch of which is shown in *Figure 18a*, is based on an inverted Olympus IX71 microscope. A 644 nm diode (ibeam smart, Toptica Photonics) and a 532 nm fiber laser (MPB Communications) are used for excitation. A spectral clean-up of the lasers is performed by the use of filters (red: Brightline HC 650/13, Semrock; green: Z532/647x, Chroma). After cleaning up, the laser passes through a linear polarizer (LPVISC100-MP2 510−800 nm, Thorlabs) in order to clean up the polarization before being directed to a removable quarter- (AQWP05M 400-800 nm, Thorlabs, Germany) or half-waveplate (AHWP05 M 400−800 nm, Thorlabs). The working principles of the waveplates are further described in chapters 3.2.1 and 3.2.2. The laser beam is focused in the focal plane of the objective (UPLXAPO 100×, numerical aperture (NA) = 1.45, working distance (WD) = 0.13, Olympus) through lenses mounted on a x-microstage. For sample stabilization, a nosepiece stage ((IX2-NPS, Olympus) together with an actively stabilized optical table (TS-300, JRS Scientific Instruments) are implemented. The emitted light from the sample on top of the nosepiece stage is collected by the same objective that is used in excitation and separated from the excitation light by a dichroic mirror (Dual Line

zt532/640 rpc, AHF Analysentechnik). After spectral separation, the emission light is focused through an emission filter (red: ET700/75, Chroma; green: BrightLine 582/75, AHF Analysentechnik) on an EMCCD camera (electron multiplying charge-coupled device, iXon X3 DU-897, Andor) by a lens. Data acquisition is performed by the open source microscopy software Micro-Manager operated in ImageJ.[131]

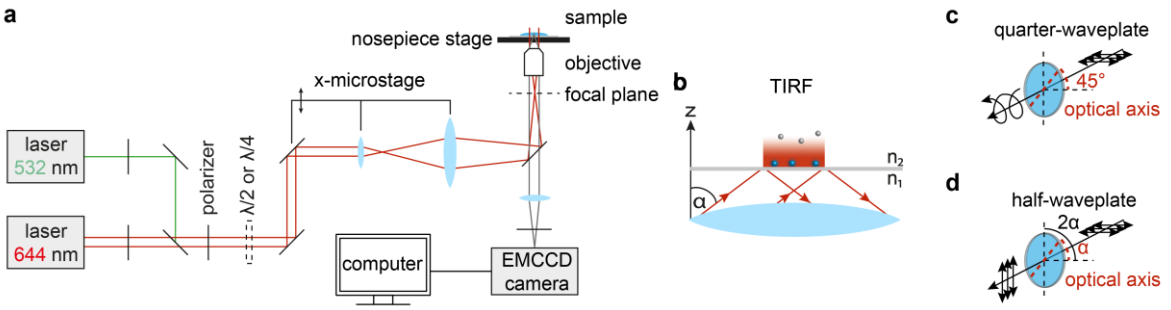

Figure 18: Scheme of the wide-field setup used in this thesis. Sketch of the wide-field setup (a) and the special illumination mode of TIRF (b). Working principles of a quarter-waveplate (c) and a half-waveplate (d).

A measurement mode of wide-field microscopy is the TIRF (total internal reflection fluorescence) microscopy.[132,133] Here, the excitation laser beam is directed to the glass interface with an angle α to the optical axis *z* (*Figure 18b*). This angle is achieved by the movement of the x-microstage. At an angle below the critical angle, given through the diffraction indices of glass (n_1) and the medium (n_2), the laser beam will be totally reflected into the direction of the denser medium. In the case of a glass-water interface, glass is the denser medium, and an evanescent field will be created in the aqueous medium. This evanescent field is propagating along the optical axis, has a maximum directly at the glass surface, and decays exponentially into the sample. The advantages of wide-field microscopy are the examination of many molecules at the same time, but still on the single-molecule level, and the suppression of the background by TIRF illumination.

Modifications in the wide-field microscope introduced in this chapter and special wide-field microscopy techniques used in this thesis are introduced and discussed in the following chapters.

3.2.1 Polarization-Resolved Wide-Field Microscopy

In this thesis, a polarization-resolved technique is implemented in a wide-field setup. The linearly polarized excitation laser beam is cleared up by a linear polarizer and then rotated with the help of a half-waveplate mounted in a rotatable motorized stage (K10CR1/M stepper motor, Thorlabs). This combination enables a stepwise rotation of the incoming linearly polarized excitation light by 2α for an incidence angle of α to the optical axis of the waveplate (*Figure 18d*). Emitters excited with different polarizations of the laser beam exhibit differences in their fluorescence intensity time traces (see *Figure 6*c in chapter 2.1.1). If the emitter is freely rotating, the emission will have a constant intensity for all excitation polarization directions and is called an isotropic emitter. If, on the other hand, the emitter is fixed in a certain orientation, the fluorescence intensity will exhibit a modulation depending on the

relative orientation between the excitation polarization and the transition dipole orientation of the emitter. The modulation is extracted from

$$M = \frac{I_{max} - I_{min}}{I_{max} + I_{min}} \quad (3.1)$$

Here, I_{max} is the maximum and I_{min} the minimum intensity of a modulated trace. In a strong modulating case ($M \approx 1$) the detected intensity reaches a maximum at an orientation where the excitation polarization matches the transition dipole orientation of the emitter and decreases to a minimum of nearly 0 for a perpendicular orientation. If the modulation value is between 0 and 1, the fluorophore is not completely oriented and fluctuates around its actual position. Using this technique, it is thus possible to obtain the absorption dipole moment orientation of single fluorophores.

3.2.2 Defocused Imaging

Orientation resolution can not only be obtained by polarization-resolved wide-field microscopy but also by a technique called defocused imaging. This technique provides information about the 3D orientation of transition dipole moments and was first introduced with immersion mirror objectives for imaging in a cryostat at low temperatures.[134,135] It can be used to extract emission dipole orientations and can be performed on a common wide-field microscope. Besides the determination of the emission dipole orientation it is also possible to extract information about the absorption dipole orientation[136], which, however, is out of the scope of this thesis.

By changing the position of the objective or camera used for detection, the image mapped on the camera changes as well.[137–139] If the sample is in focus of the objective, the mapped image shows diffraction-limited point spread functions (PSF) representing the emitting molecules. By defocusing the system, the sample is shifted away from the focal plane, and the coupling of the emission into the detection optics changes. Thus, the mapped image on the camera does not show the PSFs as in the focused case, but rather exhibits a defocused image that displays the dye's emission pattern. A defocusing of 1 µm was found to be sufficiently good to show the bipolar emission patterns and not too strong to worsen the signal-to-noise ratio.[139,140]

To excite single dipole emitters with the same probability, a circularly polarized laser beam is used. A circular polarization can be achieved by the implementation of a quarter-waveplate into the excitation beam path (*Figure 18c*). This waveplate can turn linear into circular polarized light and *vice versa*. In a defocused image, other than in focused images (*Figure 19a*), each molecule shows an emission pattern that contains information about the orientation of its emission dipole (*Figure 19b*). Thereby, the angle between the dipole and the optical axis θ and the in-plane angle ϕ (*Figure 19c*) can be used to define the defocused emission pattern and its relative orientation of transition dipole moment to the glass surface. Simulated emission patterns for a set of dipole orientations are depicted in *Figure 19d*. From these simulated images it can be concluded that ϕ rotates the emission pattern in the x-y-plane, whereas θ is showing more drastic effects, because a rotation out of the x-y-plane is changing the symmetry in the emission patterns.

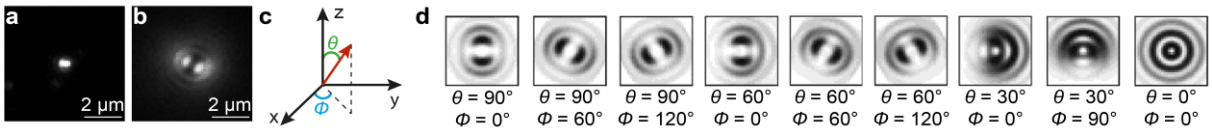

Figure 19: Defocused imaging. Focused (a) and defocused (b) images of a dipole emitter on a glass surface. (c) Coordinate system with the angle between the dipole and the optical axis θ and the in-plane angle ϕ. (d) Simulated images of dipole emitters close to a glass interface. (d) Reprinted with permission from [138].

The defocused emission patterns of emitters depend for example on the chemical structure, the surrounding medium, and environmental factors. While a dipole emitter is able to rotate freely in an aqueous solution, the situation is different in a polymer film. The polymer locks the dye in a certain position, which then becomes an anisotropic emitter with a two-lobe emission pattern arising from the emission characteristics as described in chapter 2.1.1. These films will not only lock the dye, but the thickness of the film also has an impact on the emission patterns.[138,141] Contrarily to the behavior of fixed dipoles, the isotropic case shows circular emission patterns because it emits in all directions with the same probability.

3.2.3 Super-Resolution Techniques

Optical imaging systems like light microscopes are limited in their resolution by the diffraction limit described by Ernst Abbe in 1873.[142] He found that the minimum resolvable distance *d* for light of the wavelength λ traveling through a medium is given by

$$d = \frac{\lambda}{2\mathrm{NA}} \tag{3.2}$$

Here, NA is the numerical aperture of the used microscope objective. This limitation makes it impossible to resolve distances below about one half of the wavelength. This means that distances above the diffraction limit are resolvable without special techniques (*Figure 20a*), but at distances below the diffraction limit two emitters will only be seen as one spot because the PSFs of both emitters overlap, making it impossible for the distance to be resolved (*Figure 20b*).

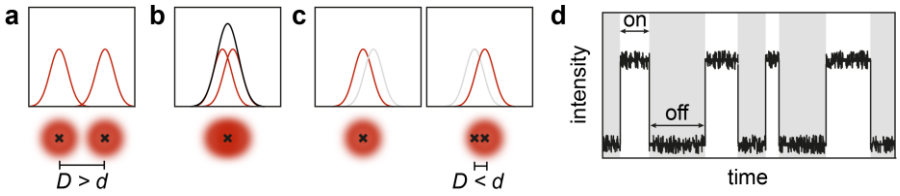

Figure 20: Blinking in super-resolution microscopy. (a) Two emitters within a distance above the diffraction limit, which are resolvable. (b) Two emitters at a distance below the diffraction limit, which cannot be resolved. (c) Sequential blinking of the emitters in (b), with each emitter being localized at a different time making the distance resolvable. (d) Intensity versus time trace with no intensity for the "off" and high intensity for the "on" state.

The resolution Δx is inversely proportional to the square root of detected photon number *N*.

$$\Delta x \propto \frac{1}{\sqrt{N}} \tag{3.3}$$

Several techniques have been invented throughout the last years to overcome this hurdle of the diffraction limit, for example technical implementations like STED (stimulated emission depletion), where the molecule is only excited at its central position by the overlap of an excitation laser with a surrounding donut shaped depletion laser. An extension of this technique is MINFLUX[143,144] (minimal photon fluxes), a combination of structured illumination and single-molecule localization.

A second group of super-resolution techniques is single-molecule localization microscopy (SMLM). While the techniques based on technical implementations are surface scanning approaches, SMLM is based on wide-field illumination. These techniques rely on mechanisms to switch molecules between an “on” and an “off” state. The switching of molecules leads to only one molecule being “on” at a time in a diffraction-limited volume. This molecule can be localized before the next molecule is switched into the “on” state and is also localized. Accumulations of these localizations are used to calculate the diffraction-limited distance between two spots (*Figure 20c*). The fitting of the PSFs is done with a 2D-Gaussian model that reproduces the shape of the PSF:

$$f(x,y) = A\ exp\left(-\frac{1}{2}\left(\left(\frac{x-x_0}{\sigma_x}\right)^2 + \left(\frac{y-y_0}{\sigma_y}\right)^2\right)\right) \tag{3.4}$$

In equation 3.4, *A* is the amplitude, x_0 and y_0 the center coordinates and σ_x and σ_y the standard deviation of the Gaussian function. A fluorescence transient with signal fluctuations owing to “on” and “off” switching of fluorescence molecules can be seen in *Figure 20d*. The “on/off”-switching can be achieved by different methods, such as STORM[145] (stochastic optical reconstruction microscopy), where blinking between the “on” and the “off” state of fluorescent organic dyes is induced by a specific imaging buffer, or PALM[146,147] (photoactivated localization microscopy), which uses photoactivatable or photoswitchable proteins to induce blinking. A technique that is also counted towards the group of methods with stochastically blinking molecules is the technique of DNA-PAINT[148] (points accumulation for imaging in nanoscale topography), which is explained in more detail in the following chapter.

3.2.3.1 DNA-PAINT

DNA-PAINT is a far-field fluorescence nanoscopy or super-resolution fluorescence microscopy technique where sub diffraction-limited resolution is achieved by stochastic binding and unbinding of single DNA strands carrying fluorescent dyes (imager strands).[148] The advantages of DNA-PAINT are the independence of photobleaching of fluorescent dyes thanks to a continued strand exchange and the fact that switching of the molecules does not rely on harsh buffer conditions as required in STORM experiments. Also, the laser power does not need to be as high as in STED measurements, and no harmful UV light has to be used.

In DNA-PAINT measurements, a DNA origami structure is modified with protrusions of a specific DNA sequence of the length of a few base pairs. These specific sequences can bind single stranded imager strands with a complementary sequence (e.g. 8 bp long) and an attached fluorescent dye (*Figure 21a*). The short binding sequence thereby only leads to a transient binding of the imager strands. In the bound

state the fluorophore is assigned to the “on” state, whereas after dissociation of the imager strand the molecule is in the “off” state. The stochastically binding and dissociation leads to only a few emitters being in the “on” state at the same time in one imaging frame. Thereby, only one binding event will be recognized per DNA origami structure. The kinetics of this mechanism can be tuned by the concentration and the length of the imager strand.

After data acquisition an image reconstruction is performed, where each spot in a frame gets fitted by a Gaussian function, with the center of the function being the molecules position in the lateral plane. The framewise integration over the “on” events leads to an accumulated localization of the binding sides and previously diffraction-limited images (*Figure 21b*) are reconstructed into super-resolved images (*Figure 21c*). Distances in the designed sample structure can be extracted from the accumulated spots.

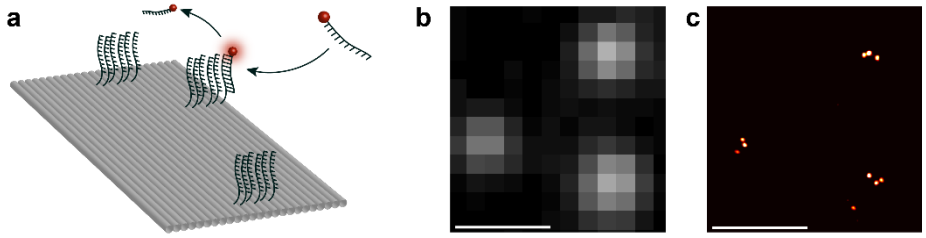

Figure 21: The principle of DNA-PAINT. (a) Sketch of the DNA-PAINT technique with protruding strands on the DNA origami structure for imager binding (short single strands with red dye). (b) shows a diffraction-limited image of the super-resolved image in (c), which illustrates the irregular triangular pattern of the structure sketched in (a). Scale bar in (b) and (c) is 500 nm.

With the help of DNA-PAINT the best lateral resolution of 6 nm was obtained[149,150], whereas the axial resolution was pushed down to about 2 nm by the implementation of graphene surfaces that exhibits an energy transfer to the fluorescing molecules in close proximity with a d^{-4} dependency.[43]

4. Overview of Published Work

4.1 Publication 1: Directing Single-Molecule Emission with DNA Origami-Assembled Optical Antennas

In the associated publication P1, the influence of a plasmonic nanoantenna on the absorption and emission characteristics of a fluorescent dye is studied. The influence of nanoparticles on single photon emitters, like organic dyes, has already been extensively studied.[151,152] It is known that the geometry of an antenna assembly is important for the coupling efficiency of the dye-antenna system. Also it has been demonstrated in theoretical studies[11,39] as well as in experiments[22] that the antenna's main resonance mode is dominating the emission processes, but a clear visualization of this effect has not been shown so far.

To address and visualize the effect of plasmonic antennas on the absorption and emission of a fluorescent dye, DNA nanotechnology is used as a bread board for the dye-antenna assembly. In order to perform the measurements on a single molecule level, the self-assembled antenna structures are immobilized on a glass surface. First, a defocused image (*Figure 22a and b)* is acquired to extract the emission dipole orientation, and second, a polarization-resolved measurement is carried out for the extraction of the absorption dipole orientation. To perform the aforementioned measurements, slight changes in the excitation pathway of a home-build wide-field setup have to be made for both techniques (see chapters 3.2.1 and 3.2.2).

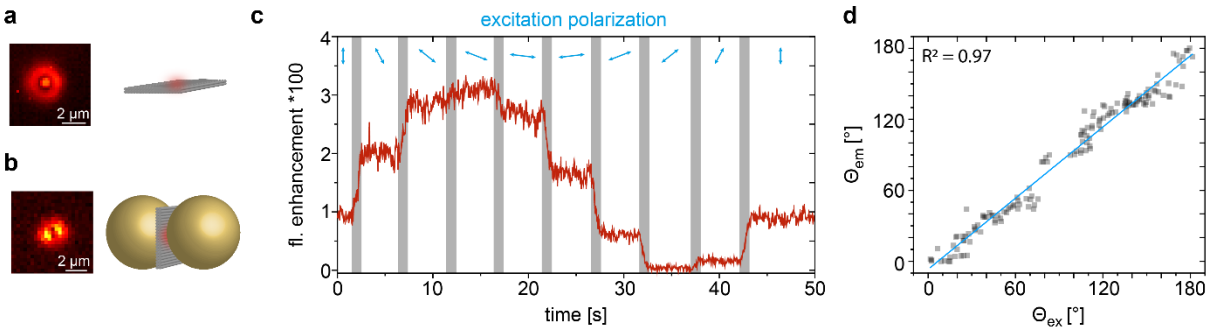

Figure 22: Measurements of correlative defocused imaging and polarization-resolved spectroscopy. (a) and (b) show exemplary defocused images of a single emitter in a DNA origami structure and an emitter coupled to a plasmonic antenna, respectively. (c) depicts an exemplary transient for the polarization-resolved wide-field measurements of a dye coupled to a plasmonic antenna. Correlation of the emission (extracted from b) and excitation dipole orientations (extracted from c) of the dimer structures show good agreement (d). Reprinted with permission from [13].

The emission dipole orientation is extracted from the defocused images, where attention has to be paid on the radiation characteristics of a dipole emitter, which is perpendicular to its dipole orientation (also see section 2.1.1). Fluorescence transients from the polarization-resolved wide-field measurements show a modulation in the fluorescence intensity signal of a dye coupled to a plasmonic antenna (*Figure 22c*). The acquired modulating trace provides information about the absorption dipole orientation, which

is extracted by fitting the modulated values with a cosine-square function and searching for the maximum. Hence, it is not only possible to illustrate that the emission of a previously isotropic emitter becomes directional (*Figure 22b*) through the dye-OA coupling, but also that the absorption transition dipole (*Figure 22c*) is affected in a similar way. The isotropy of the single dye in emission can be seen in the defocused emission pattern of the single dye (*Figure 22a*) and in absorption in a non-modulating trace in the polarization-resolved measurement. Apart from a directionality of both transition dipole moments a co-alignment is also shown (*Figure 22d*), meaning that the antenna's main resonance mode is dominating emission as well as absorption processes.

4.1.1 Associated Publication P1

Directing Single-Molecule Emission with DNA Origami-Assembled Optical Antennas

by

Kristina Hübner, Mauricio Pilo-Pais, Florian Selbach, Tim Liedl, Philip Tinnefeld, Fernando D. Stefani, Guillermo Acuna

Published in

Nano Letters, 2019, 19 (9), 6629-6634

The full publication and supporting information are attached in appendix A1.

4.2 Publication 2: Determining the In-Plane Orientation and Binding Mode of Single Fluorescent Dyes in DNA Origami Structures

The relative orientations of fluorescent dyes are of great interest in studies like FRET or plasmonic devices like dipole antennas.[11] Whereas the orientation of bulky elements like gold nanorods can easily be performed with electron beam lithography[125,153] or on DNA origami structures[154,155], it is challenging to control the orientation of single fluorescent dyes. Dyes can be attached in two different ways to DNA origami structures. The first way is to attach them non-covalently through dye DNA interactions. These dyes can be separated into groups of intercalators, groove binders and dyes that adhere to the dsDNA backbone.[54] While an orientation control is gained, geometric and stoichiometric control are not given. The second approach to bind fluorophores to DNA is covalently through linkers. These linkers are often amino-C6 linkers attached to the 3'- or 5'-end of DNA, or internally. Through this technique a geometric and stoichiometric control is reached, but it lacks the orientation control of intercalators. Fluorophores attached to DNA exhibit the ability to rotate freely around their point of linkage if in an aqueous solution. If measured dried on a surface or embedded in polymer films, this rotational freedom is lost, and the dyes stick randomly to DNA. The advantage of rotational freedom is also lost in aqueous surroundings if the dyes interact with DNA. These interactions can result from $\pi-\pi$ stacking or hydrogen bond formation. Although fluorescent molecules have the ability to stick in preferred orientations in DNA, methods to resolve these orientations do not exist. Hence, in the associated publication P2 a combined measurement procedure is introduced to analyze the relative orientations of single fluorescent dyes in DNA origami structures.

To investigate the in-plane orientation of these dyes, the techniques of DNA-PAINT and polarization-resolved wide-field microscopy are combined in order to extract information about the DNA origami structure orientation and the orientation of the fluorescent dye in the structure. A patterning on the rectangular DNA origami structure makes it possible to resolve the orientation of the rectangle on the glass surface with super-resolved DNA-PAINT images (gray square and line in *Figure 23a*). Polarization-resolved wide-field imaging on the other hand shows modulated fluorescence intensity transients. The spatial orientation φ of the dye's transition dipole orientation can be extracted from these modulated transients. The relative angle Φ of the transition dipole on the DNA origami structures can be calculated from both extracted orientations. With the help of the aforementioned procedure a set of seven samples is analyzed, in which on the one hand the molecular surrounding is changed and on the other hand the fluorescent dye itself is varied. Dyes under study are ATTO 647N (*Figure 23d*), ATTO 643 (*Figure 23e*), a hydrophilic version of ATTO 647N, which is supposed to be less sticky, and the cyanine dye Cy5 (*Figure 23f*). We find that different orientations can be taken by the fluorophores in slightly modified environments (sample 1 and 2). In sample 1 (*Figure 23c*) showing a gap created by two missing nucleotides adjacent to the fluorescent dye, all dyes have similar orientations (sample 1 in *Figure 23d-f*). However, a minor change in the surrounding by closing the previously open gap changes the situation (sample 2, *Figure 23c*) , and all dyes now show differences in the overall measured orientation distributions (sample 2 in *Figure 23d-f*). While the structural related dyes ATTO 647N and ATTO 643

still show a similar preferred orientation that peaks at different angles, the Cy5 dye does not show any tendency in its orientation.

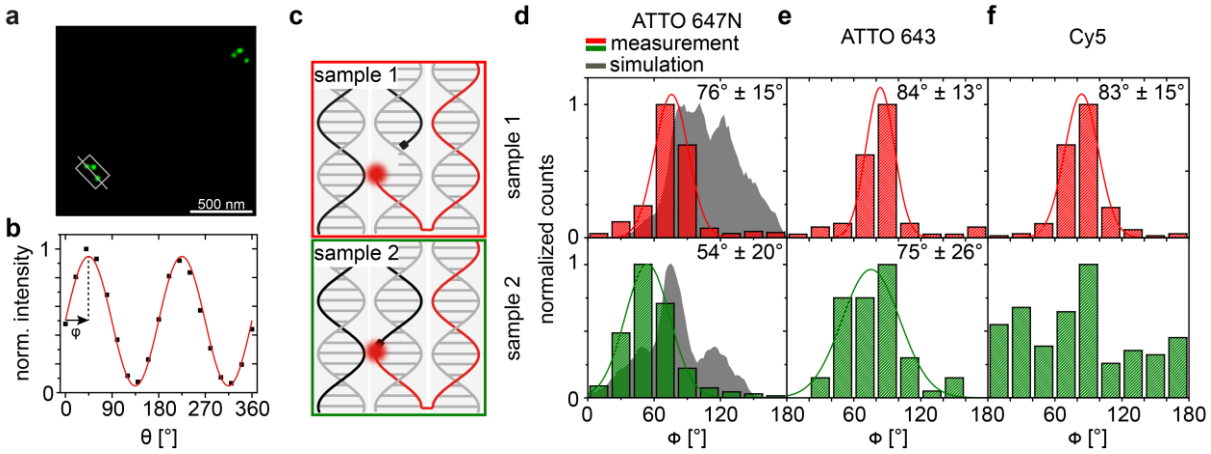

Figure 23: Measured and simulated dye orientations in two different assemblies with three different dyes. (a) DNA-PAINT image to extract the DNA origami orientation. (b) Extracted intensity values from a modulated intensity transient for each excitation polarization, with φ being the fluorophore orientation with dipole moment $\overrightarrow{\mu_G}$. (c) Sketches of sample 1 and 2 showing the DNA assembly around the fluorescent dye. (d) Measured and simulated data for the ATTO 647N orientation. (e) and (f) show the measured orientations for ATTO 643 and Cy5 in the same assemblies as for ATTO 647N. Reprinted with permission from [156].

Additional molecular dynamics (MD) simulations are used to revisit the measured dye orientations on the structural molecular level. In order to minimize the computational costs, only small segments of three short DNA helices with the dye on the middle helix are simulated (similar to *Figure 23*c). From the MD simulations, dye orientations are extracted and set into context with the measured orientations. The MD simulations show that in sample 1 the dyes seem to arrange themselves in the created gap, something which is also recognized from experimental data, whereas in sample 2 different geometries are visited. Besides the orientations matching the experimental data, the simulations also yield additional occupied states. This distribution broadening can be attributed to the short sampling time, which leads to an incomplete representation of the energy landscape. On the other hand, the simulations help to rationalize the measured results. The conformational states visited at the measured angles coincide with possible interactions in the varied geometries of the different samples.

4.2.1 Associated Publication P2

Determining the In-Plane Orientation and Binding Mode of Single Fluorescent Dyes in DNA Origami Structures

by

Kristina Hübner, Himanshu Joshi, Aleksei Aksimentiev, Fernando D. Stefani, Philip Tinnefeld, Guillermo P. Acuna

Published in

ACS Nano, 2021, 15 (3), 5109-5117

The full publication and supporting information are attached in appendix A2.

4.3 Publication 3: Salt-Induced Conformational Switching of a Flat Rectangular DNA Origami Structure

A plethora of controlled and stochastic fluctuating structures have been implemented in different fields of science. The movements of these flexible structures are often actuated by specific structural motifs. The controlled switching of a hinge-like DNA origami structure, for example, could be controlled by strand displacement reactions[72] or changes in salt concentration.[157] Furthermore, robotic arms responding to external electric fields have been introduced.[73] The stability of DNA origami structures as well as several of the flexible elements of the systems highly rely on salt identity and concentration.[158] First studies have shown that the measured distances in a DNA-PAINT experiment on a rectangular DNA origami structure vary for different salt concentrations. It has been found that the long distance on the rectangle stays nearly constant, while the diagonal distance decreases for a change in salt concentration from 0 to 500 mM $MgCl_2$.[63] In addition, other studies have demonstrated that different salts can occupy different places in a DNA double helix[159,160] or DNA origami structure[62,161].

In the associated publication P3 the impact of the concentration of bivalent cations on a 2D DNA origami rectangle (NRO) is studied in detail. To this end, the NRO is modified in two different ways and investigated from medium (12 mM) up to high (1000 mM) salt concentrations of $MgCl_2$ and $CaCl_2$. In the first assay, a DNA-PAINT experiment is performed (*Figure 24a* and *b*). For this purpose, DNA-PAINT binding sequences are attached on both long edges of the NRO to bind imager strands. An analysis of the distance between the two resolved lines at increased salt concentrations reveals a reduction in the measured distances (*Figure 24c*) and nicely reproduces the aforementioned studies[63]. Besides the size-reduced NROs, DNA origami structures, which seem to be collapsed (visualized by only one line in the SR images and indicated by yellow arrows in *Figure 24b*) are also present. To further investigate these DNA origami structures and answer the question of underlying dynamics in these systems, an energy transfer assay is designed on the same structure. In this assay, the energy transfer occurs between a red fluorophore (ATTO 647N) in one corner of the NRO and a 10 nm gold NP attached in the central region of the NRO. In order to only focus on structures with the complete energy transfer assembly, a green dye (ATTO 532) underneath the NP reports on NP binding. The fluorescence lifetime of the dyes is extracted with the help of FLIM, and a quenching in fluorescence intensity and lifetime can be related to a movement of the dye and therefore the whole NRO. This quenching is observed in fluorescence lifetime images in a salt-exchange experiment showing a reversibility in the quenching effect (*Figure 24d*). A more detailed analysis to resolve dynamics of the systems is performed in a salt-titration experiment (12–1000 mM $MgCl_2$) with the recording of single-molecule transients. Furthermore, the titration experiment reveals how the structure behaves at intermediate salt concentrations. The same experimental procedure is repeated for the bivalent cation calcium. This ion shows stronger affinity to DNA, and an earlier occupation of the quenched fluorescence lifetime state is expected. This expectation is confirmed by measurements (*Figure 24e*). Furthermore, the data illustrates that the ATTO 647N does not slowly approach the NP but that a two-state system of the NRO is present. The two states are assigned to a flat (*Figure 24f*) and a rolled-up (*Figure 24g*) geometry of the NRO, whereby

the rolled-up geometry is stabilized by the high concentration of the bivalent ions that bridge the two opposing sides of the NRO.

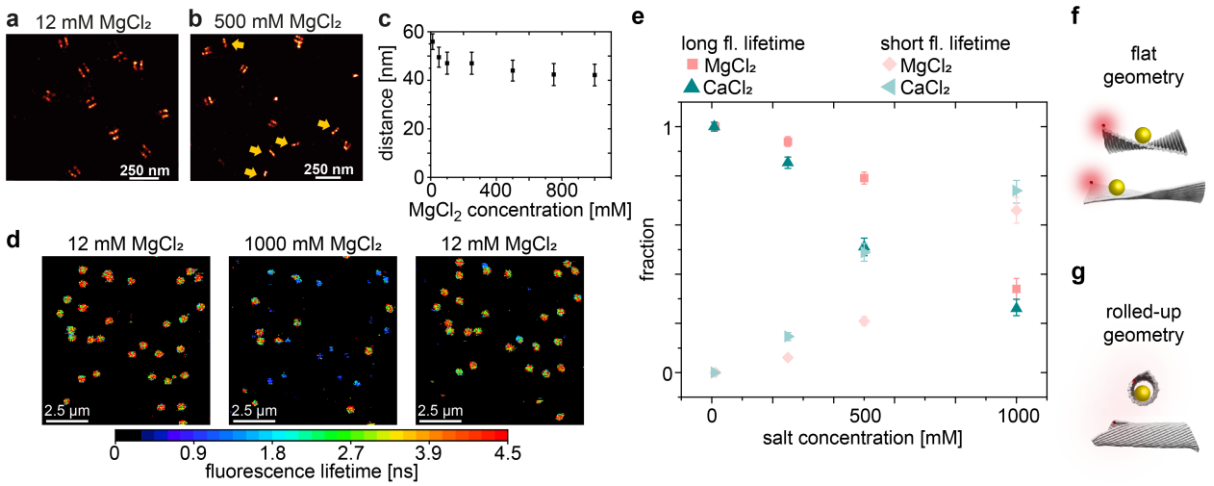

Figure 24: Super-resolved DNA-PAINT images and fluorescence lifetime quenching in a dynamic DNA origami assembly at different salt concentrations. Super-resolved DNA-PAINT images of the NRO labeled at the long sides at 12 mM $MgCl_2$ showing two parallel lines (a) and at 500 mM $MgCl_2$ with a significant fraction of structures showing one line (marked by yellow arrows; b). (c) Measured distances between the two parallel lines indicating a decrease with an increased $MgCl_2$ concentration. (d) Consecutive fluorescence lifetime images of the same area at 12, 1000 and 12 mM $MgCl_2$ to demonstrate the changes in the fluorescence lifetime and the recovery of the original system. (e) Results from titration experiments for Mg^{2+} and Ca^{2+} ion concentrations showing the fractions of long and short fluorescence lifetimes to illustrate the changes between the different concentrations. Data is taken from fluorescence lifetime transients for several single structures. (f) shows the flat geometry associated with the parallel lines and a long fluorescence lifetime in DNA-PAINT and FLIM images. (g) Rolled-up geometry of the rectangular DNA origami structure associated with one line and a short fluorescence lifetime in (b) and (d).

Both measurements show that a structural change in the flat NRO takes place with increasing salt concentrations. Additionally, calculations are performed to reveal the rolling-up axis in the NRO, which can be along the DNA helices or diagonal on the DNA origami rectangle.

4.3.1 Associated Publication P3

Salt-Induced Conformational Switching of a Flat Rectangular DNA Origami Structure

by

Kristina Hübner, Mario Raab, Johann Bohlen, Julian Bauer, Philip Tinnefeld

Published in

Nanoscale, 2022, 14, 7898-7905

The full publication and supporting information are attached in appendix A3.

5. Conclusion and Outlook

The thesis shows that dye orientations play an important role in fluorescent dye-OA assemblies. Depending on the relative orientation with respect to the OAs axis, the fluorophore experiences a strong fluorescence enhancement or nearly complete suppression. As the fluorophore's orientation plays a decisive role in OA coupling, an assay is developed to report on the relative orientation of a fluorophore in a DNA origami structure. With the help of this assay, orientations of different fluorophores are extracted in a rectangular DNA origami structure in various nano-environments. Not only fluorophores in DNA origami structures can be caught in preferred orientations but also dynamic DNA structures, like Holliday Junctions. In these junctions it is neither the immediate surrounding of DNA nor the chemical structures that are the driving forces for structural changes, but bivalent cations that can bridge DNA helices inducing long-lived salt-nucleic acid interactions. Salts have also been shown to be inevitable to contribute to the stability of DNA origami structures. So it has been further illustrated that strongly elevated concentrations of bivalent cations can substantially impact the geometric conformation of a rectangular DNA origami structure.

Publication P1 analyzes how an OA is directing the absorption and emission of a single coupled fluorophore. To this end, a red fluorescent dye is coupled to an OA in order to study the effect of the antenna on the absorption and emission directionality. For this purpose, the coupled system is compared to a DNA origami structure with only the dye incorporated. To extract the information about the dipole orientations, polarization-resolved wide-field measurements and defocused imaging are used to obtain the absorption and emission dipole orientations, respectively. Both measurements are performed for the reference sample and the coupled dye-OA system revealing that both absorption and emission dipole orientations are rotationally free in the reference and become anisotropic in the coupled system. A correlation between both extracted dipole orientations shows a good alignment. It can be concluded from these experiments that the main resonance mode of the OA is directing the absorption and emission of a coupled dye through efficient dye-antenna coupling in a parallel orientation and a quenching in the perpendicular orientation of the dye to the OA's axis. Using these studies as a basis, more complex systems could be engineered like nanoantenna systems for color routing[162–165] and directional emission. Color routing could, for example, be achieved with bimetallic dimer antenna systems[166–169]. While bimetallic antennas show the ability to route light of different wavelength into different directions (*Figure 25a* and *b*), trimer gold structures[170] or constructed Yagi Uda antennas[5,125,171,172] could serve as directors (*Figure 25c*). DNA functionalization of gold and silver NPs as well as fluorescent dyes linked to single stranded DNA allow the assembly of such a bimetallic antenna on a DNA origami structure. To build the color routing assembly, a silver and gold NP can be bound on a DNA origami structure with a green–red FRET pair in the hot spot region. If the antenna is illuminated with a green laser, the green dye transfers energy to the red dye and the emission is then directed by the asymmetric antenna in direction of the Au NP (*Figure 25a*). After acceptor bleaching, the green dye is fluorescing and the emission light is guided into the Ag NP direction (*Figure 25b*). Another way to switch between dyes would be to use chemical adducts that induce blinking, similar as in super-resolution localization microscopy.[173,174] Alternatively, dyes showing the ability of spectral shifts could be employed.[175,176] Thus, if measured with the defocused imaging technique, the emission patterns

should change during the measurement indicating the bleaching/switching process of the dyes and the routing ability of the bimetallic antenna.

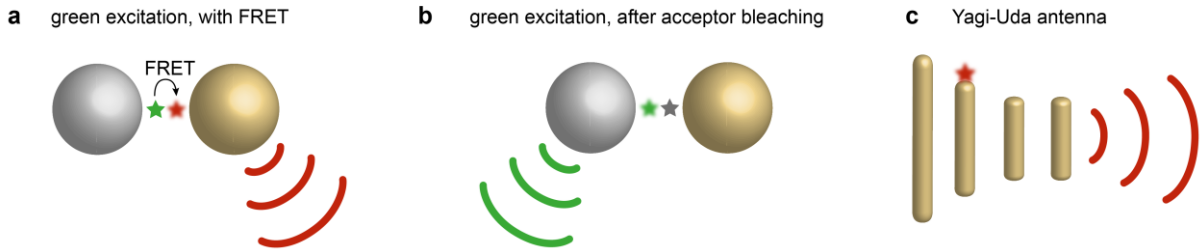

Figure 25: Sketches of different color routing assemblies. Color routing in a bimetallic antenna built from a silver and gold NP with a FRET pair in the hot spot region. (a) Green excitation leads to FRET from the green to the red dye and to red emission in direction of the gold NP, and (b) after acceptor bleaching the emission gets routed into the direction of the silver NP. (c) Constructed Yagi-Uda antenna to direct the emission of a coupled fluorescent dye.

Another assembly that could be realized on DNA origami structures is the construction of a Yagi-Uda antenna built from gold nanorods and a fluorophore (*Figure 25c*). This fluorophore needs to be positioned close to the nanorod in front of the reflector (last, largest nanorod), also named the feed element, to guide the fluorescence signal towards the smaller nanorod elements, called directors. A combination of the discussed routing and directionality of emitted fluorescence signals could offer the opportunity to build optical computing systems with single elements that are able to “talk” to each other via fluorescence light signals.

As the orientation of the fluorescence molecules in, for example, OA assemblies is so important, publication P2 introduces a method for measuring preferred orientations of fluorophores in a rectangular DNA origami structure. In order to extract the orientations, two measurement techniques are combined: DNA-PAINT to extract the lateral orientation of the DNA origami structure and polarization-resolved wide-field imaging, which enables the determination of the lateral orientation of the fluorescent dye. The relation between both angles gives the relative orientation of the dye in the DNA origami structure. Three red dyes (ATTO 647N, ATTO 643 and Cy5) are studied in different nano-environments, so in total seven different configurations are analyzed with regard to their preference to take fixed orientations.

It has been found that the close nano-environment has a strong impact on the dyes’ preferred orientations in the DNA origami structure. Thus, in the sample in which two base pairs in the DNA helix adjacent to the fluorophore’s position are left out (sample 1 described in chapter 4.2), all three dyes orient themselves in a the created gap and show similar orientation distributions. After closing this gap (sample 2 described in chapter 4.2), the structural identity of the dyes itself plays an important role, and different orientations are taken in the DNA origami structure. This is shown by the fact that structurally similar dyes (ATTO 643 and ATTO 647N) have the same orientations, whereas a structurally different type of dye (Cy5) yields different orientation distributions. Some of the measured orientations are reproduced at the molecular level by MD simulations. The simulations help to identify the geometric and structural arrangement of the dyes in the DNA origami structures. However, the MD simulations have some limitations, for example the short sampling time. The short time of 1 µs is not sufficient to represent

the complete energy landscape. Also, a clear parametrization of the interaction between dyes and DNA is not given, which could lead to further uncertainties. To validate both the measured and simulated orientations, both values are compared. So on the one hand it is analyzed if the orientations measured are also visited in the MD simulations, and on the other hand the corresponding structures from MD simulations are set into context. Through the variations made in the sample design, different binding states can be occupied by the dyes. A comparison of the orientations in experiment and simulation of all these dyes and states shows that the orientations from MD simulations are reasonable in the context of the measurements. As the measurements taken within the framework of this thesis are limited to a selection of red fluorescent dyes, these studies could be extended to a broader range of dyes in the red but also to other wavelength regimes. In addition to extending the studies to a broader range of dyes, the surrounding environment could also be studied in greater detail. Thus, different base pair combinations in the direct vicinity of the fluorescent dye could possibly affect the orientation. Also, a more detailed study of the effect of varying positions (e.g. close to a cross over) and types of linkage (3'-, 5'-, or internal-link, different linker length) could be interesting.[177] A more in-depth and extensive analysis of these parameters would allow the assembly of FRET pairs or OA systems with controlled dye orientations, making them extremely efficient as the interactions are dependent on the dipole orientations.

As mentioned above, the energy transfer in FRET assemblies is highly dependent on the relative orientations between the involved dyes. *Figure 26* exemplarily shows the distance-dependent FRET efficiency for the orientation factors κ^2 = 2/3 and κ^2 = 4. In a head-to-tail arrangement κ^2 is at maximum (4), but for assemblies linked to DNA and studied in an aqueous surrounding, the dyes are assumed to rotate freely, and an average κ^2 of 2/3 is used for the calculation of the energy transfer efficiency.[3] The change of the orientation factor also leads to a change of the energy transfer efficiency. The distance showing an energy transfer of 50% (d_0) for an ATTO 542-ATTO 647N FRET pair, for example, would change from 6.3 nm to 8.5 nm for the rotational free and the aligned case, respectively. This means that not only the energy transfer efficiency changes at a defined distance but also the working range.

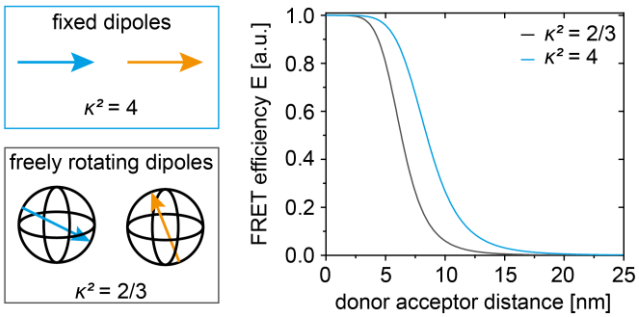

Figure 26: Dipole orientations in a FRET assembly. A head-to-tail and rotational free orientation of interacting dipoles with different orientation factors (κ^2) are shown. Depending on the orientation factors, the d_0 value changes for an ATTO 542-ATTO 647N FRET pair, with the value being larger for the dipoles fixed in a head-to-tail alignment as compared to that of the free rotating dipoles. (Values calculated on fpbase.org)

If the parameter of the relative orientations in FRET assemblies can be controlled through a defined modeling of the molecular surrounding to keep the dyes fixed, it is possible to not only create efficient two-color FRET pairs but also to improve photonic wires[178–182] that are based on energy transfer between dyes assembled in a linear arrangement.

Arranging transition dipoles of fluorescent dyes in DNA origami structures is still a formidable challenge since it includes the study of dyes in different environmental surroundings that vary depending on the dye's position. So it might also be interesting not only to focus on dyes attached via one linker to the DNA strand, but to study doubly linked dyes in more detail. These can be set under tension so they take defined orientations that might not depend on the direct molecular surrounding. However, there is an easier way to improve FRET measurements in DNA origami structures that could be achieved by using the technique in this thesis. If the orientation of both dyes could be measured before the FRET pair is assembled, an accurate orientation factor could be extracted. This would help to later calculate more precisely the distance measured via FRET.

Unlike in FRET studies, in OA assemblies the relative orientation of a dye in a dimer construct of two NPs is important (see discussion in chapter 2.2.3). Thus, if it were possible to align a fluorophore to the OA's axis, this would lead to the strongest possible coupling and fluorescence enhancement. The ability to control the orientation of fluorophores in OAs would result in a high fluorescence enhancement factor and narrow distributions. So, a broadening in the distributions would most probably emerge from an inhomogeneity in the NP's shape because large particles show facets and varieties in their diameter. This factor, in turn, could be controlled by the use of ultrasmooth spherical NPs[183] (which are discussed in publication P1). When these two factors are under control, only the accuracy of the gap size and the exact positions of the NPs and the dye can lead to uncertainty and distribution broadening. However, the gap size and NPs' positions should be controlled by the use of DNA origami structures.

The last part of the thesis introduced in chapter 4.3 and discussed further in the associated publication P3 covers the influence of high bivalent ion concentrations on a 2D rectangular DNA origami structure. With the help of DNA-PAINT measurements, structural changes in the rectangular DNA origami structure are revealed, which on the one hand show compacted versions of the two designed parallel lines. This structural change was already shown in previous studies which observed that the long and diagonal distances on the DNA origami rectangle measured by DNA-PAINT showed changes from normal (12 mM) to high (500 mM) salt concentrations.[63] On the other hand, however, there are also structures showing only one line in the super-resolved images. In order to study these structures in greater detail, an energy transfer assay is designed on the same DNA origami structure. This energy transfer based on a 10 nm gold NP and a red fluorescent dye (ATTO 647N) can report on structural changes due to a quenching of the fluorescence intensity of the red dye. This quenching occurs when the dye approaches the NP. With confocal fluorescence lifetime imaging it is possible to observe structural changes and even a dynamic switching between two states. The structural change is assigned to a rolling-up of the rectangular DNA origami structure into a tube-like shape, which is further proven by theoretical distance calculations and correlations with fluorescence lifetime values at different dye-NP distances of previously published studies[19]. Furthermore, it is shown that the structural change in the rectangular DNA origami structure is a reversible process recovering the original non-quenched

fluorescence lifetime state after a salt exchange from 1000 mM to 12 mM of Mg^{2+}. Additionally, it is proven that the mechanism is not only prone to the concentration of magnesium ions but that calcium ions can induce the same effect. While the two-dimensional DNA origami structure shows a rather strong response to the concentration of bivalent cations, the same effect is not observed for three-dimensional structures. The studied structure is built from many parallel and stacked helices, which provides a high robustness. Thus, high concentrations of bivalent ions do not show a strong influence. These findings again show the importance of ions in stabilizing DNA origami structures. With this knowledge, DNA origami structures could be more compacted so they are more robust in assays where a high stiffness of the structures is needed. It is furthermore recognized that after a buffer exchange from magnesium to calcium (or *vice versa*) and a subsequent salt titration with the exchanged ion, DNA origami structures are only weakly or not responding to the increased salt concentrations. This could be attributed to some kind of memory effect, meaning that ions stay bound to the DNA origami structure and are not completely washed out. This finding is important, as folding DNA origami structures works best with magnesium ions, but in some experiments these ions should be removed and replaced by different kinds of ions. If the incubation of the new measurement buffer is not long enough or washing steps are not executed carefully, magnesium ions, for example, could stay attached to the DNA origami structure. This work proves that there is no need of special motifs like joints or hinges to build switchable DNA origami structures and that the addition of bivalent cations at high concentrations can be used as an actuating mechanism. Usually strand hybridization and displacement reactions are practiced to switch DNA origami structures, where relatively long incubation times are needed. In the presented work, the reaction time is very fast, and first structural changes can be monitored directly after the addition of high salt concentrations.

This thesis covers the interactions between fluorescent dyes and plasmonic NPs and fluorescent dyes and close nano-environments as well as the effect of cations on a DNA origami structure. In order to study these kind of interactions, three single-molecule assays are developed within this thesis. The introduced measurement procedures set out the basis for a couple of new measurements. The combination of polarization-resolved wide-field imaging and defocused imaging enables the measurement of the absorption as well as the emission dipole orientations in the same molecules. These methods can help to also investigate and understand more complex assemblies, for example in prospective optical computing systems, to reveal the principles in the single elements. Polarization-resolved wide-field imaging in combination with the DNA-PAINT super-resolution technique, on the other hand, offer possibilities for broad studies on molecular orientations of fluorescent dyes in DNA origami structures. An advantage of the performed measurements is that the orientations of the DNA origami structures as well as the orientations of the helices in the structures and the angles of the attached fluorescent dyes can be determined. In combination with MD simulations, even insights in the molecular orientations of the dyes in the DNA origami structures can be revealed. The presented assay could help to make FRET measurements and distance calculations more accurate. Lastly, by combining DNA-PAINT measurements and scanning confocal lifetime imaging, it is possible to not only gain structural information of DNA origami structures but also to observe dynamic systems, thus reaching a high structural and temporal resolution in two and three dimensions. Conclusively, this work reports on new single-molecule assays to be adopted in fluorescence microscopy research. These assays serve to

understand and design fluorescence color routing and optical communication circuits. Dye orientation control and analysis can help to create photonic nanowires and improve FRET calculations. In addition, the fortuitous finding of switchable two-dimensional DNA origami structures at increased salt concentrations without the use of special motifs is made. This assay demonstrates the binding of different cations and introduces an actuating mechanism in switchable DNA origami structures.

6. List of Abbreviations

A	adenine
AFM	atomic force microscopy
AOTF	acousto-optical tunable filter
APD	avalanche photo diode
BSA	bovine serum albumin
bp	base pairs
DNA	deoxyribonucleic acid
C	cytosine
EMCCD	electron multiplying charge-coupled device
EOM	electro-optical modulator
exc.	excitation
FE	fluorescence enhancement
fl.	fluorescence
FLIM	fluorescence lifetime imaging microscopy
FRET	Förster-resonance-energy-transfer
G	guanine
IC	internal conversion
IRF	instrument response function
ISC	intersystem crossing
LSPR	localized surface plasmon resonance
MD	molecular dynamics
MINFLUX	minimal emission fluxes
NIR	near infrared
NP	nanoparticle
nr	non radiative
OA	optical antenna
PAINT	points accumulation for imaging in nanoscale topography

PALM	photoactivated localization microscopy
phos	phosphorescence
PMD	photonic mode density
PSF	point spread function
r	radiative
ROX	reducing and oxidizing
SMFM	single-molecules fluorescence microscopy
STED	stimulated emission depletion
STORM	stochastic optical reconstruction microscopy
T	thymine
TCSPC	time correlated single photon counting
TIRF	total internal reflection
UV	ultraviolet

7. List of Literature

[1] G. G. Stokes. XXX. On the change of refrangibility of light, *Phil. Trans. R. Soc.* **1852**, *142*, 463–562.

[2] S. Shashkova, M. C. Leake. Single-molecule fluorescence microscopy review: shedding new light on old problems, *Bioscience reports* **2017**, *37* (4).

[3] J. R. Lakowicz, *Principles of fluorescence spectroscopy*, Springer, New York **2006**.

[4] W. E. Moerner, Y. Shechtman, Q. Wang. Single-molecule spectroscopy and imaging over the decades, *Faraday discussions* **2015**, *184*, 9–36.

[5] L. Novotny, N. van Hulst. Antennas for light, *Nature Photon* **2011**, *5* (2), 83–90.

[6] E. A. Coronado, E. R. Encina, F. D. Stefani. Optical properties of metallic nanoparticles: manipulating light, heat and forces at the nanoscale, *Nanoscale* **2011**, *3* (10), 4042–4059.

[7] P. Holzmeister, E. Pibiri, J. J. Schmied, T. Sen, G. P. Acuna, P. Tinnefeld. Quantum yield and excitation rate of single molecules close to metallic nanostructures, *Nature communications* **2014**, *5*, 5356.

[8] P. Bharadwaj, B. Deutsch, L. Novotny. Optical Antennas, *Adv. Opt. Photon.* **2009**, *1* (3), 438.

[9] N. J. Halas, S. Lal, W.-S. Chang, S. Link, P. Nordlander. Plasmons in strongly coupled metallic nanostructures, *Chemical reviews* **2011**, *111* (6), 3913–3961.

[10] A. Kinkhabwala, Z. Yu, S. Fan, Y. Avlasevich, K. Müllen, W. E. Moerner. Large single-molecule fluorescence enhancements produced by a bowtie nanoantenna, *Nature Photon* **2009**, *3* (11), 654–657.

[11] G. P. Acuna, F. M. Möller, P. Holzmeister, S. Beater, B. Lalkens, P. Tinnefeld. Fluorescence enhancement at docking sites of DNA-directed self-assembled nanoantennas, *Science* **2012**, *338* (6106), 506–510.

[12] M. P. Busson, B. Rolly, B. Stout, N. Bonod, S. Bidault. Accelerated single photon emission from dye molecule-driven nanoantennas assembled on DNA, *Nat Commun* **2012**, *3* (1), 962.

[13] K. Hübner, M. Pilo-Pais, F. Selbach, T. Liedl, P. Tinnefeld, F. D. Stefani, G. P. Acuna. Directing Single-Molecule Emission with DNA Origami-Assembled Optical Antennas, *Nano Lett.* **2019**, *19* (9), 6629–6634.

[14] C. Vietz, B. Lalkens, G. P. Acuna, P. Tinnefeld. Functionalizing large nanoparticles for small gaps in dimer nanoantennas, *New J. Phys.* **2016**, *18* (4), 45012.

[15] M. P. Busson, B. Rolly, B. Stout, N. Bonod, E. Larquet, A. Polman, S. Bidault. Optical and topological characterization of gold nanoparticle dimers linked by a single DNA double strand, *Nano Lett.* **2011**, *11* (11), 5060–5065.

[16] P. W. K. Rothemund. Folding DNA to create nanoscale shapes and patterns, *Nature* **2006**, *440* (7082), 297–302.

[17] N. C. Seeman. Nucleic acid junctions and lattices, *Journal of Theoretical Biology* **1982**, *99* (2), 237–247.

[18] S. M. Douglas, H. Dietz, T. Liedl, B. Högberg, F. Graf, W. M. Shih. Self-assembly of DNA into nanoscale three-dimensional shapes, *Nature* **2009**, *459* (7245), 414–418.

[19] G. P. Acuna, M. Bucher, I. H. Stein, C. Steinhauer, A. Kuzyk, P. Holzmeister, R. Schreiber, A. Moroz, F. D. Stefani, T. Liedl, F. C. Simmel, P. Tinnefeld. Distance dependence of single-fluorophore quenching by gold nanoparticles studied on DNA origami, *ACS nano* **2012**, *6* (4), 3189–3195.

[20] F. M. Möller, P. Holzmeister, T. Sen, G. P. Acuna, P. Tinnefeld. Angular modulation of single-molecule fluorescence by gold nanoparticles on DNA origami templates, *Nanophotonics* **2013**, *2* (3), 167–172.

[21] J. Bohlen, Á. Cuartero-González, E. Pibiri, D. Ruhlandt, A. I. Fernández-Domínguez, P. Tinnefeld, G. P. Acuna. Plasmon-assisted Förster resonance energy transfer at the single-molecule level in the moderate quenching regime, *Nanoscale* **2019**, *11* (16), 7674–7681.

[22] A. Puchkova, C. Vietz, E. Pibiri, B. Wünsch, M. Sanz Paz, G. P. Acuna, P. Tinnefeld. DNA Origami Nanoantennas with over 5000-fold Fluorescence Enhancement and Single-Molecule Detection at 25 µM, *Nano letters* **2015**, *15* (12), 8354–8359.

[23] C. Vietz, I. Kaminska, M. Sanz Paz, P. Tinnefeld, G. P. Acuna. Broadband Fluorescence Enhancement with Self-Assembled Silver Nanoparticle Optical Antennas, *ACS nano* **2017**, *11* (5), 4969–4975.

[24] J. V. Pellegrotti, G. P. Acuna, A. Puchkova, P. Holzmeister, A. Gietl, B. Lalkens, F. D. Stefani, P. Tinnefeld. Controlled reduction of photobleaching in DNA origami-gold nanoparticle hybrids, *Nano letters* **2014**, *14* (5), 2831–2836.

[25] S. E. Ochmann, C. Vietz, K. Trofymchuk, G. P. Acuna, B. Lalkens, P. Tinnefeld. Optical Nanoantenna for Single Molecule-Based Detection of Zika Virus Nucleic Acids without Molecular Multiplication, *Analytical chemistry* **2017**, *89* (23), 13000–13007.

[26] C. Vietz, B. Lalkens, G. P. Acuna, P. Tinnefeld. Synergistic Combination of Unquenching and Plasmonic Fluorescence Enhancement in Fluorogenic Nucleic Acid Hybridization Probes, *Nano letters* **2017**, *17* (10), 6496–6500.

[27] K. Trofymchuk, V. Glembockyte, L. Grabenhorst, F. Steiner, C. Vietz, C. Close, M. Pfeiffer, L. Richter, M. L. Schütte, F. Selbach, R. Yaadav, J. Zähringer, Q. Wei, A. Ozcan, B. Lalkens, G. P. Acuna, P. Tinnefeld. Addressable nanoantennas with cleared hotspots for single-molecule detection on a portable smartphone microscope, *Nature communications* **2021**, *12* (1), 950.

[28] I. Kaminska, J. Bohlen, S. Mackowski, P. Tinnefeld, G. P. Acuna. Strong Plasmonic Enhancement of a Single Peridinin-Chlorophyll a-Protein Complex on DNA Origami-Based Optical Antennas, *ACS nano* **2018**, *12* (2), 1650–1655.

[29] P. Kühler, E.-M. Roller, R. Schreiber, T. Liedl, T. Lohmüller, J. Feldmann. Plasmonic DNA-origami nanoantennas for surface-enhanced Raman spectroscopy, *Nano letters* **2014**, *14* (5), 2914–2919.

[30] W. Fang, S. Jia, J. Chao, L. Wang, X. Duan, H. Liu, Q. Li, X. Zuo, L. Wang, L. Wang, N. Liu, C. Fan. Quantizing single-molecule surface-enhanced Raman scattering with DNA origami metamolecules, *Science advances* **2019**, *5* (9), eaau4506.

[31] S. Simoncelli, E.-M. Roller, P. Urban, R. Schreiber, A. J. Turberfield, T. Liedl, T. Lohmüller. Quantitative Single-Molecule Surface-Enhanced Raman Scattering by Optothermal Tuning of DNA Origami-Assembled Plasmonic Nanoantennas, *ACS nano* **2016**, *10* (11), 9809–9815.

[32] V. V. Thacker, L. O. Herrmann, D. O. Sigle, T. Zhang, T. Liedl, J. J. Baumberg, U. F. Keyser. DNA origami based assembly of gold nanoparticle dimers for surface-enhanced Raman scattering, *Nature communications* **2014**, *5*, 3448.

[33] J. J. Mock, M. Barbic, D. R. Smith, D. A. Schultz, S. Schultz. Shape effects in plasmon resonance of individual colloidal silver nanoparticles, *The Journal of Chemical Physics* **2002**, *116* (15), 6755–6759.

[34] P. Anger, P. Bharadwaj, L. Novotny. Enhancement and quenching of single-molecule fluorescence, *Physical review letters* **2006**, *96* (11), 113002.

[35] E. M. S. Stennett, N. Ma, A. van der Vaart, M. Levitus. Photophysical and dynamical properties of doubly linked Cy3-DNA constructs, *J. Phys. Chem. B* **2014**, *118* (1), 152–163.

[36] J. J. Mock, R. T. Hill, A. Degiron, S. Zauscher, A. Chilkoti, D. R. Smith. Distance-dependent plasmon resonant coupling between a gold nanoparticle and gold film, *Nano Lett.* **2008**, *8* (8), 2245–2252.

[37] L. Rogobete, F. Kaminski, M. Agio, V. Sandoghdar. Design of plasmonic nanoantennae for enhancing spontaneous emission, *Optics letters* **2007**, *32* (12), 1623–1625.

[38] L. A. Blanco, F. J. García de Abajo. Spontaneous emission enhancement near nanoparticles, *Journal of Quantitative Spectroscopy and Radiative Transfer* **2004**, *89* (1-4), 37–42.

[39] J.-W. Liaw, C.-S. Chen, J.-H. Chen. Enhancement or quenching effect of metallic nanodimer on spontaneous emission, *Journal of Quantitative Spectroscopy and Radiative Transfer* **2010**, *111* (3), 454–465.

[40] T. Förster. Zwischenmolekulare Energiewanderung und Fluoreszenz, *Ann. Phys.* **1948**, *437* (1-2), 55–75.

[41] B. Hellenkamp, S. Schmid, O. Doroshenko, O. Opanasyuk, R. Kühnemuth, S. Rezaei Adariani, B. Ambrose, M. Aznauryan, A. Barth, V. Birkedal, M. E. Bowen, H. Chen, T. Cordes, T. Eilert, C. Fijen, C. Gebhardt, M. Götz, G. Gouridis, E. Gratton, T. Ha, P. Hao, C. A. Hanke, A. Hartmann, J. Hendrix, L. L. Hildebrandt, V. Hirschfeld, J. Hohlbein, B. Hua, C. G. Hübner, E. Kallis, A. N. Kapanidis, J.-Y. Kim, G. Krainer, D. C. Lamb, N. K. Lee, E. A. Lemke, B. Levesque, M. Levitus, J. J. McCann, N. Naredi-Rainer, D. Nettels, T. Ngo, R. Qiu, N. C. Robb, C. Röcker, H. Sanabria, M. Schlierf, T. Schröder, B. Schuler, H. Seidel, L. Streit, J. Thurn, P. Tinnefeld, S. Tyagi, N. Vandenberk, A. M. Vera, K. R. Weninger, B. Wünsch, I. S. Yanez-Orozco, J. Michaelis, C. A. M. Seidel, T. D. Craggs, T. Hugel. Precision and accuracy of single-molecule FRET measurements-a multi-laboratory benchmark study, *Nature methods* **2018**, *15* (9), 669–676.

[42] I. Kaminska, J. Bohlen, S. Rocchetti, F. Selbach, G. P. Acuna, P. Tinnefeld. Distance Dependence of Single-Molecule Energy Transfer to Graphene Measured with DNA Origami Nanopositioners, *Nano Lett.* **2019**, *19* (7), 4257–4262.

[43] I. Kamińska, J. Bohlen, R. Yaadav, P. Schüler, M. Raab, T. Schröder, J. Zähringer, K. Zielonka, S. Krause, P. Tinnefeld. Graphene Energy Transfer for Single-Molecule Biophysics, Biosensing, and Super-Resolution Microscopy, *Advanced materials (Deerfield Beach, Fla.)* **2021**, *33* (24), e2101099.

[44] A. Ghosh, A. Sharma, A. I. Chizhik, S. Isbaner, D. Ruhlandt, R. Tsukanov, I. Gregor, N. Karedla, J. Enderlein. Graphene-based metal-induced energy transfer for sub-nanometre optical localization, *Nature Photon* **2019**, *13* (12), 860–865.

[45] A. I. Chizhik, J. Rother, I. Gregor, A. Janshoff, J. Enderlein. Metal-induced energy transfer for live cell nanoscopy, *Nature Photon* **2014**, *8* (2), 124–127.

[46] N. Karedla, A. M. Chizhik, S. C. Stein, D. Ruhlandt, I. Gregor, A. I. Chizhik, J. Enderlein. Three-dimensional single-molecule localization with nanometer accuracy using Metal-Induced Energy Transfer (MIET) imaging, *The Journal of Chemical Physics* **2018**, *148* (20), 204201.

[47] O. Nevskyi, R. Tsukanov, I. Gregor, N. Karedla, J. Enderlein. Fluorescence polarization filtering for accurate single molecule localization, *APL Photonics* **2020**, *5* (6), 61302.

[48] J. Engelhardt, J. Keller, P. Hoyer, M. Reuss, T. Staudt, S. W. Hell. Molecular orientation affects localization accuracy in superresolution far-field fluorescence microscopy, *Nano Lett.* **2011**, *11* (1), 209–213.

[49] M. D. Lew, W. E. Moerner. Azimuthal polarization filtering for accurate, precise, and robust single-molecule localization microscopy, *Nano Lett.* **2014**, *14* (11), 6407–6413.

[50] M. P. Backlund, A. Arbabi, P. N. Petrov, E. Arbabi, S. Saurabh, A. Faraon, W. E. Moerner. Removing Orientation-Induced Localization Biases in Single-Molecule Microscopy Using a Broadband Metasurface Mask, *Nature Photon* **2016**, *10*, 459–462.

[51] M. D. Lew, M. P. Backlund, W. E. Moerner. Rotational mobility of single molecules affects localization accuracy in super-resolution fluorescence microscopy, *Nano Lett.* **2013**, *13* (9), 3967–3972.

[52] S. Pal, Z. Deng, H. Wang, S. Zou, Y. Liu, H. Yan. DNA directed self-assembly of anisotropic plasmonic nanostructures, *Journal of the American Chemical Society* **2011**, *133* (44), 17606–17609.

[53] P. Zhan, T. Wen, Z.-G. Wang, Y. He, J. Shi, T. Wang, X. Liu, G. Lu, B. Ding. DNA Origami Directed Assembly of Gold Bowtie Nanoantennas for Single-Molecule Surface-Enhanced Raman Scattering, *Angewandte Chemie (International ed. in English)* **2018**, *57* (11), 2846–2850.

[54] H. Ihmels, D. Otto, in *Supermolecular Dye Chemistry*, Vol. 258 (Ed.: F. Würthner), Springer-Verlag **2005**, p. 161.

[55] A. Gopinath, C. Thachuk, A. Mitskovets, H. A. Atwater, D. Kirkpatrick, P. W. K. Rothemund. Absolute and arbitrary orientation of single-molecule shapes, *Science* **2021**, *371* (6531).

[56] J. Ouellet, S. Schorr, A. Iqbal, T. J. Wilson, D. M. J. Lilley. Orientation of cyanine fluorophores terminally attached to DNA via long, flexible tethers, *Biophysical journal* **2011**, *101* (5), 1148–1154.

[57] P. D. Cunningham, A. Khachatrian, S. Buckhout-White, J. R. Deschamps, E. R. Goldman, I. L. Medintz, J. S. Melinger. Resonance energy transfer in DNA duplexes labeled with localized dyes, *J. Phys. Chem. B* **2014**, *118* (50), 14555–14565.

[58] K. I. Mortensen, J. Sung, H. Flyvbjerg, J. A. Spudich. Optimized measurements of separations and angles between intra-molecular fluorescent markers, *Nature communications* **2015**, *6*, 8621.

[59] R. Holliday. A mechanism for gene conversion in fungi, *Genet. Res.* **1964**, *5* (2), 282–304.

[60] C. Hyeon, J. Lee, J. Yoon, S. Hohng, D. Thirumalai. Hidden complexity in the isomerization dynamics of Holliday junctions, *Nature chemistry* **2012**, *4* (11), 907–914.

[61] A. Gietl, P. Holzmeister, D. Grohmann, P. Tinnefeld. DNA origami as biocompatible surface to match single-molecule and ensemble experiments, *Nucleic acids research* **2012**, *40* (14), e110.

[62] C. Kielar, Y. Xin, B. Shen, M. A. Kostiainen, G. Grundmeier, V. Linko, A. Keller. On the Stability of DNA Origami Nanostructures in Low-Magnesium Buffers, *Angewandte Chemie (International ed. in English)* **2018**, *57* (30), 9470–9474.

[63] J. J. Schmied, M. Raab, C. Forthmann, E. Pibiri, B. Wünsch, T. Dammeyer, P. Tinnefeld. DNA origami-based standards for quantitative fluorescence microscopy, *Nature protocols* **2014**, *9* (6), 1367–1391.

[64] C. K. Wong, C. Tang, J. S. Schreck, J. P. K. Doye, *Characterizing the free-energy landscapes of DNA origamis* **2021**.

[65] M. D. E. Jepsen, R. S. Sørensen, C. Maffeo, A. Aksimentiev, J. Kjems, V. Birkedal. Single molecule analysis of structural fluctuations in DNA nanostructures, *Nanoscale* **2019**, *11* (39), 18475–18482.

[66] M. DeLuca, Z. Shi, C. E. Castro, G. Arya. Dynamic DNA nanotechnology: toward functional nanoscale devices, *Nanoscale Horiz.* **2020**, *5* (2), 182–201.

[67] L. K. Bruetzel, P. U. Walker, T. Gerling, H. Dietz, J. Lipfert. Time-Resolved Small-Angle X-ray Scattering Reveals Millisecond Transitions of a DNA Origami Switch, *Nano letters* **2018**, *18* (4), 2672–2676.

[68] R. Li, H. Chen, H. Lee, J. H. Choi. Conformational Control of DNA Origami by DNA Oligomers, Intercalators and UV Light, *Methods and protocols* **2021**, *4* (2).

[69] C. Albrecht, K. Blank, M. Lalic-Mülthaler, S. Hirler, T. Mai, I. Gilbert, S. Schiffmann, T. Bayer, H. Clausen-Schaumann, H. E. Gaub. DNA: a programmable force sensor, *Science* **2003**, *301* (5631), 367–370.

[70] F. Kühner, J. Morfill, R. A. Neher, K. Blank, H. E. Gaub. Force-induced DNA slippage, *Biophysical journal* **2007**, *92* (7), 2491–2497.

[71] R. Li, H. Chen, H. Lee, J. H. Choi. Elucidating the Mechanical Energy for Cyclization of a DNA Origami Tile, *Applied Sciences* **2021**, *11* (5), 2357.

[72] A. E. Marras, L. Zhou, H.-J. Su, C. E. Castro. Programmable motion of DNA origami mechanisms, *Proceedings of the National Academy of Sciences of the United States of America* **2015**, *112* (3), 713–718.

[73] E. Kopperger, J. List, S. Madhira, F. Rothfischer, D. C. Lamb, F. C. Simmel. A self-assembled nanoscale robotic arm controlled by electric fields, *Science (New York, N.Y.)* **2018**, *359* (6373), 296–301.

[74] A. Kuzyk, R. Schreiber, H. Zhang, A. O. Govorov, T. Liedl, N. Liu. Reconfigurable 3D plasmonic metamolecules, *Nature materials* **2014**, *13* (9), 862–866.

[75] C. K. McLaughlin, G. D. Hamblin, K. D. Hänni, J. W. Conway, M. K. Nayak, K. M. M. Carneiro, H. S. Bazzi, H. F. Sleiman. Three-dimensional organization of block copolymers on "DNA-minimal" scaffolds, *Journal of the American Chemical Society* **2012**, *134* (9), 4280–4286.

[76] M. Planck. Zur Theorie des Gesetzes der Energieverteilung im Normalspectrum, *Verhandlungen der Deutschen physikalischen Gesellschaft 2* **1900**, *17* (245).

[77] J. Franck, E. G. Dymond. Elementary processes of photochemical reactions, *Trans. Faraday Soc.* **1926**, *21*, 536–542.

[78] E. Condon. A Theory of Intensity Distribution in Band Systems, *Phys. Rev.* **1926**, *28* (6), 1182–1201.

[79] M. Born, R. Oppenheimer. Zur Quantentheorie der Molekeln, *Ann. Phys.* **1927**, *389* (20), 457–484.

[80] A. Jablonski. Efficiency of Anti-Stokes Fluorescence in Dyes, *Nature* **1933**, *131* (3319), 839–840.

[81] M. Kasha. Characterization of electronic transitions in complex molecules, *Discuss. Faraday Soc.* **1950**, *9*, 14–19.

[82] ATTO-TEC GmbH, *ATTO 647N* **2021**, https://www.atto-tec.com/product_info.php?language=de&info=p114_atto-647n.html.

[83] P. J. Walla, *Modern Biophysical Chemistry: Detection and Analysis of Biomolecules*, Wiley-VCH Verlag GmbH & Co. KGaA, Weinheim, Germany **2014**.

[84] E. H. Hellen, D. Axelrod. Fluorescence emission at dielectric and metal-film interfaces, *J. Opt. Soc. Am. B* **1987**, *4* (3), 337.

[85] Stefan Geissbühler, *Structural and Functional Stochastic Super-Resolution Microscopy*, Lausanne **2013**.

[86] J. Widengren, R. Rigler. Mechanisms of photobleaching investigated by fluorescence correlation spectroscopy, *Bioimaging* **1996**, *4* (3), 149–157.

[87] J. Raba, H. A. Mottola. Glucose Oxidase as an Analytical Reagent, *Critical Reviews in Analytical Chemistry* **1995**, *25* (1), 1–42.

[88] C. E. Aitken, R. A. Marshall, J. D. Puglisi. An oxygen scavenging system for improvement of dye stability in single-molecule fluorescence experiments, *Biophysical journal* **2008**, *94* (5), 1826–1835.

[89] J. Vogelsang, R. Kasper, C. Steinhauer, B. Person, M. Heilemann, M. Sauer, P. Tinnefeld. A reducing and oxidizing system minimizes photobleaching and blinking of fluorescent dyes, *Angewandte Chemie (International ed. in English)* **2008**, *47* (29), 5465–5469.

[90] T. Cordes, J. Vogelsang, P. Tinnefeld. On the mechanism of Trolox as antiblinking and antibleaching reagent, *Journal of the American Chemical Society* **2009**, *131* (14), 5018–5019.

[91] U. Leonhardt. Invisibility cup, *Nature Photon* **2007**, *1* (4), 207–208.

[92] P. Drude. Zur Elektronentheorie der Metalle, *Ann. Phys.* **1900**, *306* (3), 566–613.

[93] P. Drude. Zur Elektronentheorie der Metalle; II. Teil. Galvanomagnetische und thermomagnetische Effecte, *Ann. Phys.* **1900**, *308* (11), 369–402.

[94] A. Sommerfeld, H. Bethe, *Elektronentheorie der Metalle*, Springer Berlin Heidelberg, Berlin, Heidelberg **1967**.

[95] Gustav Mie. Beiträge zur Optik trüber Medien, speziell kolloidaler Metallösungen, *Annalen der Physik* **1908**, *4* (25), 377–445.

[96] P. K. Jain, M. A. El-Sayed. Plasmonic coupling in noble metal nanostructures, *Chemical Physics Letters* **2010**, *487* (4-6), 153–164.

[97] E. Dulkeith, A. C. Morteani, T. Niedereichholz, T. A. Klar, J. Feldmann, S. A. Levi, F. C. J. M. van Veggel, D. N. Reinhoudt, M. Möller, D. I. Gittins. Fluorescence quenching of dye molecules near gold nanoparticles: radiative and nonradiative effects, *Physical review letters* **2002**, *89* (20), 203002.

[98] P. J. Schuck, D. P. Fromm, A. Sundaramurthy, G. S. Kino, W. E. Moerner. Improving the mismatch between light and nanoscale objects with gold bowtie nanoantennas, *Physical review letters* **2005**, *94* (1), 17402.

[99] X. Cui, F. Qin, Q. Ruan, X. Zhuo, J. Wang. Circular Gold Nanodisks with Synthetically Tunable Diameters and Thicknesses, *Adv. Funct. Mater.* **2018**, *28* (11), 1705516.

[100] J. Pang, I. G. Theodorou, A. Centeno, P. K. Petrov, N. M. Alford, M. P. Ryan, F. Xie. Gold nanodisc arrays as near infrared metal-enhanced fluorescence platforms with tuneable enhancement factors, *J. Mater. Chem. C* **2017**, *5* (4), 917–925.

[101] L. Fabris. Gold Nanostars in Biology and Medicine: Understanding Physicochemical Properties to Broaden Applicability, *J. Phys. Chem. C* **2020**, *124* (49), 26540–26553.

[102] F. Liebig, R. Henning, R. M. Sarhan, C. Prietzel, C. N. Z. Schmitt, M. Bargheer, J. Koetz. A simple one-step procedure to synthesise gold nanostars in concentrated aqueous surfactant solutions, *RSC Adv.* **2019**, *9* (41), 23633–23641.

[103] nanoComposix, *The Science of Plasmonics* **2021**, https://nanocomposix.com/pages/the-science-of-plasmonics.

[104] K. L. Kelly, E. Coronado, L. L. Zhao, G. C. Schatz. The Optical Properties of Metal Nanoparticles: The Influence of Size, Shape, and Dielectric Environment, *J. Phys. Chem. B* **2003**, *107* (3), 668–677.

[105] L. M. Liz-Marzán. Tailoring surface plasmons through the morphology and assembly of metal nanoparticles, *Langmuir the ACS journal of surfaces and colloids* **2006**, *22* (1), 32–41.

[106] S. Eustis, M. A. El-Sayed. Why gold nanoparticles are more precious than pretty gold: noble metal surface plasmon resonance and its enhancement of the radiative and nonradiative properties of nanocrystals of different shapes, *Chemical Society reviews* **2006**, *35* (3), 209–217.

[107] U. Kreibig, M. Vollmer, *Optical Properties of Metal Clusters*, Springer Berlin Heidelberg, Berlin, Heidelberg **1995**.

[108] V. Myroshnychenko, J. Rodríguez-Fernández, I. Pastoriza-Santos, A. M. Funston, C. Novo, P. Mulvaney, L. M. Liz-Marzán, F. J. García de Abajo. Modelling the optical response of gold nanoparticles, *Chemical Society reviews* **2008**, *37* (9), 1792–1805.

[109] C. Clavero. Plasmon-induced hot-electron generation at nanoparticle/metal-oxide interfaces for photovoltaic and photocatalytic devices, *Nature Photon* **2014**, *8* (2), 95–103.

[110] S. Asano, G. Yamamoto. Light scattering by a spheroidal particle, *Applied optics* **1975**, *14* (1), 29–49.

[111] Rayleigh. On the dynamical theory of gratings, *Proceedings of the Royal Society of London. Series A* **1907**, *79* (532), 399–416.

[112] R. B. M. Schasfoort, A. J. Tudos, *Handbook of Surface Plasmon Resonance*, Royal Society of Chemistry, Cambridge **2008**.

[113] W. L. Barnes. Particle plasmons: Why shape matters, *American Journal of Physics* **2016**, *84* (8), 593–601.

[114] C. F. Bohren, D. R. Huffman, *Absorption and Scattering of Light by Small Particles*, Wiley, Hoboken **2008**.

[115]L. Novotny, B. Hecht, *Principles of nano-optics*, Cambridge University Press, Cambridge [etc.] **2006**.

[116]H. C. de van Hulst, *Light scattering by small particles*, LSC Communications; Dover Publications, Inc, [New York], New York **2018**.

[117]J.-S. Huang, J. Kern, P. Geisler, P. Weinmann, M. Kamp, A. Forchel, P. Biagioni, B. Hecht. Mode imaging and selection in strongly coupled nanoantennas, *Nano letters* **2010**, *10* (6), 2105–2110.

[118]E. Petryayeva, U. J. Krull. Localized surface plasmon resonance: nanostructures, bioassays and biosensing--a review, *Analytica Chimica Acta* **2011**, *706* (1), 8–24.

[119]L. Grabenhorst, K. Trofymchuk, F. Steiner, V. Glembockyte, P. Tinnefeld. Fluorophore photostability and saturation in the hotspot of DNA origami nanoantennas, *Methods and applications in fluorescence* **2020**, *8* (2), 24003.

[120]G. W. Ford, W. H. Weber. Electromagnetic interactions of molecules with metal surfaces, *Physics Reports* **1984**, *113* (4), 195–287.

[121]S. Kühn, U. Håkanson, L. Rogobete, V. Sandoghdar. Enhancement of single-molecule fluorescence using a gold nanoparticle as an optical nanoantenna, *Physical review letters* **2006**, *97* (1), 17402.

[122]P. Bharadwaj, L. Novotny. Spectral dependence of single molecule fluorescence enhancement, *Optics express* **2007**, *15* (21), 14266–14274.

[123]J. R. Lakowicz, Y. Shen, S. D'Auria, J. Malicka, J. Fang, Z. Gryczynski, I. Gryczynski. Radiative decay engineering. 2. Effects of Silver Island films on fluorescence intensity, lifetimes, and resonance energy transfer, *Analytical biochemistry* **2002**, *301* (2), 261–277.

[124]C. Vandenbem, D. Brayer, L. S. Froufe-Pérez, R. Carminati. Controlling the quantum yield of a dipole emitter with coupled plasmonic modes, *Phys. Rev. B* **2010**, *81* (8).

[125]A. G. Curto, G. Volpe, T. H. Taminiau, M. P. Kreuzer, R. Quidant, N. F. van Hulst. Unidirectional emission of a quantum dot coupled to a nanoantenna, *Science (New York, N.Y.)* **2010**, *329* (5994), 930–933.

[126]R. E. Dickerson, H. R. Drew, B. N. Conner, R. M. Wing, A. V. Fratini, M. L. Kopka. The Anatomy of A-, B-, and Z-DNA, *Science* **1982**, *216*, 475–485.

[127]J. D. WATSON, F. H. CRICK. Molecular structure of nucleic acids; a structure for deoxyribose nucleic acid, *Nature* **1953**, *171* (4356), 737–738.

[128]S. M. Douglas, A. H. Marblestone, S. Teerapittayanon, A. Vazquez, G. M. Church, W. M. Shih. Rapid prototyping of 3D DNA-origami shapes with caDNAno, *Nucleic acids research* **2009**, *37* (15), 5001–5006.

[129]K. F. Wagenbauer, F. A. S. Engelhardt, E. Stahl, V. K. Hechtl, P. Stömmer, F. Seebacher, L. Meregalli, P. Ketterer, T. Gerling, H. Dietz. How We Make DNA Origami, *Chembiochem a European journal of chemical biology* **2017**, *18* (19), 1873–1885.

[130]M. D. Egger, M. Petrăn. New reflected-light microscope for viewing unstained brain and ganglion cells, *Science (New York, N.Y.)* **1967**, *157* (3786), 305–307.

[131]A. Edelstein, N. Amodaj, K. Hoover, R. Vale, N. Stuurman. Computer control of microscopes using μManager, *Current Protocols in Molecular Biology* **2010**, *Chapter 14* (1), Unit14.20.

[132]E. J. AMBROSE. A surface contact microscope for the study of cell movements, *Nature* **1956**, *178* (4543), 1194.

[133]D. Axelrod. Cell-substrate contacts illuminated by total internal reflection fluorescence, *The Journal of cell biology* **1981**, *89* (1), 141–145.

[134]J. Jasny, J. Sepiol. Single Molecules Observed by Immersion Mirror Objective. A Novel Method of Finding the Orientation of Radiating Dipole, *Chemical Physics Letters* **1997**, *273*, 439–443.

[135]J. Sepiol, J. Jasny, J. Keller, U. P. Wild. Single Molecules Observed by Immersion Mirror Objective. The Orientation of Terrylene Molecules via the Direction of its Transition Dipole Moment, *Chemical Physics Letters* **1997**, *273*, 444–448.

[136]N. Karedla, S. C. Stein, D. Hähnel, I. Gregor, A. Chizhik, J. Enderlein. Simultaneous Measurement of the Three-Dimensional Orientation of Excitation and Emission Dipoles, *Physical review letters* **2015**, *115* (17), 173002.

[137]H. Uji-i, S. M. Melnikov, A. Deres, G. Bergamini, F. de Schryver, A. Herrmann, K. Müllen, J. Enderlein, J. Hofkens. Visualizing spatial and temporal heterogeneity of single molecule rotational diffusion in a glassy polymer by defocused wide-field imaging, *Polymer* **2006**, *47* (7), 2511–2518.

[138]D. Patra, I. Gregor, J. Enderlein. Image Analysis of Defocused Single-Molecule Images for Three-Dimensional Molecule Orientation Studies, *J. Phys. Chem. A* **2004**, *108* (33), 6836–6841.

[139]M. Böhmer, J. Enderlein. Orientation imaging of single molecules by wide-field epifluorescence microscopy, *J. Opt. Soc. Am. B* **2003**, *20* (3), 554.

[140]T. Li, Q. Li, Y. Xu, X.-J. Chen, Q.-F. Dai, H. Liu, S. Lan, S. Tie, L.-J. Wu. Three-dimensional orientation sensors by defocused imaging of gold nanorods through an ordinary wide-field microscope, *ACS nano* **2012**, *6* (2), 1268–1277.

[141]H. Uji-i, A. Deres, B. Muls, S. Melnikov, J. Enderlein, J. Hofkens, in *Fluorescence of supermolecules, polymers, and nanosystems*, Vol. 4 (Ed.: M. N. Berberan-Santos), Springer Berlin Heidelberg **2008**, p. 257.

[142]E. Abbe. Beiträge zur Theorie des Mikroskops und der mikroskopischen Wahrnehmung, *Archiv f. mikrosk. Anatomie* **1873**, *9* (1), 413–468.

[143]F. Balzarotti, Y. Eilers, K. C. Gwosch, A. H. Gynnå, V. Westphal, F. D. Stefani, J. Elf, S. W. Hell. Nanometer resolution imaging and tracking of fluorescent molecules with minimal photon fluxes, *Science* **2017**, *355* (6325), 606–612.

[144]L. A. Masullo, F. Steiner, J. Zähringer, L. F. Lopez, J. Bohlen, L. Richter, F. Cole, P. Tinnefeld, F. D. Stefani. Pulsed Interleaved MINFLUX, *Nano Lett.* **2021**, *21* (1), 840–846.

[145]M. J. Rust, M. Bates, X. Zhuang. Sub-diffraction-limit imaging by stochastic optical reconstruction microscopy (STORM), *Nature methods* **2006**, *3* (10), 793–795.

[146]E. Betzig, G. H. Patterson, R. Sougrat, O. W. Lindwasser, S. Olenych, J. S. Bonifacino, M. W. Davidson, J. Lippincott-Schwartz, H. F. Hess. Imaging intracellular fluorescent proteins at nanometer resolution, *Science* **2006**, *313* (5793), 1642–1645.

[147]S. T. Hess, T. P. K. Girirajan, M. D. Mason. Ultra-high resolution imaging by fluorescence photoactivation localization microscopy, *Biophysical journal* **2006**, *91* (11), 4258–4272.

[148]R. Jungmann, C. Steinhauer, M. Scheible, A. Kuzyk, P. Tinnefeld, F. C. Simmel. Single-molecule kinetics and super-resolution microscopy by fluorescence imaging of transient binding on DNA origami, *Nano letters* **2010**, *10* (11), 4756–4761.

[149]M. Raab, J. J. Schmied, I. Jusuk, C. Forthmann, P. Tinnefeld. Fluorescence microscopy with 6 nm resolution on DNA origami, *Chemphyschem a European journal of chemical physics and physical chemistry* **2014**, *15* (12), 2431–2435.

[150]M. Dai, R. Jungmann, P. Yin. Optical imaging of individual biomolecules in densely packed clusters, *Nature nanotechnology* **2016**, *11* (9), 798–807.

[151]A. T. M. Yeşilyurt, J.-S. Huang, *Adv. Optical Mater.* **2021**.

[152]F. Nicoli, T. Zhang, K. Hübner, B. Jin, F. Selbach, G. Acuna, C. Argyropoulos, T. Liedl, M. Pilo-Pais. DNA-Mediated Self-Assembly of Plasmonic Antennas with a Single Quantum Dot in the Hot Spot, *Small (Weinheim an der Bergstrasse, Germany)* **2019**, *15* (26), e1804418.

[153]T. H. Taminiau, F. D. Stefani, F. B. Segerink, N. F. van Hulst. Optical antennas direct single-molecule emission, *Nature Photon* **2008**, *2* (4), 234–237.

[154]L. M. Kneer, E.-M. Roller, L. V. Besteiro, R. Schreiber, A. O. Govorov, T. Liedl. Circular Dichroism of Chiral Molecules in DNA-Assembled Plasmonic Hotspots, *ACS nano* **2018**, *12* (9), 9110–9115.

[155]L. Nguyen, M. Dass, M. F. Ober, L. V. Besteiro, Z. M. Wang, B. Nickel, A. O. Govorov, T. Liedl, A. Heuer-Jungemann. Chiral Assembly of Gold-Silver Core-Shell Plasmonic Nanorods on DNA Origami with Strong Optical Activity, *ACS nano* **2020**, *14* (6), 7454–7461.

[156]K. Hübner, H. Joshi, A. Aksimentiev, F. D. Stefani, P. Tinnefeld, G. P. Acuna. Determining the In-Plane Orientation and Binding Mode of Single Fluorescent Dyes in DNA Origami Structures, *ACS nano* **2021**, *15* (3), 5109–5117.

[157]A. E. Marras, Z. Shi, M. G. Lindell, R. A. Patton, C.-M. Huang, L. Zhou, H.-J. Su, G. Arya, C. E. Castro. Cation-Activated Avidity for Rapid Reconfiguration of DNA Nanodevices, *ACS nano* **2018**, *12* (9), 9484–9494.

[158]F. Kroener, L. Traxler, A. Heerwig, U. Rant, M. Mertig. Magnesium-Dependent Electrical Actuation and Stability of DNA Origami Rods, *ACS applied materials & interfaces* **2019**, *11* (2), 2295–2301.

[159]T. K. Chiu, R. E. Dickerson. 1 A crystal structures of B-DNA reveal sequence-specific binding and groove-specific bending of DNA by magnesium and calcium, *Journal of molecular biology* **2000**, *301* (4), 915–945.

[160]B. Luan, A. Aksimentiev. DNA attraction in monovalent and divalent electrolytes, *Journal of the American Chemical Society* **2008**, *130* (47), 15754–15755.

[161]J. A. L. Roodhuizen, P. J. T. M. Hendrikx, P. A. J. Hilbers, T. F. A. de Greef, A. J. Markvoort. Counterion-Dependent Mechanisms of DNA Origami Nanostructure Stabilization Revealed by Atomistic Molecular Simulation, *ACS nano* **2019**, *13* (9), 10798–10809.

[162]S. Bidault, M. Mivelle, N. Bonod. Dielectric nanoantennas to manipulate solid-state light emission, *Journal of Applied Physics* **2019**, *126* (9), 94104.

[163]P. Albella, T. Shibanuma, S. A. Maier. Switchable directional scattering of electromagnetic radiation with subwavelength asymmetric silicon dimers, *Scientific reports* **2015**, *5*, 18322.

[164]A. Devilez, B. Stout, N. Bonod. Compact metallo-dielectric optical antenna for ultra directional and enhanced radiative emission, *ACS nano* **2010**, *4* (6), 3390–3396.

[165]H. Shen, R. Y. Chou, Y. Y. Hui, Y. He, Y. Cheng, H.-C. Chang, L. Tong, Q. Gong, G. Lu. Directional fluorescence emission from a compact plasmonic-diamond hybrid nanostructure, *Laser & Photonics Reviews* **2016**, *10* (4), 647–655.

[166]R. E. Noskov, A. E. Krasnok, Y. S. Kivshar. Nonlinear metal–dielectric nanoantennas for light switching and routing, *New J. Phys.* **2012**, *14* (9), 93005.

[167]S. Sheikholeslami, Y. Jun, P. K. Jain, A. P. Alivisatos. Coupling of optical resonances in a compositionally asymmetric plasmonic nanoparticle dimer, *Nano letters* **2010**, *10* (7), 2655–2660.

[168]T. Shegai, S. Chen, V. D. Miljković, G. Zengin, P. Johansson, M. Käll. A bimetallic nanoantenna for directional colour routing, *Nature communications* **2011**, *2*, 481.

[169]T. Shegai, P. Johansson, C. Langhammer, M. Käll. Directional scattering and hydrogen sensing by bimetallic Pd-Au nanoantennas, *Nano letters* **2012**, *12* (5), 2464–2469.

[170]K. Yao, Y. Liu. Controlling Electric and Magnetic Resonances for Ultracompact Nanoantennas with Tunable Directionality, *ACS Photonics* **2016**, *3* (6), 953–963.

[171]T. Coenen, E. J. R. Vesseur, A. Polman, A. F. Koenderink. Directional emission from plasmonic Yagi-Uda antennas probed by angle-resolved cathodoluminescence spectroscopy, *Nano letters* **2011**, *11* (9), 3779–3784.

[172]T. Pakizeh, M. Käll. Unidirectional ultracompact optical nanoantennas, *Nano letters* **2009**, *9* (6), 2343–2349.

[173]J. Vogelsang, C. Steinhauer, C. Forthmann, I. H. Stein, B. Person-Skegro, T. Cordes, P. Tinnefeld. Make them blink: probes for super-resolution microscopy, *Chemphyschem a European journal of chemical physics and physical chemistry* **2010**, *11* (12), 2475–2490.

[174]G. T. Dempsey, J. C. Vaughan, K. H. Chen, M. Bates, X. Zhuang. Evaluation of fluorophores for optimal performance in localization-based super-resolution imaging, *Nature methods* **2011**, *8* (12), 1027–1036.

[175]S. J. J. Kwok, M. Choi, B. Bhayana, X. Zhang, C. Ran, S.-H. Yun. Two-photon excited photoconversion of cyanine-based dyes, *Scientific reports* **2016**, *6*, 23866.

[176]D. A. Helmerich, G. Beliu, S. S. Matikonda, M. J. Schnermann, M. Sauer. Photoblueing of organic dyes can cause artifacts in super-resolution microscopy, *Nature methods* **2021**, *18* (3), 253–257.

[177]D. Mathur, Y. C. Kim, S. A. Díaz, P. D. Cunningham, B. S. Rolczynski, M. G. Ancona, I. L. Medintz, J. S. Melinger. Can a DNA Origami Structure Constrain the Position and Orientation of an Attached Dye Molecule?, *J. Phys. Chem. C* **2021**, *125* (2), 1509–1522.

[178]I. H. Stein, C. Steinhauer, P. Tinnefeld. Single-molecule four-color FRET visualizes energy-transfer paths on DNA origami, *Journal of the American Chemical Society* **2011**, *133* (12), 4193–4195.

[179]R. W. Wagner, J. S. Lindsey. A molecular photonic wire, *J. Am. Chem. Soc.* **1994**, *116* (21), 9759–9760.

[180]G. Sánchez-Mosteiro, E. M. H. P. van Dijk, J. Hernando, M. Heilemann, P. Tinnefeld, M. Sauer, F. Koberlin, M. Patting, M. Wahl, R. Erdmann, N. F. van Hulst, M. F. García-Parajó. DNA-based molecular wires: multiple emission pathways of individual constructs, *J. Phys. Chem. B* **2006**, *110* (51), 26349–26353.

[181]J. K. Hannestad, P. Sandin, B. Albinsson. Self-assembled DNA photonic wire for long-range energy transfer, *J. Am. Chem. Soc.* **2008**, *130* (47), 15889–15895.

[182]P. Tinnefeld, M. Heilemann, M. Sauer. Design of molecular photonic wires based on multistep electronic excitation transfer, *Chemphyschem a European journal of chemical physics and physical chemistry* **2005**, *6* (2), 217–222.

[183]J. H. Yoon, F. Selbach, L. Langolf, S. Schlücker. Precision Plasmonics: Ideal Dimers of Gold Nanospheres for Precision Plasmonics: Synthesis and Characterization at the Single-Particle Level for Identification of Higher Order Modes (Small 4/2018), *Small* **2018**, *14* (4), 1870018.

[184]K. Hübner, M. Raab, J. Bohlen, J. Bauer, P. Tinnefeld, Salt-Induced Conformational Switching of a Flat Rectangular DNA Origami Structure, *Nanoscale* **2022**, *14*, 7898-7905.

8. List of Figures

9. Full List of Publications of the Dissertation

Publications

K. Hübner, M. Pilo-Pais, F. Selbach, T. Liedl, P. Tinnefeld, F. D. Stefani, G. P. Acuna, Directing Single-Molecule Emission with DNA Origami-Assembled Optical Antennas, *Nano Letters*, **2019**, *19* (9), 6629-6634.

K. Hübner, H. Joshi, A. Aksimentiev, F. D. Stefani, P. Tinnefeld, G. P. Acuna, Determinig the In-Plane Orientation and Binding Mode of Single Fluorescent Dyes in DNA Origami Structures, *ACS Nano*, **2021**, *15* (3),5109-5117.

K. Hübner, M. Raab, J. Bohlen, P. Tinnefeld, Salt-Induced Conformational Switching of a Flat Rectangular DNA Origami Structure, *Nanoscale*, **2022**, *14*, 7898-7905.

F. Nicoli, T. Zhang, **K. Hübner**, B. Jin, F. Selbach, G. Acuna, C. Argyropoulos, T. Liedl, M. Pilo-Pais, DNA-Mediated Self-Assembly of Plasmonic Antennas with a Single Quantum Dot in the Hot Spot, *Small*, **2019**, *15* (26), 1804418 (1-8).

Conference Contributions

K. Hübner, I. Bald, P. Tinnefeld, G. Acuna, Directed emission of fluorescent dyes coupled to optical antennas on DNA origami, Future Trends in DNA-based Nanotechnology, Dresden, 2017. (Poster)

K. Hübner, Y. Choi, I. Bald, M. Pilo-Pais, P. Tinnefeld, G. Acuna, Orientation Imaging of Fluorescent Dyes Coupled to Gold Nanoparticle Dimers, CeNS Retreat, Kleinwalsertal, 2018. (Poster)

K. Hübner, Y. Choi, I. Bald, M. Pilo-Pais, P. Tinnefeld, G. Acuna, Coupling of Fluorescent Dyes and Optical Antennas Visualized by Defocused Imaging, Gold 2018, Paris, 2018. (Poster)

K. Hübner, C. Vietz, I. Kaminska, S. Ochmann, Q. Wei, A. Ozcan, P. Tinnefeld, G. Acuna, DNA Origami Nanophotonics: Gold Optical Antennas for Fluorescence Enhancement and Diagnostics Applications, Gold 2018, Paris, 2018. (Talk)

K. Hübner, M. Pilo-Pais, F. Selbach, T. Liedl, P. Tinnefeld, F. Stefani, G. Acuna, Visualizing the Emission Directivity of Fluorescent Dyes Coupled to Optical Antennas by Defocused Wide-Field Imaging, 25th Aniversary Workshop on “Single Molecule Spectroscopy and Super-Resolution Microscopy in the Life Science, Berlin, 2019. (Poster)

K. Hübner, M. Pilo-Pais, F. Selbach, T. Liedl, P. Tinnefeld, F. Stefani, G. Acuna, Directed Emission of Fluorescent Dyes Coupled to Optical Antennas, CeNS/CRC235 Workshop “Evolving Nanoscience”, Venedig, 2019. (Poster)

10. Acknowledgements

At this point, I want to thank everyone who supported me during the last years and helped to make this work possible.

First I want to thank Prof. Dr. Philip Tinnefeld for giving me the opportunity to do my PhD thesis in his working group and supervising my projects. Furthermore, I want to thank him for numerous fruitful scientific discussions and the chance to work on many different interesting projects.

I would like to thank Prof. Dr. Guillermo Acuna for his support and supervision of my projects, fruitful scientific discussions and long skype meetings on data discussion.

I would especially like to to thank my collaboration partners Prof. Dr. Fernando Stefani, Dr. Mauricio Pilo-Pais and Dr. Himanshu Joshi. Thank you for all the scientific discussions we had, sample preparations and the performance of MD simulations.

Grateful thanks to Bettina Wünsch for introducing me to the lab, supervising my master thesis and our continued good collaboration in the lab.

A special thank you goes to Bettina, Tim, Florian St. and Mario who helped me with setup questions and the programming of analysis software.

I would like to thank Ija Jusuk for supporting me in the lab, but also for exploring Munich together on the weekends and a lot of fun besides the daily work.

I would also like to especially thank Kateryna for the funny and exhausting hours we spent together on building the confocal setup.

Dr. Moritz Ehrl deserves my gratitude for handling the bureaucracy behind the lab work and for keeping everything state of the art. Furthermore, I would like to thank the permanent staff Mrs. Talk and Mrs. Steger. Special thanks also goes to Angelika for keeping the labs running.

A special credit should also be given to my office mates, who always provided a nice working environment and made long days feeling short. These include the Braunschweig office girls (Kathi, Sarah and Bettina) and later the fellows from the Munich office (Sarah, Kateryna, Andres and Florian Se.).

Also, I would like to thank all people who moved together with me from Braunschweig to Munich (Sarah, Kateryna, Ija, Mario, Carsten, Tim, Johann, Andres, Florian Se., Lennart). Thank you for making the arrival easier, for funny Friday evening activities and tours through Munich.

I also want to thank all my former and current colleagues, who helped to provide a nice and productive working environment (Fiona, Martina, Jonas, Karina, Lars, Melanie, Michi, Tim, Patrick, Renukka, Julian, Ece, Cindy, Izabela and Viki).

Furthermore, I would like to thank Kateryna, Florian, Johann and Doro for proofreading.

The biggest thank you, of course, goes to my family, especially to my parents who made all this possible for me and always supported me in everything I wanted to do. Also my siblings Jens, Thorben and Hanna who constantly encouraged me to stick to my aims and had an open ear whenever necessary. Thank you also to the rest of my family who never gave up asking and trying to understand what I was working on. And at last, a warm and very big thank you goes to Johann, who always supports and motivates me.

11. Appendix

A1 Associated Publication P1

Directing Single-Molecule Emission with DNA Origami-Assembled Optical Antennas

by

Kristina Hübner, Mauricio Pilo-Pais, Florian Selbach, Tim Liedl, Philip Tinnefeld, Fernando D. Stefani, Guillermo Acuna

Reprinted with permission from *Nano Lett.* 2019, 19, 9, 6629–6634.

NANO LETTERS Letter
Cite This: Nano Lett. 2019, 19, 6629−6634 pubs.acs.org/NanoLett

Directing Single-Molecule Emission with DNA Origami-Assembled Optical Antennas

Kristina Hübner,[†] Mauricio Pilo-Pais,[‡,⊥] Florian Selbach,[†] Tim Liedl,[‡] Philip Tinnefeld,[*,†] Fernando D. Stefani,[*,§,∥] and Guillermo P. Acuna[*,⊥]

[†]Department of Chemistry and Center for NanoScience, Ludwig-Maximilians-Universität München, Butenandtstr. 5-13 Haus E, 81377 München, Germany

[‡]Faculty of Physics and Center for NanoScience, Ludwig-Maximilians-Universität München, Geschwister-Scholl-Platz 1, 80539 München, Germany

[§]Centro de Investigaciones en Bionanociencias (CIBION), Consejo Nacional de Investigaciones Científicas y Técnicas (CONICET), Godoy Cruz 2390, C1425FQD, Ciudad Autónoma de Buenos Aires, Argentina

[∥]Departamento de Física, Facultad de Ciencias Exactas y Naturales, Universidad de Buenos Aires, Güiraldes 2620, C1428EHA, Ciudad Autónoma de Buenos Aires, Argentina

[⊥]Department of Physics, University of Fribourg, Chemin du Musée 3, Fribourg CH-1700, Switzerland

Supporting Information

ABSTRACT: We demonstrate the capability of DNA self-assembled optical antennas to direct the emission of an individual fluorophore, which is free to rotate. DNA origami is used to fabricate optical antennas composed of two colloidal gold nanoparticles separated by a predefined gap and to place a single Cy5 fluorophore near the gap center. Although the fluorophore is able to rotate, its excitation and far-field emission is mediated by the antenna, with the emission directionality following a dipolar pattern according to the antenna main resonant mode. This work is intended to set out the basis for manipulating the emission pattern of single molecules with self-assembled optical antennas based on colloidal nanoparticles.

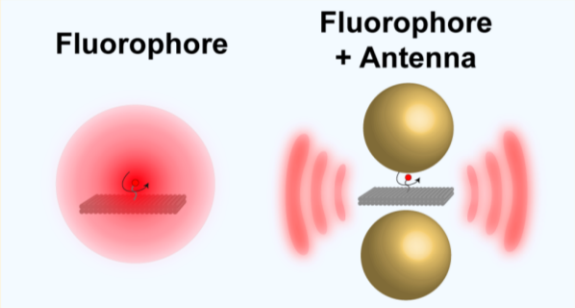

KEYWORDS: *plasmonics, nanophotonics, metallic nanoparticles, DNA origami, optical antennas*

Optical antennas (OAs)[1] represent the counterparts of radio- and microwave antennas within the visible spectrum. Essentially, OAs are built from metallic nanoparticles (NPs) whose localized surface plasmon resonances enable the control of light fields at the nanoscale.[2] OAs can be engineered to manipulate the photophysical behavior of single photon emitters such as organic fluorophores or quantum dots placed in their vicinity.[3] Pioneering examples are the "bow tie" OAs used to demonstrate enhancement of the fluorescence intensity of organic dyes placed at the hotspot between the gold elements[4] and the monopole, and "Yagi-Uda" OAs used to demonstrate directionality in the emission of single emitters.[5−7] These examples share the fabrication approach based on electron beam lithography. Generally, top-down nanofabrication techniques such as e-beam lithography or ion beam milling offer great geometrical design versatility, but they also exhibit shortcomings. They are serial, which limits their throughput. The 3D fabrication and organization of (antenna) elements is difficult and limited to some degree of rotation of the sample with respect to the beam. There exist limitations to the quality and number of materials that can be used and combined. As a result, attaining OAs made of monocrystalline elements, as well as combining different materials, is challenging. Finally, it is virtually impossible to position single photon emitters with controlled stoichiometry in the near-field of the OAs with nanometer precision.[1]

The advent of the DNA origami technique[8] opened up new pathways for nanophotonics[9−16] as colloidal metallic NPs could be self-assembled in a parallel manner to form OAs. Furthermore, single photon emitters could be positioned in the near-field of OAs with nanometer precision and stoichiometric control. Following this approach, the performance of OAs could be revisited at the single-molecule level with higher geometrical control and more robust statistics,[17−20] including their influence on the photophysical behavior of single photon emitters, such as the electronic transition rates,[21] photostability,[22] fluorescence resonance energy transfer (FRET),[23−25] surface-enhanced Raman scattering,[26−28] strong coupling,[29] and super-resolution localization.[30]

Received: July 15, 2019
Revised: August 20, 2019
Published: August 26, 2019

DOI: 10.1021/acs.nanolett.9b02886
Nano Lett. 2019, 19, 6629−6634

DNA origami has turned out to be extremely efficient to organize NPs on nanometric geometries with high degree of positional and orientational control.[31,32] The situation is different for single photon emitters. Whereas their position can be controlled well, orienting them over predefined directions in DNA origami remains an open challenge.[33−36] In order to incorporate single fluorophores to DNA origami structures, they are attached to the backbone or a base of a short single-stranded DNA, hereafter termed "staple", which later binds to its complementary sequence on the DNA scaffold strand. One fluorophore can be bound to one or two staples through single or double linkers, respectively.[37] Fluorophores integrated into DNA origami structures can exhibit a variety of behaviors, from free to rotate over fixed in an undefined orientation to confined in orientation, depending on their coupling chemistry, molecular structure, charge, and immediate surrounding environment.[23]

In this contribution, we investigate the emission directivity of rotating single fluorophores coupled to OAs. Cy5 fluorophores incorporated to DNA origami structures as shown in Figure 1A, which are able to rotate, do not present any directionality in excitation or emission. In contrast, in the presence of a dipolar OA, both their excitation and emission are enhanced and become directional according to the antenna mode.

A schematic of the OA-Cy5 fluorophore system is shown Figure 1A. A two-layered, rectangular DNA origami sheet with a size of ∼50 nm × 60 nm × 5 nm is used to accommodate two ultrasmooth spherical Au NPs[38] with a diameter of 60 nm, each one at opposite sides of the origami. At approximately the center of the DNA origami structure, a single Cy5 fluorophore is incorporated at the 3′ end of a DNA single strand (see inset in Figure 1A). In this way, the single Cy5 molecule is located near the center of the 13 nm gap between the two Au NPs and is able to rotate when in solution. Figure 1B shows exemplary TEM images of the dimer OAs illustrating the quality of our structures. The absorption and emission spectra of the Cy5 fluorophore employed together with a numerical simulation of the absorption and scattering cross section of the OA are included in Figure 1C. The OAs were self-assembled in solution. For fluorescence measurements, OAs were immobilized on a glass coverslip previously functionalized with BSA-biotin, neutravidin, and biotinylated single-stranded DNA complementary to the single-stranded DNA on the Au NP surface. As a result, OAs are expected to lie flat with their interparticle (main) axis parallel to the substrate surface. All optical measurements were performed in buffer (see Supporting Information for sample preparation and measurements details).

Functionalized NPs are mixed in high excess to the DNA origami structure to maximize the yield of dimer OAs. Gel electrophoresis permits to separate the desired structure from unbound NPs and any other unintentionally formed species resulting in a solution containing close to 100% of the target dimer structure. Figure 1D shows the distinct fluorescence lifetimes of the reference, monomer, and dimer samples obtained from single-molecule traces (details on the time-resolved single-molecule fluorescence measurements are given in the SI). As expected, the interaction between the fluorophores and the Au NPs reduces the fluorescence lifetime, with a more pronounced effect for dimer structures.[17] The excited state lifetime of the Cy5 in the origami sheet is reduced from 1.7 to 0.6 ns when one Au NP is attached, and to 0.2 ns

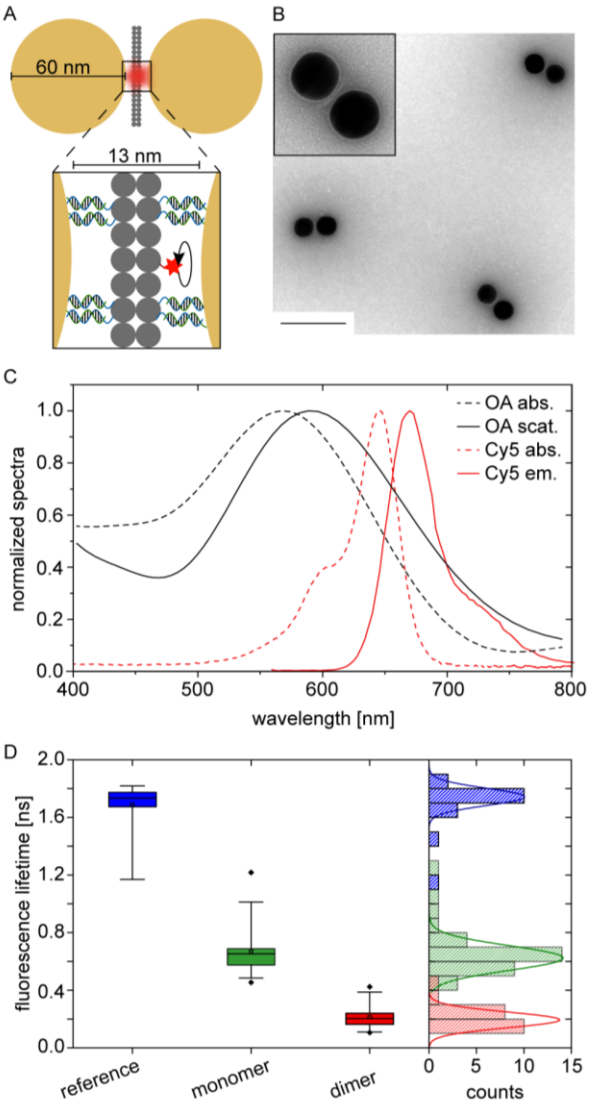

Figure 1. (A) Sketch of the OA-Cy5 structure composed of two gold NPs self-assembled onto a rectangular DNA origami. The inset depicts a close-up of the NP gap where the single Cy5 fluorophore is incorporated. (B) TEM images of the dimer structures (scale bar is 200 nm). (C) Absorption and emission spectra of Cy5 together with the absorption and scattering cross section of the OA dimer. (D) Fluorescence lifetime histogram of samples containing two NPs (dimers), one NP (monomers), and the reference structure without NPs.

(limited by the instrumental response) when the dimer OA is formed. The relatively sharp lifetime distributions and TEM images reflect the quality of the preparation and the purity of the samples used in this study.

Two different single-molecule fluorescence measurements were performed on each of the individual OAs in order to determine the directionality imposed by the OA on the excitation and on the emission of the single fluorophores. The directionality of the emission was determined by wide-field defocused imaging.[39] The directionality of the excitation was probed by monitoring the fluorescence intensity while rotating

DOI: 10.1021/acs.nanolett.9b02886
Nano Lett. 2019, 19, 6629−6634

the direction of polarization of a linearly polarized laser used for excitation.

The fluorescence emission of molecules close to a planar interface has been extensively studied.[39,40] The angular emission pattern depends strongly on the orientation of the molecular emission dipole with respect to the interface. In Figures2A–C, we include simulations for the emission patterns

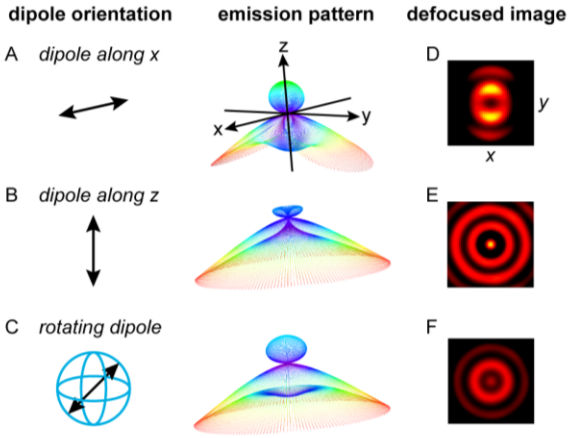

Figure 2. Simulated emission patterns and defocused images of an emitter located 40 nm above a water (n_w = 1.33, $z > 0$)–glass (n_g = 1.5, $z < 0$) interface (on the water side). The emission wavelength is 670 nm. Defocused images are calculated for the situation where the objective–sample distance has been reduced by 1 μm from the focal plane. (A) Dipolar emitter oriented parallel to the water–glass interface along the x axis. (B) Dipolar emitter oriented perpendicular to the water–glass interface. (C) Isotropic emitter, corresponding to the case of the dipolar emitter that rotates faster than the measurement time.

of a parallel, perpendicular and free to rotate Cy5 molecule placed 40 nm above the water–glass interface (on the water half-space). In all cases molecules emit preferentially into the glass half-space and at angles close to the critical angle of total internal reflection, but with distinct angular emission patterns. While the emission pattern of perpendicular molecules has rotational symmetry with respect to the surface normal, the pattern of a parallel molecule has two lobes separated by a gap along the dipole direction. For a fluorophore free to rotate, the emission pattern corresponds to the isotropic average of dipolar patterns with all possible orientations and has thus radial symmetry. Defocused imaging is a way to access experimentally the angular emission pattern of single molecules.[39,41] Figures 2D–F include the calculated defocused images of molecules oriented parallel, perpendicular, and freely rotating when reducing the objective–sample distance by 1 μm from the focal plane.

Figure 3 shows typical defocused images (~1 μm) of both, Cy5 fluorophores conjugated to the center of the DNA origami platform with and without OAs. The rotational symmetry of Cy5 samples without OAs demonstrates that the Cy5 fluorophores are able to rotate on a time scale faster than the image acquisition time. Remarkably, the emission patterns of Cy5 molecules change qualitatively when they are coupled to the dimer OAs. In this case, the rotational symmetry is lost, and all detected emission patterns present the two lobes characteristic of an in-plane dipole. Each individual pattern of an OA-Cy5 structure has a different in-plane orientation. In the presence of a dipolar OA, a rotating fluorophore operating at frequencies below the OA's resonance[2,42] will couple to the resonant antenna mode when aligned parallel to the antenna's main axis.[22,43] Under this orientation, the emission is expected to be enhanced and directional with a dipolar pattern.[44] In contrast, for a perpendicular orientation, the fluorophore's radiative rate can be significantly suppressed leading to a negligible emission into the far-field.[45–47] This behavior becomes intuitive when picturing the interactions between the Cy5 and its image charges produced on the NPs[48] (Figure 3C). A perpendicularly oriented dipole is canceled out by its image dipole (Figure 3C-I), whereas a parallel oriented dipole is reinforced (Figure 3C-II). Therefore, despite the fact that the single Cy5 fluorophore is able to rotate, the presence of the OA will enhance and mediate the fluorophore's emission when its orientation is parallel to the main OA axis and suppress it when perpendicular. This is confirmed by numerical simulations of the fluorophore's quantum yield for the two orientations depicted in Figure 3C (see Figure S3). For each defocused pattern in Figure 3B, we extract θ_{em} defined as the main in-plane emission angle.

Next, we studied the excitation directionality with the polarization-resolved excitation measurements. For each single structure, as the ones shown on Figure 3, fluorescent transients were extracted while rotating the incident light polarization. Exemplary transients are included in Figure 4A, where fluorescence enhancement (FE) refers to the fluorescence intensity normalized to the average fluorescence intensity of the reference structures (without NPs). The incident light

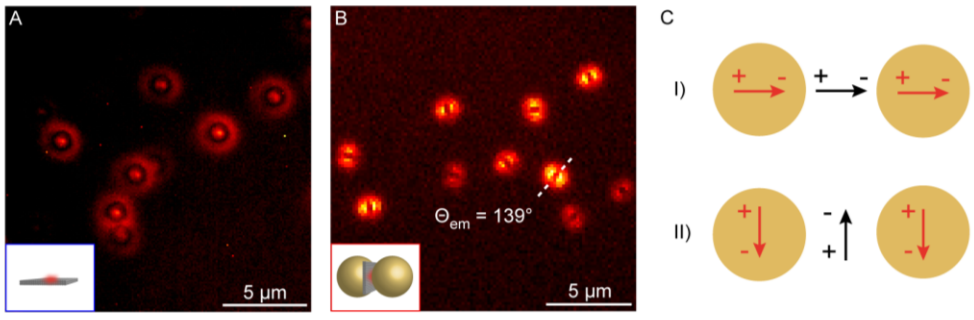

Figure 3. Defocused images of (A) the Cy5 reference sample and (B) the OA-Cy5 structures. The in-plane emission angle θ_{em} is highlighted for a single OA. (C) Sketch of the image charges induced by a fluorophore on the OA elements. The black arrows represent the fluorophore's emission dipole moment, whereas the red arrows represent the induced dipoles in the NPs.

DOI: 10.1021/acs.nanolett.9b02886
Nano Lett. 2019, 19, 6629–6634

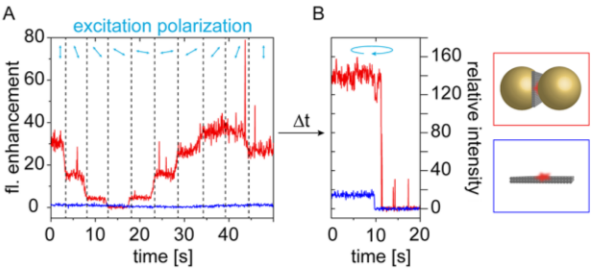

Figure 4. (A) Transients of fluorescence intensity for varying polarization angle of the excitation for the reference (no NP, blue) and OAs (NP dimer, red). The OA intensity is normalized to the average of the reference intensity and thus represents the fluorescence enhancement (FE). During the first 50 s, the incident polarization is rotated. (B) Afterwards, the incident light power is increased and its polarization is turned circular in order to bleach the fluorophores to verify a single-step photobleaching.

polarization angle is rotated by 20°, sweeping a range of 180°. Finally, the fluorophores are photobleached using increased laser power and circularly polarized light to prove single-step bleaching behavior (Figure 4B). For the reference structures, fluorescence transients show negligible variations with the incident polarization angle. This is in line with our previous observation that Cy5 is able to rotate faster than the integration time. In contrast, the transients of OA-Cy5 structures show a clear periodic dependence with the incident polarization angle. As expected for a dipolar dimer OA, the electric field enhancement reaches the highest value when the incident light is polarized along the antenna axis.[49]

From these measurements, we extracted the polarization angle of maximum excitation θ_{ex}, which corresponds to the in-plane orientation of each OA. We note that for our analysis we considered only OAs that showed a clear cosine square response to the polarization angle and a single-step photobleaching, assuring that we probed dipolar OAs with a single fluorophore.

Finally, we combined the results of the independent measurements displayed in Figures 3B and 4A in order to study the emission and excitation directionality of each OA. Figure 5 displays a scatter plot of θ_{em} versus θ_{ex} for 147 randomly oriented dimer OAs with a single Cy5 fluorophore.

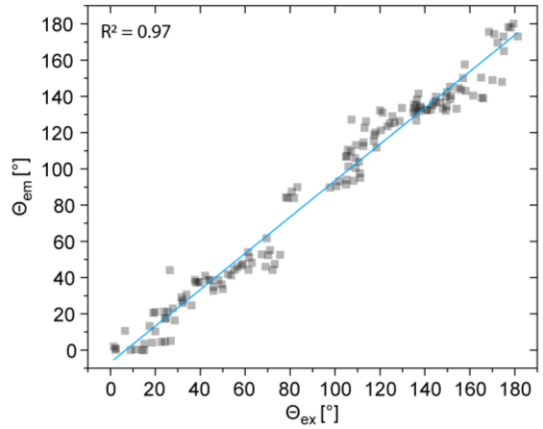

Figure 5. Scatter plot of the in-plane angles of emission θ_{em} and excitation θ_{ex} for 147 individual OAs.

The strong correlation between both angles θ_{em} and θ_{ex} confirms that the OAs impose directionality to the rotating fluorophores both on excitation and emission according to the antenna's main resonant mode.

In summary, using the DNA origami technique we self-assembled dipolar optical antennas made of two closely spaced gold nanoparticles with a single fluorescent molecule at their gap. By means of single-molecule measurements of the emission pattern and the polarization of maximum excitation, we showed that the excitation and emission of single fluorophores that are able to rotate can be made directional with optical antennas, according to the antenna's main resonant mode. These experiments provide a solid ground for more sophisticated photon routing experiments using single emitters and self-assembled optical antennas.[50,51]

■ ASSOCIATED CONTENT

Supporting Information

The Supporting Information is available free of charge on the ACS Publications website at DOI: 10.1021/acs.nanolett.9b02886.

Detailed information on gold nanoparticle fabrication, DNA origami folding, optical antenna assembly and immobilization, imaging systems, analysis, and numerical simulations (PDF)

■ AUTHOR INFORMATION

Corresponding Authors

*E-mail: philip.tinnefeld@cup.uni-muenchen.de (P.T.).
*E-mail: fernando.stefani@df.uba.ar (F.D.S.).
*E-mail: guillermo.acuna@unifr.ch (G.P.A.).

ORCID

Tim Liedl: 0000-0002-0040-0173
Philip Tinnefeld: 0000-0003-4290-7770
Fernando D. Stefani: 0000-0002-3277-7215
Guillermo P. Acuna: 0000-0001-8066-2677

Notes

The authors declare no competing financial interest.

■ ACKNOWLEDGMENTS

We would like to thank Mario Raab, Ija Jusuk, Florian Steiner, Jan Vogelsang, and Johann Bohlen for fruitful discussion. This work was supported by the Swiss National Science Foundation through the National Center of Competence in Research Bio-Inspired Materials, with grants PICT2013-0792 and PICT-2014-0739 of the Agencia Nacional de Promoción Científica y Tecnológica (ANPCYT, Argentina). P.T. and G.P.A. acknowledge support by the DFG (AC 279/2-1 and TI 329/9-1, INST 86/1904-1 FUGG, excellence cluster e-conversion). M.P. and T.L. thank the financial support from the European Research Council (ERC) through the starting grant 336440 (ORCA) and the DFG through the excellence cluster e-conversion. F.D.S. thanks the support of the Max-Planck-Society and the Alexander von Humboldt Foundation.

■ REFERENCES

(1) Novotny, L.; Van Hulst, N. Antennas for Light. *Nat. Photonics* **2011**, *5* (2), 83−90.
(2) Biagioni, P.; Huang, J.-S.; Hecht, B. Nanoantennas for Visible and Infrared Radiation. *Rep. Prog. Phys.* **2012**, *75* (2), 024402.
(3) Koenderink, A. F. Single-Photon Nanoantennas. *ACS Photonics* **2017**, *4*, 710−722.

DOI: 10.1021/acs.nanolett.9b02886
Nano Lett. 2019, 19, 6629−6634

(4) Kinkhabwala, A.; Yu, Z.; Fan, S.; Avlasevich, Y.; Müllen, K.; Moerner, W. E. Large Single-Molecule Fluorescence Enhancements Produced by a Bowtie Nanoantenna. *Nat. Photonics* **2009**, *3* (11), 654−657.
(5) Taminiau, T. H.; Stefani, F. D.; Segerink, F. B.; Van Hulst, N. F. Optical Antennas Direct Single-Molecule Emission. *Nat. Photonics* **2008**, *2* (4), 234−237.
(6) Curto, A. G.; Volpe, G.; Taminiau, T. H.; Kreuzer, M. P.; Quidant, R.; Van Hulst, N. F. Unidirectional Emission of a Quantum Dot Coupled to a Nanoantenna. *Science (Washington, DC, U. S.)* **2010**, *329* (5994), 930−933.
(7) Aouani, H.; Mahboub, O.; Devaux, E.; Rigneault, H.; Ebbesen, T. W.; Wenger, J. Large Molecular Fluorescence Enhancement by a Nanoaperture with Plasmonic Corrugations. *Opt. Express* **2011**, *19* (14), 13056.
(8) Rothemund, P. W. K. Folding DNA to Create Nanoscale Shapes and Patterns. *Nature* **2006**, *440*, 297−302.
(9) Kuzyk, A.; Jungmann, R.; Acuna, G. P.; Liu, N. DNA Origami Route for Nanophotonics. *ACS Photonics* **2018**, *5* (4), 1151−1163.
(10) Pilo-Pais, M.; Acuna, G. P.; Tinnefeld, P.; Liedl, T. Sculpting Light by Arranging Optical Components with DNA Nanostructures. *MRS Bull.* **2017**, *42* (12), 936−942.
(11) Liu, N.; Liedl, T. DNA-Assembled Advanced Plasmonic Architectures. *Chem. Rev.* **2018**, *118* (6), 3032−3053.
(12) Samanta, A.; Banerjee, S.; Liu, Y. DNA Nanotechnology for Nanophotonic Applications. *Nanoscale* **2015**, *7* (6), 2210−2220.
(13) Lan, X.; Wang, Q. DNA-Programmed Self-Assembly of Photonic Nanoarchitectures. *NPG Asia Mater.* **2014**, *6* (4), e97−e97.
(14) Wang, P.; Meyer, T. A.; Pan, V.; Dutta, P. K.; Ke, Y. The Beauty and Utility of DNA Origami. *Chem.* **2017**, *2* (3), 359−382.
(15) Madsen, M.; Gothelf, K. V. Chemistries for DNA Nanotechnology. *Chem. Rev.* **2019**. DOI: 10.1021/acs.chemrev.8b00570.
(16) Gopinath, A.; Miyazono, E.; Faraon, A.; Rothemund, P. W. K. Engineering and Mapping Nanocavity Emission via Precision Placement of DNA Origami. *Nature* **2016**, *535* (7612), 401−405.
(17) Acuna, G. P.; Möller, F. M.; Holzmeister, P.; Beater, S.; Lalkens, B.; Tinnefeld, P. Fluorescence Enhancement at Docking Sites of DNA-Directed Self-Assembled Nanoantennas. *Science (Washington, DC, U. S.)* **2012**, *338* (6106), 506−510.
(18) Prinz, J.; Heck, C.; Ellerik, L.; Merk, V.; Bald, I. DNA Origami Based Au−Ag-Core−Shell Nanoparticle Dimers with Single-Molecule SERS Sensitivity. *Nanoscale* **2016**, *8* (10), 5612−5620.
(19) Simoncelli, S.; Roller, E.-M.; Urban, P.; Schreiber, R.; Turberfield, A. J.; Liedl, T.; Lohmüller, T. Quantitative Single-Molecule Surface-Enhanced Raman Scattering by Optothermal Tuning of DNA Origami-Assembled Plasmonic Nanoantennas. *ACS Nano* **2016**, *10* (11), 9809−9815.
(20) Chikkaraddy, R.; Turek, V. A.; Kongsuwan, N.; Benz, F.; Carnegie, C.; van de Goor, T.; de Nijs, B.; Demetriadou, A.; Hess, O.; Keyser, U. F.; et al. Mapping Nanoscale Hotspots with Single-Molecule Emitters Assembled into Plasmonic Nanocavities Using DNA Origami. *Nano Lett.* **2018**, *18* (1), 405−411.
(21) Holzmeister, P.; Pibiri, E.; Schmied, J. J.; Sen, T.; Acuna, G. P.; Tinnefeld, P. Quantum Yield and Excitation Rate of Single Molecules Close to Metallic Nanostructures. *Nat. Commun.* **2014**, *5* (1), 5356.
(22) Kaminska, I.; Vietz, C.; Cuartero-González, Á.; Tinnefeld, P.; Fernández-Domínguez, A. I.; Acuna, G. P. Strong Plasmonic Enhancement of Single Molecule Photostability in Silver Dimer Optical Antennas. *Nanophotonics* **2018**, *7* (3), 643−649.
(23) Aissaoui, N.; Moth-Poulsen, K.; Käll, M.; Johansson, P.; Wilhelmsson, L. M.; Albinsson, B. FRET Enhancement Close to Gold Nanoparticles Positioned in DNA Origami Constructs. *Nanoscale* **2017**, *9* (2), 673−683.
(24) Vietz, C.; Lalkens, B.; Acuna, G. P.; Tinnefeld, P. Synergistic Combination of Unquenching and Plasmonic Fluorescence Enhancement in Fluorogenic Nucleic Acid Hybridization Probes. *Nano Lett.* **2017**, *17* (10), 6496−6500.
(25) Bohlen, J.; Cuartero-González, Á.; Pibiri, E.; Ruhlandt, D.; Fernández-Domínguez, A. I.; Tinnefeld, P.; Acuna, G. P. Plasmon-Assisted Förster Resonance Energy Transfer at the Single-Molecule Level in the Moderate Quenching Regime. *Nanoscale* **2019**, *11* (16), 7674−7681.
(26) Thacker, V. V.; Herrmann, L. O.; Sigle, D. O.; Zhang, T.; Liedl, T.; Baumberg, J. J.; Keyser, U. F. DNA Origami Based Assembly of Gold Nanoparticle Dimers for Surface-Enhanced Raman Scattering. *Nat. Commun.* **2014**, *5* (1), 3448.
(27) Prinz, J.; Schreiber, B.; Olejko, L.; Oertel, J.; Rackwitz, J.; Keller, A.; Bald, I. DNA Origami Substrates for Highly Sensitive Surface-Enhanced Raman Scattering. *J. Phys. Chem. Lett.* **2013**, *4* (23), 4140−4145.
(28) Kühler, P.; Roller, E. M.; Schreiber, R.; Liedl, T.; Lohmüller, T.; Feldmann, J. Plasmonic DNA-Origami Nanoantennas for Surface-Enhanced Raman Spectroscopy. *Nano Lett.* **2014**, *14* (5), 2914−2919.
(29) Ojambati, O. S.; Chikkaraddy, R.; Deacon, W. D.; Horton, M.; Kos, D.; Turek, V. A.; Keyser, U. F.; Baumberg, J. J. Quantum Electrodynamics at Room Temperature Coupling a Single Vibrating Molecule with a Plasmonic Nanocavity. *Nat. Commun.* **2019**, *10* (1), 1049.
(30) Raab, M.; Vietz, C.; Stefani, F. D.; Acuna, G. P.; Tinnefeld, P. Shifting Molecular Localization by Plasmonic Coupling in a Single-Molecule Mirage. *Nat. Commun.* **2017**, *8* (1), 13966.
(31) Pal, S.; Deng, Z.; Wang, H.; Zou, S.; Liu, Y.; Yan, H. DNA Directed Self-Assembly of Anisotropic Plasmonic Nanostructures. *J. Am. Chem. Soc.* **2011**, *133* (44), 17606−17609.
(32) Zhan, P.; Wen, T.; Wang, Z.; He, Y.; Shi, J.; Wang, T.; Liu, X.; Lu, G.; Ding, B. DNA Origami Directed Assembly of Gold Bowtie Nanoantennas for Single-Molecule Surface-Enhanced Raman Scattering. *Angew. Chem., Int. Ed.* **2018**, *57* (11), 2846−2850.
(33) de Torres, J.; Mivelle, M.; Moparthi, S. B.; Rigneault, H.; Van Hulst, N. F.; García-Parajó, M. F.; Margeat, E.; Wenger, J. Plasmonic Nanoantennas Enable Forbidden Förster Dipole−Dipole Energy Transfer and Enhance the FRET Efficiency. *Nano Lett.* **2016**, *16* (10), 6222−6230.
(34) Kroutil, O.; Romancová, I.; Šíp, M.; Chval, Z. Cy3 and Cy5 Dyes Terminally Attached to 5′C End of DNA: Structure, Dynamics, and Energetics. *J. Phys. Chem. B* **2014**, *118* (47), 13564−13572.
(35) Boulais, É.; Sawaya, N. P. D.; Veneziano, R.; Andreoni, A.; Banal, J. L.; Kondo, T.; Mandal, S.; Lin, S.; Schlau-Cohen, G. S.; Woodbury, N. W.; et al. Programmed Coherent Coupling in a Synthetic DNA-Based Excitonic Circuit. *Nat. Mater.* **2018**, *17* (2), 159−166.
(36) Gopinath, A.; Thachuk, C.; Mitskovets, A.; Atwater, H. A.; Kirkpatrick, D.; Rothemund, P. W. K. Absolute and Arbitrary Orientation of Single Molecule Shapes. *arXiv:1808.04544*, **2018**.
(37) Stennett, E. M. S.; Ma, N.; van der Vaart, A.; Levitus, M. Photophysical and Dynamical Properties of Doubly Linked Cy3-DNA Constructs. *J. Phys. Chem. B* **2014**, *118* (1), 152−163.
(38) Yoon, J. H.; Selbach, F.; Langolf, L.; Schlücker, S. Ideal Dimers of Gold Nanospheres for Precision Plasmonics: Synthesis and Characterization at the Single-Particle Level for Identification of Higher Order Modes. *Small* **2018**, *14* (4), 1702754.
(39) Böhmer, M.; Enderlein, J. Orientation Imaging of Single Molecules by Wide-Field Epifluorescence Microscopy. *J. Opt. Soc. Am. B* **2003**, *20* (3), 554−559.
(40) Novotny, L.; Hecht, B. *Principles of Nano-Optics*, 2nd ed.; Cambridge University Press: Cambridge, 2012.
(41) Ghosh, S.; Chizhik, A. M.; Yang, G.; Karedla, N.; Gregor, I.; Oron, D.; Weiss, S.; Enderlein, J.; Chizhik, A. I. Excitation and Emission Transition Dipoles of Type-II Semiconductor Nanorods. *Nano Lett.* **2019**, *19* (3), 1695−1700.
(42) Mertens, H.; Koenderink, A. F.; Polman, A. Plasmon-Enhanced Luminescence near Noble-Metal Nanospheres: Comparison of Exact Theory and an Improved Gersten and Nitzan Model. *Phys. Rev. B: Condens. Matter Mater. Phys.* **2007**, 115123.
(43) Pellegrotti, J. V.; Acuna, G. P.; Puchkova, A.; Holzmeister, P.; Gietl, A.; Lalkens, B.; Stefani, F. D.; Tinnefeld, P. Controlled Reduction of Photobleaching in DNA Origami-Gold Nanoparticle Hybrids. *Nano Lett.* **2014**, *14* (5), 2831−2836.

DOI: 10.1021/acs.nanolett.9b02886
Nano Lett. 2019, 19, 6629−6634

(44) Rogobete, L.; Kaminski, F.; Agio, M.; Sandoghdar, V. Design of Plasmonic Nanoantennae for Enhancing Spontaneous Emission. *Opt. Lett.* **2007**, *32*, 1623.
(45) Blanco, L. A.; García de Abajo, F. J. Spontaneous Emission Enhancement near Nanoparticles. *J. Quant. Spectrosc. Radiat. Transfer* **2004**, *89*, 37.
(46) Busson, M. P.; Rolly, B.; Stout, B.; Bonod, N.; Bidault, S. Accelerated Single Photon Emission from Dye Molecule-Driven Nanoantennas Assembled on DNA. *Nat. Commun.* **2012**, 1964.
(47) Liaw, J. W.; Chen, C. S.; Chen, J. H. Enhancement or Quenching Effect of Metallic Nanodimer on Spontaneous Emission. *J. Quant. Spectrosc. Radiat. Transfer* **2010**, *111*, 454.
(48) Mock, J. J.; Hill, R. T.; Degiron, A.; Zauscher, S.; Chilkoti, A.; Smith, D. R. Distance-Dependent Plasmon Resonant Coupling between a Gold Nanoparticle and Gold Film. *Nano Lett.* **2008**, *8* (8), 2245−2252.
(49) Puchkova, A.; Vietz, C.; Pibiri, E.; Wünsch, B.; Sanz Paz, M.; Acuna, G. P.; Tinnefeld, P. DNA Origami Nanoantennas with over 5000-Fold Fluorescence Enhancement and Single-Molecule Detection at 25 Mm. *Nano Lett.* **2015**, *15* (12), 8354−8359.
(50) Toscano, G.; Raza, S.; Jauho, A.-P.; Mortensen, N. A.; Wubs, M. Modified Field Enhancement in Plasmonic Nanowire Dimers Due to Nonlocal Response. *Nat. Commun.* **2011**, *2* (1), 481.
(51) Yao, K.; Liu, Y. Controlling Electric and Magnetic Resonances for Ultracompact Nanoantennas with Tunable Directionality. *ACS Photonics* **2016**, *3* (6), 953−963.

DOI: 10.1021/acs.nanolett.9b02886
Nano Lett. 2019, 19, 6629−6634

Supporting Information

Directing single-molecule emission with DNA origami-assembled optical antennas

Kristina Hübner[1], Mauricio Pilo-Pais[2, 5], Florian Selbach[1], Tim Liedl[2], Philip Tinnefeld[1], Fernando D. Stefani[3,4*] and Guillermo P. Acuna[5*]*

[1] Department of Chemistry and Center for NanoScience, Ludwig-Maximilians-Universität München, Butenandtstr. 5-13 Haus E, 81377 München, Germany

[2]Faculty of Physics and Center for NanoScience, Ludwig-Maximilians-Universität München, Geschwister-Scholl-Platz 1, 80539 München, Germany

[3]Centro de Investigaciones en Bionanociencias (CIBION), Consejo Nacional de Investigaciones Científicas y Técnicas (CONICET), Godoy Cruz 2390, C1425FQD Ciudad Autónoma de Buenos Aires, Argentina

[4]Departamento de Física, Facultad de Ciencias Exactas y Naturales, Universidad de Buenos Aires, Güiraldes 2620, C1428EHA Ciudad Autónoma de Buenos Aires, Argentina

[5]Department of Physics, University of Fribourg, Chemin du Musée 3, Fribourg CH-1700, Switzerland

1. Gold Nanoparticle Fabrication

Synthesis of gold nanoparticles (Au NPs): 60 nm spherical gold NPs were synthesized by a four-step seed growth and etching method[1,2]. Small gold clusters were prepared by reduction of Au^{3+} ions with sodium borohydride in cetyltrimethylammonium bromide (CTAB) solution. These clusters were grown to small seed nanoparticles by further addition of Au^{3+} ions and ascorbic acid in CTAB solution. Further larger polyhedron nanoparticles were formed by anisotropic growth of seed particles in cetyltrimethylammonium chloride (CTAC) solution with Au^{3+} ions and ascorbic acid. Spherical NPs were obtained by etching the surface of nanopolyhedrons by addition of Au^{3+} ions in CTAB solution. The experimental details of the individual steps are specified below.

Clusters: $HAuCl_4$ solution (10 mM, 250 µL) was mixed with a CTAB solution (100 mM, 9.75 mL), followed by rapid injection of a freshly prepared ice-cold $NaBH_4$ solution (10 mM, 600 µL). The mixture was left undisturbed for 3 h at 30 °C.

Seeds: The prepared cluster solution (300 µL) was injected into a growth solution of CTAB (100 mM, 2.44 mL), deionized water (D.I. water; 47.5 mL), $HAuCl_4$ solution (10 mM, 1 mL), and ascorbic acid solution (100 mM, 3.75 mL). The reaction mixture was gently shaken and then left undisturbed for 3 h at 30 °C. The colloid was washed by centrifugation (11500 × g, 40 min) and redispersed in D.I. water (12.5 mL).

Nanopolyhedrons: The seed solution (3.6 mL) was added into a CTAC solution (25 mM, 300 mL). After the sequential addition of ascorbic acid solution (100 mM, 7.5 mL) and $HAuCl_4$ solution (10 mM, 15 mL), the mixture solution was kept undisturbed for 3 h at 30 °C and then washed by centrifugation (1750 × g, 30 min) and redispersion in CTAB solution (20 mM, 5 mL).

Au NPs: The nanopolyhedron solution (5 mL) was diluted by the addition of CTAB solution (20 mM, 250 mL), followed by the addition of $HAuCl_4$ solution (10 mM, 1.9 mL). After stirring (550 rpm, 2 h, 40 °C), the mixture was washed twice with D.I. water (centrifugation at 1750 × g for 30 min) and redispersed finally in D.I. water (10 mL).

2. Sample Preparation

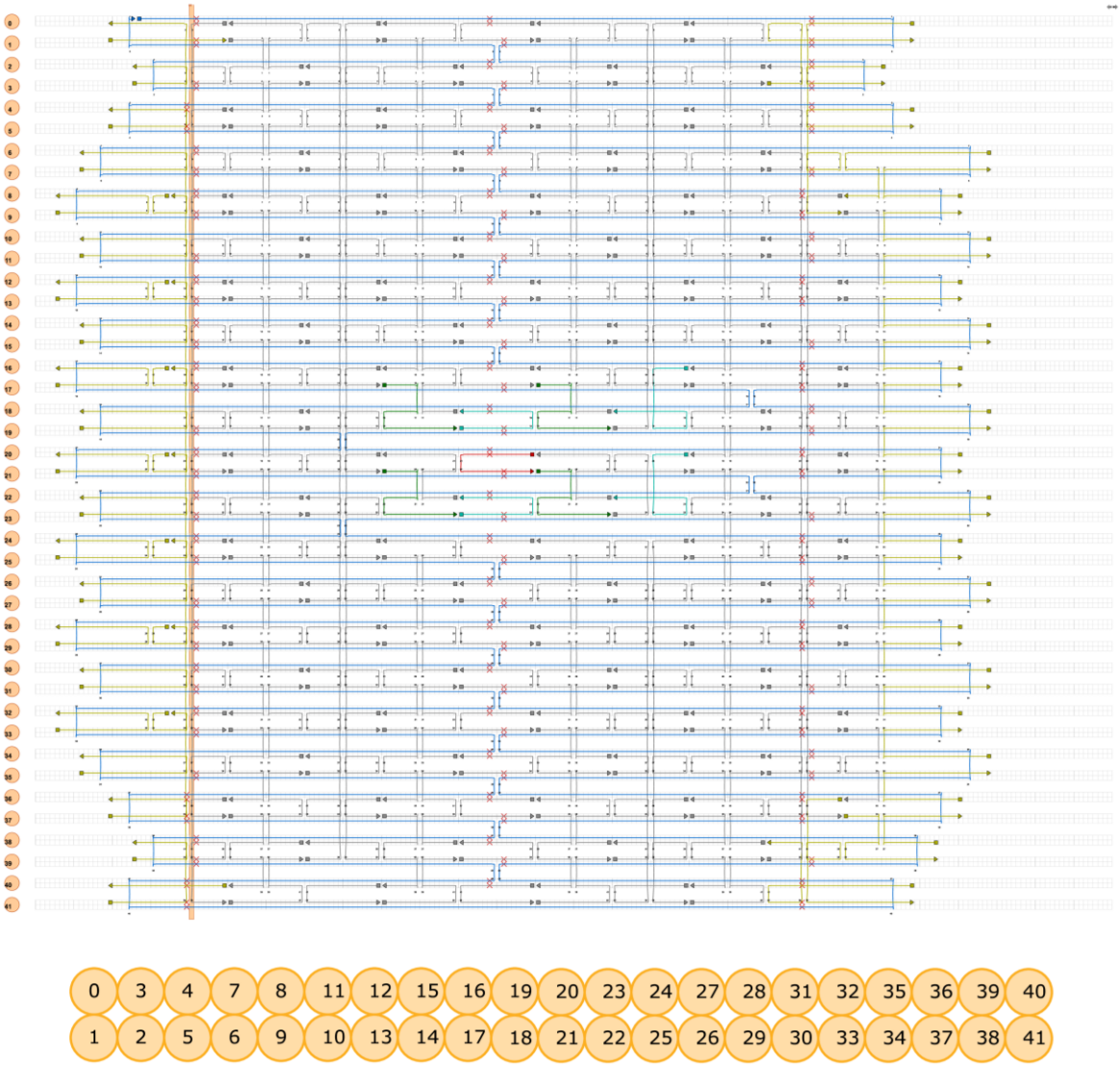

Figure S 1: *2LS DNA origami design. Scaffold (blue), staples (gray), Cy5 modified staples (red), handles (green and turquoise), and endcaps (yellow).*

The DNA origami structure was designed using CaDNAno[3] and visualized for twist correction using CanDo[4]. It consists of a square lattice design that folds onto a 2-layers sheet (2LS) of size ~60 nm×50 nm×5 nm. An attachment binding site with four 15-nuclotides long handles (15xA) is located at the center of each of the two layers of the 2LS origami. Each binding site is aimed to attach a single 60 nm Au NP. The CaDNAno design is shown in Figure S1, with the scaffold portrayed in blue, the core staples in gray, the handles on each layer in green and turquoise, the staple with Cy5 in red, and the endcaps in yellow. The endcaps contain CCCC extensions to prevent base-stacking interactions between origamis.

Handles	5´staple AAAAAAAAAAAAAAA 3’
Cy5	5’ staple TTT Cy5 3’
Endcaps	5’ CCCC staple CCCC 3’ *or* 5’ CCCC staple 3’ *or* 5’ staple CCCC 3’
Thiol-DNA	5’ Thiol C6 TTTTTTTTTTTTTTTTTT 3’

Table S 1*: Modified DNA strands. Handles contain a 15xA extension, the Cy5 staple has a 3-T spacer, and the endcaps 4xC extension(s). Thiolated DNA has a 15xT which is complementary to the handles sequence.*

The 2LS DNA origami structure was folded using a p7249 scaffold (single-stranded M13mp18 bacteriophage genome, in-house produced), staple strands (Eurofins Genomics, Germany), and modified strands (Biomers.net GmbH, Germany and Eurofins Genomics, Germany) in a 1xTAE buffer (40 mM Tris, 40 mM acetatic acid, 1 mM EDTA, pH 8) and 12 mM $MgCl_2$ using a 1:10 scaffold:staples ratio (10 nM scaffold final concentration). The solution was heated to 75 °C, held for 5 minutes, brought to 65 °C, and ramped down to 25 °C at a rate of 1 °C/ 20 mins. The folded DNA origami structure was purified from excess staple strands using gel electrophoresis. All gels were ran using a 1% agarose gel, 1xTAE buffer with 11 mM $MgCl_2$ for 2.5 hours at 4 V/ cm. The appropriate 2LS origami band was cut out and squeezed from the gel using cover slips wrapped in

parafilm. Only side lanes of the gel were post-stained and used as markers to cut the appropriate band to avoid staining the origami used on this study. The concentration was determined via UV-Vis absorption spectroscopy (Nanodrop).

Thiolated DNA (Thiol-C6-15xT, Biomers.net GmbH, Germany) was mixed with ultrasmooth Au NPs (see section 1), adjusted to 0.03% SDS and frozen for 30 mins[5]. Excess DNA was removed using gel electrophoresis. This step also ensures the removal of any self-aggregated dimer formed during the NP functionalization. The concentration was determined via UV-Vis absorption spectroscopy (Nanodrop).

The purified 2LS origami was mixed with the purified Au NPs using an excess of five Au NPs per binding site and adding NaCl to a final concentration of 500 mM. After overnight incubation, the excess of NPs was removed by gel electrophoresis and the band containing correctly formed dimers was extracted as described before.

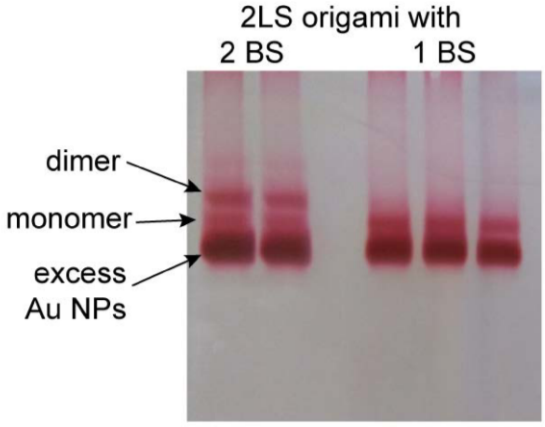

Figure S 2: *Gel image after gel electrophoresis of the designed 2LS origami with two binding sites (2 BS) and one binding side (1 BS).*

3. Surface Preparation and Sample Immobilization

For immobilization of the OA structures, the glass cover slips were first rinsed with water and then cleaned in a UV cleaning system (PSD Pro System, Novascan Technologies, USA). Afterwards, the surfaces were passivated with a BSA-biotin in PBS solution (1 mg/mL) for 1 h, neutrAvidin in PBS solution (0.5 mg/mL) for 20 min and single stranded DNA (7T for the reference and 7A for the monomer and dimer samples) with a biotin attached to the 5'-end (10 nM) for 20 min. In between all the steps, the surfaces were washed with 0.5xTE buffer containing 10 mM $MgCl_2$. The samples were incubated on the surface for 5 min and afterwards washed with buffer. Confocal and wide-field measurements were performed under oxygen removal and ROXS using trolox/troloxquinone in 1xTAE with 12 mM $MgCl_2$.[6,7]

4. Imaging Systems

4.1 Wide-Field Setup

Wide-field measurements were performed on a custom-built wide-field setup based on an inverted Olympus IX71 microscope. As excitation source a red diode laser with a wavelength of 644 nm is used (ibeam smart, Toptica Photonics, Germany). The laser gets spectrally cleaned by a cleanup filter (Brightline HC 650/13, Semrock, USA) before passing the lambda quarter (AQWP05M 400-800 nm, Thorlabs, Germany)/ lambda half waveplate (AHWP05M 400-800 nm, Thorlabs, Germany) and afterwards being focused in the back focal plane of the objective (UApo N 60x, NA = 1.49, WD = 0.1 mm, Olympus, Germany). For stabilization of the sample an actively stabilized optical table (TS-300, JRS Scientific Instruments, Switzerland) and a nosepiece stage (IX2-NPS, Olympus, Germany) were implemented to the microscope. Then the light is directed

through the objective and the sample is illuminated. Fluorescence will get collected by the same objective and separated from the excitation light by a dichroic beamsplitter (Dual Line zt532/640 rpc, AHF Analysentechnik, Germany). Afterwards the fluorescence light is filtered with an emission filter (ET 700/75, Chroma, USA) and focused by a lens on an EMCCD camera (iXon X3 DU-897, Andor, North Ireland). The videos are recorded by the open source microscopy ImageJ software Micro-Manager[8].

4.2 Confocal Setup

Confocal measurements were performed on a custom-build confocal setup based on an inverted Olympus IX81 microscope. The excitation source is a 78 MHz-pulsed laser (SuperK Extreme, NKT Photonics, Denmark), that can be tuned in a region from 400 to 2400 nm. In these experiments working at 639 nm to excite the Cy5 dye. For wavelength selection an AODS (20160 8R, Crystal Technology, Inc., USA) and an AOTF (AA.AOTF.ns:TN, AA-Opto-Electronic, France) are implemented that also clean up the spectrum of the laser. After wavelength selection a neutral density filter (ndF, OD 0-2, Thorlabs, Germany) is passed and the laser beam is coupled into a polarization maintaining single mode fiber (PM-Fiber, P1-488PM-FC-2, Thorlabs, Germany). The polarization of the laser can be controlled by the combination of a linear polarizer (LPVISE100-A, Thorlabs, Germany), an electro optical modulator (EOM, electro-optical modulator, L 0202, Qioptiq, Germany) and a lambda quarter waveplate (AQWP05M-600, Thorlabs, Germany). With these optics a circular polarization can be achieved by driving the EOM with a high frequency. Afterwards, the laser beam is coupled into the microscope body and focused on the sample placed on top of an immersion oil objective (UPlanSApo 100x, NA = 1.4, WD = 0.12 mm, Olympus, Germany). The fluorescence of the sample is collected by the same objective and separated from the excitation light by a dichroic mirror (DS, zt532/640rpc, Chroma,

USA). To filter out scattered laser light, the fluorescence is focused on a 50 µm pinhole (Linos, Germany) and afterwards directed through an emission filter (RazorEdge® 647, Semrock, USA) and again focused by a lens on the the APD (Avalanche Photo Diode, SPCM, AQR 14, Perkin Elmer, USA). Time Correlated Single Photon counting is achieved by an TCSPC system (Hydra Harp 400, PicoQuant, Germany). Scanning of the samples in x and y is realized by a piezo stage (P-517.3CL, E-501.00, Physik Instrumente GmbH&Co. KG, Germany). For data processing, a custom written LabVIEW software (National Instruments, USA) is used. To extract the fluorescence lifetime from the decays, a mono-exponential fit and a deconvolution from the instrumental response function using the program FluoFit (PicoQuant, Germany) were used.

5. Imaging

5.1 Wide-Field Imaging Series

To analyze the emission dipole orientation, the orientation of maximum absorption and the bleaching behavior, a set of different measurements were performed. In a first measurement, the laser power was set to a power density of 0.22 kW cm^{-2} and the objective was shifted towards the sample by approximately 1 µm to take defocused images of the single molecules. This shift in the objective position leads to a deliberate defocused signal on the camera chip that allows us to study the angular emission pattern. Circularly polarized light was used in order to attain uniform excitation of all OA-Cy5 photon emitter structures that are randomly oriented on the glass. Second, after completion of the defocused imaging, the sample is placed back to focus for single molecule studies. These measurements are performed while stepwise rotating the linearly polarized excitation light by spinning the lambda half waveplate for ten degrees nine times every five

seconds. Third, the incident polarization is switched back to circular and the laser power density is increased to 3.04 kW cm^{-2} in order to bleach in a reduced amount of time all the fluorophores present in the imaged field of view. This final step allows us to filter out the signals arising from aggregates of NPs or DNA origami structures and to only consider structures with a single bleaching step, a signature of the presence of a single molecule.

5.2 Confocal Measurements

In order to study the yield of dimer structures, we performed confocal measurements. We used the fluorescence lifetime of the different samples to distinguish dimer from monomer and reference structures. Samples were first scanned with a circularly polarized laser beam and afterwards spots were picked and measured until a single bleaching step occurred.

6. Simulations

Numerical simulations were performed using a Finite Difference Frequency Domain (FDFD) commercial software (CST STUDIO SUITE, Microwave module). The Cy5 fluorophores were modelled by a small (0.1 nm) current source oscillating at 447 THz, corresponding to the wavelength of maximum fluorescence emission of Cy5. The emission pattern generated by the dipolar current source was calculated for the experimental geometry: a glass (n = 1.515) – water (n = 1.33) interface, the current source (fluorophore) was placed on the water side at 40 nm from the glass-water interface, oriented parallel or perpendicular to the interface. The simulated images were calculated by plotting the electric field generated on each position of the selected image plane $\mathbf{r} = (\rho \cos \varphi; \rho \sin \varphi\,; z)$, integrating the fraction of the emission pattern collected by the objective lens:

$$E_j(\boldsymbol{r}) = C \int_0^{2\pi} \int_{\theta_{min}}^{\theta_{max}} \sqrt{\cos\theta}\ E_{0j}(\theta,\psi)\ e^{ik(\rho \sin\theta\,(\cos(\psi-\varphi))+z\cos\theta)} \sin\theta\, d\theta\, d\psi$$

where j stands for x, y, or z (Cartesian components of the field). The solid angle is integrated in spherical coordinates. The azimuth angle is integrated all around the z-axis, and the focusing angle range (θ_{min} and θ_{max}) depends on the NA of the objective. $k = 2\pi/\lambda$. $E_{0j}(\theta,\psi)$ is the j component of the emission pattern field parametrized in the azimuthal and polar angles (θ,ψ).

For the quantum yield simulations we followed the procedure included in [9].

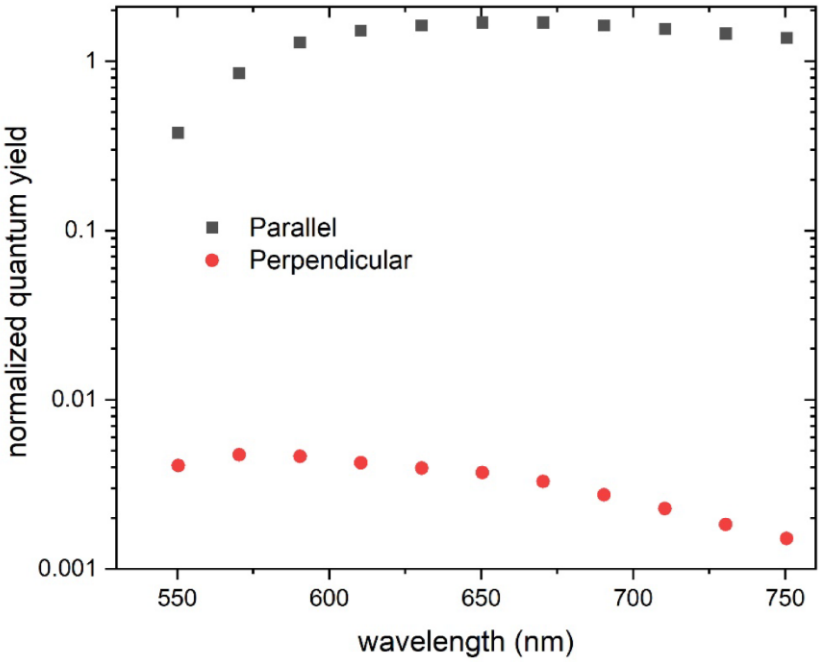

Figure S 3: *Simulated quantum yield for the Cy5 fluorophore located at the hotspot of the OA normalized to the quantum yield without the OA (0.27) for two orientations, along the dimer main axis (parallel) and perpendicular.*

7. Data Analysis

For extraction of the fluorescence enhancement, modulation and angle of maximum excitation the modulating time traces of single molecules are processed and fitted (Figure S 4). Therefore, a mean

fluorescence enhancement value for each excitation polarization is extracted. The extracted values are then fitted with a cosine square function.

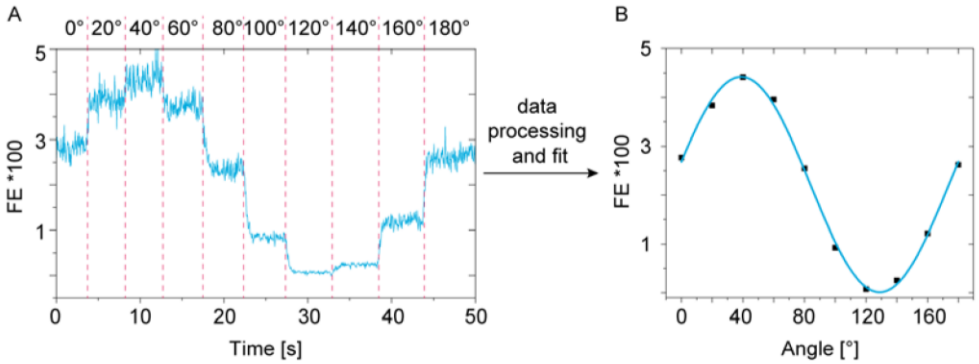

Figure S 4: *Trace from the polarization resolved excitation measurements of a single Cy5 molecule (A). (B) Extracted mean intensity for all polarizations fitted by a cosine square function.*

By this fitting, the maximum fluorescence enhancement that corresponds to the angle of maximum excitation can be extracted.

References

(1) Darvishzadeh-Varcheie, M.; Guclu, C.; Ragan, R.; Boyraz, O.; Capolino, F. Electric Field Enhancement with Plasmonic Colloidal Nanoantennas Excited by a Silicon Nitride Waveguide. *Opt. Express* **2016**.

(2) Yoon, J. H.; Selbach, F.; Langolf, L.; Schlücker, S. Ideal Dimers of Gold Nanospheres for Precision Plasmonics: Synthesis and Characterization at the Single-Particle Level for Identification of Higher Order Modes. *Small* **2018**, *14* (4), 1702754.

(3) Douglas, S. M.; Marblestone, A. H.; Teerapittayanon, S.; Vazquez, A.; Church, G. M.; Shih, W. M. Rapid Prototyping of 3D DNA-Origami Shapes with CaDNAno. *Nucleic Acids Res.* **2009**.

(4) Kim, D.-N.; Kilchherr, F.; Dietz, H.; Bathe, M. Quantitative Prediction of 3D Solution Shape and Flexibility of Nucleic Acid Nanostructures. *Nucleic Acids Res.* **2012**.

(5) Liu, B.; Liu, J. Freezing Directed Construction of Bio/Nano Interfaces: Reagentless Conjugation, Denser Spherical Nucleic Acids, and Better Nanoflares. *J. Am. Chem. Soc.* **2017**, *139* (28), 9471–9474.

(6) Vogelsang, J.; Kasper, R.; Steinhauer, C.; Person, B.; Heilemann, M.; Sauer, M.; Tinnefeld, P. A Reducing and Oxidizing System Minimizes Photobleaching and Blinking of Fluorescent Dyes. *Angew. Chemie - Int. Ed.* **2008**.

(7) Cordes, T.; Vogelsang, J.; Tinnefeld, P. On the Mechanism of Trolox as Antiblinking and Antibleaching Reagent. *J. Am. Chem. Soc.* **2009**.

(8) Edelstein, A.; Amodaj, N.; Hoover, K.; Vale, R.; Stuurman, N. Computer Control of

Microscopes Using Manager. *Current Protocols in Molecular Biology*. 2010.

(9) Acuna, G. P.; Möller, F. M.; Holzmeister, P.; Beater, S.; Lalkens, B.; Tinnefeld, P. Fluorescence Enhancement at Docking Sites of DNA-Directed Self-Assembled Nanoantennas. *Science (80-.).* **2012**, *338* (6106), 506–510.

A2 Associated Publication P2

Determining the In-Plane Orientation and Binding Mode of Single Fluorescent Dyes in DNA Origami Structures

by

Kristina Hübner, Himanshu Joshi, Aleksei Aksimentiev, Fernando D. Stefani, Philip Tinnefeld, Guillermo P. Acuna

Reprinted with permission from *ACS Nano* 2021, 15, 3, 5109–5117.

ACSNANO

www.acsnano.org

ARTICLE

Determining the In-Plane Orientation and Binding Mode of Single Fluorescent Dyes in DNA Origami Structures

Kristina Hübner, Himanshu Joshi, Aleksei Aksimentiev, Fernando D. Stefani,* Philip Tinnefeld,* and Guillermo P. Acuna*

Cite This: *ACS Nano* 2021, 15, 5109–5117 Read Online

ACCESS | Metrics & More | Article Recommendations | Supporting Information

ABSTRACT: We present a technique to determine the orientation of single fluorophores attached to DNA origami structures based on two measurements. First, the orientation of the absorption transition dipole of the molecule is determined through a polarization-resolved excitation measurement. Second, the orientation of the DNA origami structure is obtained from a DNA-PAINT nanoscopy measurement. Both measurements are performed consecutively on a fluorescence wide-field microscope. We employed this approach to study the orientation of single ATTO 647N, ATTO 643, and Cy5 fluorophores covalently attached to a 2D rectangular DNA origami structure with different nanoenvironments, achieved by changing both the fluorophores' binding position and immediate vicinity. Our results show that when fluorophores are incorporated with additional space, for example, by omitting nucleotides in an elsewise double-stranded environment, they tend to stick to the DNA and to adopt a preferred orientation that depends more on the specific molecular environment than on the fluorophore type. With the aid of all-atom molecular dynamics simulations, we rationalized our observations and provide insight into the fluorophores' probable binding modes. We believe this work constitutes an important step toward manipulating the orientation of single fluorophores in DNA origami structures, which is vital for the development of more efficient and reproducible self-assembled nanophotonic devices.

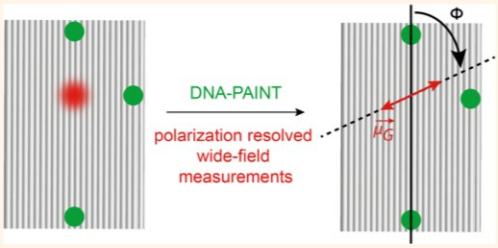

KEYWORDS: *DNA nanotechnology, super-resolution microscopy, DNA-PAINT, single-molecule fluorescence, polarization-resolved microscopy*

The DNA origami technique[1] is revolutionizing nanofabrication by molecular self-assembly because it provides control and versatility to organize different molecules and nanoparticles in well-defined geometric arrangements. In particular, this technique has proven extremely useful to fabricate nanophotonic devices with specific functions by setting single-photon emitters (SPEs), such as fluorescent molecules or quantum dots, and metallic nanoparticles (MNPs) in precise geometries with high positional and stoichiometric control.[2−4] In some cases, DNA origami structures are used to host solely MNPs like in chiral plasmonic structures[5−7] or DNA sensors based on circular dichroism.[8,9] In others, only SPEs are organized, such as in multichromophoric Förster resonance energy transfer (FRET) chains capable of transporting optical excitations[10−13] or FRET-based DNA sensors.[14,15] Finally, DNA origami structures have also been used to construct more complex hybrid nanostructures, where SPEs and MNPs acting as optical nanoantennas (OAs) were combined to enhance the interaction of molecules with light. Examples include OAs for enhanced fluorescence[16−18] or Raman[19−22] spectroscopy, plasmon-assisted FRET,[23,24] strong-coupling at room temperature,[25,26] and directional emission.[27,28]

Importantly, the efficiency of nanophotonic devices depends not only on the relative position of their components but also on their relative orientation. For example, in order to form a directional OA, two or more nanorod elements must be placed side-by-side in a parallel fashion.[29,30] Similarly, the efficiency of dipole−dipole interactions between two fluorophores (FRET) depends, among several factors, on the relative orientation of the fluorophores through the κ^2 factor. This factor ranges from 0 (for perpendicular transition dipoles) to the maximum value of 4 when their transition dipoles are aligned.[31] Regarding the

Received: December 8, 2020
Accepted: February 25, 2021
Published: March 4, 2021

https://dx.doi.org/10.1021/acsnano.0c10259
ACS Nano 2021, 15, 5109−5117

interaction between optically active molecules and OAs, the effect is 2-fold. The molecular excitation rate is proportional to $\langle \vec{E} \cdot \vec{\mu}_G \rangle^2$, with $\vec{\mu}_G$ the absorption transition dipole moment of the molecule and $\vec{E}$ the electric field at the molecule's position arising from the sum of the incident field and the field induced by the OA.[32] The molecular radiative decay rate also depends on the relative orientation between the emission transition dipole moment $\vec{\mu}_E$ and the OA, leading to a wide range of effects, from strong enhancement to virtually complete suppression of photon emission.[27,33−35]

So far, various protocols have been introduced to incorporate anisotropic MNPs, such as gold nanorods[36] and triangular plates,[37] in DNA origami structures with positional and orientational control. In contrast, while the DNA origami technique routinely enables the assembly of molecules with high positional accuracy, controlling the orientation of single molecules remains challenging. Basically, there are two kinds of strategies to incorporate molecules into DNA origami structures. The first one is the well-known, noncovalent binding to double-stranded DNA (dsDNA) helices. This approach offers orientational control because different molecules bind differently to the dsDNA structure, depending on the chemical structure. Some bind preferentially in between bases (intercalators); others bind to the minor or major groove (groove binders), or externally along the dsDNA chain.[38] Gopinath *et al.*[39] reported an example of this approach, labeling DNA origami structures with the intercalating dye TOTO-3, which forms an angle of 70° ± 10° between $\vec{\mu}_G$ and the dsDNA helix. Unfortunately, this level of orientational control[40] comes at the expense of losing stoichiometric and positioning control as it is not possible to predefine the positions nor the number of binding molecules.

The second strategy to incorporate molecules into a DNA origami structure consists of attaching them covalently to specific constituent single-stranded DNA (ssDNA) staples,[41] at either the 5′- or 3′-ends, or internally, using, for example, an amino-C6 linker. This approach provides high positional and stoichiometric control to incorporate molecules in DNA origami structures.[10] However, in contrast to the case of DNA binding molecules, the resulting orientation of molecules is not yet predictable. This is due, in part, to the complexity of the interaction between small molecules and DNA which depends not only on the molecular identity but also on the type of linker and the surrounding environment.[24] Also, no method of general applicability has been available to reliably determine the orientation of single molecules with respect to DNA origami structures. Earlier works have addressed the orientation of fluorophores linked to DNA using FRET.[42−45] For example, it was found that Cy3 and Cy5 dye molecules attached to dsDNA maintain a preferential orientation when linked *via* a three-carbon linker due to blunt end sticking[46] but present a high degree of rotational freedom when other linkers are used.[45] FRET measurements have the advantage that they can be conducted at the single-molecule level, but they do not address the orientation of fluorophores with respect to the DNA structure. Instead, they report on the relative orientation between donor and acceptor molecules, and that measurement relies strongly on an accurate determination of the donor−acceptor separation distance. More recently, the position and orientation of single molecules attached to short dsDNA chains were determined through single-molecule localization techniques.[47−49] Because the dsDNA chains were shorter than the persistence length, they could be considered rectilinear, and the relative orientation of the fluorophores with respect to the dsDNA could be inferred at the cost of the DNA being physically adsorbed to a positively charged surface.

Here, we present a technique of general applicability to study the orientation of single fluorescent molecules in DNA origami structures. It is based on two independent measurements that can be performed consecutively on surface-immobilized DNA origami structures using a wide-field fluorescence microscope. First, a polarization-resolved excitation measurement is used to determine the 2D orientation of the target fluorescent molecules. Second, a super-resolution (nanoscopy) measurement using the DNA-PAINT technique[50] is used to retrieve the orientation of the DNA origami "host" structure. The DNA origami hosts the dsDNA that the dyes are bound to in a fixed horizontal orientation while maintaining its physiological buffer environment. With this technique, we initially determined the orientation of single ATTO 647N molecules covalently attached to a rectangular DNA origami structure in three configurations with different expected nanoenvironments. For every case, the ATTO 647N delivered a nearly Gaussian distribution of orientations with a distinct mean orientation. Then, we performed analogous experiments with ATTO 643 and Cy5 fluorophores for two configurations in order to determine the hierarchy between the two main factors that affect the final orientation: nanoenvironment and fluorophore identity. Finally, using molecular dynamics simulations, we assigned the observed orientations to molecular structures and interactions that are likely related to the true conformations. Overall, these results enable the design and fabrication of highly efficient nanophotonic devices by self-assembly using DNA origami structures, where SPEs could be set not only with high positional and stoichiometric control but also with orientational control.

RESULTS AND DISCUSSION

A schematic of the sample employed is shown in Figure 1a. It consists of a 2D rectangular DNA origami structure (85 nm × 71 nm) based on 24 helices with different modifications. A single ATTO 647N, ATTO 643, or Cy5 molecule (indicated by a red spot in Figure 1a) was covalently attached to a defined base of an ssDNA staple through a single C6-linker. For the DNA-PAINT measurements, we further extended 18 ssDNA staples with an 11-nucleotide sequence to form three binding sites (green spots in Figure 1a, top view), arranged in an asymmetric pattern. In order to immobilize the samples onto glass coverslips, six biotinylated ssDNA staples are incorporated into the DNA origami structure (blue spots in Figure 1a, bottom view) on the hereafter defined underside of the DNA origami structure.

The ATTO 647N fluorophore was selected not only for its brightness and photostability but also because it is moderately hydrophobic, carries a net electrical charge of +1, and tends to stick to surfaces and DNA.[51,52] This sticking can be hydrophobic, due to an interaction with the hydrophobic core of the DNA, or electrostatic, due to an interaction with the negatively charged DNA phosphate backbone. ATTO 643 is a hydrophilic version of the ATTO 647N and shows a reduced tendency for unspecific sticking. The Cy5 fluorophore is a member of the group of cyanine dyes and carries a net charge of +1. In this work, we want to address the question of whether fluorophores show preferential binding sites depending on the position and motional freedom within the DNA origami structure. To this end, we prepared three samples where a single fluorophore is linked in different ways to the DNA origami structure, always

https://dx.doi.org/10.1021/acsnano.0c10259
ACS Nano 2021, 15, 5109−5117

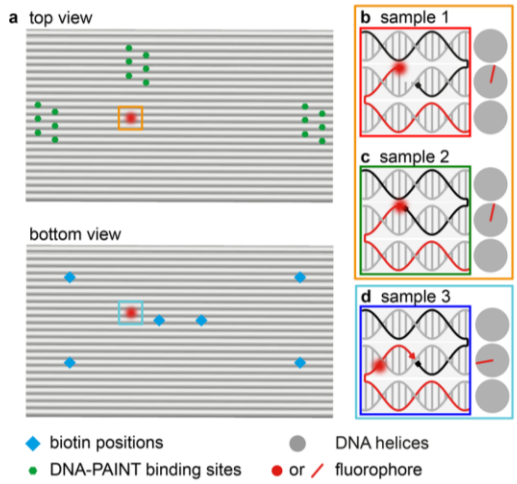

Figure 1. (a) Sketch of the top and bottom view of the rectangular DNA origami structure including different modifications: 6 biotins (blue), a single fluorophore (ATTO 647N, ATTO 643, or Cy5; red), and 18 DNA sequences (green) forming three binding sites for DNA-PAINT measurements in an asymmetric pattern. (b–d) Inset of the DNA helical winding highlighting the position of the ssDNA staple (red line) labeled with the fluorophore (red spot), the adjacent ssDNA staple (black line), and the scaffold strand (gray line) for the three samples employed.

covalently attached but with different local environments. In samples 1 and 2, the fluorophore (highlighted with an orange square in the top view of Figure 1a) is linked at the same position in the helix, facing toward the neighboring helix (Figure 1b,c). This is achieved through a modification at the 3′-end of the corresponding ssDNA staple (Supporting Information, Figure S1a). The difference between these samples is that in sample 1 the next adjacent ssDNA staple after the fluorophore modification is shortened by two nucleotides (Figure 1b), whereas in sample 2 the adjacent ssDNA staple is not shortened (Figure 1c). Thus, the fluorophore is expected to have more freedom to find a favorable position in sample 1. In sample 3, the fluorophore (highlighted by a blue square in the bottom view of Figure 1a) is incorporated at a different position using an internal modification of an ssDNA staple in a different helix (Supporting Information, Figure S1b) so that the fluorophore is facing toward the underside of the DNA origami structure (Figure 1d). Samples 1 and 2 were prepared for all three fluorophores (ATTO 647N, ATTO 643, and Cy5) whereas sample 3 was solely fabricated with a single ATTO 647N fluorophore.

Measurements were performed in a home-built wide-field microscope equipped with both green (532 nm) and red (644 nm) lasers for fluorescence excitation. The polarization-resolved measurements were carried out under epifluorescence illumination, by stepwise rotating the linear polarization of the red laser excitation by 20° every five seconds. This procedure was repeated 18 times to cover twice an excitation polarization range of 180°. An example fluorescence trace showing a periodic intensity modulation is shown in Figure 2a. This modulation can be quantified as $M = \frac{I_{max} - I_{min}}{I_{max} + I_{min}}$, with I_{max} and I_{min} the highest and lowest intensity values extracted from each trace, respectively. Histograms showing the distributions of the modulation for all samples and fluorophores are included in the Supporting Information in Figure S2. We only considered single-molecule traces showing a significant modulation[47] (*i.e.*, $M > 0.15$) in order to exclude samples in which the fluorophore is relatively free to rotate and thus cannot be studied with the forthcoming analysis. Table S1 includes the number of traces studied and the fraction that met this condition for each sample and fluorophore. For the traces with $M > 0.15$, we attribute the excitation

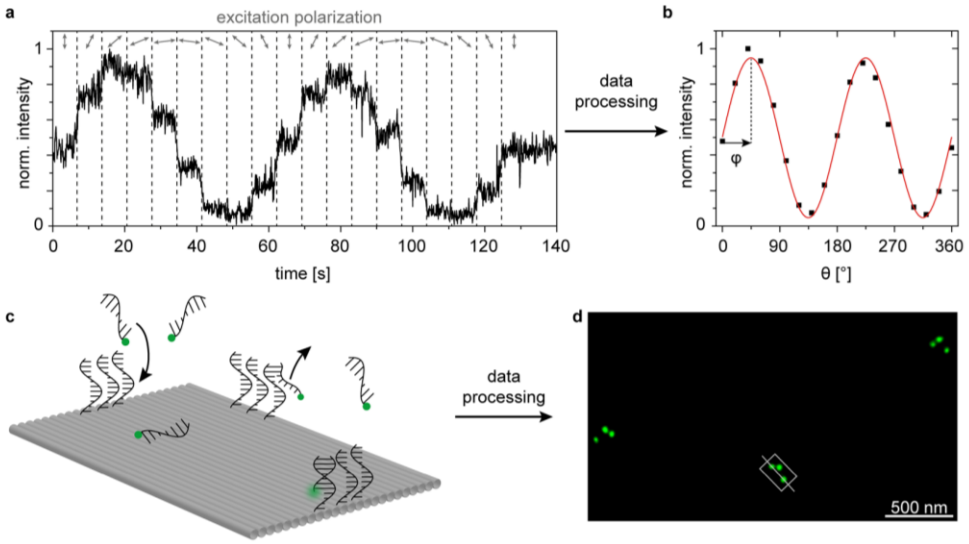

Figure 2. (a) Polarization-resolved excitation measurements. Exemplary ATTO 647N fluorescence trace obtained by rotating the incident polarization angle (θ) by 20° every five seconds. (b) Mean fluorescence intensity vs θ together with a $\cos^2$ fit to obtain the in-plane orientation (φ) of the excitation transition dipole moment $\vec{\mu}_G$ with respect to the microscope. (c) DNA-PAINT nanoscopy measurements. Sketch of the binding and unbinding of the imager strands labeled with a single ATTO 542 onto the DNA-PAINT binding sites. (d) Super-resolved DNA-PAINT image corresponding to three DNA origami structures showing the asymmetric triangular pattern. Based on this image, the orientation in 2D as well as the binding geometry (upright or upside down) of each DNA origami (gray rectangle) can be extracted (gray line).

https://dx.doi.org/10.1021/acsnano.0c10259
ACS Nano 2021, 15, 5109–5117

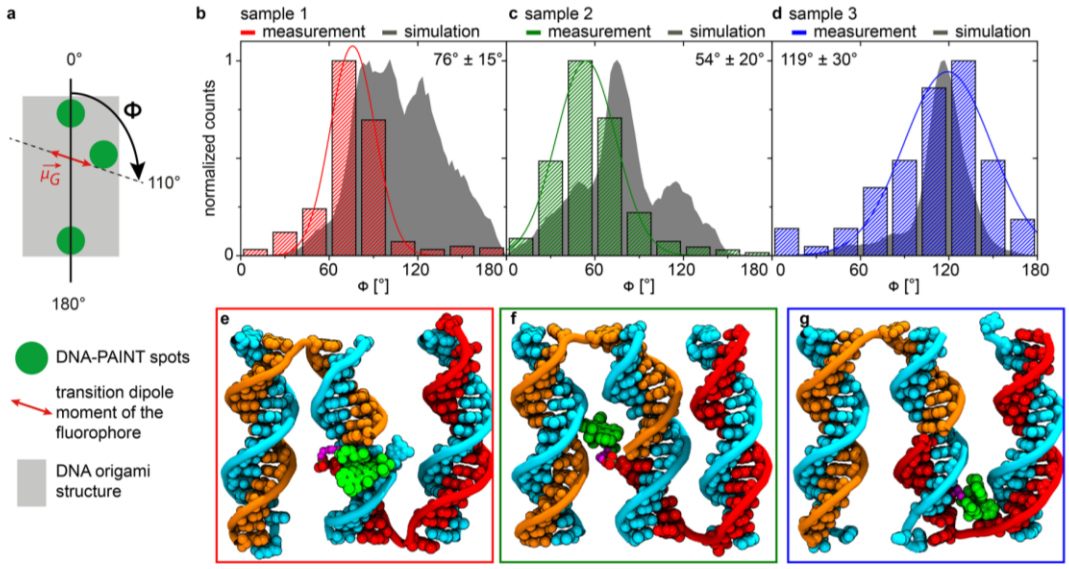

Figure 3. (a) Coordinate system employed to estimate the angle ϕ that the fluorophore (*i.e.*, its $\vec{\mu}_G$) forms with the DNA origami host structure. (b–d) Distributions of ϕ for ATTO 647N on the three samples obtained experimentally (bars) and from all-atom MD simulations (shaded gray curves). The experimental distributions are fitted with a Gaussian function; its mean value and the standard deviation are shown next to the plot. Each simulation histogram shows data from two independent runs, 1 μs long, sampled every 20 ps. (e–g) Conformations of ATTO 647N from all-atom MD simulations corresponding to the average experimental orientation of the three samples. The ATTO 647N is shown in green, the staple strand carrying the ATTO 647N in red, and the C6-linker in magenta, and the adjacent staple and scaffold strands are shown in orange and blue, respectively.

modulation to fluorophores spending a considerable fraction of the time bound to the DNA origami structure. For each polarization, the mean intensity was extracted and plotted against the incident polarization angle θ. The resulting intensity vs θ curve was fitted to a $\cos^2(\theta - \varphi)$ function, as shown in Figure 2b. The obtained value of φ corresponds to the in-plane orientation of the fluorophore's absorption transition dipole moment, $\vec{\mu}_G$.

Next, we performed DNA-PAINT imaging by adding a solution containing 3 nM 7-nucleotide ssDNA sequences (imager strands) labeled with a single ATTO 542 dye (Figure 2c). Every transient binding of an imager strand to one of the three binding sites leads to a fluorescence spot on the camera image which is used to precisely localize the binding site. The reconstructed super-resolved images reveal the triangular asymmetric pattern of each DNA origami structure (Figure 2d), which not only provides the orientation of each DNA origami rectangle on the glass coverslip but also shows whether it was immobilized upright or upside down (for further information, see Figure S3). For this 2D DNA origami, the structure can self-assemble with the biotin modifications ending on the "upper-side" as previously reported.[53,54] We determined that approximately 33% of all the DNA origami structures studied were bound to the glass coverslip with the "upper-side" facing toward the glass surface. This does not affect our analysis, as shown in Figure S4 of the Supporting Information.

By combining both sets of measurements, we obtained the angle of each fluorophore ($\vec{\mu}_G$) with respect to the dsDNA helix of its host DNA origami structure. We called this angle ϕ, defined according to the coordinate system shown in Figure 3a. Figure 3b–d shows the distributions of ϕ obtained for the three samples labeled with a single ATTO 647N. Based on a Gaussian fit to each distribution, the mean orientations are found to be ϕ = 76° ± 15°, 54° ± 20°, and 119° ± 30° for samples 1, 2, and 3, respectively. The distinct distributions of ϕ reveal that the notorious stickiness of ATTO 647N to DNA strongly depends on the specific nanoenvironment. This is especially illustrated by a more than 20° difference in the average molecular orientation for samples 1 and 2, which differ only by two missing nucleotides in sample 1.

In order to rationalize these findings, we performed all-atom molecular dynamics (MD) simulations of the relevant three-helix fragments taken from the experimental DNA origami designs (see Figure 3e–g and Figure S5a). Two independent simulations, each 1 μs long, were performed for each system (the videos from the simulations for each sample are included in the Supporting Information, movies S1, S2, and S3). From these simulations, we extracted the in-plane orientation of the fluorophore (ϕ) at 20 ps time steps. The obtained distributions of ϕ are additionally shown in Figure 3b–d (gray). For sample 3, we find an exquisite agreement between experiment and simulations. The broadening of the experimental data can likely be assigned to possible wobbling of the overall structure. On the other hand, samples 1 and 2 exhibit larger differences between experiment and simulation. Visual inspection of the simulation videos reveals that several, very different conformations of the dye within the DNA origami structure are visited for relatively long times indicating that the energy landscape might be too rugged to allow for a representative sampling of all possible conformations within the time scale accessible to the simulations. *Vice versa*, by searching in the simulations for conformations that match the experimental ϕ-values, we extracted conformations that are likely to be visited for longer times in the experiments (alternative conformations representing different subpopulations of the simulations are shown in Figure S5e).

https://dx.doi.org/10.1021/acsnano.0c10259
ACS Nano 2021, 15, 5109–5117

A great finding arises from the comparison of the results obtained with sample 1 and 2, that only differ by two missing nucleotides in sample 1. Interestingly, the simulated conformations of sample 1 with ϕ-values matching the experiments are characterized by intercalation of the dye at the position of the two missing nucleotides (see representative structure in Figure 3e). In contrast, for sample 2, the subpopulation of the simulation with the ϕ-values matching the experimental average distinguishes itself by the interaction of the dye with the neighboring helix (see representative structure in Figure 3f). In analogy, we also extracted a representative conformation of sample 3 (Figure 3g) that reveals potential reasons for the better agreement of experiment and simulation. For sample 3, the dye is located closer to a crossover of a neighboring helix which creates a preferential binding pocket (Figure 3g).

In addition, we performed measurements on samples 1 and 2 with single ATTO 643 and Cy5 fluorophores. The measured distributions of ϕ are shown in Figure 4, where the previous

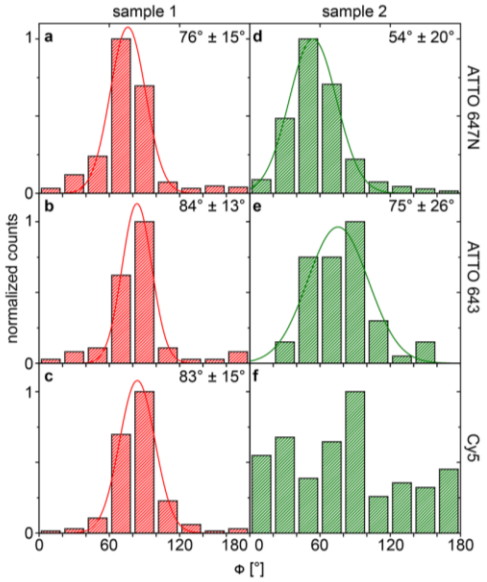

Figure 4. Distributions of ϕ for ATTO 647N, ATTO 643, and Cy5 fluorophores incorporated in the DNA origami structure in samples 1 and 2. The curves are fits to a Gaussian function; the mean and standard deviations are shown next to the plots.

results for ATTO 647N are added for comparison. For sample 1, narrow distributions of ϕ were obtained for every fluorophore characterized by similar mean values of 76° ± 15°, 84° ± 13°, and 83° ± 15° for ATTO 647N, ATTO 643, and Cy5, respectively. Also, for this sample, the fraction of traces showing a modulation $M > 0.15$ was larger than 90% for the three dyes. In contrast, for sample 2, broader distributions of ϕ were measured with more dissimilar mean values of 54° ± 20° and 75° ± 26° for ATTO 647N and ATTO 643, respectively. For Cy5, the obtained distribution of ϕ in sample 2 was nearly uniform, indicating that Cy5 finds no preferential orientation under these conditions. Sample 2 also showed different behaviors in the fraction of modulating traces for the three fluorophores. While ATTO 647N and Cy5 show a considerably high fraction of modulating traces (61% and 88%, respectively), only 20% of the traces registered for ATTO 643 showed significant modulation. Similar to our simulations of the ATTO 647N systems, in our simulations of the Cy5 dye-conjugated DNA constructs (Supporting Information, Figure S6 and Movies S4 and S5), the dye was observed to interact strongly with the unpaired DNA nucleotides in sample 1 and with the grooves of the DNA helices in sample 2. Overall, these results confirm that in sample 1 the fluorophores adopt similar orientations in the space left by the two missing nucleotides. In sample 2, without the extra available space, the fluorophore orients in a less defined manner with a stronger dependence on the fluorophore type.

CONCLUSION

In summary, we have developed a technique to determine the in-plane orientation of fluorescent molecules covalently attached to DNA origami structures. This technique combines a polarization-resolved excitation measurement and DNA-PAINT nanoscopy and can be implemented in wide-field fluorescence microscopes. We applied this approach to study the orientation of different fluorophores covalently incorporated into DNA origami structures in three different ways, each one generating a different local environment for the fluorophores. We showed that ATTO 647N, one of the most used dyes in single-molecule experiments, not only strongly sticks to DNA but also adopts preferential binding geometries depending on the local environment. MD simulations of the corresponding experimental systems showed that the local environment of a dye conjugated to DNA can qualitatively change the manner in which the dye interacts with the DNA and thereby affect the preferential orientation of the dye. Although we found the conformational sampling afforded by our brute-force MD simulations to be insufficient to quantitatively predict the preferential orientation of the dyes, the simulations nevertheless yielded substantial structural information to assign probable conformations for each sample studied and allow us to extract likely binding modes.

Importantly, we find that leaving extra space to a terminally attached fluorophore (*e.g.*, by shortening the adjacent staple strand) leads to stronger binding and a narrower, more defined distribution of dye orientations. These findings were validated by experiments with three different fluorophores: ATTO 647N, ATTO 643, and Cy5. In contrast, an internally attached fluorophore in the DNA strand (sample 3) does not lead to a narrower distribution of orientations.

The dynamics of dye molecules around a DNA helix is governed by a complex interplay of electrostatic and hydrophobic interactions. This complexity imposes a considerable challenge for the accurate prediction of the final orientation of the molecules within a DNA origami structure. The experimental approach presented here should be applicable to other dyes and a variety of relevant samples using, *e.g.*, bis-functional fluorescent dyes. Further measurements of molecular orientation, incorporating 3D techniques,[55] in combination with MD simulations, will enable the generation of sufficient empirical knowledge to finally predict and manipulate molecular orientation in DNA origami structures. This, in turn, will lead to much more efficient and reproducible self-assembled nano-photonic applications.[56]

METHODS

DNA Origami. The rectangular DNA origami structure was designed using CaDNAno.[57] It is based on a 7249-nucleotide long scaffold extracted from a M13mp18 bacteriophage and folded into the desired rectangular shape with the help of 186 staples (see the SI, Section S6) mixed with a 10-fold excess of staples to scaffold. Unmodified staple strands were purchased from IDT; biotin-function-

https://dx.doi.org/10.1021/acsnano.0c10259
ACS Nano 2021, 15, 5109−5117

alized staples as well as the dye labeled staple strands with ATTO 647N, ATTO 643, and Cy5 for sample 1 and 2 were purchased from Eurofins Genomics GmbH and for sample 3 with ATTO 647N from Biomers GmbH. The fluorophores used here are linked through a C6-linker to the single-stranded DNA either on the 3′-end in samples 1 and 2 (Figure S1a) or internally in sample 3 (Figure S1b). A temperature ramp is driven to self-assemble the scaffold and staple mixture to the designed rectangular DNA origami structure. The mixture first was heated to a temperature of 70 °C, where it stayed for 5 min; then, the temperature was decreased down to 24 °C following a ramp of 1 °C min^{-1}. To get rid of the excess of staple strands, agarose gel electrophoresis is used as a purification method. To this end, a 1.5% agarose gel (Biozym LE agarose) containing ROTIGelStain (Roth) as an intercalating dye for DNA is made. Additionally, a 10× BlueJuice gel loading buffer (Thermo Fischer Scientific) is used to load the gel pockets with the unpurified DNA origami structures. The gel runs at 80 V for 90 min in a 0.5× TAE 11 mM $MgCl_2$ buffer, cooled in an ice water bath. After electrophoresis, the bands in the gel containing the DNA origami structure were cut out and squeezed with a glass slide to extract the purified DNA origami structures. The final concentration of the DNA origami structures was determined on a Nanodrop 2000 spectrophotometer (Thermo Fisher Scientific).

Surface Preparation and Immobilization. For surface immobilization, glass slides were rinsed with Milli-Q water and cleaned in a UV cleaning system (PSD Pro System, Novascan Technologies). After cleaning, two slides were glued together with double-sided adhesive tape forming a chamber between the two slides. The surface was passivated with BSA biotin (1 mg/mL, Sigma-Aldrich Chemie GmbH) and neutrAvidin (0.5 mg/mL, Sigma-Aldrich Chemie GmbH), both incubated for 15 min and washed with 1× PBS buffer after incubation. Then, the DNA origami structure can be immobilized in a buffer containing 12 mM $MgCl_2$ *via* biotins binding to the functionalized surface. For the fluorescence measurements, the buffer was exchanged to a buffer containing a reducing and oxidizing (ROX) system as well as oxygen scavenging agents in order to increase the photostability of the fluorophores. In particular, we used trolox/troloxquinone as the reducing and oxidizing system, in addition to glucose oxidase for oxygen removal in a 1× TAE buffer containing 2 M NaCl.[58,59]

Wide-Field Setup. Measurements were performed on a home-built wide-field microscope based on an inverted Olympus IX71 microscope. For excitation, a 644 nm diode laser (ibeam smart, Toptica Photonics) and 532 nm fiber laser (MPB Communications) are used. Spectral clean-up of the lasers' emission is performed through the following filters: Brightline HC 650/13, Semrock (red range); and Z532/647x, Chroma (green range). After spectral cleaning, the laser is directed through a linear polarizer (LPVISC100-MP2 510−800 nm, Thorlabs) to clean up the polarization of the beam and a lambda half waveplate (AHWP05 M 400−800 nm, Thorlabs) mounted in a rotatable motorized stage (K10CR1/M stepper motor, Thorlabs). The laser is then focused on the back focal plane of the objective (UPLXAPO 100×, numerical aperture (NA) = 1.45, working distance (WD) = 0.13, Olympus). For sample stabilization, an actively stabilized optical table (TS-300, JRS Scientific Instruments) and a nosepiece stage (IX2-NPS, Olympus) are implemented. The emitted light is redirected through the objective and spectrally separated from the excitation laser by a dichroic beamsplitter (Dual Line zt532/640 rpc, AHF Analysentechnik). The fluorescence light is filtered by an emission filter in the red range (ET 700/75, Chroma) as well as in the green range (BrightLine 582/75, AHF Analysentechnik) and focused onto an EMCCD camera (iXon X3 DU-897, Andor). Data acquisitioning is performed by the open source microscopy imageJ software Micro-Manager.[60]

Simulations. All MD simulations were performed using program NAMD2,[61] a 2 fs integration time step, 2−2−6 multiple time stepping, periodic boundary conditions, and particle mesh Ewald (PME) method over a 1 Å resolution grid to calculate the long-range electrostatic interaction.[62] The Nosé−Hoover Langevin piston[63] and Langevin thermostat were used to maintain the constant pressure and temperature in the system. An 8−10−12 Å cutoff scheme was used to calculate van der Waals and short-range electrostatic forces. The SETTLE algorithm[64] was applied to keep water molecules rigid whereas the RATTLE algorithm[65] constrained all other covalent bonds involving hydrogen atoms. CHARMM36 force field parameters described the bonded and nonbonded interactions among DNA water and ions.[66] The force-field parameters of the dye molecules (ATTO 647N and Cy5) covalently conjugated with the C6 linker to DNA were obtained using the CHARMM General Force Field (CGenFF) web server.[67] We used custom nonbonded fix (NBFIX) corrections to improve the nonbonded interaction among DNA and ions.[68] The coordinates of the system were saved at an interval of 20 ps. Visualization, analysis, and postprocessing of the simulation trajectories were performed using VMD[69] and CPPTRAJ.[70]

We created three all-atom models of rectangular DNA origami systems corresponding to the three different dye modification used in experiments, namely, sample 1, 2, and 3. The CaDNAno design of the DNA origami plate was converted to an idealized all-atom representation using a previously described method.[71] In order to create a realistic and smaller analogue of the DNA origami suitable for the all-atom simulations, we kept only a 15 base-pair long section of the DNA helix containing the dye molecule along with two nearby DNA helices. Next, using a set of custom translation and rotational transformations, we placed the dye molecules near the DNA helix to match the respective chemical structure. The bond between DNA and C6 conjugated dye molecules (ATTO 647N and Cy5) was created using the psfgen module of VMD. In sample 1 and 2, the dye molecules were connected to the backbone of the DNA whereas, in sample 3, it was connected to the thymine base.

The resulting systems were solvated with TIP3P water molecules[72] using the Solvate plugin of VMD.[69] Potassium, sodium, and chloride ions were added to produce the experimental buffer conditions (12.5 mM KCl and 2 M NaCl) using the autoionize plugin of VMD. Each final system measured 9 × 8 × 9 nm^3 and contained approximately 60 000 atoms (Figure S5a).

The assembled systems were subjected to energy minimization using the conjugate gradient method to remove the steric clashes between the solute and solvent. Following that, we equilibrated each system for 10 ns while harmonically restraining the C1′ atoms of DNA using a spring constant of 1 kcal mol^{-1} $Å^{-2}$. Subsequently, we equilibrated the systems for an additional 10 ns with weaker harmonic restraints using a spring constant of 0.1 kcal mol^{-1} $Å^{-2}$ while maintaining the hydrogen bonds between the complementary base-pairs of DNA using the extrabond utility of NAMD. Finally, we removed all the restraints (except the terminal C1′ atoms of each DNA strand) and performed approximately 1 μs long simulations of the systems using a constant number of atoms, pressure (P = 1 bar), and temperature (T = 298 K) ensemble. In order to mimic the connection of the DNA helices to the rest of the DNA origami plate, we harmonically restrained the terminal atoms of each DNA strand using a spring constant of 0.1 kcal mol^{-1} $Å^{-2}$. Two sets of simulations were carried out for each design to improve sampling of the conformational space.

ASSOCIATED CONTENT

Supporting Information

The Supporting Information is available free of charge at https://pubs.acs.org/doi/10.1021/acsnano.0c10259.

Movie S1: 1 μs long MD simulation trajectories of the ATTO 647N dye in sample 1 in the dye-conjugated DNA system (MPG)

Movie S2: 1 μs long MD simulation trajectories of the ATTO 647N dye in sample 2 in the dye-conjugated DNA system (MPG)

Movie S3: 1 μs long MD simulation trajectories of the ATTO 647N dye in sample 3 in the dye-conjugated DNA system (MPG)

Movie S4: 1 μs long MD simulation trajectories of Cy5 in sample 1 in the dye-conjugated DNA system (MPG)

Movie S5: 1 μs long MD simulation trajectories of Cy5 in sample 2 in the dye-conjugated DNA system (MPG)

https://dx.doi.org/10.1021/acsnano.0c10259
ACS Nano 2021, 15, 5109−5117

Linking chemistry of the ATTO 647N to DNA, data on the modulation, DNA-PAINT analysis, comparison of the orientation data for flipped and nonflipped populations, simulation data, and the DNA origami staple strands (PDF)

AUTHOR INFORMATION

Corresponding Authors

Fernando D. Stefani − *Centro de Investigaciones en Bionanociencias (CIBION), Consejo Nacional de Investigaciones Científicas y Técnicas (CONICET), C1425FQD Ciudad Autónoma de Buenos Aires, Argentina; Departamento de Física, Facultad de Ciencias Exactas y Naturales, Universidad de Buenos Aires, C1428EHA Ciudad Autónoma de Buenos Aires, Argentina*; Email: fernando.stefani@df.uba.ar

Philip Tinnefeld − *Department of Chemistry and Center for NanoScience, Ludwig-Maximilians-Universität München, 81377 München, Germany*; orcid.org/0000-0003-4290-7770; Email: philip.tinnefeld@cup.uni-muenchen.de

Guillermo P. Acuna − *Department of Physics, University of Fribourg, Fribourg CH-1700, Switzerland*; orcid.org/0000-0001-8066-2677; Email: guillermo.acuna@unifr.ch

Authors

Kristina Hübner − *Department of Chemistry and Center for NanoScience, Ludwig-Maximilians-Universität München, 81377 München, Germany*; orcid.org/0000-0002-6476-5446

Himanshu Joshi − *Department of Physics, University of Illinois at Urbana−Champaign, Urbana, Illinois 61801, United States*; orcid.org/0000-0003-0769-524X

Aleksei Aksimentiev − *Department of Physics, University of Illinois at Urbana−Champaign, Urbana, Illinois 61801, United States*; orcid.org/0000-0002-6042-8442

Complete contact information is available at: https://pubs.acs.org/10.1021/acsnano.0c10259

Notes

The authors declare no competing financial interest.

ACKNOWLEDGMENTS

We thank Mario Raab for help with the wide-field setup and Florian Steiner for modification of the analysis software. H.J. and A.A. acknowledge support from the National Science Foundation (DMR-1827346). Computer time was provided through the Extreme Science and Engineering Discovery Environment (XSEDE) allocation MCA05S028 and the Leadership Resource Allocation MCB20012 on Frontera at Texas Advanced Computing Center. G.P.A. acknowledges support from the Swiss National Science Foundation (200021_184687) and from the ITN SuperCol funded by the European Union's Horizon 2020 research and innovation program under the Marie Skłodowska-Curie grant agreement 860914. P.T. acknowledges financial support by the BMBF (SIBOF, 03VP03891). This work was funded by the Deutsche Forschungsgemeinschaft (DFG, German Research Foundation) under German Excellence Strategy, EXC 2089/1-390776260 and INST 86/1904-1 FUGG, TI 329/9-2. F.D.S. is thankful for the financial support by CONICET, ANPCYT projects PICT2013-0792 and PICT-2014-0739, the Max-Planck-Society, and the Alexander von Humboldt Foundation.

REFERENCES

(1) Rothemund, P. W. K. Folding DNA to Create Nanoscale Shapes and Patterns. *Nature* **2006**, *440*, 297−302.
(2) Pilo-Pais, M.; Acuna, G. P.; Tinnefeld, P.; Liedl, T. Sculpting Light by Arranging Optical Components with DNA Nanostructures. *MRS Bull.* **2017**, *42* (12), 936−942.
(3) Kuzyk, A.; Jungmann, R.; Acuna, G. P.; Liu, N. DNA Origami Route for Nanophotonics. *ACS Photonics* **2018**, *5* (4), 1151−1163.
(4) Liu, N.; Liedl, T. DNA-Assembled Advanced Plasmonic Architectures. *Chem. Rev.* **2018**, *118* (6), 3032−3053.
(5) Hentschel, M.; Schäferling, M.; Duan, X.; Giessen, H.; Liu, N. Chiral Plasmonics. *Science Advances.* **2017**, *3* (5), 1−12.
(6) Neubrech, F.; Hentschel, M.; Liu, N. Reconfigurable Plasmonic Chirality: Fundamentals and Applications. *Adv. Mater.* **2020**, *32* (41), 1905640.
(7) Kuzyk, A.; Schreiber, R.; Fan, Z.; Pardatscher, G.; Roller, E. M.; Högele, A.; Simmel, F. C.; Govorov, A. O.; Liedl, T. DNA-Based Self-Assembly of Chiral Plasmonic Nanostructures with Tailored Optical Response. *Nature* **2012**, *483* (7389), 311−314.
(8) Kuzyk, A.; Schreiber, R.; Zhang, H.; Govorov, A. O.; Liedl, T.; Liu, N. Reconfigurable 3D Plasmonic Metamolecules. *Nat. Mater.* **2014**, *13* (9), 862−866.
(9) Huang, Y.; Nguyen, M.-K.; Natarajan, A. K.; Nguyen, V. H.; Kuzyk, A. A DNA Origami-Based Chiral Plasmonic Sensing Device. *ACS Appl. Mater. Interfaces* **2018**, *10* (51), 44221−44225.
(10) Stein, I. H.; Steinhauer, C.; Tinnefeld, P. Single-Molecule Four-Color FRET Visualizes Energy-Transfer Paths on DNA Origami. *J. Am. Chem. Soc.* **2011**, *133* (12), 4193−4195.
(11) Nicoli, F.; Barth, A.; Bae, W.; Neukirchinger, F.; Crevenna, A. H.; Lamb, D. C.; Liedl, T. Directional Photonic Wire Mediated by Homo-Förster Resonance Energy Transfer on a DNA Origami Platform. *ACS Nano* **2017**, *11*, 11264−11272.
(12) Olejko, L.; Bald, I. FRET Efficiency and Antenna Effect in Multi-Color DNA Origami-Based Light Harvesting Systems. *RSC Adv.* **2017**, *7* (39), 23924−23934.
(13) Dutta, P. K.; Varghese, R.; Nangreave, J.; Lin, S.; Yan, H.; Liu, Y. DNA-Directed Artificial Light-Harvesting Antenna. *J. Am. Chem. Soc.* **2011**, *133*, 11985−11993.
(14) Selnihhin, D.; Sparvath, S. M.; Preus, S.; Birkedal, V.; Andersen, E. S. Multifluorophore DNA Origami Beacon as a Biosensing Platform. *ACS Nano* **2018**, *12*, 5699−5708.
(15) Andersen, E. S.; Dong, M.; Nielsen, M. M.; Jahn, K.; Subramani, R.; Mamdouh, W.; Golas, M. M.; Sander, B.; Stark, H.; Oliveira, C. L. P.; Pedersen, J. S.; Birkedal, V.; Besenbacher, F.; Gothelf, K. V.; Kjems, J. Self-Assembly of a Nanoscale DNA Box with a Controllable Lid. *Nature* **2009**, *459*, 73−76.
(16) Kaminska, I.; Bohlen, J.; Mackowski, S.; Tinnefeld, P.; Acuna, G. P. Strong Plasmonic Enhancement of a Single Peridinin−Chlorophyll a − Protein Complex on DNA Origami-Based Optical Antennas. *ACS Nano* **2018**, *12* (2), 1650−1655.
(17) Kaminska, I.; Vietz, C.; Cuartero-González, Á.; Tinnefeld, P.; Fernández-Domínguez, A. I.; Acuna, G. P. Strong Plasmonic Enhancement of Single Molecule Photostability in Silver Dimer Optical Antennas. *Nanophotonics* **2018**, *7* (3), 643−649.
(18) Vietz, C.; Kaminska, I.; Sanz Paz, M.; Tinnefeld, P.; Acuna, G. P. Broadband Fluorescence Enhancement with Self-Assembled Silver Nanoparticle Optical Antennas. *ACS Nano* **2017**, *11* (5), 4969−4975.
(19) Prinz, J.; Heck, C.; Ellerik, L.; Merk, V.; Bald, I. DNA Origami Based Au−Ag-Core−Shell Nanoparticle Dimers with Single-Molecule SERS Sensitivity. *Nanoscale* **2016**, *8* (10), 5612−5620.
(20) Simoncelli, S.; Roller, E.-M.; Urban, P.; Schreiber, R.; Turberfield, A. J.; Liedl, T.; Lohmüller, T. Quantitative Single-Molecule Surface-Enhanced Raman Scattering by Optothermal Tuning of DNA Origami-Assembled Plasmonic Nanoantennas. *ACS Nano* **2016**, *10* (11), 9809−9815.
(21) Thacker, V. V.; Herrmann, L. O.; Sigle, D. O.; Zhang, T.; Liedl, T.; Baumberg, J. J.; Keyser, U. F. DNA Origami Based Assembly of Gold Nanoparticle Dimers for Surface-Enhanced Raman Scattering. *Nat. Commun.* **2014**, *5*, 3448.

(22) Kühler, P.; Roller, E. M.; Schreiber, R.; Liedl, T.; Lohmüller, T.; Feldmann, J. Plasmonic DNA-Origami Nanoantennas for Surface-Enhanced Raman Spectroscopy. *Nano Lett.* **2014**, *14* (5), 2914−2919.
(23) Bohlen, J.; Cuartero-González, Á.; Pibiri, E.; Ruhlandt, D.; Fernández-Domínguez, A. I.; Tinnefeld, P.; Acuna, G. P. Plasmon-Assisted Förster Resonance Energy Transfer at the Single-Molecule Level in the Moderate Quenching Regime. *Nanoscale* **2019**, *11* (16), 7674−7681.
(24) Aissaoui, N.; Moth-Poulsen, K.; Käll, M.; Johansson, P.; Wilhelmsson, L. M.; Albinsson, B. FRET Enhancement Close to Gold Nanoparticles Positioned in DNA Origami Constructs. *Nanoscale* **2017**, *9* (2), 673−683.
(25) Ojambati, O. S.; Chikkaraddy, R.; Deacon, W. D.; Horton, M.; Kos, D.; Turek, V. A.; Keyser, U. F.; Baumberg, J. J. Quantum Electrodynamics at Room Temperature Coupling a Single Vibrating Molecule with a Plasmonic Nanocavity. *Nat. Commun.* **2019**, *10* (1), 1049.
(26) Roller, E.-M.; Argyropoulos, C.; Högele, A.; Liedl, T.; Pilo-Pais, M. Plasmon−Exciton Coupling Using DNA Templates. *Nano Lett.* **2016**, *16*, 5962−5966.
(27) Hübner, K.; Pilo-Pais, M.; Selbach, F.; Liedl, T.; Tinnefeld, P.; Stefani, F. D.; Acuna, G. P. Directing Single-Molecule Emission with DNA Origami-Assembled Optical Antennas. *Nano Lett.* **2019**, *19* (9), 6629−6634.
(28) Raab, M.; Vietz, C.; Stefani, F. D.; Acuna, G. P.; Tinnefeld, P. Shifting Molecular Localization by Plasmonic Coupling in a Single-Molecule Mirage. *Nat. Commun.* **2017**, *8* (1), 13966.
(29) Curto, A. G.; Volpe, G.; Taminiau, T. H.; Kreuzer, M. P.; Quidant, R.; Van Hulst, N. F. Unidirectional Emission of a Quantum Dot Coupled to a Nanoantenna. *Science* **2010**, *329* (5994), 930−933.
(30) Pakizeh, T.; Käll, M. Unidirectional Ultracompact Optical Nanoantennas. *Nano Lett.* **2009**, *9*, 2343−2349.
(31) Lakowicz, J. R. *Principles of Fluorescence Spectroscopy*, 3rd ed.; Springer US: Baltimore, 2006; pp 443−475.
(32) Anger, P.; Bharadwaj, P.; Novotny, L. Enhancement and Quenching of Single-Molecule Fluorescence. *Phys. Rev. Lett.* **2006**, *96* (11), 113002.
(33) Blanco, L. A.; García de Abajo, F. J. Spontaneous Emission Enhancement near Nanoparticles. *J. Quant. Spectrosc. Radiat. Transfer* **2004**, *89*, 37−40.
(34) Rogobete, L.; Kaminski, F.; Agio, M.; Sandoghdar, V. Design of Plasmonic Nanoantennae for Enhancing Spontaneous Emission. *Opt. Lett.* **2007**, *32* (12), 1623−1625.
(35) Mock, J. J.; Hill, R. T.; Degiron, A.; Zauscher, S.; Chilkoti, A.; Smith, D. R. Distance-Dependent Plasmon Resonant Coupling between a Gold Nanoparticle and Gold Film. *Nano Lett.* **2008**, *8* (8), 2245−2252.
(36) Pal, S.; Deng, Z.; Wang, H.; Zou, S.; Liu, Y.; Yan, H. DNA Directed Self-Assembly of Anisotropic Plasmonic Nanostructures. *J. Am. Chem. Soc.* **2011**, *133* (44), 17606−17609.
(37) Zhan, P.; Wen, T.; Wang, Z.; He, Y.; Shi, J.; Wang, T.; Liu, X.; Lu, G.; Ding, B. DNA Origami Directed Assembly of Gold Bowtie Nanoantennas for Single-Molecule Surface-Enhanced Raman Scattering. *Angew. Chem., Int. Ed.* **2018**, *57* (11), 2846−2850.
(38) Ihmels, H.; Otto, D. Intercalation of Organic Dye Molecules into Double-Stranded DNA - General Principles and Recent Developments. *Top. Curr. Chem.* **2005**, *258*, 161−204.
(39) Gopinath, A.; Thachuk, C.; Mitskovets, A.; Atwater, H. A.; Kirkpatrick, D.; Rothemund, P. W. K. Absolute and Arbitrary Orientation of Single Molecule Shapes. *Science* **2021**, *371* (6531), eabd6179.
(40) Boulais, É.; Sawaya, N. P. D.; Veneziano, R.; Andreoni, A.; Banal, J. L.; Kondo, T.; Mandal, S.; Lin, S.; Schlau-Cohen, G. S.; Woodbury, N. W.; Yan, H.; Aspuru-Guzik, A.; Bathe, M. Programmed Coherent Coupling in a Synthetic DNA-Based Excitonic Circuit. *Nat. Mater.* **2018**, *17* (2), 159−166.
(41) Loretan, M.; Domljanovic, I.; Lakatos, M.; Rüegg, C.; Acuna, G. P. DNA Origami as Emerging Technology for the Engineering of Fluorescent and Plasmonic-Based Biosensors. *Materials* **2020**, *13* (9), 2185.
(42) Norman, D. G.; Grainger, R. J.; Uhrín, D.; Lilley, D. M. J. Location of Cyanine-3 on Double-Stranded DNA: Importance for Fluorescence Resonance Energy Transfer Studies. *Biochemistry* **2000**, *39* (21), 6317−6324.
(43) Iqbal, A.; Arslan, S.; Okumus, B.; Wilson, T. J.; Giraud, G.; Norman, D. G.; Ha, T.; Lilley, D. M. J. Orientation Dependence in Fluorescent Energy Transfer between Cy3 and Cy5 Terminally Attached to Double-Stranded Nucleic Acids. *Proc. Natl. Acad. Sci. U. S. A.* **2008**, *105* (32), 11176−11181.
(44) Ranjit, S.; Gurunathan, K.; Levitus, M. Photophysics of Backbone Fluorescent DNA Modifications: Reducing Uncertainties in FRET. *J. Phys. Chem. B* **2009**, *113* (22), 7861−7866.
(45) Cunningham, P. D.; Khachatrian, A.; Buckhout-White, S.; Deschamps, J. R.; Goldman, E. R.; Medintz, I. L.; Melinger, J. S. Resonance Energy Transfer in DNA Duplexes Labeled with Localized Dyes. *J. Phys. Chem. B* **2014**, *118* (59), 14555−14565.
(46) Ouellet, J.; Schorr, S.; Iqbal, A.; Wilson, T. J.; Lilley, D. M. J. Orientation of Cyanine Fluorophores Terminally Attached to DNA *via* Long, Flexible Tethers. *Biophys. J.* **2011**, *101* (5), 1148−1154.
(47) Mortensen, K. I.; Sung, J.; Flyvbjerg, H.; Spudich, J. A. Optimized Measurements of Separations and Angles between Intra-Molecular Fluorescent Markers. *Nat. Commun.* **2015**, *6* (1), 8621.
(48) Backer, A. S.; Lee, M. Y.; Moerner, W. E. Enhanced DNA Imaging Using Super-Resolution Microscopy and Simultaneous Single-Molecule Orientation Measurements. *Optica* **2016**, *3* (6), 659.
(49) Monneret, S.; Bertaux, N.; Savatier, J.; Shaban, H. A.; Mavrakis, M.; Valades Cruz, C. A.; Kress, A.; Brasselet, S. Quantitative Nanoscale Imaging of Orientational Order in Biological Filaments by Polarized Superresolution Microscopy. *Proc. Natl. Acad. Sci. U. S. A.* **2016**, *113* (7), E820−E828.
(50) Jungmann, R.; Steinhauer, C.; Scheible, M.; Kuzyk, A.; Tinnefeld, P.; Simmel, F. C. Single-Molecule Kinetics and Super-Resolution Microscopy by Fluorescence Imaging of Transient Binding on DNA Origami. *Nano Lett.* **2010**, *10* (11), 4756−4761.
(51) Vandenberk, N.; Barth, A.; Borrenberghs, D.; Hofkens, J.; Hendrix, J. Evaluation of Blue and Far-Red Dye Pairs in Single-Molecule Förster Resonance Energy Transfer Experiments. *J. Phys. Chem. B* **2018**, *122* (15), 4249−4266.
(52) Kalinin, S.; Sisamakis, E.; Magennis, S. W.; Felekyan, S.; Seidel, C. A. M. On the Origin of Broadening of Single-Molecule FRET Efficiency Distributions beyond Shot Noise Limits. *J. Phys. Chem. B* **2010**, *114* (18), 6197−6206.
(53) Wu, N.; Czajkowsky, D. M.; Zhang, J.; Qu, J.; Ye, M.; Zeng, D.; Zhou, X.; Hu, J.; Shao, Z.; Li, B.; Fan, C. Molecular Threading and Tunable Molecular Recognition on DNA Origami Nanostructures. *J. Am. Chem. Soc.* **2013**, *135* (33), 12172−12175.
(54) Jungmann, R.; Avendaño, M. S.; Woehrstein, J. B.; Dai, M.; Shih, W. M.; Yin, P. Multiplexed 3D Cellular Super-Resolution Imaging with DNA-PAINT and Exchange-PAINT. *Nat. Methods* **2014**, *11* (3), 313−318.
(55) Böhmer, M.; Enderlein, J. Orientation Imaging of Single Molecules by Wide-Field Epifluorescence Microscopy. *J. Opt. Soc. Am. B* **2003**, *20* (3), 554−559.
(56) Koenderink, A. F. Single-Photon Nanoantennas. *ACS Photonics* **2017**, *4* (4), 710−722.
(57) Douglas, S. M.; Marblestone, A. H.; Teerapittayanon, S.; Vazquez, A.; Church, G. M.; Shih, W. M. Rapid Prototyping of 3D DNA-Origami Shapes with CaDNAno. *Nucleic Acids Res.* **2009**, *37* (15), 5001−5006.
(58) Vogelsang, J.; Kasper, R.; Steinhauer, C.; Person, B.; Heilemann, M.; Sauer, M.; Tinnefeld, P. A Reducing and Oxidizing System Minimizes Photobleaching and Blinking of Fluorescent Dyes. *Angew. Chem., Int. Ed.* **2008**, *47* (29), 5465−5469.
(59) Cordes, T.; Vogelsang, J.; Tinnefeld, P. On the Mechanism of Trolox as Antiblinking and Antibleaching Reagent. *J. Am. Chem. Soc.* **2009**, *131* (14), 5018−5019.

(60) Edelstein, A.; Amodaj, N.; Hoover, K.; Vale, R.; Stuurman, N. Computer Control of Microscopes Using Manager. *Current Protocols in Molecular Biology.* **2010**, *92*, 14.20.1−14.20.17.
(61) Phillips, J. C.; Hardy, D. J.; Maia, J. D. C.; Stone, J. E.; Ribeiro, J. V.; Bernardi, R. C.; Buch, R.; Fiorin, G.; Hénin, J.; Jiang, W.; McGreevy, R.; Melo, M. C. R.; Radak, B. K.; Skeel, R. D.; Singharoy, A.; Wang, Y.; Roux, B.; Aksimentiev, A.; Luthey-Schulten, Z.; Kale, L. V.; et al. Scalable Molecular Dynamics on CPU and GPU Architectures with NAMD. *J. Chem. Phys.* **2020**, *153*, 044130−1−33.
(62) Batcho, P. F.; Case, D. A.; Schlick, T. Optimized Particle-Mesh Ewald/Multiple-Time Step Integration for Molecular Dynamics Simulations. *J. Chem. Phys.* **2001**, *115* (9), 4003−4018.
(63) Feller, S. E.; Zhang, Y.; Pastor, R. W.; Brooks, B. R. Constant Pressure Molecular Dynamics Simulation: The Langevin Piston Method. *J. Chem. Phys.* **1995**, *103*, 4613−4621.
(64) Miyamoto, S.; Kollman, P. A. Settle: An Analytical Version of the SHAKE and RATTLE Algorithm for Rigid Water Models. *J. Comput. Chem.* **1992**, *13* (8), 952−962.
(65) Andersen, H. C. Rattle: A "Velocity" Version of the Shake Algorithm for Molecular Dynamics Calculations. *J. Comput. Phys.* **1983**, *52*, 24−34.
(66) Hart, K.; Foloppe, N.; Baker, C. M.; Denning, E. J.; Nilsson, L.; MacKerell, A. D. Optimization of the CHARMM Additive Force Field for DNA: Improved Treatment of the BI/BII Conformational Equilibrium. *J. Chem. Theory Comput.* **2012**, *8* (1), 348−362.
(67) Vanommeslaeghe, K.; MacKerell, A. D. Automation of the CHARMM General Force Field (CGenFF) I: Bond Perception and Atom Typing. *J. Chem. Inf. Model.* **2012**, *52* (12), 3144−3154.
(68) Yoo, J.; Aksimentiev, A. Improved Parametrization of Li + , Na + , K + , and Mg 2+ Ions for All-Atom Molecular Dynamics Simulations of Nucleic Acid Systems. *J. Phys. Chem. Lett.* **2012**, *3* (1), 45−50.
(69) Humphrey, W.; Dalke, A.; Schulten, K. VMD: Visual Molecular Dynamics. *J. Mol. Graphics* **1996**, *14* (1), 33−38.
(70) Case, D. A.; Babin, V.; Berryman, J.; Betz, R. M.; Cai, Q.; Cerutti, D. S.; Cheatham, III, T. E.; Darden, T. A.; Duke, R. E.; Gohlke, H.; Goetz, A. W.; Gusarov, S.; Homeyer, N.; Janowski, P.; Kaus, J.; Kolossvary, I.; Kovalenko, A.; Lee, T. S.; LeGrand, S.; Luchko, T.; et al. *Manual AMBER 14*; University of California: San Francisco, 2014.
(71) Yoo, J.; Aksimentiev, A. *In Situ* Structure and Dynamics of DNA Origami Determined through Molecular Dynamics Simulations. *Proc. Natl. Acad. Sci. U. S. A.* **2013**, *110* (50), 20099−20104.
(72) Jorgensen, W. L.; Chandrasekhar, J.; Madura, J. D.; Impey, R. W.; Klein, M. L. Comparison of Simple Potential Functions for Simulating Liquid Water. *J. Chem. Phys.* **1983**, *79*, 926−935.

https://dx.doi.org/10.1021/acsnano.0c10259
ACS Nano 2021, 15, 5109−5117

Supporting Information

Determining The In-Plane Orientation and Binding Mode of Single Fluorescent Dyes in DNA Origami Structures

Kristina Hübner[1], Himanshu Joshi[2], Aleksei Aksimentiev[2], Fernando D. Stefani[3,4]*

Philip Tinnefeld[1] and Guillermo P. Acuna[5*]*

[1] Department of Chemistry and Center for NanoScience, Ludwig-Maximilians-Universität München, Butenandtstr. 5-13 Haus E, 81377 München, Germany

[2] Department of Physics, University of Illinois at Urbana−Champaign, Urbana, Illinois 61801, United States

[3] Centro de Investigaciones en Bionanociencias (CIBION), Consejo Nacional de Investigaciones Científicas y Técnicas (CONICET), Godoy Cruz 2390, C1425FQD Ciudad Autónoma de Buenos Aires, Argentina

[4] Departamento de Física, Facultad de Ciencias Exactas y Naturales, Universidad de Buenos Aires, Güiraldes 2620, C1428EHA Ciudad Autónoma de Buenos Aires, Argentina

[5] Department of Physics, University of Fribourg, Chemin du Musée 3, Fribourg CH-1700, Switzerland

1. Linking chemistry of ATTO 647N to DNA

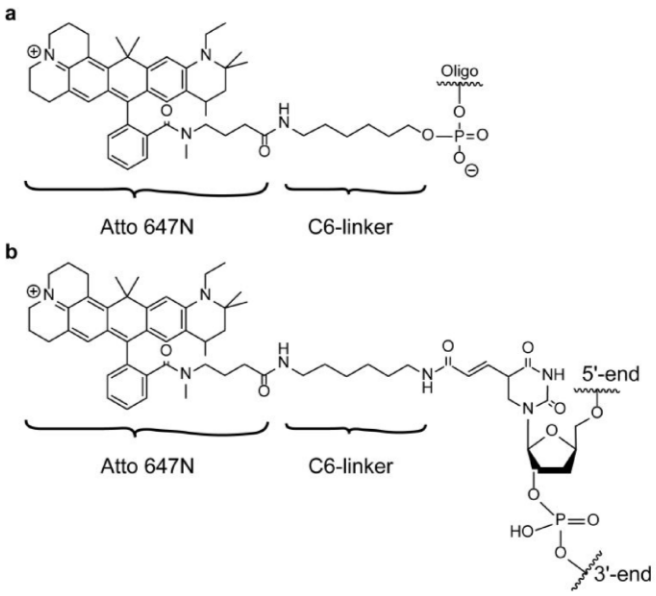

Figure S1: ATTO 647N linked through a C6 linker to DNA, at the 3´-end (a) or internally via a thymine (b).

2. Modulation Data

Table S1: Number of traces that meet the condition of a modulation threshold of M >0.15 for each studied sample with the probed fluorophores.

structure	fluorophore	modulating fraction ($M > 0.15$)
sample 1	ATTO 647N	95 % (out of 301)
	ATTO 643	93 % (out of 72)
	Cy5	95 % (out of 151)
sample 2	ATTO 647N	61 % (out of 303)
	ATTO 643	20 % (out of 319)
	Cy5	88 % (out of 162)
sample 3	ATTO 647N	73 % (out of 224)

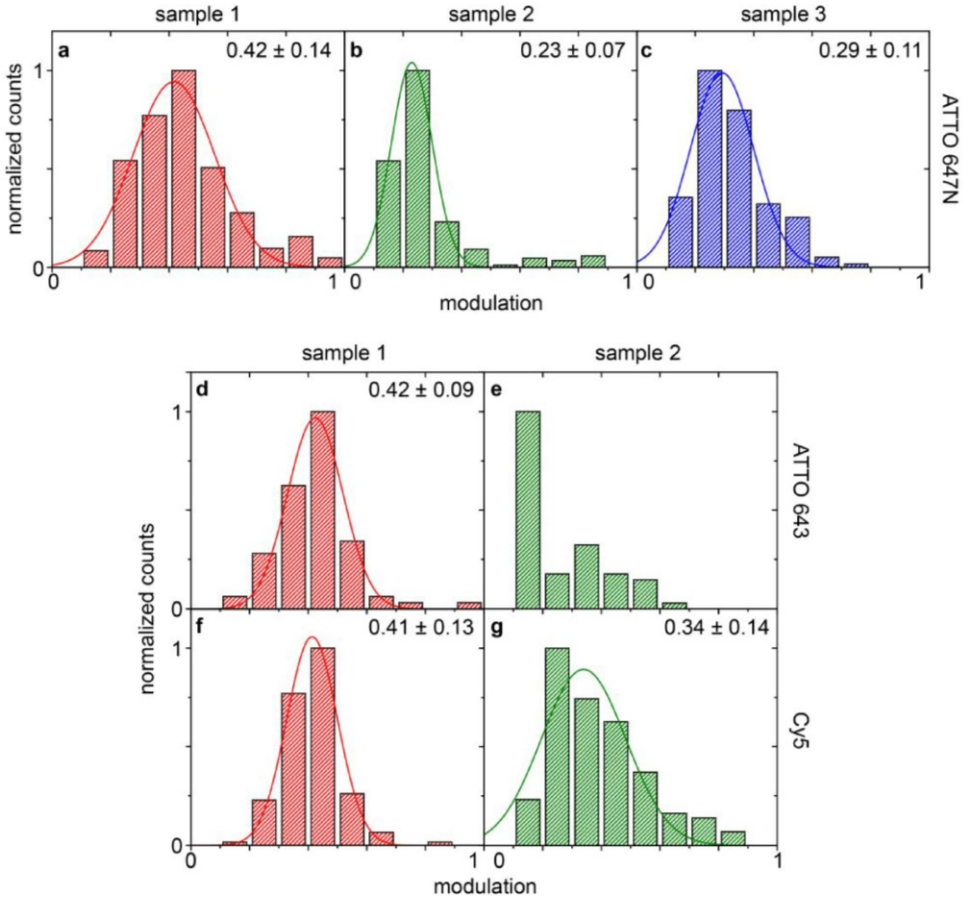

Figure S2: Modulation distributions with standard deviation of the three measured samples with the ATTO 647N dye (a-c). Modulation data for sample 1 and 2 with the dyes ATTO 643 (d-e) and Cy5 (f-g).

3. DNA-PAINT Data

Due to the design of the DNA origami rectangle an upside down binding of the structure to the functionalized surface is possible. The chiral DNA-PAINT pattern on the DNA origami structure enables to distinguish flipped from non-flipped structures. Figure S 3a shows a schematic of the chiral DNA-PAINT pattern and figure S 3b shows an image with the two different binding possibilities, facing with the top up (orange square) or down (green square).

Furthermore, we can make a distance analysis of the measured DNA origami structures showing that the measured distances (figure S 3c) fit well to the designed distances. For this kind of analysis the super resolution data were first processed with the open source software Picasso[1]. The localization files were exported for further analysis with self-written Labview software.

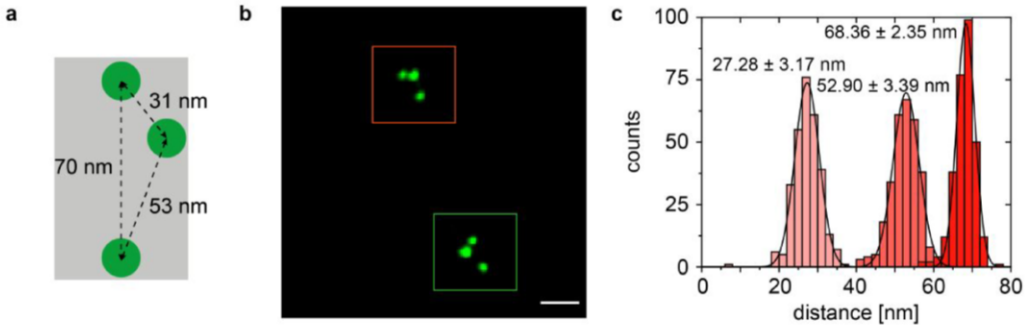

Figure S3: DNA-PAINT super resolution sample design and data. Showing a schematic of the asymmetric DNA-PAINT pattern (a) and super-resolved images of the DNA-PAINT measurements (b, scale bar 100 nm), where structures lying with the top up (orange square) or down (green square) can be distinguished. A histogram (c) is showing the measured distances for the asymmetric pattern for 297 molecules.

4. ATTO 647N dye orientation of flipped and non-flipped DNA origami structures

If both populations, non-flipped and flipped origami structures distinguished by the super resolved images in figure S3, are plotted separately the histograms draw similar distributions. This indicates that the orientation of the DNA origami structure on the surface does not has an influence on the ATTO 647N dye sticking to the DNA. The histograms are plotted in figure S 4 and fitted with Gaussian distribution functions to extract the mean orientation with their standard deviations.

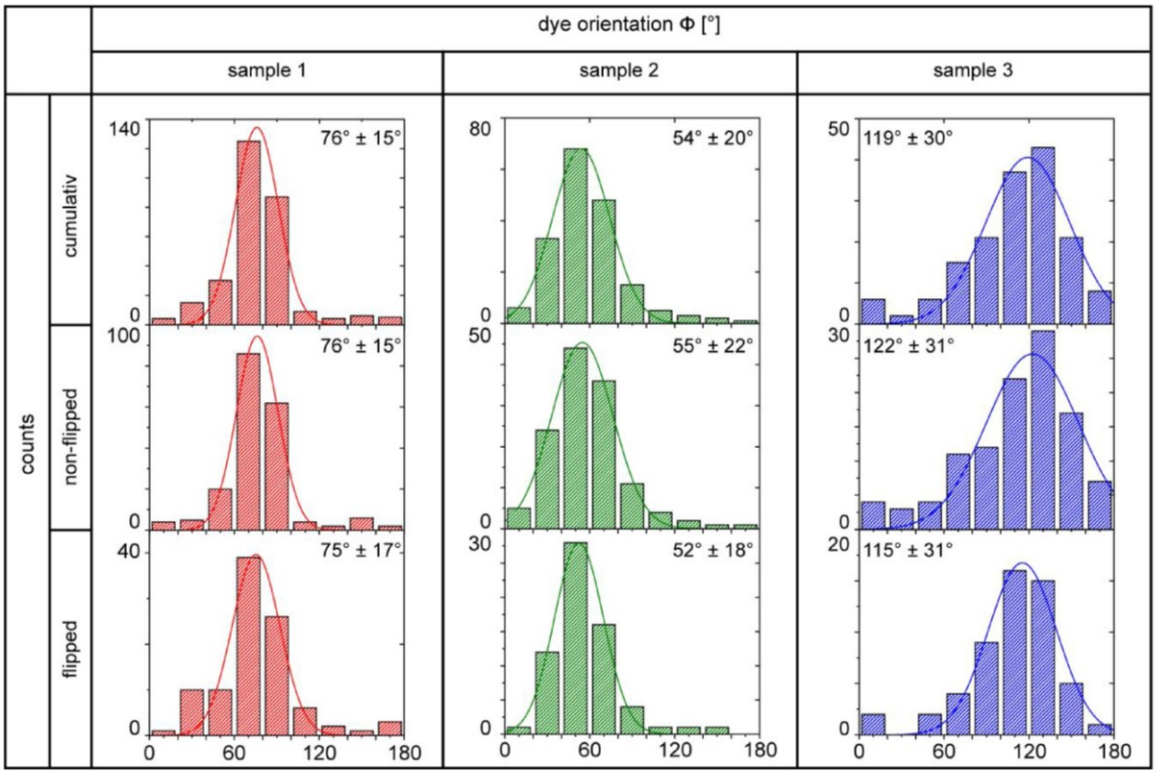

Figure S4: ATTO 647N dye orientation distributions with standard deviations of the three samples. Separated Histograms of non-flipped and flipped samples show the same distributions as the combined histograms in the first row.

5. All-atom molecular dynamics simulations

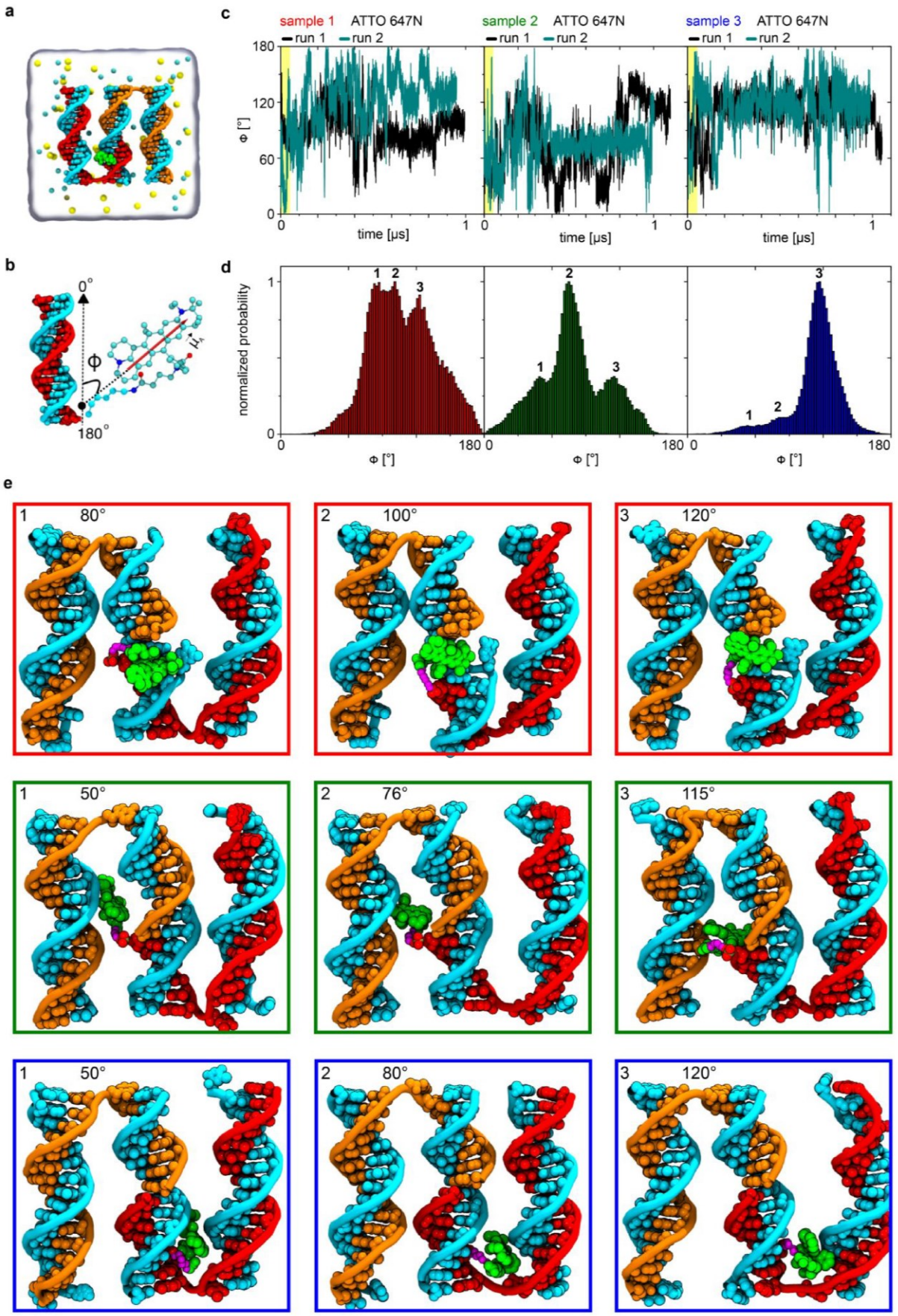
a
b
0°
ϕ
180°
μ_x
c
sample 1 ATTO 647N
sample 2 ATTO 647N
sample 3 ATTO 647N
run 1
run 2
Φ [°]
time [µs]
d
normalized probability
Φ [°]
e
1 80°
2 100°
3 120°
1 50°
2 76°
3 115°
1 50°
2 80°
3 120°

Figure S5: (a) A representative snapshot of the fully assembled all-atom model of the ATTO 647N dye-conjugated DNA system. The template strand of the DNA origami structure is shown in cyan, the staple strand carrying the dye molecule is shown in red and the other staple strand is shown in orange. The atoms of the dye molecule are shown using green spheres whereas the atoms of the C6 anchor between the dye and the DNA are shown using magenta spheres. Sodium, potassium and chloride ions are shown using yellow, tan and light cyan spheres, respectively. The volume occupied by water molecules is represented by a semi-transparent white surface. (b) Schematics illustrating the definition of the angle (ϕ) between the helical axis of the DNA and the dipole moment of the ATTO 647N dye molecule. (c) The angle between the helical axis of the DNA and the dye molecule's dipole as a function of simulation time for sample 1, 2, and 3. The first 50 ns of each trace (yellow rectangle) were excluded from the histogram analysis. (d). Histograms of the ϕ angles observed in the MD simulations of samples 1-3 with the preferred orientations marked (1-3). (e) Microscopic configurations of the simulation systems corresponding to the preferred orientations of the dye labelled 1-3 in panel d. Red, green and blue boundary box indicates microscopic configurations extracted from the MD trajectories of sample 1, 2, and 3, respectively.

In addition to the simulations of the ATTO 647N dye-conjugated DNA system described in the main text and Figure S5, four 1 μs-long equilibrium all-atom molecular dynamics simulations were performed to study the orientation of a Cy5 dye conjugated to DNA in sample 1 and 2 geometries, two independent simulations for each sample. Supplementary movie S4 and S5 illustrate the simulation trajectories. During the simulations, the Cy5 dyes were observed to sample a wide range of orientations with respect to the DNA axis (Figure S6 a, b). For sample 1, where the next two DNA bases after the attached dye were missing, the Cy5 dye was frequently observed to engage in base stacking interactions with the unpaired nucleotides. For sample 2, where all bases ware paired, the Cy5 dye was observed to transiently bind to minor and major groves of its parent and neighboring DNA helices. The helical structure of the DNA near the dye attachment point was better preserved in sample 2 than in sample 1. Unfortunately, the simulation trajectories were too short to sample Cy5 orientations with enough statistics to make quantitative conclusions about the preferred orientation of the dye.

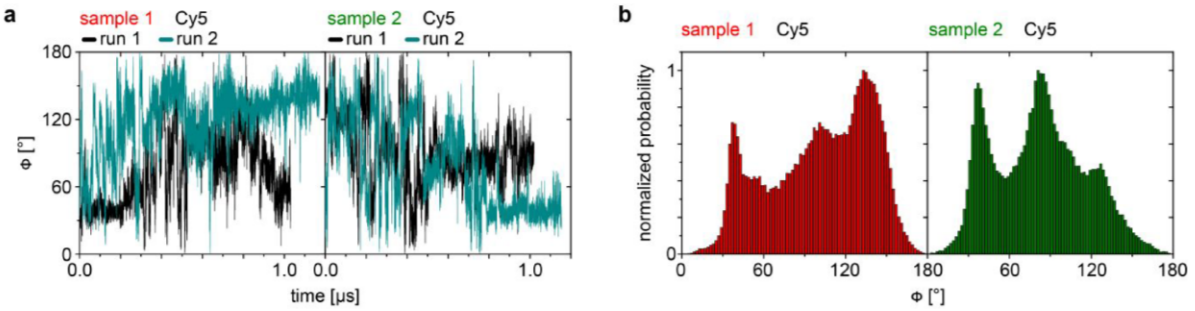

Figure S6: (a) Angle between the helical axis of DNA and the Cy5 molecule's dipole as a function of simulation time for sample 1 and 2. Two independent simulations were performed for each sample. (b) Histograms of the angle distribution for sample 1 and sample 2 simulations. The first 50 ns of each simulation (yellow region in panel a) were excluded from the histogram analysis.

6. Supplementary movies

Supplementary movies S1, S2 and S3 show a 1 μs long MD simulation trajectories of the ATTO 647N dye-conjugated DNA systems corresponding to sample 1, 2 and 3, respectively. Supplementary movies S4 and S5 shows the 1 μs long MD simulation trajectories of the Cy5 dye-conjugated DNA systems corresponding to sample 1 and 2, respectively. The scaffold strand of the DNA origami structure is shown in cyan, the staple strand carrying the dye molecule is shown in red and the other staple strand is shown in orange. The atoms of the dye molecule are shown using green spheres whereas the atoms of C6 molecules (anchor between the dye and DNA) are shown using magenta spheres. Water and counter ions are not shown for clarity.

7. DNA origami ssDNA strands

Table 1: Unmodified ssDNA strands

Sequence (5‘-> 3‘)	Number
AGTATAAAGTTCAGCTAATGCAGATGTCTTTC	1
AATACTGCCCAAAAGGAATTACGTGGCTCA	2
ATCCCAATGAGAATTAACTGAACAGTTACCAG	3
TGGAACAACCGCCTGGCCCTGAGGCCCGCT	4
GAGGGTAGGATTCAAAAGGGTGAGACATCCAA	5
TTTCGGAAGTGCCGTCGAGAGGGTGAGTTTCG	6
CTACCATAGTTTGAGTAACATTTAAAATAT	7
GCCTCCCTCAGAATGGAAAGCGCAGTAACAGT	8
AGAAAACAAAGAAGATGATGAAACAGGCTGCG	9
AAAGCACTAAATCGGAACCCTAATCCAGTT	10
AATTGAGAATTCTGTCCAGACGACTAAACCAA	11
TAGGTAAACTATTTTTGAGAGATCAAACGTTA	12
AGGCAAAGGGAAGGGCGATCGGCAATTCCA	13
CATTTGAAGGCGAATTATTCATTTTTGTTTGG	14
ATACCCAACAGTATGTTAGCAAATTAGAGC	15
CTTTAGGGCCTGCAACAGTGCCAATACGTG	16
TGTAGCCATTAAAATTCGCATTAAATGCCGGA	17
CACCAGAAAGGTTGAGGCAGGTCATGAAAG	18
TTCCAGTCGTAATCATGGTCATAAAAGGGG	19
TCAAGTTTCATTAAAGGTGAATATAAAAGA	20
ACCCTTCTGACCTGAAAGCGTAAGACGCTGAG	21
GCGAAAAATCCCTTATAAATCAAGCCGGCG	22
TTATTACGAAGAACTGGCATGATTGCGAGAGG	23
AAAGGCCGGAGACAGCTAGCTGATAAATTAATTTTTGT	24
AAATCACCTTCCAGTAAGCGTCAGTAATAA	25
CATCAAGTAAAACGAACTAACGAGTTGAGA	26
TTAGGATTGGCTGAGACTCCTCAATAACCGAT	27
AGCGCGATGATAAATTGTGTCGTGACGAGA	28
TGACAACTCGCTGAGGCTTGCATTATACCA	29

Sequence (5‘-> 3‘)	Number
TAATCAGCGGATTGACCGTAATCGTAACCG	30
GATGTGCTTCAGGAAGATCGCACAATGTGA	31
ACCGATTGTCGGCATTTTCGGTCATAATCA	32
GCCCTTCAGAGTCCACTATTAAAGGGTGCCGT	33
GCGAACCTCCAAGAACGGGTATGACAATAA	34
CTTTTACAAAATCGTCGCTATTAGCGATAG	35
AAACAGCTTTTTGCGGGATCGTCAACACTAAA	36
AAATTAAGTTGACCATTAGATACTTTTGCG	37
TACCGAGCTCGAATTCGGGAAACCTGTCGTGCAGCTGATT	38
AAGGAAACATAAAGGTGGCAACATTATCACCG	39
CTTAGATTTAAGGCGTTAAATAAAGCCTGT	40
ACCTTGCTTGGTCAGTTGGCAAAGAGCGGA	41
TAAATGAATTTTCTGTATGGGATTAATTTCTT	42
ACAAACGGAAAAGCCCCAAAAACACTGGAGCA	43
ATTATACTAAGAAACCACCAGAAGTCAACAGT	44
CTCGTATTAGAAATTGCGTAGATACAGTAC	45
CAGAAGATTAGATAATACATTTGTCGACAA	46
ATTTTAAAATCAAAATTATTTGCACGGATTCG	47
TTTATCAGGACAGCATCGGAACGACACCAACCTAAAACGA	48
TTGACAGGCCACCACCAGAGCCGCGATTTGTA	49
CGTAAAACAGAAATAAAAATCCTTTGCCCGAAAGATTAGA	50
GTTTATCAATATGCGTTATACAAACCGACCGTGTGATAAA	51
CTGAGCAAAAATTAATTACATTTTGGGTTA	52
ATGCAGATACATAACGGGAATCGTCATAAATAAAGCAAAG	53
GTATAGCAAACAGTTAATGCCCAATCCTCA	54
ATATTCGGAACCATCGCCCACGCAGAGAAGGA	55
TTATACCACCAAATCAACGTAACGAACGAG	56
GCTATCAGAAATGCAATGCCTGAATTAGCA	57
TCACCGACGCACCGTAATCAGTAGCAGAACCG	58
ATTATCATTCAATATAATCCTGACAATTAC	59
TTGCTCCTTTCAAATATCGCGTTTGAGGGGGT	60
GCCAGTTAGAGGGTAATTGAGCGCTTTAAGAA	61

Sequence (5‘-> 3‘)	Number
CAGGAGGTGGGGTCAGTGCCTTGAGTCTCTGAATTTACCG	62
GAAATTATTGCCTTTAGCGTCAGACCGGAACC	63
AGGCTCCAGAGGCTTTGAGGACACGGGTAA	64
ATACATACCGAGGAAACGCAATAAGAAGCGCATTAGACGG	65
TTAATGAACTAGAGGATCCCCGGGGGGGTAACG	66
GCCATCAAGCTCATTTTTTAACCACAAATCCA	67
AAGTAAGCAGACACCACGGAATAATATTGACG	68
AGCCAGCAATTGAGGAAGGTTATCATCATTTT	69
ATTACCTTTGAATAAGGCTTGCCCAAATCCGC	70
CGAAAGACTTTGATAAGAGGTCATATTTCGCA	71
CGATAGCATTGAGCCATTTGGGAACGTAGAAA	72
TCACCAGTACAAACTACAACGCCTAGTACCAG	73
TTAAAGCCAGAGCCGCCACCCTCGACAGAA	74
TCATTCAGATGCGATTTTAAGAACAGGCATAG	75
CCAGGGTTGCCAGTTTGAGGGGACCCGTGGGA	76
ACAACATGCCAACGCTCAACAGTCTTCTGA	77
GTAATAAGTTAGGCAGAGGCATTTATGATATT	78
AGACGACAAAGAAGTTTTGCCATAATTCGAGCTTCAA	79
GATGGCTTATCAAAAAGATTAAGAGCGTCC	80
TAAATCAAAATAATTCGCGTCTCGGAAACC	81
TTAACGTCTAACATAAAAACAGGTAACGGA	82
AACGCAAAGATAGCCGAACAAACCCTGAAC	83
ACGGCTACAAAAGGAGCCTTTAATGTGAGAAT	84
ACACTCATCCATGTTACTTAGCCGAAAGCTGC	85
TTAACACCAGCACTAACAACTAATCGTTATTA	86
GCCGTCAAAAAACAGAGGTGAGGCCTATTAGT	87
ATCGCAAGTATGTAAATGCTGATGATAGGAAC	88
TAAATCATATAACCTGTTTAGCTAACCTTTAA	89
CATGTAATAGAATATAAAGTACCAAGCCGT	90
CCTGATTGCAATATATGTGAGTGATCAATAGT	91
CCTAAATCAAAATCATAGGTCTAAACAGTA	92
TGAAAGGAGCAAATGAAAAATCTAGAGATAGA	93

Sequence (5‘-> 3‘)	Number
GACCTGCTCTTTGACCCCCAGCGAGGGAGTTA	94
CCCGATTTAGAGCTTGACGGGGAAAAAGAATA	95
CATAAATCTTTGAATACCAAGTGTTAGAAC	96
GCGAGTAAAAATATTTAAATTGTTACAAAG	97
AATGGTCAACAGGCAAGGCAAAGAGTAATGTG	98
GACCAACTAATGCCACTACGAAGGGGGTAGCA	99
ACCTTTTTATTTTAGTTAATTTCATAGGGCTT	100
GCAAGGCCTCACCAGTAGCACCATGGGCTTGA	101
CAACTGTTGCGCCATTCGCCATTCAAACATCA	102
GACAAAAGGTAAAGTAATCGCCATATTTAACAAAACTTTT	103
AATACGTTTGAAAGAGGACAGACTGACCTT	104
CAGCGAAACTTGCTTTCGAGGTGTTGCTAA	105
TATAACTAACAAAGAACGCGAGAACGCCAA	106
ATCCCCCTATACCACATTCAACTAGAAAAATC	107
TATTAAGAAGCGGGGTTTTGCTCGTAGCAT	108
CCACCCTCTATTCACAAACAAATACCTGCCTA	109
TCAAATATAACCTCCGGCTTAGGTAACAATTT	110
GATGGTTTGAACGAGTAGTAAATTTACCATTA	111
TATATTTTGTCATTGCCTGAGAGTGGAAGATTGTATAAGC	112
AAAGTCACAAAATAAACAGCCAGCGTTTTA	123
GCGGATAACCTATTATTCTGAAACAGACGATT	124
CAGCAAAAGGAAACGTCACCAATGAGCCGC	125
TCATCGCCAACAAAGTACAACGGACGCCAGCA	126
CTTTTGCAGATAAAAACCAAAATAAAGACTCC	127
CACAACAGGTGCCTAATGAGTGCCCAGCAG	128
TGCATCTTTCCCAGTCACGACGGCCTGCAG	129
CGCGCAGATTACCTTTTTTAATGGGAGAGACT	130
TTTTATTTAAGCAAATCAGATATTTTTTGT	131
GAATTTATTTAATGGTTTGAAATATTCTTACC	132
AACACCAAATTTCAACTTTAATCGTTTACC	133
GCGCAGACAAGAGGCAAAAGAATCCCTCAG	134
GTACCGCAATTCTAAGAACGCGAGTATTATTT	135

Sequence (5‘-> 3‘)	Number
GCGGAACATCTGAATAATGGAAGGTACAAAAT	136
AGCAAGCGTAGGGTTGAGTGTTGTAGGGAGCC	137
GGCCTTGAAGAGCCACCACCCTCAGAAACCAT	138
TACGTTAAAGTAATCTTGACAAGAACCGAACT	139
AAGGCCGCTGATACCGATAGTTGCGACGTTAG	140
AATAGTAAACACTATCATAACCCTCATTGTGA	141
CGGATTGCAGAGCTTAATTGCTGAAACGAGTA	142
GATTTAGTCAATAAAGCCTCAGAGAACCCTCA	143
CTTATCATTCCCGACTTGCGGGAGCCTAATTT	144
AATAGCTATCAATAGAAAATTCAACATTCA	145
CTTTAATGCGCGAACTGATAGCCCCACCAG	146
AGAAAGGAACAACTAAAGGAATTCAAAAAAA	147
ACAACTTTCAACAGTTTCAGCGGATGTATCGG	148
GCACAGACAATATTTTTGAATGGGGTCAGTA	149
TTCTACTACGCGAGCTGAAAAGGTTACCGCGC	150
CAACCGTTTCAAATCACCATCAATTCGAGCCA	151
TCAATATCGAACCTCAAATATCAATTCCGAAA	152
TAAAAGGGACATTCTGGCCAACAAAGCATC	153
GTCGACTTCGGCCAACGCGCGGGGTTTTTC	154
GCCCGTATCCGGAATAGGTGTATCAGCCCAAT	155
AACGTGGCGAGAAAGGAAGGGAAACCAGTAA	156
GCAATTCACATATTCCTGATTATCAAAGTGTA	157
AAGCCTGGTACGAGCCGGAAGCATAGATGATG	158
CAAATCAAGTTTTTTGGGGTCGAAACGTGGA	159
CTCCAACGCAGTGAGACGGGCAACCAGCTGCA	160
AACGCAAAATCGATGAACGGTACCGGTTGA	161
CCAATAGCTCATCGTAGGAATCATGGCATCAA	162
CCACCCTCATTTTCAGGGATAGCAACCGTACT	163
AGGAACCCATGTACCGTAACACTTGATATAA	164
GTTTTAACTTAGTACCGCCACCCAGAGCCA	165
CCAACAGGAGCGAACCAGACCGGAGCCTTTAC	166
TTTTCACTCAAAGGGCGAAAAACCATCACC	167

Sequence (5‘-> 3‘)	Number
TCTAAAGTTTTGTCGTCTTTCCAGCCGACAA	168
TCGGCAAATCCTGTTTGATGGTGGACCCTCAA	169
TCCACAGACAGCCCTCATAGTTAGCGTAACGA	170
AGAGAGAAAAAAATGAAAATAGCAAGCAAACT	171
TAAGAGCAAATGTTTAGACTGGATAGGAAGCC	172

Table 2: Modified ssDNA strands.

Sequence (5‘ ->3‘)	Number
Biotin strands	
Biotin-TAGAGAGTTATTTTCATTTGGGGATAGTAGTAGCATTA	173
Biotin-GAAACGATAGAAGGCTTATCCGGTCTCATCGAGAACAAGC	174
Biotin-ATAAGGGAACCGGATATTCATTACGTCAGGACGTTGGGAA	175
Biotin-AGCCACCACTGTAGCGCGTTTTCAAGGGAGGGAAGGTAAA	176
Biotin-GAGAAGAGATAACCTTGCTTCTGTTCGGGAGAAACAATAA	177
Biotin-CGGATTCTGACGACAGTATCGGCCGCAAGGCGATTAAGTT	178
DNA-PAINT functionalized strands	
ACGCTAACACCCACAAGAATTGAAAATAGCTTAAATGCCCG	179
TTTAGGACAAATGCTTTAAACAATCAGGTCTTAAATGCCCG	180
TGTAGAAATCAAGATTAGTTGCTCTTACCATTAAATGCCCG	181
AACAGTTTTGTACCAAAAACATTTTATTTCTTAAATGCCCG	182
ATATTTTGGCTTTCATCAACATTATCCAGCCATTAAATGCCCG	183
GCCTTAAACCAATCAATAATCGGCACGCGCCTTTAAATGCCCG	184
GAGAGATAGAGCGTCTTTCCAGAGGTTTTGAATTAAATGCCCG	185
GCTTTCCGATTACGCCAGCTGGCGGCTGTTTCTTAAATGCCCG	186

Sequence (5‘ ->3‘)	**Number**
TCTTCGCTGCACCGCTTCTGGTGCGGCCTTCCTTAAATGCCCG	187
GCCCGAGAGTCCACGCTGGTTTGCAGCTAACTTTAAATGCCCG	188
TTTACCCCAACATGTTTTAAATTTCCATATTTAAATGCCCG	189
AACAAGAGGGATAAAAATTTTTAGCATAAAGCTTAAATGCCCG	190
CTGTAGCTTGACTATTATAGTCAGTTCATTGATTAAATGCCCG	191
CTGTGTGATTGCGTTGCGCTCACTAGAGTTGCTTAAATGCCCG	192
CACATTAAAATTGTTATCCGCTCATGCGGGCCTTAAATGCCCG	193
GTTTATTTTGTCACAATCTTACCGAAGCCCTTTAATATCATTAAATGCCCG	194

Table 3: Replaced ssDNA strands.

Sequence (5‘ ->3‘)	**Replaced Staple Number**
Strands for sample 1	
CGAAAGACTTTGATAAGAGGTCATATTTCG-ATTO 647N	71
Strands for sample 2	
CGAAAGACTTTGATAAGAGGTCATATTTCG- ATTO 647N	71
CAAATGGTCAACAGGCAAGGCAAAGAGTAATGTG	89
Strands for sample 3	
TAAGAGCAAATGTTTAGACTGGATAG-dT ATTO 647N-AAGCC	172

Imager strand*:* CGGGCAT-ATTO 542

References

(1) Schnitzbauer, J.; Strauss, M. T.; Schlichthaerle, T.; Schueder, F.; Jungmann, R. Super-Resolution Microscopy with DNA-PAINT. *Nature protocols* **2017**, *12*, 1198–1228.

A3 Associated Publication P3

Salt-Induced Conformational Switching of a Flat Rectangular DNA Origami Structure

by

Kristina Hübner, Mario Raab, Johann Bohlen, Julian Bauer, Philip Tinnefeld

Reproduced from Ref. [184] with permission from the Royal Society of Chemistry.

Nanoscale

ROYAL SOCIETY OF CHEMISTRY

PAPER

View Article Online
View Journal

Cite this: DOI: 10.1039/d1nr07793g

Salt-induced conformational switching of a flat rectangular DNA origami structure†

Kristina Hübner, Mario Raab, Johann Bohlen, Julian Bauer and Philip Tinnefeld*

A rectangular DNA origami structure is one of the most studied and often used motif for applications in DNA nanotechnology. Here, we present two assays to study structural changes in DNA nanostructures and reveal a reversible rolling-up of the rectangular DNA origami structure induced by bivalent cations such as magnesium or calcium. First, we applied one-color and two-color superresolution DNA-PAINT with protruding strands along the long edges of the DNA origami rectangle. At increasing salt concentration, a single line instead of two lines is observed as a first indicator of rolling-up. Two-color measurements also revealed different conformations with parallel and angled edges. Second, we placed a gold nanoparticle and a dye molecule at different positions on the DNA origami structure. Distance dependent fluorescence quenching by the nanoparticle reports on dynamic transitions as well as it provides evidence that the rolling-up occurs preferentially along the diagonal of the DNA origami rectangle. The results will be helpful to test DNA structural models and the assays presented will be useful to study further structural transitions in DNA nanotechnology.

Received 25th November 2021,
Accepted 1st May 2022

DOI: 10.1039/d1nr07793g

rsc.li/nanoscale

DNA origami structures have matured into a widely adopted technique for nanofabrication and for biophysical tools.[1–6] On the one hand, the DNA origami structure has been exploited as a modular platform to arrange other molecular or nanoscale entities such as chemical functionality, proteins, antigens or nanoparticles that obtain their functionality from the precise geometric and stoichiometric arrangement.[2,7–9] On the other hand, DNA origami structures exhibit flexibility that can describe the intrinsic mechanical stiffness of a DNA origami structure.[10,11] Mechanical flexibility can also be designed by creating flexible elements such as joints,[12–15] hinges,[16] catenanes/interlocked systems,[17] and could be transiently adapted using tools of dynamic DNA nanotechnology such as strand displacement reactions.[18] Generally, the dynamic flexibility of DNA origami structures is difficult to access as structural tools usually yield average values and dynamic, little invasive tools are required including optical[10,12–15] and mechanical single-molecule methods[19–21] as well as computational tools such as molecular dynamics simulations.[22]

The rectangular DNA origami structure of the original Rothemund publication[1] and its torsion-reduced variants such as the so-called new rectangular origami (NRO)[23] have emerged as model systems to interrogate the stiffness and dynamics of a 2D nucleic acid structure.[22,24,25] Recent oxDNA[26] simulations indicated that the NRO exhibits substantial structural dynamics and tends to dynamically twist along the two diagonal axes.[27] It has also been shown that NROs can roll up and form tubes when strands protruding from one long edge hybridize to strands protruding from the opposite long axis edge. Thus, this DNA origami structure is finally rolled-up along its long axis as was visualized by atomic force microscopy.[24] In parallel, it was observed that the distance between fluorescent marks on the NRO showed salt dependent changes. Interestingly, marks along the diagonal showed decreasing distances with increasing magnesium concentration whereas marks along the axis of the DNA backbone showed slight distance increases in accordance with a model that suggest reduced distances between adjacent helices due to increased screening and higher ionic strength.[23,28]

Here, we introduced two new assays to study the flexibility of the NRO and reveal a transition between the flat form of the NRO and a rolled-up conformation that was induced by bivalent ions such as magnesium or calcium. First, we used DNA-PAINT[29] and two-color DNA-PAINT[30] on extended DNA staples along the long edges of the NRO that provides structural information. DNA-PAINT images revealed the presence of slightly compacted flat and fully rolled-up DNA origami structures at high concentration of bivalent ions. Second, we used energy transfer between a dye and a 10 nm gold nanoparticle to visualize distance changes induced by structural changes of

Department of Chemistry and Center for NanoScience, Ludwig-Maximilians-Universität München, Butenandtstr. 5-13 Haus E, 81377 München, Germany. E-mail: philip.tinnefeld@cup.uni-muenchen.de

† Electronic supplementary information (ESI) available. See DOI: https://doi.org/10.1039/d1nr07793g

the DNA origami rectangle. These measurements revealed a two-state system with dynamic switching between the flat and rolled-up conformations on a second time scale.

Overall, we revealed high flexibility of a 2D DNA origami structure that showed salt dependent structural changes not only in two but also in three dimensions. Using salt concentrations as a stimulus, different conformations of DNA origami structures were accessed even without insertion of special motifs such as hinges or joints or DNA hybridization locks. Our assays for accessing the structural properties of the DNA origami structure provided high time resolution (energy transfer assay) and high structural information (DNA PAINT imaging) on the single-molecule level, overall yielding a comprehensive picture of the underlying processes.

Results and discussion

The NRO consists of 24 helices organized in a square lattice with dimensions of 71 × 85 nm (Fig. 1a). The structure is a twist-corrected version of the original RRO[1] called NRO.[23] We immobilized the NRO on BSA-biotin-NeutrAvidin coated coverslip by incorporating two biotin-labeled staple strands. The locations of the biotin strands were chosen close to the center of the DNA origami structure so that maximal conformational freedom of the DNA origami structure was maintained while excluding rotational degrees of freedom.[31]

In the first assay, we designed a DNA-PAINT (points accumulation for imaging in nanoscale topography) experiment to study the salt-dependence of the structure of the DNA origami rectangle.[23] We therefore equipped 56 staple strands with 11 bp single-stranded protrusions. The protruding strands were located along the long edges of the DNA origami structure (Fig. 1a). A 6 bp imager strand labeled with ATTO 655 transiently binds to the protruding docking strands with binding times on the millisecond time scale. Imaging by TIRF microscopy and subsequently localizing the single-molecule binding events yields superresolved images of the DNA origami structures (see Fig. 1b and c, and ESI for experimental methods†). The two parallel lines on the DNA origami structure were clearly resolved. Comparing DNA-PAINT images in Fig. 1b obtained at low Mg^{2+} concentration (12 mM) and Fig. 1c (high Mg^{2+}, 500 mM) gave the impression that the lines had a smaller distance at higher Mg^{2+} concentration. For quantification, structures showing two parallel lines were picked and the distance between the lines was extracted with home-written LabView software. The distances are plotted in Fig. 1d and clearly show a decrease in the measured distance at an increase of the salt concentration. These findings reproduced well the reported distance reduction along the diagonal of the NRO.[23] Based on the data of the previous work, a distance reduction along the short edge of the NRO from 0 to 500 mM $MgCl_2$ of 37% was calculated.[23] The distance reduction found in our data was 21% for an increase of salt from 12 to 500 mM $MgCl_2$. As the distance reduction was most pronounced at low Mg^{2+} concentration and saturated beyond 100–200 mM $MgCl_2$ both data sets showed a good match. The origin of the reduced distance lies in the increased screening of repulsive charges in the backbones of parallel oriented DNA helices at higher salt concentrations.[28]

Besides DNA origami structures showing the two lines (as for all DNA origami structures at 12 mM $MgCl_2$ in Fig. 1b) DNA origami structures showing only one line in superresolution experiments appeared at higher Mg^{2+} concentration (see yellow arrows in Fig. 1c). For these one-line structures, we suspected a conformation in which the two lines collapsed on top of each other. Rolling-up of the DNA origami rectangles could yield such a superposition of the edges.

To better visualize the collapsed structures, we substituted one of the lines on the NRO for the one-color experiment by a second sequence to perform two-color DNA-PAINT experiments (Fig. 2a and b). This sequence showed a repetitive sequence[32] on the DNA origami structure with a length of 12 bp. In order to perform the two-color experiment additional to the ATTO 655 imager an imager strand complementary to the second sequence with a length of 7 bp and a Cy3B attached to it was used. The two-color experiment corroborates the idea that the single-line structures also seen in the one-color measurements (Fig. 2c and d) indeed represent structures in which the two sides of the DNA origami rectangle are

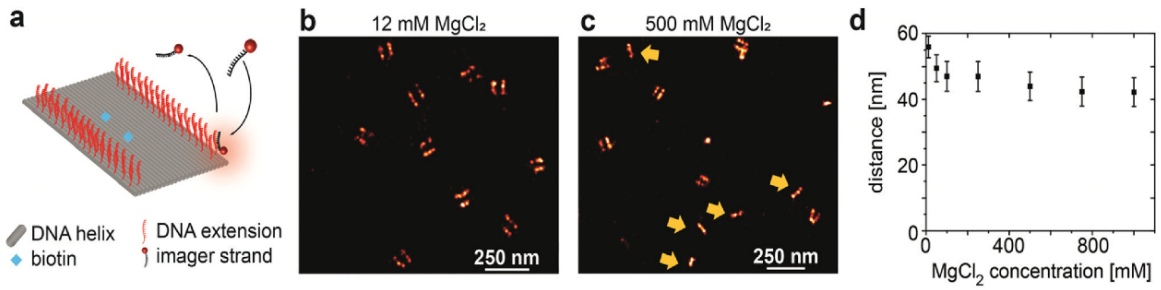

Fig. 1 (a) Sketch of the rectangular DNA origami structure used for DNA-PAINT measurements with extended staple strands for imager binding and biotin labels for surface immobilization. Exemplary superresolved DNA-PAINT images of the two lines on the DNA origami structure at 12 mM $MgCl_2$ (b) and at 500 mM $MgCl_2$ (c). (d) Distances and standard deviation of the two parallel lines on the DNA origami structures measured as a function of salt concentrations.

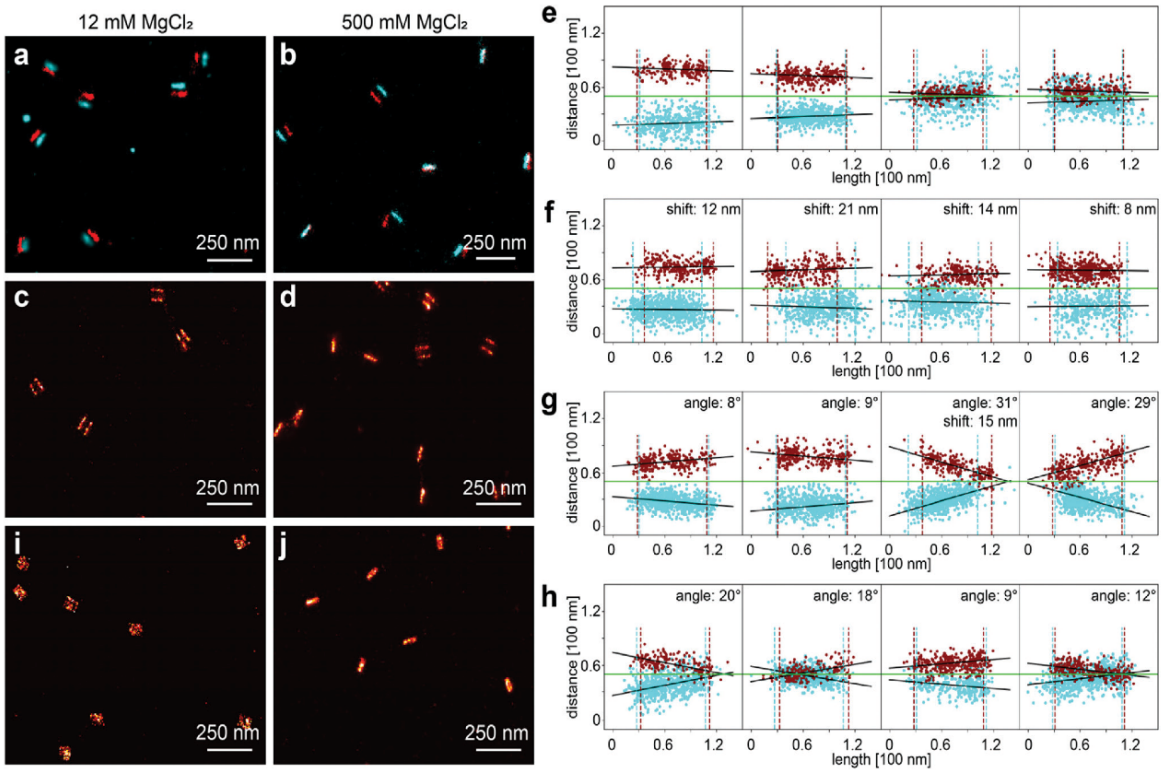

Fig. 2 Two-color (a and b) and one-color (c and d) DNA-PAINT experiments of the DNA origami rectangle labeled along the long sites at 12 and 500 mM $MgCl_2$. (e)–(h) show exemplary structures of the two color experiment in (b). (e) Exemplary structures of the DNA origami structure in the unshifted flat and rolled-up state. (f) DNA origami structures showing a shift (difference between the cyan and red dashed lines) between the green (cyan) and the red (red) imaged sites. Tilted lines with different angles of two separated (g) and overlapping (h) lines. Superresolved one-color images of a DNA origami rectangle labeled with a 6 nm grid at 12 and 500 mM $MgCl_2$ (i and j).

collapsed on top of each other (see white structures in false color images of Fig. 2b). Interestingly, having a closer look at structural details of individual structures we find quite different arrangements that indicate possible geometries of the rolled-up structures (Fig. 2e–h). First, we find structures with parallel lines that could indicate rolling-up along an axis parallel to the axis of the DNA double-helices in the DNA origami structure (Fig. 2e). We, however, also observe a similar fraction of structures that exhibit parallel lines but show a longitudinal offset (Fig. 2f). This geometry was expected for rolling-up around a diagonal axis of the DNA origami structure. Next, we found many structures with non-parallel lines implying angles between the sides. When these structures have longitudinal offset rolling-up occurred incompletely from one side about a diagonal axis (see Fig. 2g, 3rd example). More often, however, we observe angles without an offset. This could be explained if rolling up occurs from both edges starting from the same short side of the DNA origami rectangle forming a cone-like structure.

An observation made with the two-color experiments was that the fraction of fully rolled-up structures (*i.e.* only a single line visible) at 500 mM $MgCl_2$ was reduced from 30% to 15%. We suppose that the different sequences used in the two DNA-PAINT experiments could have an impact on the rolling up of the DNA origami rectangles and that the rolled-up structures are stabilized by interactions between the protruding docking strands. To this end, we carried out an additional experiment with the whole DNA origami structure covered with docking strands in a grid with 6 nm distances between adjacent docking strands. At low magnesium concentration, these DNA origami structures appear as rectangular patches in the superresolution image (Fig. 2i). At high magnesium concentration, however, almost 100% of the structures collapse into a single line (Fig. 2j). Inspection of the docking site sequence used for one-color DNA-PAINT reveals that up to four AT interactions can occur that could cooperatively stabilize the rolled-up structures. These interactions are absent between the different PAINT sequences of the two-color experiment which might explain the sequence dependent results.

To get further insight into the DNA origami conformation and to test whether the magnesium induced conformational transition also occurs in the absence of stabilizing interactions between protruding DNA PAINT docking strands, we designed a second assay that reported on local and dynamic conformational changes by energy transfer between a donor dye and a 10 nm gold nanoparticle as acceptor. The advantage of

energy transfer from a dye to a nanoparticle in comparison to the energy transfer between two dyes (Förster Resonance Energy Transfer, (FRET)) is that the distance dependence is shallower and exhibits a longer distance range with 10.4 nm distance for 50% energy transfer efficiency.[33] In addition, acceptor photobleaching is avoided.

A single red fluorophore (ATTO 647N) was placed close to one corner of the NRO and a 10 nm gold nanoparticle was placed in the front central part of the structure (Fig. 3a). This location of the nanoparticle was chosen so that putative distance changes associated with a rolling-up of the NRO were within the dynamic range of the assay.

We used two-color confocal single-molecule microscopy on a home-built setup with pulsed 532 nm and 639 nm excitation and detection by time-correlated single-photon counting (see ESI for methods and details of the optical setup†). The binding of a nanoparticle to each individual DNA origami structure was verified by a green fluorescent dye (ATTO 532) placed in close proximity to the NP binding site. Confocal scans with alternating 532 nm and 639 nm excitation were recorded. First, the confocal scans with 532 nm excitation were analyzed. Therefore, the fluorescence intensity scan image (Fig. 3b) was transformed into a fluorescence lifetime image (Fig. 3c) by pixel-wise fluorescence lifetime fitting probing the presence of a NP. Spots showing a reduced fluorescence lifetime around 1 ns indicated NP binding as seen in the fluorescence lifetime image (Fig. 3c). The fluorescence lifetime histogram in Fig. 3d shows the high yield of NP binding as the unquenched fluorescence lifetime of ATTO 532 was 3.8 ns. We carried out controls to ensure that the fluorescence lifetimes of the dyes were independent of ion concentration (Fig. S2a and b†).

Next, the scan with 639 nm excitation reported on the properties of the geometry-indicating dye ATTO 647N. To this end, fluorescence intensity scans were taken in a salt exchange experiment (Fig. 3e). Following the same procedure as for the analysis of the green ATTO 532 dye the fluorescence intensity images (Fig. 3e) were converted into fluorescence lifetime images (Fig. 3f). For further analysis of the fluorescence lifetime distributions, only spots were considered for which the presence of a NP was verified by the shortened fluorescence lifetime of the ATTO 532 dye in the previous 532 nm scan. As seen in Fig. 3f, at 12 mM $MgCl_2$, the fluorescence lifetime of ATTO 647N was unquenched with a distribution around 4 ns (Fig. 3g). The unquenched population indicated that no strong conformational changes were detected at 12 mM $MgCl_2$, *i.e.* in a range where superresolution imaging yielded a measurable distance reduction along the diagonal.[23] After incubation for 30 min with higher Mg^{2+} concentration of 1000 mM, the fluorescence intensity scans showed darker spots that were corre-

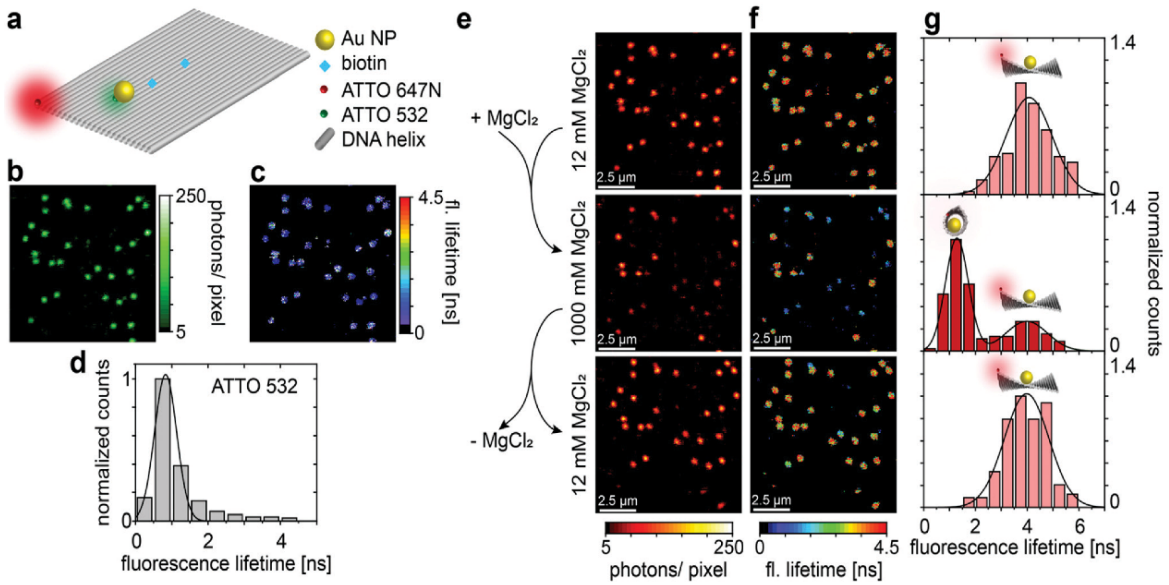

Fig. 3 Sketch of the rectangular DNA origami structure (a) with attached ATTO 647N (red), ATTO 532 (green) located under a 10 nm gold nanoparticle (Au NP, yellow) and biotins (blue) on the bottom side of the DNA origami structure. (b) Fluorescence intensity scan image with 532 nm excitation showing the fluorescence of ATTO 532. (c) Fluorescence lifetime image corresponding to the fluorescence intensity image in (b). (d) Spot-integrated fluorescence lifetime distribution of the quenched ATTO 532 spots from images such as in (b). The shortened fluorescence lifetime compared to the unquenched fluorescence lifetime of 4.0 ns indicates quantitative NP binding. (e) Consecutive confocal scan images with an excitation of 639 nm to detect the fluorescence of ATTO 647N in a salt exchange experiment. In (e), the same area was scanned three times, at a concentration of 12 mM $MgCl_2$, after the addition of a higher salt buffer at 1000 mM $MgCl_2$, and after salt reduction to 12 mM $MgCl_2$. (f) Fluorescence lifetime images corresponding to the fluorescence intensity images in (e). (g) Distributions of the fluorescence lifetime of ATTO 647N extracted from the scan images in (f) revealing two populations for the rolled-up (1.2 ns) and flat (4.0 ns) DNA origami geometries. The rolling-up and recovery experiment was performed for in total 144 DNA origami structures.

View Article Online
Nanoscale Paper

lated with decreased fluorescence lifetime (see consecutive images of the same area in Fig. 3e and f). Integrating all photons from a single-molecule spot for fluorescence lifetime fitting, we created fluorescence lifetime histograms of the DNA origami structures under the different conditions. Fig. 3g shows a histogram with the undisturbed fluorescence lifetime of 4.0 ns at 12 mM $MgCl_2$ and the additional fluorescence lifetime population at 1.2 ns for 1000 mM $MgCl_2$. 1.2 ns corresponded to an estimated distance between the dye and the nanoparticle surface of about 7.5 nm which agreed with a rolled-up conformation of the DNA origami structure (see sketches in Fig. 3g and ESI section 9†).[33] The fraction that was not changing shape could be related to local surface interactions which might be stronger for some DNA origami structures than for others. Next, we studied the reversibility of this structural transition and reduced the Mg^{2+} concentration back to 12 mM. In the scans of the same area, all spots that had the shortened fluorescence lifetime at 1000 mM Mg^{2+} returned to the long fluorescence lifetime around 4 ns (only molecules were considered that were detected in all three scans). The full recovery showed the reversibility of the transition that also occurs in the absence of DNA PAINT docking strands (Fig. 3f and g).

To also answer the question whether the transition to the quenched state was gradually dependent on Mg^{2+} or whether we observed a two-state system we studied the Mg^{2+} dependence with additional steps at 250 mM and at 500 mM. For each molecule considered for fluorescence lifetime histograms, the presence of the Au-nanoparticle was ensured by the shortened fluorescence lifetime of the reference dye ATTO 532 (Fig. 4a). The fluorescence lifetime histograms were extracted from fluorescence transients of molecules placed in the confocal laser spot (Fig. 4b). Interestingly, we observed the same fluorescence lifetime populations at 1.3 ns and at 4.0 ns for all concentrations but the fraction of the short fluorescence lifetime populations was constantly increasing (Fig. 4b). Higher concentrations of 1500 mM $MgCl_2$ did however not lead to a further increase of the low fluorescence lifetime fraction (ESI Fig. S2†). We concluded that the transition occurred between two defined states different to the gradual distance changes observed by superresolution microscopy for lower Mg^{2+} concentrations (see superresolution images in Fig. 1 and ref. 23).

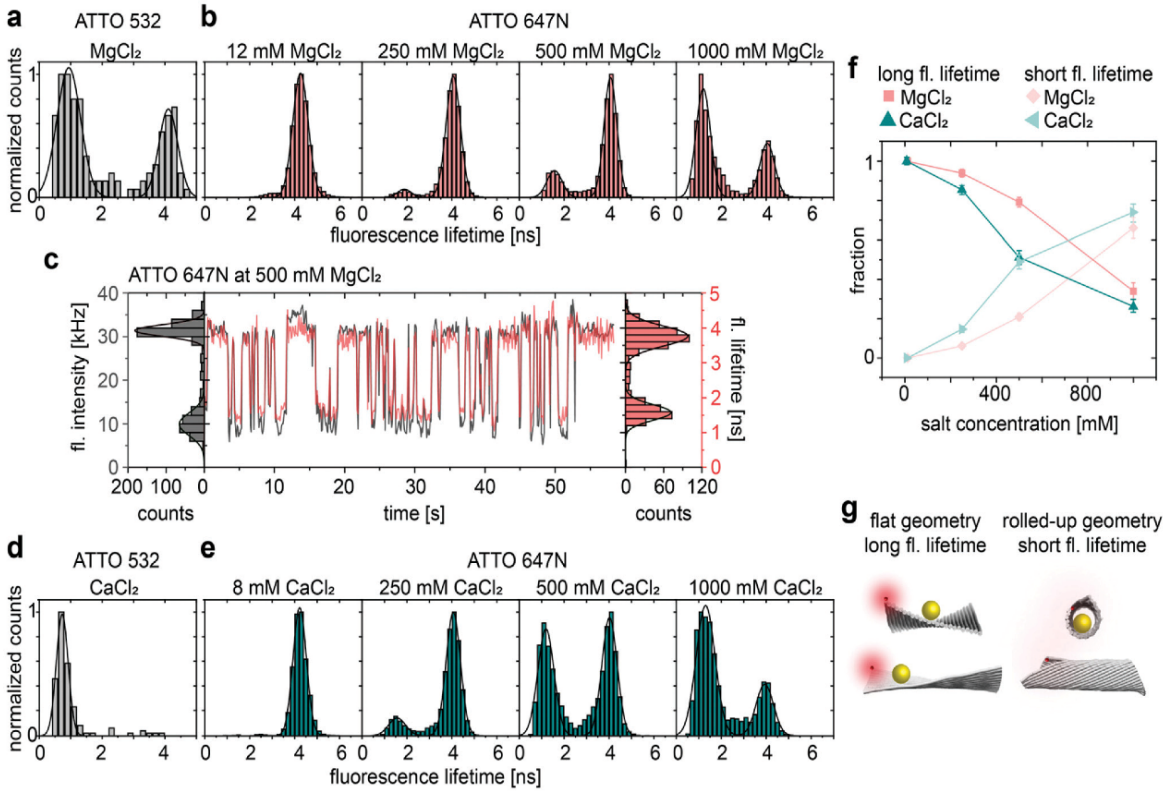

Fig. 4 (a) Fluorescence lifetime histograms of ATTO 532 (a) and of ATTO 647N in a titration experiment with $MgCl_2$ (b; 12–1000 mM $MgCl_2$). (c) Fluorescence intensity and lifetime transients of ATTO 647N with corresponding histograms at 500 mM $MgCl_2$ at a binning of 100 ms showing fluctuations between two states. (d) Fluorescence lifetime histograms of ATTO 532 (d) and of ATTO 647N in a titration experiment with $CaCl_2$ (e; 8–1000 mM $CaCl_2$). Spots integrated into the histograms in (b) and (e) showed a quenched fluorescence lifetime of the ATTO 532 reference dye. Both distributions showed two fluorescence lifetime populations at 4.0 ns and at 1.3 ns. (f) Summary of the data from (b) and (e) showing the particular fractions of long and short fluorescence lifetime at different salt concentrations for $MgCl_2$ (rose) and $CaCl_2$ (turquois). (g) Supposed geometries of the DNA origami structure at 4.0 ns and 1.3 ns corresponding to a flat and rolled-up state (images modified from CanDo simulations[34,35]).

In many cases, the transients showed strong fluorescence intensity fluctuations that were directly correlated with fluorescence lifetime fluctuations (see exemplary transient in Fig. 4c recorded at 500 mM Mg^{2+}). Obviously, many DNA origami structures (20–30% of all transients except for the 12 mM Mg^{2+} transients) dynamically switched between the two states with some additional fluctuations especially in the regime of weak quenching. These dynamics were well in accordance with the idea that the rectangular DNA origami structure is a highly flexible, dynamic structure.[24,25,27,36] However, one conformation with small distance between dye and nanoparticle was clearly preferred over other intermediate populations yielding the 1.2 ns population visible in the fluorescence lifetime histograms.

The fact that the structural transition is induced by the bivalent cations was confirmed by corresponding measurements with calcium instead of magnesium. The results of the calcium titration experiment are illustrated in Fig. 4d and e and show the same tendency as in the magnesium experiment. The shortened fluorescence lifetime of the reference dye ATTO 532 was again used to select DNA origami structures with Au-nanoparticle. The short fluorescence lifetime population of ATTO 647N started to be more pronounced for lower cation concentrations of calcium than magnesium. These findings are summarized in Fig. 4f, where the fractions of long (dark colors) and short (light colors) fluorescent lifetime populations were plotted against the different salt concentrations of Mg^{2+} (rose) and Ca^{2+} (turquois). The stronger response of the DNA origami structure in the Ca^{2+} titration was likely related to the stronger affinity of the cation to the DNA. As the hydration shell of Ca^{2+} is softer than the one of Mg^{2+} water ligands could be replaced more easily and the cation could reach places that are not accessible for magnesium.[37] In this context, we made the peculiar observation that the rolling-up of the DNA origami structure was suppressed when directly switching from Mg^{2+} to Ca^{2+} indicating different binding sites of the two ions and a kind of memory effect even after extensive washing that was in accordance with long-lived salt-nucleic acid interactions also observed for Holliday Junctions[38] (see details in ESI and Fig. S3†).

All data discussed so far were in accordance with the idea of salt-induced rolling-up of the DNA origami structure but left open the question of the preferential axis about which rolling-up occurs. Rolling-up could occur parallel to the long axis as suggested for rolling-up by hybridization[24] or along the diagonal as suggested by oxDNA simulations[27] and for intercalator-induced twisting.[25] We therefore estimated the expected dye-nanoparticle distance from geometrical models of the rolling-up around the two different axes (see ESI section 9 and Fig. S4† for details) and compared to the experimental distance of 7.5 nm. For rolling-up parallel to the long axis of the DNA origami structure a distance of 12.2 nm was calculated and a distance of 8.5 nm was determined for rolling-up parallel to the diagonal of the DNA origami structure showing a clear tendency that rolling-up is more likely to occur around the diagonal axis in accordance with the fluctuation dynamics observed in simulations.[27] By superresolution imaging, we observed that interactions of DNA-PAINT docking strands promoted rolling-up. For a maximized number of interactions of the docking strands also rolling-up about the parallel axis could be promoted indicating a rather shallow energy landscape with respect to the axis of the transformation. Overall, our observations were in agreement with a fluctuating rectangular DNA origami structure that was caught in a rolled-up conformation when the concentration of bivalent ions was high enough to connect the two sides of the DNA origami structure by salt-bridges.

Finally, we wondered whether high salt concentration also had a substantial influence on the functioning of complex 3D DNA origami devices. Here we studied Holliday Junction[39] dynamics in a DNA origami force clamp[40,41] and found that high Mg^{2+} concentration did not substantially alter the force applied to the Holliday Junction (see discussion in ESI section 10 and Fig. S5†). This is in accordance with our idea that the salt is not directly modulating the structure of the DNA origami rectangle *e.g.* by changing the helicity but helped to capture one specific conformation by connecting the long edges of the rectangular DNA origami structure by salt bridges.

Conclusion

We designed two single-molecule assays to study structural influences of bivalent cations on the rectangular DNA origami structure. Both DNA-PAINT and dye-nanoparticle energy transfer experiments indicated a rolling-up of the rectangular DNA origami structure when the salt concentration was increased. The two-state switching between a flat and a rolled-up conformation was different to the moderate gradual distance changes at low Mg^{2+} concentration that was observed previously by superresolution microscopy. Superresolution two-color experiments revealed different conformations of the two edges with respect to each other. The dye-nanoparticle energy transfer experiment revealed the dynamic nature of the reversible transition and also provided evidence that rolling-up preferentially occurred around the diagonal axis of the DNA origami structure in the absence of additional docking site interactions. We suppose that the rolled-up conformation was a result of cation bridging between the backbones at high salt. The experiments were well-suited to compare to structural models of DNA origami structures as rolling-up around the diagonal axis was predicted by oxDNA simulations. In addition, the presented assays should be well-suited to study other structural transitions in DNA nanotechnology and can even help to reveal how different ions such as calcium and magnesium interact differently with DNA.

Conflicts of interest

There are no conflicts to declare.

Acknowledgements

P.T. acknowledges financial support by the BMBF (SIBOF, 03VP03891). This work was funded by the Deutsche Forschungsgemeinschaft (DFG, German Research Foundation) INST 86/1904-1 FUGG, TI 329/9-2 as well as DFG under German Excellence Strategy, EXC 2089/1-390776260 and ID 201269156 – SFB1032, and the Bavarian Ministry of Science and the Arts through the ONE MUNICH Project "Munich Multiscale Biofabrication".

References

1 P. W. K. Rothemund, Folding DNA to create nanoscale shapes and patterns, *Nature*, 2006, **440**, 297–302.
2 B. Saccà and C. M. Niemeyer, DNA origami: the art of folding DNA, *Angew. Chem., Int. Ed.*, 2012, **51**, 58–66.
3 P. Wang, T. A. Meyer, V. Pan, P. K. Dutta and Y. Ke, The Beauty and Utility of DNA Origami, *Chem*, 2017, **2**, 359–382.
4 S. M. Douglas, H. Dietz, T. Liedl, B. Högberg, F. Graf and W. M. Shih, Self-assembly of DNA into nanoscale three-dimensional shapes, *Nature*, 2009, **459**, 414–418.
5 H. Ramezani and H. Dietz, Building machines with DNA molecules, *Nat. Rev. Genet.*, 2020, **21**, 5–26.
6 J. Ji, D. Karna and H. Mao, DNA origami nano-mechanics, *Chem. Soc. Rev.*, 2021, **50**, 11966–11978.
7 A. Kuzyk, R. Jungmann, G. P. Acuna and N. Liu, DNA Origami Route for Nanophotonics, *ACS Photonics*, 2018, **5**, 1151–1163.
8 B. Ding, Z. Deng, H. Yan, S. Cabrini, R. N. Zuckermann and J. Bokor, Gold nanoparticle self-similar chain structure organized by DNA origami, *J. Am. Chem. Soc.*, 2010, **132**, 3248–3249.
9 M. Pilo-Pais, G. P. Acuna, P. Tinnefeld and T. Liedl, Sculpting Light by Arranging Optical Components with DNA Nanostructures, *MRS Bull.*, 2017, **42**, 936–942.
10 M. DeLuca, Z. Shi, C. E. Castro and G. Arya, Dynamic DNA nanotechnology: toward functional nanoscale devices, *Nanoscale Horiz.*, 2020, **5**, 182–201.
11 S. Nummelin, B. Shen, P. Piskunen, Q. Liu, M. A. Kostiainen and V. Linko, Robotic DNA Nanostructures, *ACS Synth. Biol.*, 2020, **9**, 1923–1940.
12 M. D. E. Jepsen, R. S. Sørensen, C. Maffeo, A. Aksimentiev, J. Kjems and V. Birkedal, Single molecule analysis of structural fluctuations in DNA nanostructures, *Nanoscale*, 2019, **11**, 18475–18482.
13 E. Kopperger, J. List, S. Madhira, F. Rothfischer, D. C. Lamb and F. C. Simmel, A self-assembled nanoscale robotic arm controlled by electric fields, *Science*, 2018, **359**, 296–301.
14 A. Kuzyk, R. Schreiber, H. Zhang, A. O. Govorov, T. Liedl and N. Liu, Reconfigurable 3D plasmonic metamolecules, *Nat. Mater.*, 2014, **13**, 862–866.
15 L. K. Bruetzel, P. U. Walker, T. Gerling, H. Dietz and J. Lipfert, Time-Resolved Small-Angle X-ray Scattering Reveals Millisecond Transitions of a DNA Origami Switch, *Nano Lett.*, 2018, **18**, 2672–2676.
16 A. E. Marras, L. Zhou, H.-J. Su and C. E. Castro, Programmable motion of DNA origami mechanisms, *Proc. Natl. Acad. Sci. U. S. A.*, 2015, **112**, 713–718.
17 C. K. McLaughlin, G. D. Hamblin, K. D. Hänni, J. W. Conway, M. K. Nayak, K. M. M. Carneiro, H. S. Bazzi and H. F. Sleiman, Three-dimensional organization of block copolymers on "DNA-minimal" scaffolds, *J. Am. Chem. Soc.*, 2012, **134**, 4280–4286.
18 B. Yurke, A. J. Turberfield, A. P. Mills, F. C. Simmel and J. L. Neumann, A DNA-fuelled molecular machine made of DNA, *Nature*, 2000, **406**, 605–608.
19 C. Albrecht, K. Blank, M. Lalic-Mülthaler, S. Hirler, T. Mai, I. Gilbert, S. Schiffmann, T. Bayer, H. Clausen-Schaumann and H. E. Gaub, DNA: a programmable force sensor, *Science*, 2003, **301**, 367–370.
20 F. Kühner, J. Morfill, R. A. Neher, K. Blank and H. E. Gaub, Force-induced DNA slippage, *Biophys. J.*, 2007, **92**, 2491–2497.
21 R. Li, H. Chen, H. Lee and J. H. Choi, Conformational Control of DNA Origami by DNA Oligomers, Intercalators and UV Light, *Methods Protoc.*, 2021, **4**, 38.
22 R. Li, H. Chen, H. Lee and J. H. Choi, *Elucidating the Mechanical Energy for Cyclization of a DNA Origami Tile*, 2021.
23 J. J. Schmied, M. Raab, C. Forthmann, E. Pibiri, B. Wünsch, T. Dammeyer and P. Tinnefeld, DNA origami-based standards for quantitative fluorescence microscopy, *Nat. Protoc.*, 2014, **9**, 1367–1391.
24 H. Chen, T.-W. Weng, M. M. Riccitelli, Y. Cui, J. Irudayaraj and J. H. Choi, Understanding the mechanical properties of DNA origami tiles and controlling the kinetics of their folding and unfolding reconfiguration, *J. Am. Chem. Soc.*, 2014, **136**, 6995–7005.
25 H. Chen, H. Zhang, J. Pan, T.-G. Cha, S. Li, J. Andréasson and J. H. Choi, Dynamic and Progressive Control of DNA Origami Conformation by Modulating DNA Helicity with Chemical Adducts, *ACS Nano*, 2016, **10**, 4989–4996.
26 J. P. K. Doye, H. Fowler, D. Prešern, J. Bohlin, L. Rovigatti, F. Romano, P. Šulc, C. K. Wong, A. A. Louis, J. S. Schreck, M. C. Engel, M. Matthies, E. Benson, E. Poppleton and B. E. K. Snodin, *The oxDNA coarse-grained model as a tool to simulate DNA origami*, 2020, **https://arxiv.org/pdf/2004.05052v1**.
27 C. K. Wong, C. Tang, J. S. Schreck and J. P. K. Doye, *Characterizing the free-energy landscapes of DNA origamis*, 2021, **https://arxiv.org/pdf/2108.06517v1**.
28 C.-Y. Li, E. A. Hemmig, J. Kong, J. Yoo, S. Hernández-Ainsa, U. F. Keyser and A. Aksimentiev, Ionic conductivity, structural deformation, and programmable anisotropy of DNA origami in electric field, *ACS Nano*, 2015, **9**, 1420–1433.

29 R. Jungmann, C. Steinhauer, M. Scheible, A. Kuzyk, P. Tinnefeld and F. C. Simmel, Single-molecule kinetics and super-resolution microscopy by fluorescence imaging of transient binding on DNA origami, *Nano Lett.*, 2010, **10**, 4756–4761.
30 T. Cordes, J. Vogelsang, C. Steinhauer, I. H. Stein, C. Forthmann, A. Gietl, J. J. Schmied, G. P. Acuna, S. Laurien, B. Lalkens and P. Tinnefeld, in *Far-field optical nanoscopy*, ed. P. Tinnefeld, C. Eggeling and S. W. Hell, Springer, Berlin, 2015, pp. 215–242.
31 C. Steinhauer, R. Jungmann, T. L. Sobey, F. C. Simmel and P. Tinnefeld, DNA origami as a nanoscopic ruler for super-resolution microscopy, *Angew. Chem., Int. Ed.*, 2009, **48**, 8870–8873.
32 S. Strauss and R. Jungmann, Up to 100-fold speed-up and multiplexing in optimized DNA-PAINT, *Nat. Methods*, 2020, **17**, 789–791.
33 G. P. Acuna, M. Bucher, I. H. Stein, C. Steinhauer, A. Kuzyk, P. Holzmeister, R. Schreiber, A. Moroz, F. D. Stefani, T. Liedl, F. C. Simmel and P. Tinnefeld, Distance dependence of single-fluorophore quenching by gold nanoparticles studied on DNA origami, *ACS Nano*, 2012, **6**, 3189–3195.
34 D.-N. Kim, F. Kilchherr, H. Dietz and M. Bathe, Quantitative prediction of 3D solution shape and flexibility of nucleic acid nanostructures, *Nucleic Acids Res.*, 2012, **40**, 2862–2868.
35 C. E. Castro, F. Kilchherr, D.-N. Kim, E. L. Shiao, T. Wauer, P. Wortmann, M. Bathe and H. Dietz, A primer to scaffolded DNA origami, *Nat. Methods*, 2011, **8**, 221–229.
36 B. E. K. Snodin, F. Randisi, M. Mosayebi, P. Šulc, J. S. Schreck, F. Romano, T. E. Ouldridge, R. Tsukanov, E. Nir, A. A. Louis and J. P. K. Doye, Introducing improved structural properties and salt dependence into a coarse-grained model of DNA, *J. Chem. Phys.*, 2015, **142**, 234901.
37 T. K. Chiu and R. E. Dickerson, 1 A crystal structures of B-DNA reveal sequence-specific binding and groove-specific bending of DNA by magnesium and calcium, *J. Mol. Biol.*, 2000, **301**, 915–945.
38 C. Hyeon, J. Lee, J. Yoon, S. Hohng and D. Thirumalai, Hidden complexity in the isomerization dynamics of Holliday junctions, *Nat. Chem.*, 2012, **4**, 907–914.
39 R. Holliday, A mechanism for gene conversion in fungi, *Genet. Res.*, 1964, **5**, 282–304.
40 P. C. Nickels, B. Wünsch, P. Holzmeister, W. Bae, L. M. Kneer, D. Grohmann, P. Tinnefeld and T. Liedl, Molecular force spectroscopy with a DNA origami-based nanoscopic force clamp, *Science*, 2016, **354**, 305–307.
41 K. Kramm, T. Schröder, J. Gouge, A. M. Vera, K. Gupta, F. B. Heiss, T. Liedl, C. Engel, I. Berger, A. Vannini, P. Tinnefeld and D. Grohmann, DNA origami-based single-molecule force spectroscopy elucidates RNA Polymerase III pre-initiation complex stability, *Nat. Commun.*, 2020, **11**, 2828.

Supporting Information

Salt-Induced Conformational Switching of a Flat Rectangular DNA Origami Structure

Kristina Hübner[1], Mario Raab[1], Johann Bohlen[1], Julian Bauer[1], Philip Tinnefeld[1]

[1] Department of Chemistry and Center for NanoScience, Ludwig-Maximilians-Universität München, Butenandtstr. 5-13 Haus E, 81377 München, Germany

1. DNA Origami Structure

The DNA origami structure was designed using the CaDNAno software.[1] A 7249-nucleotide long single stranded DNA sequence (scaffold) from the M13mp18 bacteriophage was folded into the designed 71 x 85 nm rectangular shape by the help of short single stranded staple strands. The staple strands were mixed with the scaffold strand in a 10-fold excess. Unmodified staple strands were purchased from IDT, biotinylated strands, nanoparticle binding strands and the ATTO 647N strand were purchased from Eurofins Genomics GmbH. The DNA origami structures were folded using a temperature ramp starting at 70 °C held for 5 min and then the temperature was stepwise decreased with a gradient of 1 °C per minute down to 25 °C. After the folding process, excess staple strands were removed from the sample by gel electrophoresis. Therefore, a 1.5% agarose gel (Biozym LE Agarose) was prepared. A gel electrophoresis chamber was filled with the running buffer (0.5xTAE 11 mM $MgCl_2$) and the pockets of the gel were loaded with the unpurified samples and a 10x BlueJuice™ Gel loading buffer (Thermo Fischer Scientific). The cooled electrophoresis ran at 80 V for 90 min, afterwards the bands containing the purified DNA origami structures were cut out and squeezed with a glass slide to retrieve the purified DNA origami structures. The final concentration of the sample was determined on a Nanodrop 2000 spectralphotometer (Thermo Fischer Scientific).

In order to proof the correct folding and to validate that the rectangular structure of the DNA origami was also stable in the $CaCl_2$ buffer, AFM images were acquired (Figure S1).

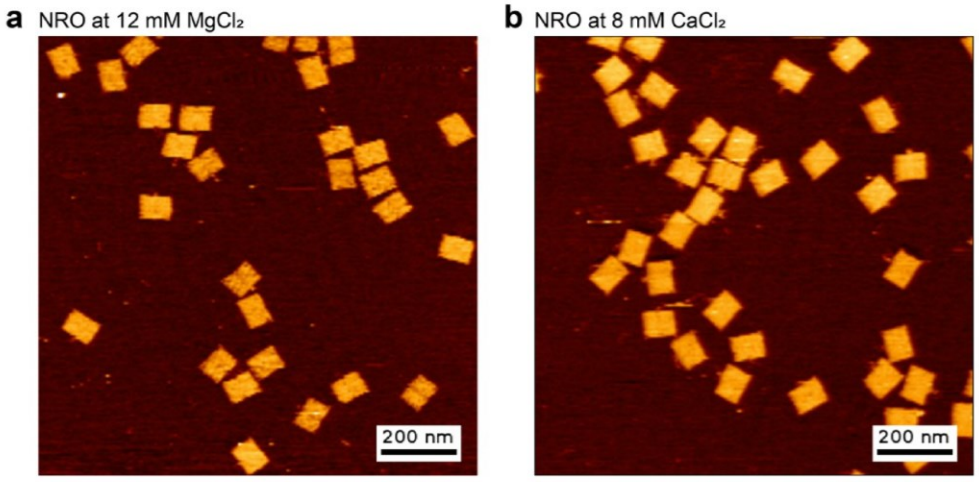

Figure S1: AFM images of the purified rectangular DNA origami structures (NRO) at 12 mM $MgCl_2$ (a) and at 8 mM $CaCl_2$ (b).

For the AFM measurements a Nanowizard 3 ultra (JPK, Berlin) equipped with a cantilever (BL-AC-40TS, Olympus, Japan) was used. The mica surface (plano, Berlin) was cleaved with

adhesive tape and incubated for 5 min with 10 µL 0.01 M NiCl2 solution to positively charge the surface. After incubation, the surface was cleaned three times with 300 µL ultrapure water and gently dried under a constant air flow. The DNA origami solution was diluted with AFM-buffer (40 mM Tris, 2 mM EDTA, 12.5 mM $Mg(OAc)_2 \bullet 6\ H_2O$) to a final concentration of 1 nM, added to the mica surface and incubated for 5 min. The mica surface afterwards was washed three times with 300 µL AFM-buffer and filled up to a volume of 1.2 mL AFM-buffer. 3 x 3 µm images were taken with a scanning speed of 1 Hz and a resolution of 512x512 pixels. The images were processed with the JPK data Processing software (JPK, Berlin).

2. Gold Nanoparticle Functionalization

Gold nanoparticles (Au NP) were decorated with single stranded DNA sequences for attachment to DNA origami structures. For this purpose, 2 mL of 10 nm Au NPs were mixed with 20 µL 10% Tween20 and 20 µL potassium phosphate buffer (4:5 mixture of 1 M monobasic and dibasic potassium phosphate, Sigma Aldrich). The mixture was heated to 40 °C and 30 µL of 2 nmol thiol-modified single stranded DNA functionalized at the 3'-end (T_{25}, Ella Biotech) were added. A salting procedure to reach a final concentration of 750 mM NaCl was carried out by adding a 1xPBS buffer with 3300 mM NaCl every 3 minutes. After salting, unbound DNA strands were removed by centrifugation at 14000 g for 45 min. In this step, the functionalized NPs precipitated and the unbound DNA strands stayed in solution, that was removed after each centrifugation step. The functionalized and concentrated Au NPs were re-diluted after each step with a 1xPBS 10 mM NaCl, 2.11 mM P8709 buffer (Sigma Aldrich). After seven centrifugation steps the particles were kept at high concentration.

3. Sample Preparation for Confocal Measurements

For measurements, the DNA origami constructs were immobilized on functionalized coverslips. The coverslips (24 mm x 60 mm, 170 µm thickness; Carl Roth GmbH) were rinsed with Milli-Q water and cleaned in a UV cleaning system (PSD Pro System, Novascan Technologies) for 30 min at 100 °C. After the cleaning, a micro adhesive SecureSeal™ Hybridization Chamber (Grace Bio-Labs) was glued onto the coverslip. The surfaces were incubated first with BSA-biotin (1 mg/mL, Sigma Aldrich) for 10 min and second with neutrAvidin (0.5 mg/mL, Sigma Aldrich). After each incubation step, the surfaces were washed with 1xPBS buffer. The DNA origami structures were immobilized with a concentration of

30 pM in a 1xTAE 12 mM $MgCl_2$ buffer. After incubation of the DNA origami structures the functionalized Au NPs were attached to the DNA origami structures by incubation in a 1xTAE 750 mM NaCl buffer for 30 min. Then unbound NPs were washed out by a 1xTAE 750 mM NaCl buffer. Later the buffer was replaced by the measurement buffer based on a 1xTAE buffer with X mM $MgCl_2$/$CaCl_2$ (X = 12/8, 250, 500, 1000) that also contained trolox/troloxquinone as reducing and oxidizing system (ROXS, 1x TAE, 2 mM trolox/troloxquinone, 1% (w/v) D-(+)-glucose; Sigma Aldrich) as well as glucose/glucose oxidase as oxygen scavenging agent (1 mg/mL glucose oxidase, 0.4% (v/v) catalase (50 µg/mL), 30% glycerol, 12.5 mM KCl in 50 mM TRIS; Sigma Aldrich) to acquire long fluorescence transients.[2,3]

4. Sample Preparation for Wide-Field Measurements

For wide-field measurements, LabTek™ chamber slides (Thermo Fisher Scientific Inc.) were incubated with Helmanex overnight and afterwards washed with a 1xPBS buffer. After cleaning, the surface was functionalized using the same protocol for BSA-biotin and neutrAvidin as described above. The DNA origami structures were immobilized by incubating the coverlips with a 30 pM concentration in a 1xTE 12 mM $MgCl_2$ buffer. For measurements, the buffer was exchanged to a 1xTAE buffer containing different concentrations of imager strands (6 bp, ATTO 655 or 7 bp, Cy3B) for the DNA-PAINT experiments (see *Table S1, S2 and S3*).

Table S1: Concentrations of imager strands used at different $MgCl_2$ concentrations.

c($MgCl_2$) [mM]	**c(imager strand) [pM]**
12	250
50	1000
100	1000
250	250
500	500
750	500
1000	1000

Table S2: Concentrations of imager strands used in the two-color experiments at different salt concentrations.

c($MgCl_2$) [mM]	**c(red imager strand) [pM]**	**c(green imager strand) [pM]**
12	1000	750
500	3000	1500

Table S3: Concentrations of imager strands used at different $MgCl_2$ concentrations.

c($MgCl_2$) [mM]	**c(imager strand) [pM]**
12	250
500	1000

5. Confocal Setup

Confocal measurements were performed on a home-built confocal setup based on an inverted Olympus IX81 microscope. For excitation, a 78 MHz pulsed white light laser (SuperK Extreme, NKT Photonics) was used. The wavelength was set to 639 nm and 532 nm by an AOTF (201608R, Crystal Technology Inc.). To alternate the red and green excitation a second AOTF (AA.AOTF.nsTN, A-Opto-Electronic) was used. The excitation laser passed through a neutral density filter (ndF, OF 0-2, Thorlabs) and was coupled into a polarization maintaining single-mode fiber (PM-Fiber, P1-488PM-FC-2, Thorlabs). After the fiber, the laser was sent through a linear polarizer (LPVISE100-A, Thorlabs) and a lambda quarter waveplate (AQWP05M-600, Thorlabs) to obtain circularly-polarized light. The laser was focused on the sample by an immersion oil objective (UPlanSApo 100x, NA = 1.4, WD = 0.12 mm, Olympus). Scanning of the sample in x and y direction was performed by a piezo stage (P-517.3CL, E-501.00, Physik Instrumente GmbH & Co. KG). Fluorescence light was collected by the same objective and separated from the excitation light by a dichroic mirror (DS, zt532/640rpc, Chroma). The transmitted light was focused onto a 50 µm pinhole (Linos) to filter out scattered laser light. Green and red fluorescence signals were split into two pathways by a dichroic mirror. Each signal was filtered (RazorEdge 647, Semrock Inc. for the red channel; BrightLine HC 582/75, Semrock Inc. for the green channel) and focused by a lens onto the active area of an APD (Avalanche Photo Diode, SPCM, AQR 14, Perkin Elmer). A TSCPC system (Hydra Harp 400, PicoQuant) was used for time-correlated single-photon counting. Data Processing was performed by a custom-written LabVIEW software (National Instruments).

6. Wide-Field Setup

DNA-PAINT measurements were performed on a home-built wide-field microscope based on an inverted Olympus IX71 microscope. As excitation source, a 644 nm diode laser (ibeam smart, Toptica Photonics) was used that was spectrally cleaned-up by a filter (Brightline HC 650/13, Semrock). The laser was focused in the back-focal plane of the objective (UPLXAPO 100X, numerical aperture (NA) = 1.45, working distance (WD) = 0.13, Olympus). The light was directed to the sample situated on top of a nosepiece stage (IX2-NPS, Olympus). The nosepiece stage together with an actively stabilized optical table (TS-300, JRS Scientific Instruments) stabilized the sample for the measurements. Emission light was collected by the same objective as for excitation and directed through a dichroic beamsplitter (Dual Line zt532/ 640 rpc, AHF Analysentechnik) to separate from excitation light. The emission light was filtered (ET 700/75, Chroma) before it was focused onto an EMCCD camera (iXon X3, DU-897, Andor). For data acquisition, the open source imageJ software Micro-Manager was used.[4]

7. Reference and Incubation Studies

Reference measurements of the DNA origami structures without any attached NP were carried out to study whether high salt concentrations of magnesium (Figure S2a) or calcium (Figure S3b) influenced the fluorescence lifetime of the fluorescent dye. The fluorescence lifetime distributions measured for the different reference assemblies all showed the same distributions and therefore no influence of the high salt concentration on the dye alone was seen.

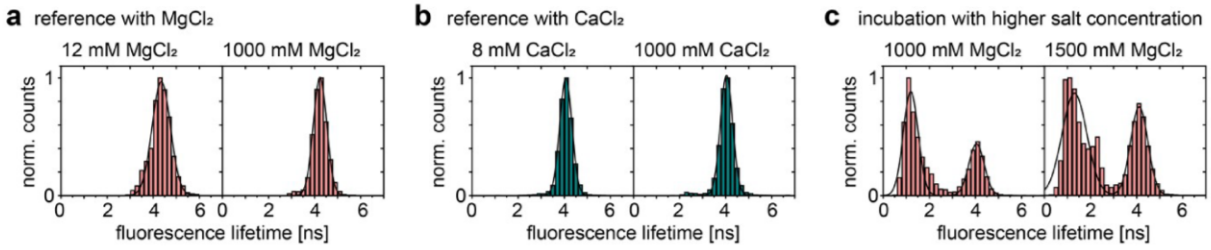

Figure S2: Reference measurements of the fluorescence lifetime of ATTO 647N in DNA origami structures without Au NP at low (12 mM/ 8 mM) and high salt (1000 mM) for $MgCl_2$ (a) and $CaCl_2$ (b). Fluorescence lifetime histogram for DNA origami structures with an attached 10 nm Au NP incubated at 1500 mM $MgCl_2$ (c).

To study whether salt concentrations higher than 1000 mM $MgCl_2$ had an influence on the fluorescence lifetime distributions and hence the rolling-up of the DNA origami structures an

experiment with a concentration of 1500 mM $MgCl_2$ was performed. Figure S2c shows no impact of the higher salt concentration.

8. Calcium to Magnesium and *vice versa* Experiments

A memory effect in DNA was observed in a salt exchange experiment. We immobilized DNA origami structures on a glass surface and attached a nanoparticle in a 1xTAE buffer containing 12 mM $MgCl_2$. After immobilization, we performed experiments in a 1xTAE buffer containing 8 mM and 1000 mM $CaCl_2$ (Figure S3a i) and ii)). Contrary to our expectations the observed fluorescence lifetime distributions were not reproducing the $MgCl_2$ experiments as only a minor quenched population showed up (Figure S3a ii). To ensure the quality of our samples, we changed the buffer to 1000 mM $MgCl_2$, but a quenched fluorescence lifetime population was not observed (Figure S3a iii)). Even washing with a buffer containing 2 M NaCl (Figure S3a iv)) or overnight incubation in 1 M $MgCl_2$ (Figure S3a v)) could not show the expected fluorescence lifetime quenching in the histograms.

The ion exchange measurement was also performed in the opposite direction to first prove that the DNA origami structures were able to undergo the structural change observed in the fluorescence lifetime quenching. The measurements with 12 mM and 1000 mM $MgCl_2$ (Figure S3b i and ii)) reproduced well the effect shown in Figure 2 in the manuscript. After proving the functionality of the DNA origami structures, a recovery of the flat state by a change to 8 mM $CaCl_2$ was shown (Figure S3b iii)). Now a titration experiment with $CaCl_2$ was performed to reproduce the histograms obtained with $MgCl_2$. Therefore, fluorescence intensity transients were taken at 8 and 1000 mM $CaCl_2$ and converted into fluorescence lifetime transients summed up in fluorescence lifetime histograms in Figure S3b iv) and v). This time a small fraction of DNA origami structures was showing a rolling-up as indicated by the quenched fluorescence lifetime population. Still, the fraction of rolled-up DNA origami structures was lower than in the magnesium experiments.

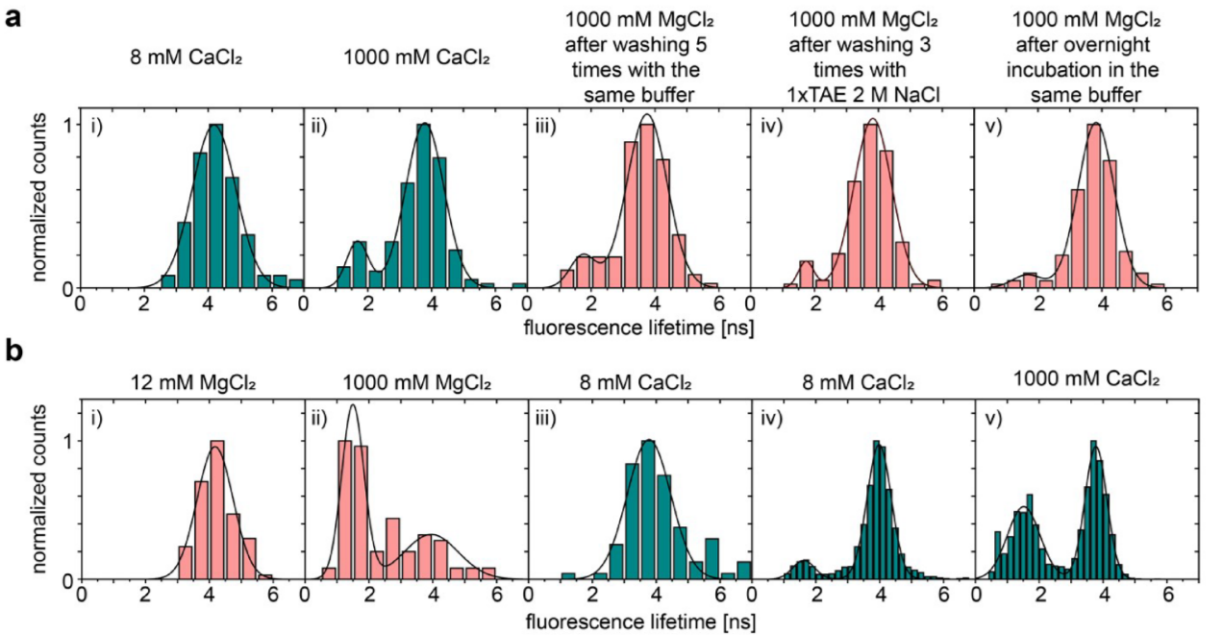

Figure S3: (a) Fluorescence lifetime distributions of ATTO 647N from scan images for i) 8 mM $CaCl_2$ and ii) 1000 mM $CaCl_2$. After the calcium measurements the buffer was exchanged to magnesium with different incubation methods: iii) washing 5 times with 1000 mM $MgCl_2$, iv) washing 3 times with 2 M NaCl then adding 1000 mM $CaCl_2$, v) overnight incubation with 1000 mM $CaCl_2$. (b) Fluorescence lifetime distributions from scan images for i) 8 mM $MgCl_2$ and ii) 1000 mM $MgCl_2$. The high magnesium concentration measurement was recovered with 8 mM $CaCl_2$ (iii). After switching between the rolled up and open state the sample was treated with calcium ions for two measurements, distributions (iv) an (v) show the histograms from fluorescence lifetime transient for 8 mM $CaCl_2$ and 1000 mM $CaCl_2$.

These measurements showed that it is crucial to decide which incubation step is done in which buffer and in which order. We assume this effect to be related to ion species binding stably to DNA inducing a kind of memory effect in the DNA. Once an ion is bound tightly, it influences the binding of other ions in the vicinity and can hinder ions of different kind to interact with the DNA the way they would do in the absence of the first bound ion.

Finally, we found that an attachment of the nanoparticle in 1xTAE with 750 mM NaCl and afterwards several washing steps and overnight incubation in 1xTAE with 8 mM $CaCl_2$ for the calcium titration experiments helped to overcome this kinetic blocking of the conformational changes upon ion exchange.

9. Distance Calculation

We calculated the distances of the red fluorescent dye to the gold nanoparticle's surface in the flat and rolled-up state of the DNA origami structure. For all calculations we used the theorem of Pythagoras. In a relaxed geometry (Figure S4a) the fluorophore was 33 nm away from the NP which is out of the range for energy transfer between the fluorescent dye and the NP. As the DNA origami structure rolls up the dye approached the NP and the fluorescence lifetime gets quenched. We assumed two possible axes of rolling-up of the DNA origami structure. One axis was parallel to the DNA origami helices (black dashed line in Figure S4a) and the other possible axis was a diagonal axis (green dashed line in Figure S4a) on the DNA origami rectangle. The distance between the ATTO 467N and the NP's surface for parallel rolling-up was calculated with a $D_{NP,\ dye}$ of 12.2 nm. In a diagonal rolling-up geometry the edge with the ATTO 647N bound is not directly approaching the opposing edge, but is shifted. This geometric point we calculated to be 30% of the of the long axis. A diagonal rolling-up leads to a different diameter of the formed DNA origami tube. Based on this assumption, a dye nanoparticle distance of $D_{NP,\ dye}$ of 8.3 nm was calculated for the diagonal rolling-up.

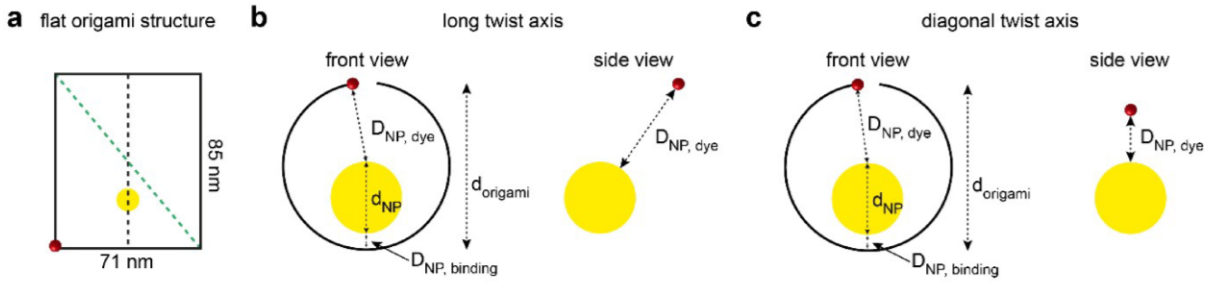

Figure S4: Schematic of the DNA origami rectangle with dimensions of 71 x 85 nm (a). The two lines are indicating possible directions of bending, which are along the DNA helices (black dashed line) or diagonal (green dashed line). The yellow circle is presenting the gold nanoparticle. (b) Sketches of the front and side view of the rolled-up DNA origami structure along the parallel axis with a DNA tube diameter of $d_{origami}$ of 22.6 nm and a calculated distance between the dye and nanoparticle $D_{NP,\ dye}$ of 12.2 nm. (c) Sketches of the front and side view of the rolling-up of the DNA origami structure along the diagonal axis with $d_{origami}$ 24.3 nm and $D_{NP,\ dye}$ of 8.3 nm. In both geometries the diameter of the nanoparticle d_{NP} is 10 nm and the nanoparticle binding distance between particle and DNA origami structure $D_{NP,\ binding}$ is 4 nm.

If the measured data is compared to earlier work[5], the fluorescence lifetime at a distance of 8.3 nm is quenched by 62%. For ATTO 647N this quenching would result in a fluorescence lifetime of 1.5 ns. This value is close to the measured fluorescence lifetime of 1.3 ns. The

quenching in rolling-up along the parallel axis of the DNA origami structure in turn would only lead to a quenching of 39% and thus a fluorescence lifetime of 2.9 ns would be expected.

10. Dynamics of a Holliday Junction

To study the influence of different salt concentrations on dynamic structures and on 3D DNA origami structures a Holliday Junction on the surface (HJ_{only}) and in a force clamp[6] DNA origamis structure (HJ_{FC}) was analyzed. In recent years, Holliday junctions have become a reference to study DNA dynamics by single-molecule FRET and its sensitivity to environmental conditions.[7,8] The Holliday Junction contains four different oligonucleotides and fluctuates between two stacked conformations. Two out of four oligonucleotides were labeled with dyes (Cy3/Cy5) which can non-radiatively transfer energy via FRET from the donor (Cy3) to the acceptor dye (Cy5). Switching between the two conformations was visualized by FRET changes between a high-FRET (h. FRET) and a low-FRET state (l. FRET; Figure S5a). It is generally known that the kinetics of switching is strongly slowed down with increasing concentration of bivalent ions.[9] We immobilized HJs via neutrAvidin-biotin interactions on BSA-biotin coated coverslips (Figure S54a). Representative FRET transients are shown in Figure S5b for low (12.5 mM, rose) and high (1000 mM, red) magnesium concentration and directly revealed the reduced rate of the transitions.

Next, we incorporated the HJ into a DNA origami force clamp[6,10] in which two arms of the HJ were connected to a rigid DNA origami frame (Figure S5c). Depending on the length of the connecting single-stranded DNA regions, an entropic force is exerted on the HJ yielding a preference for one conformational state (here the high-FRET state) over the other. The applied approximately 4 pN yielded an increased fraction of the high-FRET state directly visible in the representative transients of Figure S5d both at low and high Mg^{2+} concentration.

For statistical analysis, we histogrammed all the dwell times measured and calculated the equilibrium constant *K* (Figure S5e) which is given by:

$$K_{HJ,\ c(MgCl_2)} = \frac{t_{h.\ FRET,\ HJ,\ c(MgCl_2)}}{t_{l.\ FRET,\ HJ,\ c(MgCl_2)}} \qquad (1)$$

K illustrates that the higher salt concentration shifted the equilibrium to the low-FRET state which was observed for the HJ_{only} and HJ_{FC} samples. Interestingly, K changed by a factor R of roughly 1.5 for both samples with R calculated as

$$R_{HJ,\ c(MgCl_2)} = \frac{K_{HJ,\ 12.5\ mM\ MgCl2}}{K_{HJ,\ FC,\ 1\ M\ MgCl2}} \qquad (2)$$

(see Figure S5g).

The fact that the kinetics and equilibrium constant changed similarly for the pure HJ and the HJ in the DNA origami force clamp indicated that no significant change in the structure of the force clamp itself occurred which would have an influence on the applied force. Overall, this experiment indicated that Mg^{2+} concentration did not substantially alter the structure and properties of a functional, rigid 3D DNA origami structure and showed that such devices might be functional over a broad range of ion concentration.

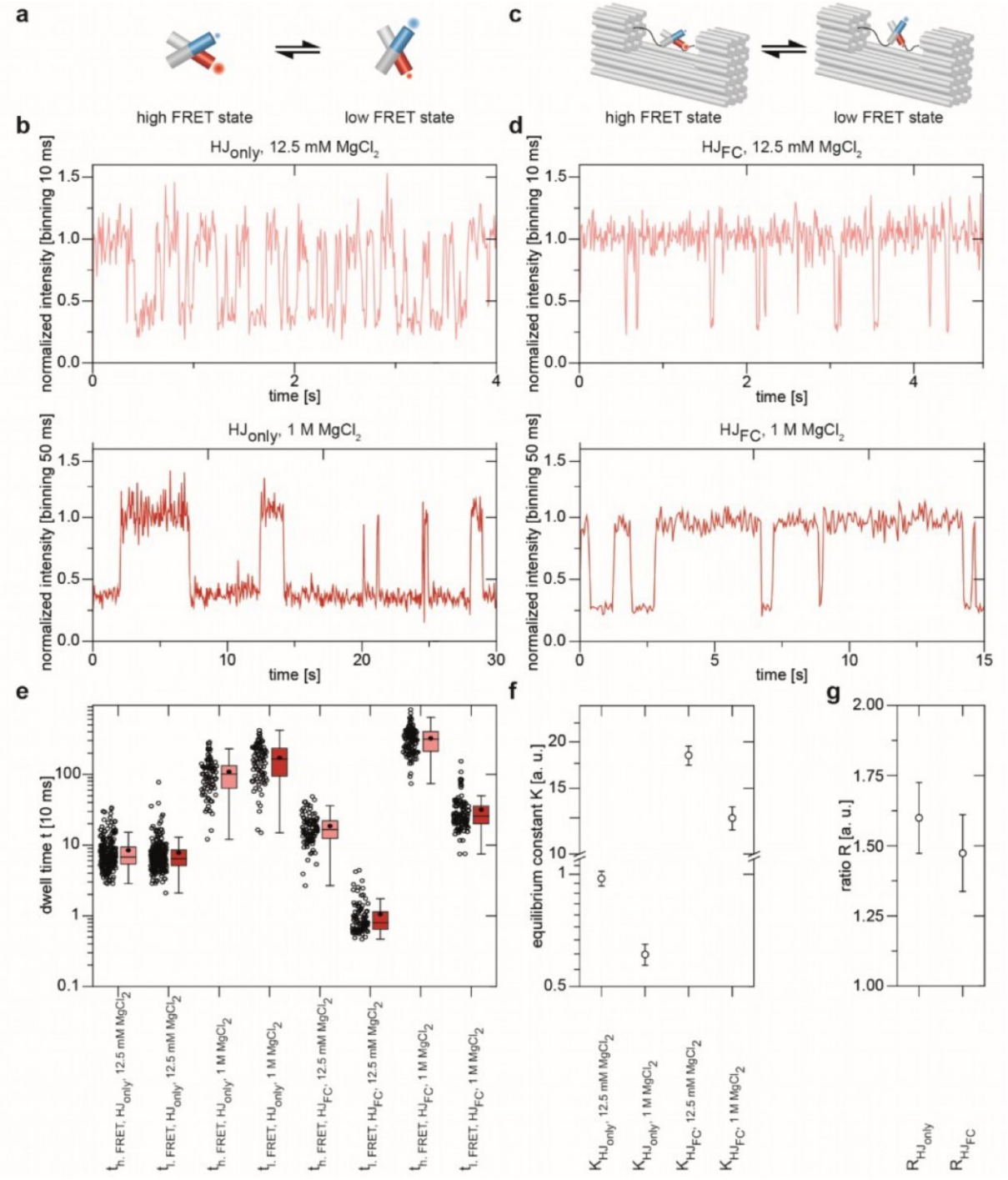

Figure S5: Illustration of the HJ only (HJ_{only}) and HJ in the DNA origami force clamp (HJ_{FC}) for observation of the salt influence. HJ only moving between the high- and low-FRET state (a) and in the FC (c). Exemplary transients of (a) are shown in (b) and of (c) in (d) with the salt concentrations of 12.5 mM and 1 M $MgCl_2$. (e) shows the dwell time t for every species obtained from a correlation analysis. The equilibrium constant between high- and low-FRET state shows a shift in the presence of higher salt concentration. By calculating the ratio R between 12.5 mM and 1 M $MgCl_2$ no significant difference is observed which is a clear indicator that high salt concentration does not have an impact on a rigid 3D DNA origami structure and dynamics.

Holliday Junction Preparation: Sequences for the Holliday Junction are shown in *Table S4*.

Table S4: Sequences of the HJ_{only}.

Oligonucleotide	Sequence (5'->3')
r	CCCACCGCTCGGCTCAACTGGG
x	biotin-TTTCCCAGTTGAGCGCTTGCTAGGG
b	Cy5-CCCTAGCAAGCCGCTGCTACGG
h	Cy3-CCGTAGCAGCGCGAGCGGTGGG

For the folding of the HJ an oligonucleotide solution with the ratio of 1:2:2:4 (x:r:b:h) in 1xTAE with 50 mM NaCl is heated to 70 °C and slowly cooled down at a rate of 1 °C/min until room temperature is reached.

DNA origami force clamp preparation: The preparation protocol and the sequences of the 4 pN force clamp were described in ref.[6]. To remove the excess of oligonucleotides gel electrophoreses was used. Therefore, 50 mL of 1.5% agarose gel (Biozym LE Agarose) were prepared in a 1xTAE buffer containing 12.5 mM $MgCl_2$ (Sigma Aldrich). The DNA origami solution was diluted with 10x BlueJuice™ Gel loading buffer (Thermo Fischer Scientific) and filled into the gel. The cooled gel ran for 2 h at 60 V, was cut with a scalpel and squeezed with a glass coverslip. The concentration of the DNA origami structure was determined with a Nanodrop 2000 spectralphotometer (Thermo Fischer Scientific).

Measurement procedure: For the measurements, a flow chamber was first incubated with BSA-biotin (1 mg/mL, Sigma Aldrich) for 10 min. After three times washing with a 1xTAE buffer with 12.5 mM $MgCl_2$ (Sigma Aldrich) the sample was incubated with neutrAvidin (1 mg/mL, Sigma Aldrich) for 10 min and washed again three times with 1xTAE buffer containing 12.5 mM $MgCl_2$ (Sigma Aldrich). Finally, the diluted DNA sample with a concentration of

25 pM was added. After adding the oxygen scavenging (1 mg/mL glucose oxidase, 0.4% (v/v) catalase (50 µg/mL), 30% glycerol, 12.5 mM KCl in 50 mM TRIS; Sigma Aldrich) and ROX system with the respective $MgCl_2$ concentration (1x TAE, 2 mM trolox/troloxquinone, 1% (w/v) D-(+)-glucose; Sigma Aldrich) the sealed sample was measured on a home-built confocal microscope (fluorescence confocal microscope II[11]).[2,3] For the measurements, a laser power between 2 and 3 µW for the green and 1 µW for the red excitation source were used. For PIE[12] measurements the laser repetition rate was set to 80 MHz. The measured data was evaluated with a home-written Labview software and the dwell times were extracted from the correlation of the FRET channel (green excitation – red detection).

11. DNA Origami ssDNA Dtrands

Table S5: Unmodified ssDNA strands.

Sequence (5'→3')	Number
AAGGCCGCTGATACCGATAGTTGCGACGTTAG	1
TCGAATTCGGGAAACCTGTCGTGCAGCTGATT	2
GATGGTTTGAACGAGTAGTAAATTTACCATTA	3
CGAAAGACTTTGATAAGAGGTCATATTTCGCA	4
TTAACGTCTAACATAAAAACAGGTAACGGA	5
TCTAAAGTTTTGTCGTCTTTCCAGCCGACAA	6
AACAAGAGGGATAAAAATTTTTAGCATAAAGC	7
AGCCAGCAATTGAGGAAGGTTATCATCATTTT	8
GATGGCTTATCAAAAAGATTAAGAGCGTCC	9
GCGGATAACCTATTATTCTGAAACAGACGATT	10
CTGAGCAAAAATTAATTACATTTTGGGTTA	11
TGTAGAAATCAAGATTAGTTGCTCTTACCA	12
CAAATCAAGTTTTTTGGGGTCGAAACGTGGA	13
TAAGAGCAAATGTTTAGACTGGATAGGAAGCC	14
TCCACAGACAGCCCTCATAGTTAGCGTAACGA	15
ACCGATTGTCGGCATTTTCGGTCATAATCA	16
TTTAGGACAAATGCTTTAAACAATCAGGTC	17
AGTATAAAGTTCAGCTAATGCAGATGTCTTTC	18
ACATAACGGGAATCGTCATAAATAAAGCAAAG	19
CAGAAGATTAGATAATACATTTGTCGACAA	20
AAGTAAGCAGACACCACGGAATAATATTGACG	21
GAGAGATAGAGCGTCTTTCCAGAGGTTTTGAA	22
GAATTTATTTAATGGTTTGAAATATTCTTACC	23
ACAACATGCCAACGCTCAACAGTCTTCTGA	24
AATACTGCCCAAAAGGAATTACGTGGCTCA	25
GAAACGATAGAAGGCTTATCCGGTCTCATCGAGAACAAGC	26
GCCGTCAAAAAACAGAGGTGAGGCCTATTAGT	27
ACCTTTTTATTTTAGTTAATTTCATAGGGCTT	28
TCAATATCGAACCTCAAATATCAATTCCGAAA	29
GTGATAAAAAGACGCTGAGAAGAGATAACCTT	30
TTTTCACTCAAAGGGCGAAAAACCATCACC	31
GAAATAAAAATCCTTTGCCCGAAAGATTAGA	32
GAGGGTAGGATTCAAAAGGGTGAGACATCCAA	33
GCCCGTATCCGGAATAGGTGTATCAGCCCAAT	34
CAACTGTTGCGCCATTCGCCATTCAAACATCA	35
TTAACACCAGCACTAACAACTAATCGTTATTA	36
GTATAGCAAACAGTTAATGCCCAATCCTCA	37
AATACGTTTGAAAGAGGACAGACTGACCTT	38
TTGACAGGCCACCACCAGAGCCGCGATTTGTA	39
AATAGTAAACACTATCATAACCCTCATTGTGA	40

Sequence (5'→3')	Number
GAAATTATTGCCTTTAGCGTCAGACCGGAACC	41
CTTTTACAAAATCGTCGCTATTAGCGATAG	42
GCTTTCCGATTACGCCAGCTGGCGGCTGTTTC	43
AACAGTTTTGTACCAAAAACATTTTATTTC	44
AAGGAAACATAAAGGTGGCAACATTATCACCG	45
AAGCCTGGTACGAGCCGGAAGCATAGATGATG	46
ACCCTTCTGACCTGAAAGCGTAAGACGCTGAG	47
ACAACTTTCAACAGTTTCAGCGGATGTATCGG	48
CCAGGGTTGCCAGTTTGAGGGGACCCGTGGGA	49
ATCGCAAGTATGTAAATGCTGATGATAGGAAC	50
CATCAAGTAAAACGAACTAACGAGTTGAGA	51
TAAAAGGGACATTCTGGCCAACAAAGCATC	52
AGAGAGAAAAAAATGAAAATAGCAAGCAAACT	53
AGCAAGCGTAGGGTTGAGTGTTGTAGGGAGCC	54
GACCTGCTCTTTGACCCCCAGCGAGGGAGTTA	55
TACGTTAAAGTAATCTTGACAAGAACCGAACT	56
CCCGATTTAGAGCTTGACGGGGAAAAAGAATA	57
TAAATCAAAATAATTCGCGTCTCGGAAACC	58
ATCCCCCTATACCACATTCAACTAGAAAAATC	59
TAAAACGAGGTCAATCATAAGGGAACCGGATA	60
AGGCTCCAGAGGCTTTGAGGACACGGGTAA	61
TCACCAGTACAAACTACAACGCCTAGTACCAG	62
GCGAAAAATCCCTTATAAATCAAGCCGGCG	63
TTTACCCCAACATGTTTTAAATTTCCATAT	64
ATACATACCGAGGAAACGCAATAAGAAGCGCATTAGACGG	65
GATGTGCTTCAGGAAGATCGCACAATGTGA	66
CAGCGAAACTTGCTTTCGAGGTGTTGCTAA	67
GCCTCCCTCAGAATGGAAAGCGCAGTAACAGT	68
TTCATTACGTCAGGACGTTGGGAAATGCAGAT	69
CATGTAATAGAATATAAAGTACCAAGCCGT	70
TTGCTCCTTTCAAATATCGCGTTTGAGGGGGT	71
AAATTAAGTTGACCATTAGATACTTTTGCG	72
GCACAGACAATATTTTTGAATGGGGTCAGTA	73
CATTTGAAGGCGAATTATTCATTTTTGTTTGG	74
CCACCCTCATTTTCAGGGATAGCAACCGTACT	75
CTTTAATGCGCGAACTGATAGCCCCACCAG	76
ATTATCATTCAATATAATCCTGACAATTAC	77
GCGAGTAAAAATATTTAAATTGTTACAAAG	78
CTGTGTGATTGCGTTGCGCTCACTAGAGTTGC	79
TTAGGATTGGCTGAGACTCCTCAATAACCGAT	80
TCTTCGCTGCACCGCTTCTGGTGCGGCCTTCC	81
ATTATACTAAGAAACCACCAGAAGTCAACAGT	82
ATTTACCGGGAACCAGAGCCACCACTGTAGCGC	83
TGACAACTCGCTGAGGCTTGCATTATACCA	84

Sequence (5'→3')	Number
CAGCAAAAGGAAACGTCACCAATGAGCCGC	85
GACCAACTAATGCCACTACGAAGGGGGTAGCA	86
GCCCTTCAGAGTCCACTATTAAAGGGTGCCGT	87
GGCCTTGAAGAGCCACCACCCTCAGAAACCAT	88
GTACCGCAATTCTAAGAACGCGAGTATTATTT	89
CTTAGATTTAAGGCGTTAAATAAAGCCTGT	90
TCAAATATAACCTCCGGCTTAGGTAACAATTT	91
GTCGACTTCGGCCAACGCGCGGGGTTTTTC	92
GCCAGTTAGAGGGTAATTGAGCGCTTTAAGAA	93
GTTTATCAATATGCGTTATACAAACCGACCGT	94
TTATTACGAAGAACTGGCATGATTGCGAGAGG	95
TGAAAGGAGCAAATGAAAAATCTAGAGATAGA	96
TGTAGCCATTAAAATTCGCATTAAATGCCGGA	97
CGCGCAGATTACCTTTTTTAATGGGAGAGACT	98
AAAGGCCGGAGACAGCTAGCTGATAAATTAATTTTTGT	99
AGGAACCCATGTACCGTAACACTTGATATAA	100
GTTTTCAAGGGAGGGAAGGTAAAGTTTATTT	101
AAAGTCACAAAATAAACAGCCAGCGTTTTA	102
AGACGACAAAGAAGTTTTGCCATAATTCGAGCTTCAA	103
AACACCAAATTTCAACTTTAATCGTTTACC	104
TTAAAGCCAGAGCCGCCACCCTCGACAGAA	105
GCCCGAGAGTCCACGCTGGTTTGCAGCTAACT	106
AACGTGGCGAGAAAGGAAGGGAAACCAGTAA	107
GCAATTCACATATTCCTGATTATCAAAGTGTA	108
TTAATGAACTAGAGGATCCCCGGGGGGTAACG	109
ATCCCAATGAGAATTAACTGAACAGTTACCAG	110
AACGCAAAATCGATGAACGGTACCGGTTGA	111
GCTATCAGAAATGCAATGCCTGAATTAGCA	112
CCAATAGCTCATCGTAGGAATCATGGCATCAA	113
ACCTTGCTTGGTCAGTTGGCAAAGAGCGGA	114
GTTTTAACTTAGTACCGCCACCCAGAGCCA	115
GCCTTAAACCAATCAATAATCGGCACGCGCCT	116
TGCATCTTTCCCAGTCACGACGGCCTGCAG	117
TATTAAGAAGCGGGGTTTTGCTCGTAGCAT	118
ACGCTAACACCCACAAGAATTGAAAATAGC	119
GCGAACCTCCAAGAACGGGTATGACAATAA	120
AAATCACCTTCCAGTAAGCGTCAGTAATAA	121
TTTTATTTAAGCAAATCAGATATTTTTTGT	122
AATGGTCAACAGGCAAGGCAAAGAGTAATGTG	123
AGAAAGGAACAACTAAAGGAATTCAAAAAAA	124
TATAAGCCAACCCGTCGGATTCTGACGACAG	125
GCCATCAAGCTCATTTTTTAACCACAAATCCA	126
CAGGAGGTGGGGTCAGTGCCTTGAGTCTCTGA	127
ACACTCATCCATGTTACTTAGCCGAAAGCTGC	128

Sequence (5'→3')	Number
CTCGTATTAGAAATTGCGTAGATACAGTAC	129
TAAATCATATAACCTGTTTAGCTAACCTTTAA	130
TAATCAGCGGATTGACCGTAATCGTAACCG	131
ACAAACGGAAAAGCCCCAAAAACACTGGAGCA	132
TCGGCAAATCCTGTTTGATGGTGGACCCTCAA	133
CTTTTGCAGATAAAAACCAAAATAAAGACTCC	134
TCATTCAGATGCGATTTTAAGAACAGGCATAG	135
GTAATAAGTTAGGCAGAGGCATTTATGATATT	136
CATAAATCTTTGAATACCAAGTGTTAGAAC	137
TCATCGCCAACAAAGTACAACGGACGCCAGCA	138
ATATTTTGGCTTTCATCAACATTATCCAGCCA	139
CCTAAATCAAAATCATAGGTCTAAACAGTA	140
TCACCGACGCACCGTAATCAGTAGCAGAACCG	141
CGATAGCATTGAGCCATTTGGGAACGTAGAAA	142
ATTTTAAAATCAAAATTATTTGCACGGATTCG	143
TATATTTTGTCATTGCCTGAGAGTGGAAGATTG	144
TCAAGTTTCATTAAAGGTGAATATAAAAGA	145
CTGTAGCTTGACTATTATAGTCAGTTCATTGA	146
CAACCGTTTCAAATCACCATCAATTCGAGCCA	147
TTAGTATCACAATAGATAAGTCCACGAGCA	148
CTACCATAGTTTGAGTAACATTTAAAATAT	149
CTCCAACGCAGTGAGACGGGCAACCAGCTGCA	150
CTTATCATTCCCGACTTGCGGGAGCCTAATTT	151
GCTTCTGTTCGGGAGAAACAATAACGTAAAACA	152
GCAAGGCCTCACCAGTAGCACCATGGGCTTGA	153
CGGATTGCAGAGCTTAATTGCTGAAACGAGTA	154
CACATTAAAATTGTTATCCGCTCATGCGGGCC	155
ATTACCTTTGAATAAGGCTTGCCCAAATCCGC	156
GCGGAACATCTGAATAATGGAAGGTACAAAAT	157
TAAATGAATTTTCTGTATGGGATTAATTTCTT	158
CACAACAGGTGCCTAATGAGTGCCCAGCAG	159
AAACAGCTTTTTGCGGGATCGTCAACACTAAA	160
GACAAAAGGTAAAGTAATCGCCATATTTAACAAAACTTTT	161
TAGGTAAACTATTTTTGAGAGATCAAACGTTA	162
GCGCAGACAAGAGGCAAAAGAATCCCTCAG	163
TTCCAGTCGTAATCATGGTCATAAAAGGGG	164
TAAATCGGGATTCCCAATTCTGCGATATAATG	165
CACCAGAAAGGTTGAGGCAGGTCATGAAAG	166
AAAGCACTAAATCGGAACCCTAATCCAGTT	167
AATTGAGAATTCTGTCCAGACGACTAAACCAA	168
ACGGCTACAAAAGGAGCCTTTAATGTGAGAAT	169
CTTTAGGGCCTGCAACAGTGCCAATACGTG	170
TAGAGAGTTATTTTCATTTGGGGATAGTAGTAGCATTA	171
TGTCACAATCTTACCGAAGCCCTTTAATATCA	172

Sequence (5'→3')	Number
CCAACAGGAGCGAACCAGACCGGAGCCTTTAC	173
AATAGCTATCAATAGAAAATTCAACATTCA	174
TGGAACAACCGCCTGGCCCTGAGGCCCGCT	175
TTATACCACCAAATCAACGTAACGAACGAG	176
ATATTCGGAACCATCGCCCACGCAGAGAAGGA	177
TTTCGGAAGTGCCGTCGAGAGGGTGAGTTTCG	178
TATAACTAACAAAGAACGCGAGAACGCCAA	179
ATACCCAACAGTATGTTAGCAAATTAGAGC	180
TATCGGCCGCAAGGCGATTAAGTTTACCGAGC	181
GATTTAGTCAATAAAGCCTCAGAGAACCCTCA	182
TTTATCAGGACAGCATCGGAACGACACCAACC	183
CCACCCTCTATTCACAAACAAATACCTGCCTA	184
AACGCAAAGATAGCCGAACAAACCCTGAAC	185
AGCGCGATGATAAATTGTGTCGTGACGAGA	186
CCTGATTGCAATATATGTGAGTGATCAATAGT	187
TTCTACTACGCGAGCTGAAAAGGTTACCGCGC	188
AGGCAAAGGGAAGGGCGATCGGCAATTCCA	189
AGAAAACAAAGAAGATGATGAAACAGGCTGCG	190

Table S6: Modified ssDNA strands.

Sequence (5'→3')	Number
biotin - GAAACGATAGAAGGCTTATCCGGTCTCATCGAGAACAAGC	26
biotin - TAGAGAGTTATTTTCATTTGGGGATAGTAGTAGCATTA	171

11.1 Energy Transfer Assembly

Table S7: Replaced ssDNA strands for confocal measurements.

Sequence (5'→3')	Number
ACGGCTACAAAAGGAGCCTTTAATGTGAGAAT - ATTO 647N	169
GATGGCTTATCAAAAA - ATTO 532 - GATTAAGAGCGTCC	9
AAATTAAGTTGACCATTAGATACTTTTGCGAAAAAAAAAAAAAAA AAAAA	72
GCTATCAGAAATGCAATGCCTGAATTAGCAAAAAAAAAAAAAAA AAAAA	112
AATGGTCAACAGGCAAGGCAAAGAGTAATGTGAAAAAAAAAAAA AAAAAAA	123
ATACATACCGAGGAAACGCAATAAGAAGCGCATTAGACGGCCAAATAA	65
AGACGACAAAGAAGTTTTGCCATAATTCGAGCTTCAATCAGGAT	103

Oligonucleotide sequence on nanoparticles (5'→3'):

TTTTTTTTTTTTTTTTTTTTTTTT-Thiol

11.2 One Color DNA-PAINT Sample

Table S8: Replaced ssDNA strands for one color DNA-PAINT measurements.

Sequence (5'→3')	Number
AAGGCCGCTGATACCGATAGTTGCGACGTTAGTTAAATGCCCG	1
TCTAAAGTTTTGTCGTCTTTCCAGCCGACAATTAAATGCCCG	6
AGCCAGCAATTGAGGAAGGTTATCATCATTTTTTAAATGCCCG	8
GCGGATAACCTATTATTCTGAAACAGACGATTTTAAATGCCCG	10
CAAATCAAGTTTTTTGGGGTCGAAACGTGGATTAAATGCCCG	13
TCCACAGACAGCCCTCATAGTTAGCGTAACGATTAAATGCCCG	15
CAGAAGATTAGATAATACATTTGTCGACAATTAAATGCCCG	20
GCCGTCAAAAAACAGAGGTGAGGCCTATTAGTTTAAATGCCCG	27
TCAATATCGAACCTCAAATATCAATTCCGAAATTAAATGCCCG	29
TTTTCACTCAAAGGGCGAAAAACCATCACCTTAAATGCCCG	31
GCCCGTATCCGGAATAGGTGTATCAGCCCAATTTAAATGCCCG	34
TTAACACCAGCACTAACAACTAATCGTTATTATTAAATGCCCG	36
GTATAGCAAACAGTTAATGCCCAATCCTCATTAAATGCCCG	37
ACCCTTCTGACCTGAAAGCGTAAGACGCTGAGTTAAATGCCCG	47
ACAACTTTCAACAGTTTCAGCGGATGTATCGGTTAAATGCCCG	48
TAAAAGGGACATTCTGGCCAACAAAGCATCTTAAATGCCCG	52
AGCAAGCGTAGGGTTGAGTGTTGTAGGGAGCCTTAAATGCCCG	54
GACCTGCTCTTTGACCCCCAGCGAGGGAGTTATTAAATGCCCG	55
CCCGATTTAGAGCTTGACGGGGAAAAAGAATATTAAATGCCCG	57
AGGCTCCAGAGGCTTTGAGGACACGGGTAATTAAATGCCCG	61
TCACCAGTACAAACTACAACGCCTAGTACCAGTTAAATGCCCG	62
GCGAAAAATCCCTTATAAATCAAGCCGGCGTTAAATGCCCG	63
CAGCGAAACTTGCTTTCGAGGTGTTGCTAATTAAATGCCCG	67
GCCTCCCTCAGAATGGAAAGCGCAGTAACAGTTTAAATGCCCG	68
GCACAGACAATATTTTTGAATGGGGTCAGTATTAAATGCCCG	73
CCACCCTCATTTTCAGGGATAGCAACCGTACTTTAAATGCCCG	75
CTTTAATGCGCGAACTGATAGCCCCACCAGTTAAATGCCCG	76
TTAGGATTGGCTGAGACTCCTCAATAACCGATTTAAATGCCCG	80
TGACAACTCGCTGAGGCTTGCATTATACCATTAAATGCCCG	84
GACCAACTAATGCCACTACGAAGGGGGTAGCATTAAATGCCCG	86
GCCCTTCAGAGTCCACTATTAAAGGGTGCCGTTTAAATGCCCG	87
TGAAAGGAGCAAATGAAAAATCTAGAGATAGATTAAATGCCCG	96
AGGAACCCATGTACCGTAACACTTGATATAATTAAATGCCCG	100
GCCCGAGAGTCCACGCTGGTTTGCAGCTAACTTTAAATGCCCG	106
AACGTGGCGAGAAAGGAAGGGAAACCAGTAATTAAATGCCCG	107
ACCTTGCTTGGTCAGTTGGCAAAGAGCGGATTAAATGCCCG	114
GTTTTAACTTAGTACCGCCACCCAGAGCCATTAAATGCCCG	115
TATTAAGAAGCGGGGTTTTGCTCGTAGCATTTAAATGCCCG	118
AAATCACCTTCCAGTAAGCGTCAGTAATAATTAAATGCCCG	121
AGAAAGGAACAACTAAAGGAATTCAAAAAAATTAAATGCCCG	124

Sequence (5'→3')	Number
CAGGAGGTGGGGTCAGTGCCTTGAGTCTCTGAATTTACCGTTAAATG CCCG	127
TCGGCAAATCCTGTTTGATGGTGGACCCTCAATTAAATGCCCG	133
TCATCGCCAACAAAGTACAACGGACGCCAGCATTAAATGCCCG	138
CTCCAACGCAGTGAGACGGGCAACCAGCTGCATTAAATGCCCG	150
TAAATGAATTTTCTGTATGGGATTAATTTCTTTTAAATGCCCG	158
AAACAGCTTTTTGCGGGATCGTCAACACTAAATTAAATGCCCG	160
GCGCAGACAAGAGGCAAAAGAATCCCTCAGTTAAATGCCCG	163
CACCAGAAAGGTTGAGGCAGGTCATGAAAGTTAAATGCCCG	166
AAAGCACTAAATCGGAACCCTAATCCAGTTTTAAATGCCCG	167
ACGGCTACAAAAGGAGCCTTTAATGTGAGAATTTAAATGCCCG	169
CTTTAGGGCCTGCAACAGTGCCAATACGTGTTAAATGCCCG	170
TGGAACAACCGCCTGGCCCTGAGGCCCGCTTTAAATGCCCG	175
ATATTCGGAACCATCGCCCACGCAGAGAAGGATTAAATGCCCG	177
TTTCGGAAGTGCCGTCGAGAGGGTGAGTTTCGTTAAATGCCCG	178
TTTATCAGGACAGCATCGGAACGACACCAACCTAAAACGATTAAATG CCCG	183
CCACCCTCTATTCACAAACAAATACCTGCCTATTAAATGCCCG	184

Imager strand (5'→3'): CGGGCA-ATTO 655

11.3 Two Color DNA-PAINT Sample

Table S9: Replaced ssDNA strands for two color DNA-PAINT measurements.

Sequence (5'→3')	Number
AAGGCCGCTGATACCGATAGTTGCGACGTTAGTTAAATGCCCG	1
TCTAAAGTTTTGTCGTCTTTCCAGCCGACAATTAAATGCCCG	6
TCCACAGACAGCCCTCATAGTTAGCGTAACGATTAAATGCCCG	15
GCCCGTATCCGGAATAGGTGTATCAGCCCAATTTAAATGCCCG	34
ACAACTTTCAACAGTTTCAGCGGATGTATCGGTTAAATGCCCG	48
GACCTGCTCTTTGACCCCCAGCGAGGGAGTTATTAAATGCCCG	55
TCACCAGTACAAACTACAACGCCTAGTACCAGTTAAATGCCCG	62
CAGCGAAACTTGCTTTCGAGGTGTTGCTAATTAAATGCCCG	67
GCCTCCCTCAGAATGGAAAGCGCAGTAACAGTTTAAATGCCCG	68
CCACCCTCATTTTCAGGGATAGCAACCGTACTTTAAATGCCCG	75
TTAGGATTGGCTGAGACTCCTCAATAACCGATTTAAATGCCCG	80
GACCAACTAATGCCACTACGAAGGGGGTAGCATTAAATGCCCG	86
AGGAACCCATGTACCGTAACACTTGATATAATTAAATGCCCG	100
GTTTTAACTTAGTACCGCCACCCAGAGCCATTAAATGCCCG	115
TATTAAGAAGCGGGGTTTTGCTCGTAGCATTTAAATGCCCG	118
AAATCACCTTCCAGTAAGCGTCAGTAATAATTAAATGCCCG	121
AGAAAGGAACAACTAAAGGAATTCAAAAAAATTAAATGCCCG	124

Sequence (5'→3')	Number
TAAATGAATTTTCTGTATGGGATTAATTTCTTTTAAATGCCCG	158
GCGCAGACAAGAGGCAAAAGAATCCCTCAGTTAAATGCCCG	163
CACCAGAAAGGTTGAGGCAGGTCATGAAAGTTAAATGCCCG	166
ACGGCTACAAAAGGAGCCTTTAATGTGAGAATTTAAATGCCCG	169
ATATTCGGAACCATCGCCCACGCAGAGAAGGATTAAATGCCCG	177
TTTCGGAAGTGCCGTCGAGAGGGTGAGTTTCGTTAAATGCCCG	178
CCACCCTCTATTCACAAACAAATACCTGCCTATTAAATGCCCG	184
TCGAATTCGGGAAACCTGTCGTGCAGCTGATTTTTCCTCCTCCT	2
CAAATCAAGTTTTTTGGGGTCGAAACGTGGATTTCCTCCTCCT	13
GCCGTCAAAAAACAGAGGTGAGGCCTATTAGTTTTCCTCCTCCT	27
TCAATATCGAACCTCAAATATCAATTCCGAAATTTCCTCCTCCT	29
TTTTCACTCAAAGGGCGAAAAACCATCACCTTTCCTCCTCCT	31
GAAATAAAAATCCTTTGCCCGAAAGATTAGATTTCCTCCTCCT	32
ACCCTTCTGACCTGAAAGCGTAAGACGCTGAGTTTCCTCCTCCT	47
TAAAAGGGACATTCTGGCCAACAAAGCATCTTTCCTCCTCCT	52
AGCAAGCGTAGGGTTGAGTGTTGTAGGGAGCCTTTCCTCCTCCT	54
CCCGATTTAGAGCTTGACGGGGAAAAAGAATATTTCCTCCTCCT	57
GCGAAAAATCCCTTATAAATCAAGCCGGCGTTTCCTCCTCCT	63
GCACAGACAATATTTTTGAATGGGGTCAGTATTTCCTCCTCCT	73
CTTTAATGCGCGAACTGATAGCCCCACCAGTTTCCTCCTCCT	76
CTGTGTGATTGCGTTGCGCTCACTAGAGTTGCTTTCCTCCTCCT	79
ATTATACTAAGAAACCACCAGAAGTCAACAGTTTTCCTCCTCCT	82
GCCCTTCAGAGTCCACTATTAAAGGGTGCCGTTTTCCTCCTCCT	87
GTCGACTTCGGCCAACGCGCGGGGTTTTTCTTTCCTCCTCCT	92
TGAAAGGAGCAAATGAAAAATCTAGAGATAGATTTCCTCCTCCT	96
AACGTGGCGAGAAAGGAAGGGAAACCAGTAATTTCCTCCTCCT	107
TCGGCAAATCCTGTTTGATGGTGGACCCTCAATTTCCTCCTCCT	133
CTACCATAGTTTGAGTAACATTTAAAATATTTTCCTCCTCCT	149
CACAACAGGTGCCTAATGAGTGCCCAGCAGTTTCCTCCTCCT	159
AAAGCACTAAATCGGAACCCTAATCCAGTTTTTCCTCCTCCT	167
CTTTAGGGCCTGCAACAGTGCCAATACGTGTTTCCTCCTCCT	170

Imager Strands (5'→3'):

CGGGCA-ATTO 655

AGGAGGA-Cy3B

11.4 NRO 6 nm Grid Sample

All strands (except 26 and 171) are extended with the aptamer sequence (TTAAATGCCCG).

Imager Strand (5'→3'): CGGGCA-ATTO 655

12. References

1 S. M. Douglas, A. H. Marblestone, S. Teerapittayanon, A. Vazquez, G. M. Church and W. M. Shih, Rapid prototyping of 3D DNA-origami shapes with caDNAno, *Nucleic acids research*, 2009, **37**, 5001–5006.

2 T. Cordes, J. Vogelsang and P. Tinnefeld, On the mechanism of Trolox as antiblinking and antibleaching reagent, *Journal of the American Chemical Society*, 2009, **131**, 5018–5019.

3 J. Vogelsang, R. Kasper, C. Steinhauer, B. Person, M. Heilemann, M. Sauer and P. Tinnefeld, A reducing and oxidizing system minimizes photobleaching and blinking of fluorescent dyes, *Angewandte Chemie (International ed. in English)*, 2008, **47**, 5465–5469.

4 A. Edelstein, N. Amodaj, K. Hoover, R. Vale and N. Stuurman, Computer control of microscopes using μManager, *Current protocols in molecular biology*, 2010, **Chapter 14**, Unit14.20.

5 G. P. Acuna, M. Bucher, I. H. Stein, C. Steinhauer, A. Kuzyk, P. Holzmeister, R. Schreiber, A. Moroz, F. D. Stefani, T. Liedl, F. C. Simmel and P. Tinnefeld, Distance dependence of single-fluorophore quenching by gold nanoparticles studied on DNA origami, *ACS nano*, 2012, **6**, 3189–3195.

6 P. C. Nickels, B. Wünsch, P. Holzmeister, W. Bae, L. M. Kneer, D. Grohmann, P. Tinnefeld and T. Liedl, Molecular force spectroscopy with a DNA origami-based nanoscopic force clamp, *Science (New York, N.Y.)*, 2016, **354**, 305–307.

7 S. A. McKinney, A.-C. Déclais, D. M. J. Lilley and T. Ha, Structural dynamics of individual Holliday junctions, *Nat Struct Biol*, 2003, **10**, 93–97.

8 C. Hyeon, J. Lee, J. Yoon, S. Hohng and D. Thirumalai, Hidden complexity in the isomerization dynamics of Holliday junctions, *Nature Chem*, 2012, **4**, 907–914.

9 A. Gietl, P. Holzmeister, D. Grohmann and P. Tinnefeld, DNA origami as biocompatible surface to match single-molecule and ensemble experiments, *Nucleic acids research*, 2012, **40**, e110.

10 K. Kramm, T. Schröder, J. Gouge, A. M. Vera, K. Gupta, F. B. Heiss, T. Liedl, C. Engel, I. Berger, A. Vannini, P. Tinnefeld and D. Grohmann, DNA origami-based single-molecule force spectroscopy elucidates RNA Polymerase III pre-initiation complex stability, *Nat Commun*, 2020, **11**, 2828.

11 I. Kamińska, J. Bohlen, R. Yaadav, P. Schüler, M. Raab, T. Schröder, J. Zähringer, K. Zielonka, S. Krause and P. Tinnefeld, Graphene Energy Transfer for Single-Molecule Biophysics, Biosensing, and Super-Resolution Microscopy, *Advanced materials (Deerfield Beach, Fla.)*, 2021, e2101099.

12 B. K. Müller, E. Zaychikov, C. Bräuchle and D. C. Lamb, Pulsed interleaved excitation, *Biophysical journal*, 2005, **89**, 3508–3522.